CIVIL & ENVIRONMENTAL ENGINEERING

RESEARCH REPORT

Effects of Debonded Strands on the Production and Performance of Prestressed Concrete Beams

by

Rigoberto Burgueño

Yi Sun

Report No. CEE-RR – 2011/01

January 2011

Research Report for MDOT under Contract No. 2006-0411/7
SPR No. 87346

Department of Civil and Environmental Engineering
Michigan State University
East Lansing, Michigan

1. Research Report RC-1546	2. Government Accession No.	3. MDOT Project Manager Steve Kahl
4. Title and Subtitle Effects of Debonded Strands on the Production and Performance of Prestressed Concrete Beams		5. Report Date January 14, 2011
7. Author(s) Rigoberto Burgueño, Ph.D. and Yi Sun		6. Performing Organization Code
9. Performing Organization Name and Address Michigan State University Department of Civil and Environmental Engineering 3546 Engineering Building East Lansing, MI 48824-1226		8. Performing Org Report No. CEE-RR – 2011/01
12. Sponsoring Agency Name and Address Michigan Department of Transportation Construction and Technology Division P.O. Box 30049 Lansing, MI 48909		10. Work Unit No. (TRAIS) 11. Contract Number: 2006-0411/7 11(a). Authorization Number: 12
15. Supplementary Notes		13. Type of Report & Period Covered 08-08-07 to 08-30-10 14. Sponsoring Agency Code

16. Abstract

Strand debonding is a common approach used to reduce cracking at the ends of pre-tensioned concrete beams. While the method has been successful to some extent, end cracking of pre-tensioned beam ends continues to be a problem. Experimental and numerical approaches were conducted in this study in order to achieve a further understanding of strand debonding. Twenty-four small-scale prestressed concrete beam units were tested and used for the calibration of nonlinear finite element models simulating concrete-strand bond behavior, while three models of AASHTO box girders were established to investigate an incident of end cracking encountered in the manufacturing of a bridge girder. The numerical simulations were in good agreement with the experiment data and damage evidence on prestressed girders production indicating that the lack of bonding will maximize the dilation of strand after release in the debonded region and that such dilation may cause concrete damage in the debonded region if there is tight contact between concrete and strand. It was also found that such problem will be eliminated if enough room is provided for the strand dilation. Thus, the use of "rigid" or oversized debonding material is recommended for strand debonding practice.

17. Key Words Strand; Debonding; Sheathed; Blanketed; Prestresss; Pre-tension; Concrete, Box Beams; Experiment; Finite Element;	18. Distribution Statement No restrictions. This document is available to the public through the Michigan Department of Transportation.

19. Security Classification (report) Unclassified	20. Security Classification (Page) Unclassified	21. No of Pages 180	22. Price

Report No. CEE-RR – 2011/01

EFFECTS OF DEBONDED STRANDS ON THE PRODUCTION AND PERFORMANCE OF PRESTRESSED CONCRETE BEAMS

by

Rigoberto Burgueño, Ph.D.
Associate Professor of Structural Engineering

Yi Sun
Graduate Research Assistant

Technical Report to Michigan DOT under Contract No. 2006-0411/7
SPR No. 87346

Department of Civil and Environmental Engineering
Michigan State University
East Lansing, MI 48824-1226

January 2011

DISCLAIMER

The opinions, findings, conclusions and recommendations presented in this report are those of the authors alone and do not necessarily represent the views and opinions of Michigan State University or the Michigan Department of Transportation.

ABSTRACT

EFFECTS OF DEBONDED STRANDS ON THE PRODUCTION AND PERFORMANCE OF PRESTRESSED CONCRETE BEAMS

by

Rigoberto Burgueño, Ph.D.
Associate Professor of Structural Engineering

Yi Sun
Graduate Research Assistant

Strand debonding is a common approach used to reduce cracking at the ends of pre-tensioned concrete beams. While the method has been successful to some extent, end cracking of pre-tensioned beam ends continues to be a problem. Experimental and numerical approaches were conducted in this study in order to achieve a further understanding of strand debonding. Twenty-four small-scale prestressed concrete beam units were tested and used for the calibration of nonlinear finite element models simulating concrete-strand bond behavior, while three models of AASHTO box girders were established to investigate an incident of end cracking encountered in the manufacturing of a bridge girder. The numerical simulations were in good agreement with the experiment data and damage evidence on prestressed girders production indicating that the lack of bonding will maximize the dilation of strand after release in the debonded region and that such dilation may cause concrete damage in the debonded region if there is tight contact between concrete and strand. It was also found that such problem will be eliminated if enough room is provided for the strand dilation. Thus, the use of “rigid” or oversized debonding material is recommended for strand debonding practice.

AKNOWLEDGEMENTS

The research described in this report was carried out under funding from the Michigan Department of Transportation, Contract 2006-0411/7, SPR No. 87346, with Mr. Steve Kahl as project manager. The financial support of MDOT and the coordination of Mr. Kahl throughout the execution of the experimental program are gratefully acknowledged. The countless hours of assistance and collaboration of Miss. Melissa Donoso in the experimental tasks of this research are particularly acknowledged. Thanks are also due to Mr. Siavosh Ravanbakhsh and Mr. Charles Meddaugh, whom, as the main technical staff of MSU's Civil Infrastructure Laboratory were instrumental for the completion of the experimental tasks in the project. The authors are also thankful to many other students that also helped along the way in the diverse experimental tasks, among them are: Aixia Shao, David Stringer, Emily Winn, Xuejian Liu, and Lindsey Diggelmann. Finally, the authors sincerely appreciate all the help and insight provided by Mr. Tom Grumbine, of the Premarc Corporation (Grand Rapids, MI) for his assistance with material supplies for the experiments and valuable information on the production of the prestressed bridge box beam considered in the analytical case study in this research.

TABLE OF CONTENTS

LIST OF TABLES

LIST OF FIGURES

(Page left blank on purpose)

Chapter 1 Introduction and Background

1.1 Statement of Problem

Strand debonding is a common procedure used in prestressed concrete members for limitation of compressive and tensile concrete stresses near the element ends, i.e., in the anchorage zone. However, a recent problem faced by the Michigan Department of Transportation (MDOT) on the production of pre-tensioned box girders with debonded strands (Figure 1) has raised questions on the adequacy of this manufacturing the design practice. While many issues are associated with the effects of debonded strands, little research has been conducted on this topic, and the available design guidelines from the AASHTO-LRFD specifications (limit to the number of unbonded strands and their arrangement) are quite simple and their wide applicability is questionable. However, no guidance exists on manufacturing practice, debonded length limits, reinforcement within the unbonded region, layout, or cutting sequence. Therefore, a better understanding of the effects of debonded strands, particularly those that can lead to distress, is needed for improved design and manufacturing practice.

Figure 1 End Damage of Pre-tensioned Box Girder

1.2 End Cracking in Pre-tensioned Concrete Beams

The transfer of stresses from prestressing strands to concrete at the end of pre-tensioned beams result in a complex stress state that can lead to concrete cracking. The type of cracking typically observed in the anchorage zone of I shape girder is schematically shown in Figure 2 [7].

The presence of these cracks is of concern since they can provide a path for the ingress of chlorides and they compromise the bond mechanisms between the strands and concrete in the end region.

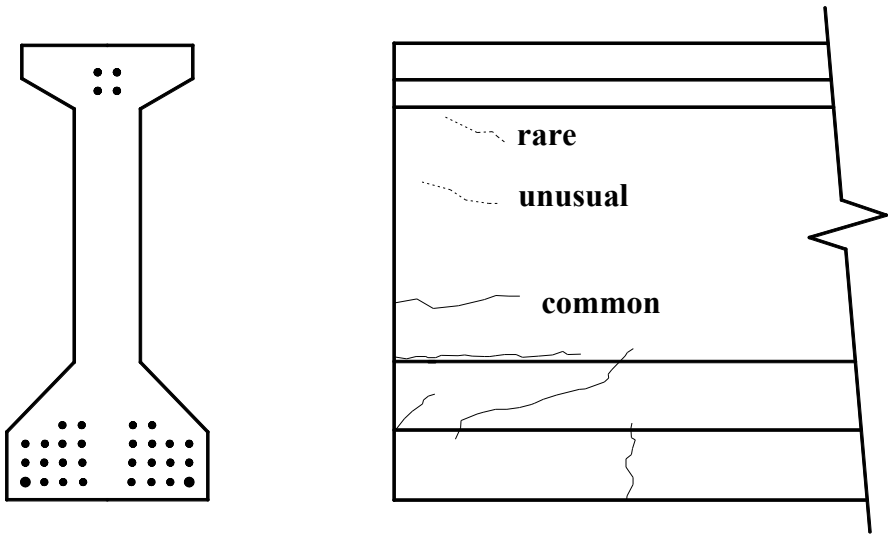

Figure 2 Typically Observed Anchorage Zone Cracks

The sources of cracking are multiple, and they include:

i) Material related: tensile strength of concrete,

ii) Design related: amount and detailing (position) of bursting resistance and confinement reinforcement, and

iii) Production related: strand release patterns [7] and length of free strand in casting bed [8].

1.3 Strand Debonding

Strand debonding is one of the methods used to eliminate or minimize cracking at beam ends. The idea of debonding is to delay the stress transfer between prestressing strand and concrete due to bond. Since the stress transfer between strand and concrete starts further into the concrete element, the stresses at the end regions are reduced. Strand debonding is normally achieved by placing plastic sheathing around the strand and two types of debondng material are currently used (both made of plastic-type materials, namely, flexible split-sheathing and a more rigid preformed tube. Details of debonding materials are discussed in Section 2.4.2.

While the use of debonded strands has been found to be generally safe [3], excessive debonding of prestressing strands can have a significant impact on the structural performance of

pre-tensioned beams [9]. Thus, care must be taken in the number of debonded strands, their debonded length, and the release pattern.

Even though the debonding of strands by means of sheathing with plastic covers has been successful to some extent, the cracking of beam ends continues to be a problem in the production of pre-tensioned concrete beams. Part of the reason for this lingering problem is that there are many influencing factors and the solutions have been based on rough ad-hoc approaches or on simple elastic stress analyses. A further understanding and investigating of the effect of strand debonding is thus necessary.

1.4 Introduction of Experimental Program

The motivation of this research project is to investigate the cracking problem in the end region of prestressed box girders. However, due to the limitation of time and facilities, it is unlikely to build and study actual box girders. As a result, the objective of the experiment program in this research is aimed at studying the bonding mechanism between 0.6 in. prestressing strand and concrete and the influences of different parameters such as releasing methodology, debonding material, debonding length, free strand length and confinement level, etc. The experiment data will also be used as reference for the bonding mechanism simulation, which will be discussed in Chapter 3 .

There are three parts in the experiment program, namely, strand bond performance evaluation, cylinder pull-out tests and bond transfer evaluation. The strand bond performance evaluation is conducted to verify the bonding quality of the prestressing used in this research. Basic bonding mechanism between strand and concrete and the effect of debonding material and confinement on bonding strength is studied with concrete cylinder pull-out tests. And then in the bond transfer evaluation part, 24 small prestressed concrete beam units with different cross section, number of prestressing strand, debonding material, deboned length, releasing methodology, free strand length confinement level, etc., are constructed and the bonding behavior between prestressed strand and concrete is investigated. The results from bond transfer evaluation will be used to calibrate the simulation of bonding mechanism in finite element models and then the bond simulation will be used in models of box girders, of which the end region will be investigated.

1.5 Research Hypotheses

The research work presented in this report was aimed at resolving the following two hypotheses:

- Concrete in the end region on pre-tensioned products may be damaged after release of prestressing strand due to the strand-concrete interaction in the debonded region, which is not considered in current design guidelines.
- Strand-concrete bond simulation calibrated with small scale beam units can be applied to full scale box girder model to investigate end cracking problems.

1.6 Research Objective

The objective of the research reported in this report was to investigate the effects of debonded strands in pre-tensioned concrete beams in terms of stress-transfer behavior and beam-end cracking through experimentally calibrated finite element models. The study was guided by completing four tasks:

I. **Experimental Characterization of Strand Bond**. The bond strength and bond behavior of fully-bonded and debonded strand in concrete by means of pull-out tests on unstressed strand.

II. **Experimental Characterization of Stress Transfer in Pre-tensioned Beams.** The bond characteristics of bonded and debonded strand in pre-tensioned element in terms of stress transfer behavior; that is, transfer length, were experimentally evaluated through 24 small-scale beams.

III. **Simulation of Strand Bond in Pre-tensioned Beams.** Three-dimensional nonlinear finite element models were developed to simulate bond behavior and calibrated with the experimental results of Task II.

IV. **Simulation Studies of Anchorage Zones in Full-Size Beams.** The stress state at the anchorage zones of actual full-size pre-tensioned bridge beams were studied through numerical simulations using nonlinear 3D finite element models to evaluate the effect of debonded strand on beam end cracking and compare with recorded field observations.

1.7 Organization of the Report

The report is organized into seven chapters. Chapter 2 provides a literature review related to strand-concrete bond and strand deboning. The definitions of important parameters related to this study are included in this chapter. Chapter 3 discusses Task I in this research, which is the investigation of bond performance of unstressed strand. The experiment to evaluate stress transfer performance in pre-tensioned concrete beam units (Task II) is introduced in Chapter 4 . Chapter 5 gives the simulation of strand-concrete bond in which the beam units in Task II are modeled and calibrated with experiment data. The calibrated parameters are then introduced to full-size box girder models which are discussed in Chapter 6 . A brief summary of the findings and conclusions drawn from this research is provided in in Chapter 7 . Detailed information from each of these chapters and data for the concrete material model used in the finite element simulations are given in the Appendices.

Chapter 2 Literature Review

This chapter provides relevant background on the problem of cracking at the ends of pre-tensioned concrete beams and the issues related to the bond between concrete and prestressing strand. A brief review of the previous work related to this topic addressed in this research is provided. This chapter is divided into five sections, namely,(1) the effect of strand release and beam end cracking, (2) bond in prestressed concrete, (3) transfer length, (4) strand debonding and (5) strand bond performance.

2.1 Effects of Strand Release and Beam End Cracking

Aimed at understanding and eliminating the vertical cracks that appear in the end region of pre-tensioned members during detensioning, a study was conducted by Mirza and Tawfik [8] in the late 1970s. Based on a relatively simple model, a theory was proposed that stated that uncut strands should be lengthened to accommodate the elastic shortening of girders as some of the strands are cut. The problem was attributed to the restraining force from the uncut strands, which leads to vertical cracks near the ends of girders, where the compression stress has not been fully transferred.

The model developed by Mirza and Tawfik was one-dimensional and based on the assumption of linear-elastic behavior of concrete and steel, a frictionless casting bed, and negligible dynamic effect. Furthermore, the use of beam theory when stresses were calculated indicated that the model could not reflect the three-dimensional character of the stress state in the beam end region.

In spite of the simplifications, several valuable conclusions were obtained from Mirza and Tawfik's study. The study considered the effects on four beam segments in a single line of a casting bed, in which the distance between the beam segments was termed 'span'. First, shorter free strand in the casting bed will lead to greater restraint forces. As a result, free strand with longer length should be provided to prevent beam end cracking. Second, the restraining forces will be largest in the span that is cut first when several free spans are present, while the same or lower restraint force will be reached if simultaneous release at each free span can be realized. Mirza and Tawfik suggested that consideration should be given to purposely release the longest free span first.

The model used by Mirza and Tawfik only accounted for longitudinal stresses. Thus, it cannot explain the cracks developed at an angle to the girder axis. Moreover, the model cannot be used to investigate the influence of strand release patterns on end cracking.

A further study on the end cracking of pre-tensioned I-shape concrete girders, including numerical and experimental investigation, was performed by Kannel et al. [7] in the late 1990s. Kannel's study overcame the limitations of Mirza and Tawfik's work. Three-dimensional finite element models were used to assess the stress state at the girder end, beam elements for the remainder of the girder, and the pre-tensioning strands were simulated with truss elements. The models used linear elastic materials but the researchers noted that their goal was not to determine exact stress levels but rather to identify trends in the stress fields.

With the noted approach the investigators studied the effect of different strand release patterns on the three dimensional stress states at the beam end region. The case studies also considered the use of debonded strands to minimize stress levels. The dynamic effects were not considered for either bonded or deboned strands. The results of the numerical models were compared with 54 in. deep pre-tensioned I-beams. The conclusions from the study were: (i) strand cutting order can dramatically change the stress field in the beam end region and reduce or eliminate cracking, (ii) selective debonding of strand can also be used to control cracking, and (iii) increasing the slope of the beam flange reduces the likelihood of horizontal cracking at the bottom flange/web interface.

While Kannel et al. evaluated the effect of strand debonding, the observed beneficial effects were related to the increase in strand free length, supporting the conclusions of Mirza and Tawfik. There are several limitations in the models used in the study of Kannel et al.: (i) strands were simulated with truss element, thus expansion of strand after release cannot be captured by the model, (ii) bond slip between concrete and strand is not captured by the model since the interaction is simulated with spring elements and thus stress concentration may happen only at the very beam end.

2.2 Bond in Prestressed Concrete

Bond between prestressing steel and concrete has been studied considerably along with the development of prestressing concrete. This parameter is of great importance since the transfer of tensile force in the prestressing strand to the concrete relies on bond and this is the basis of the

concept of prestressing concrete. The bond between strand and concrete is considered in design through semi-empirical formulations of transfer and development length to ensure proper anchorage of the prestressing strand. The bonding mechanism and importance of bond should be understood for the purpose of bond simulation, which is at the core of this study.

2.2.1 Bonding Mechanisms

Considerable research has been reported on the bond between pre-tensioned strand and concrete, and it is commonly classified into three distinct mechanisms: (1) adhesion, (2) Hoyer's effect and (3) mechanical interlock. Each of these mechanisms is explained briefly in the following:

Adhesion: This refers to the physical and chemical interlock between the microscopically rough steel surface and the cementitious material. Adhesion helps in bond transfer only when there is no relative slip of the strand with the concrete. This mechanism is relatively small and hence often neglected.

Hoyer's Effect: The prestressing strand will contact laterally and the strand diameter will decrease due to the material's Poisson's ratio upon being tensioned. When the strand is released, this lateral contraction is recovered and the strand dilates. This dilation is restrained by the surrounding hardened concrete, preventing the strand from returning to its original diameter. This restraint is in the form of a radial normal force on the strand, inducing frictional force along the axis of the strand (Figure 3). At the end of the beam, where the surrounding concrete does not exist, the strand is free to expand, and hence the strand at the end has a relatively larger diameter than the portion embedded in concrete. This produces a wedge effect. This anchorage mechanism was first described by Hoyer in 1939 [21] and it is thus commonly referred to as Hoyer's effect. The concrete resists this wedging effect transferring part of the stress from the strand to the concrete.

Mechanical Interlock: Seven wire prestressing strands consist of six wires wound in a helical shape around a single wire. When concrete is cast around the strands the hardened concrete shape matches that of the stressed twisted wire strand. Due to the match casting between the concrete and strand, the concrete resists the unwinding of the strand providing slip resistance. Mechanical interlock is the main contributor to bond when the stresses are increased beyond the initial transfer stresses.

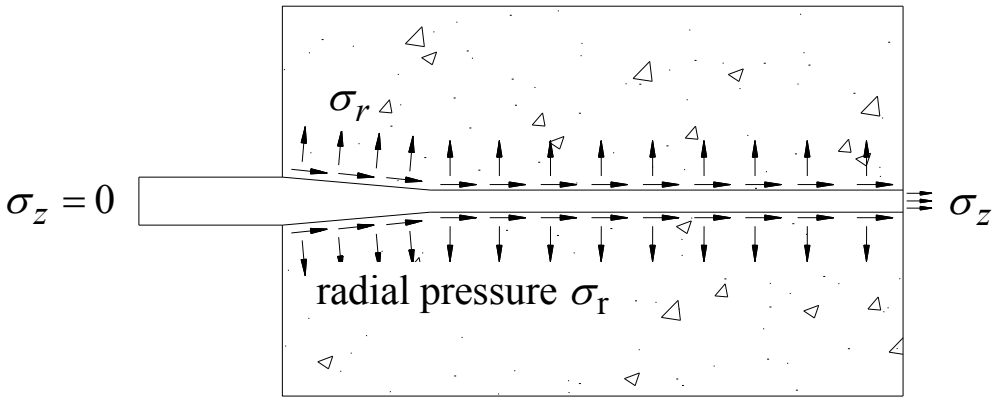

Figure 3 Hoyer's Effect

2.2.2 Prestress Transfer

The approximate distribution of the bond stress τ at transfer due to all of the mechanisms cited above is shown in Figure 4 [31]. At the location where τ becomes zero, the stress in the strand becomes equal to the effective prestress (σ_z = constant). The length associated with this is termed the bond length. This length will depend on the quality of the bond and on the transverse pressure provided by the member geometry and transverse reinforcement. The prestressing force is introduced into the member until the concrete stresses exhibit a linear distribution over the section. [31] The distance along the length of the member, after which strain compatibility between the strand and concrete is achieved and the stresses in the strand become a constant is referred to as the transfer length, L_t.

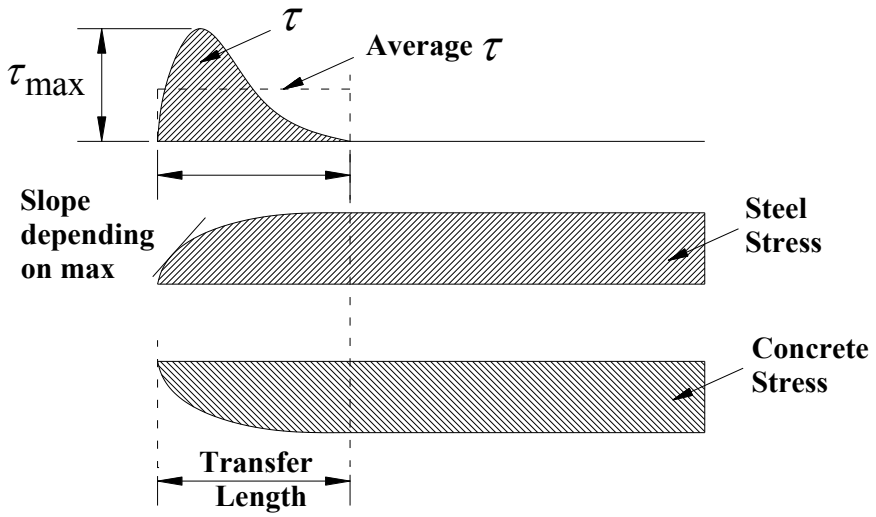

Figure 4 Bond Stress Distribution at Strand End [31]

At the face of the concrete unit the steel and concrete stresses are zero. The shear or bond stress between the strand and the concrete increases rapidly until it reaches its maximum value (bond strength), beyond which it decreases approximately according to a parabolic curve. Due to the bond effect, compressive stresses radiate from the strand into the concrete causing warping at the member end (Figure 5a) [31]. As a consequence, a zone of compressive stresses develops acting radially towards the strand. This further enhances the Hoyer effect. However, this deformation also introduces tensile stresses (Figure 5b) [31] that require the provision of transverse reinforcement.

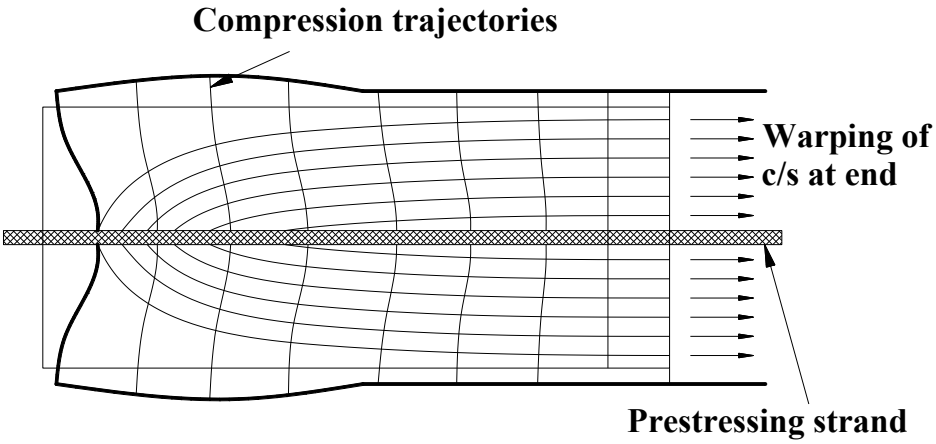

a) Compressive stresses and section warping at beam end [31]

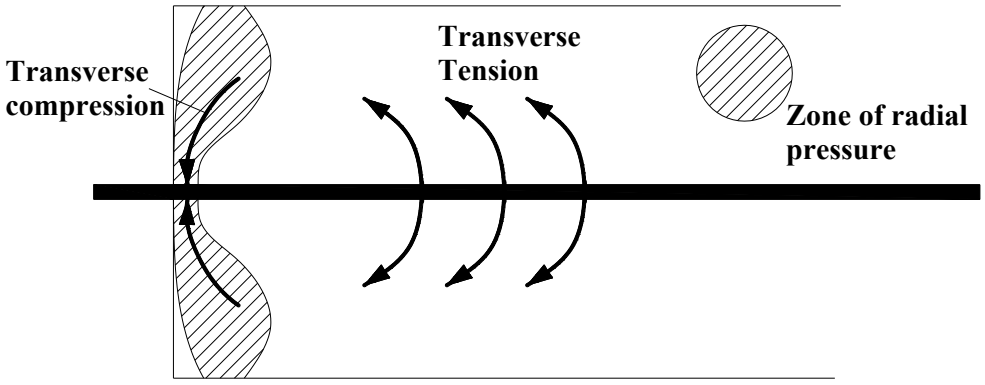

b) Tensile stresses developed due to radial compressive forces [31]

Figure 5 End Forces and Stress Distribution at the End of Bond Anchorage

Of all the mentioned mechanisms, the Hoyer effect contributes the most to "bond" upon prestress release [32][33]. Mechanical interlock is the main contributor to "bond" when the stress

in the strand is increased above the initial transfer stresses, i.e., when the concrete cracks and the strand stress levels are increased over their initial state [32][33]. The adhesion mechanism is the smallest contributor to developing bond stresses between strand and the concrete [31][33].

2.3 Transfer Length

2.3.1 Definition

In pre-tensioned concrete members, the total prestressing force is transferred to the concrete entirely by the bond between the prestressing strand and the surrounding concrete. Transfer length is defined as the bond length required to fully transfer the effective prestress (f_{se}) from the strand to the concrete.

2.3.2 Code Recommendations [1][2]

The current provisions related to bond and transfer length of prestressing strand in concrete elements by the ACI Design Recommendations (318-08) [2] and AASHTO Design Guidelines [1] are primarily based on the work of Hanson and Kaar [4]. The ACI 318-08 and the 2007 AASHTO provisions state:

Three- or seven-wire pretensioning strand shall be bonded beyond the critical section for a development length, in inches, not less than:

$$l_d = \kappa\left(f_{ps} - \frac{2}{3} f_{se}\right) d_b \qquad \textbf{(Equation 2-1)}$$

where,

l_d = development length of prestressing strand, in., $l_d = l_t + l_f$

f_{ps} = stress in prestressed strand, ksi

f_{se} = effective stress in prestressed strand, ksi

d_b = nominal strand diameter, in.

κ = 1.6 for fully bonded strand and 2.0 for partially bonded strand in pre-tensioned beams.

Equation 2-1 can be re-written as:

$$l_d = \kappa \frac{f_{se}}{3} d_b + \kappa\left(f_{ps} - f_{se}\right) d_b \qquad \textbf{(Equation 2-2)}$$

where the first and second terms represent transfer length and flexural bond length, respectively.

2.4 Strand Debonding

The transfer of stresses from the steel strands to the concrete at the end of pre-tensioned beams results in a complex stress state that can lead to concrete cracking. Two methods are commonly used to eliminate or minimize cracking at beam ends. One method consists of using draped, or deflected, strands to keep stresses at the girder ends in compression. This method has the disadvantage of increasing complexity in the production process and creating interference with possible post-tensioning ducts.

The second approach is to debond a few of the strands at the end of the girder so that their load is transferred further into the beam length. Debonding is achieved by placing a plastic sheath around the strand. However, care must be taken in the number of debonded strands, their debonded length, and the release pattern so that the cracking problem is not simply shifted further into the girder. While the use of debonded strands has been found to be generally safe, excessive debonding of prestressing strands can have a significant impact on the structural performance of the pre-tensioned beam and it is hypothesized to be a cause for beam end cracking during the strand release stage of the production process.

2.4.1 AASHTO Guidelines [1]

While both of the mentioned techniques have been in use with relative success for some time, the cracking of beam ends continues to be a problem in the production of pre-tensioned concrete beams. Part of the reason for this lingering problem is that there are many influencing factors and the solution has been based on rough ad-hoc approaches or based on simple elastic stress analyses. With regards to draped strands, code guidelines provide guidance on the stress limits that can be imparted on the beam. With regards to strand debonding, the AASHTO-LRFD specifications provide the following general guidelines.

•Not more than 40% of the strands at any one horizontal row will be debonded.

•Not more than 25% of the total strands can be debonded.

•The exterior strands of each horizontal row shall be fully bonded.

•Symmetric debonding about member centerline is required.

•Not more than 40% of the debonded strands, or four strands, whichever is greater, have the debonding terminated at any section.

•Shear investigation shall be made in the regard to the reduced horizontal force.

It follows that the noted guidelines are very general and provide no guideline in terms of detailing issues such as debonded length, distribution of debonded strands within the beam cross section, or their termination. Further, the limitations noted in the guidelines follow from concerns associated with the reduced shear capacity of the beam due to the de-tensioning of strands. It is clear that no guideline is provided on the type of debonding product that is to be used.

2.4.2 Debonding Methodology

The purpose of debonding is to eliminate the bonding mechanism between strands and concrete so that prestress is not transferred to concrete in the debonded region. In current practice, strand debonding is realized by sheathing or greasing the part of strand that needs to be debonded.

In the case of strand sheathing, there are generally two types of debonding material that are currently used, namely, split-sheathing (Figure 6 a) and preformed tubes (Figure 6 b). In the split-sheathing system, the sheathing has a continuous longitudinal split. The longitudinal split allows this plastic material to be wrapped around the tensioned strand. This is the most commonly used debonding method due to its ease of installation. Due to concerns with the infiltration of cement slurry into the slit of the debonding plastic, some Departments of Transportation (DOT), including the Michigan DOT, require use of two layers of split-sheathing with the longitudinal split of the outer layer on the opposite side of that of the inner layer sheathing. In the preformed tube option the strand needs to be ‘fed’ or pushed through the closed plastic tubing while it is being pulled along the casting bed. This process requires more advanced planning in the strand setup and may lead to some difficulties with bulkheads when casting multiple beams in a single line. This method is thus not a preferred approach.

(a) Split Sheathing

(b) Preformed Tube

Figure 6 Split-sheathing and Preformed Tube

The split-sheathing blanketing material is softer and much easier to deform, compared to the push-through preformed tube. As a result, it is expected that more room will be left around the prestressing strand if a preformed tube is used. Conversely the split-sheathing material will deform easier and create a tighter fit around the strands. In the remaining part of this report, the split sheathing may be referred as *soft debonding material* while the preformed tube may be mentioned as *rigid debonding material*.

As it will be discussed in the next section, one of the mechanisms that contribute to the bonding between strand and concrete is the mechanical interlock due to the shape of the strand and the matching shape of the surrounding concrete after hardening. Since the split-sheathing blanketing material leads to a tighter fit around the strand, the mechanical interlock may not be completely eliminated. In addition, some cement paste (or slurry) may get into the sheathing through the longitudinal split, resulting in some degree of strand-concrete bonding within intended debonded region. Based on the issues just discussed, some bonding resisting mechanism may exist within the intended debonded region when using a split-sheathing system, while debonding with push-through preformed tube can be expected to be more effective.

The split-sheathing used in this project consisted of a flexible polymer plastic slit tubing (Concrete Accessories. Inc., Norcross, GA) and the rigid debonding material consisted of a polymer plastic closed tubing with an outside diameter of 0.725 inches and a wall thickness of 0.04 inches.

Chapter 3 Bond Performance of Unstressed Strand

3.1 Introduction

This chapter deals with two parts of the experiment program in this research. Firstly the bond performance of the 0.6 in. strand used in this research was evaluated using large block pull-out tests (LBPT). Then the basic characteristics of bond mechanism between concrete and unstressed strand was studied using pull-out tests on concrete cylinder. Both fully bonded strand and unbounded strand were tested in the concrete cylinder pull-out tests.

3.2 Strand Bond Pre-Qualification

3.2.1 General

Due to the variation in bond performance in prestressing strands from different sources, it is necessary to verify the quality of the strands used in the research. The large block pull out test (LBPT), or modified Moustafa method recommended by Logan [11] was adopted for the purpose of qualifying the bond behavior of the prestressing strand used in this research.

Logan's proposed quality assessment method was originally based on 0.5 in. (13 mm) diameter, 270 ksi (1862 MPa) strand with an 18 in. (457 mm) embedment length. The strands were cast in normal weight, well vibrated concrete having a concrete strength at the time of the pull-out test between 3500 and 5900 psi (24.1 and 40.7 MPa). According to Logan, the following benchmark is recommended as the minimum acceptable pull-out, or bond, capacity:

Average peak load = 36 kips (160 kN)

Maximum standard deviation = 10 percent

Even though the strands used in Logan's test were 0.5 in. in diameter. He has suggested a modified benchmark for the 0.6 in. diameter strand. The modified benchmark uses modified block geometry as well. Instead of the 18 in. embedment used with the 0.5 in. diameter strand, Logan proposed a 20 in. embedment with the 0.6 in. diameter strand. The benchmarks for 0.6 in. diameter strands are:

Average pull-out load at first slip = 21 kips

Average peak load = 48 kips

3.2.2 Test Setup

The pull-out test concrete block is 24 in. X 24 in. X 24 in. with a total of 6 strands inside the block (see Figure 7). In Logan's test, a sleeve of 2 in. was introduced at the top concrete surface (the pull-out side) to eliminate the effects of surface spalling and concrete confinement from the loading jack. A 2 in. plastic sleeve was thus provided to the strands at both the top and bottom surfaces of the concrete block, leaving an embedment length of 20 in, as recommended by Logan for the 0.6 in. diameter strands. The concrete used in the pull-out block was as prescribed by Logan [11]. The block was provided with nominal reinforcement to prevent temperature or shrinkage cracks.

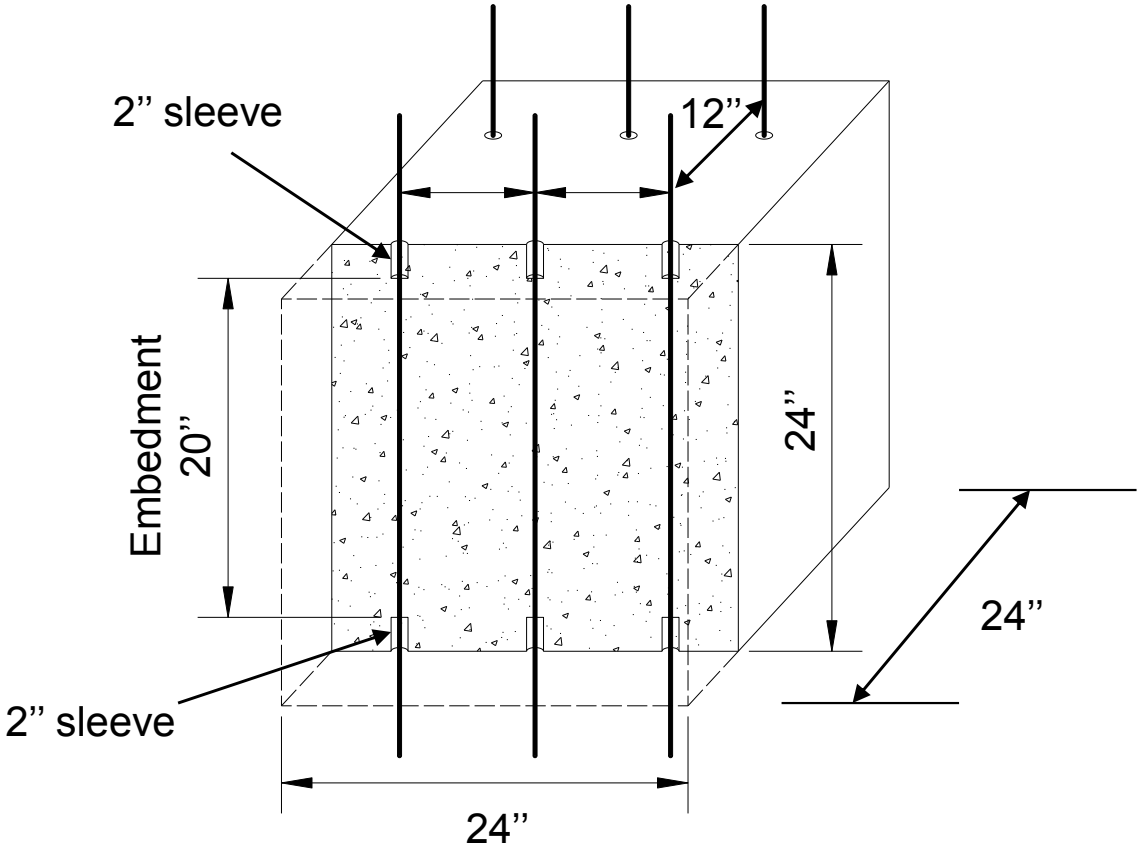

Figure 7 Pull-out Block for Large Block Pull-out Test (LBPT)

The strands were pulled out of the block in the horizontal position using a 100 ton (220 kips) hollow-core hydraulic jack with a ram stroke of 6 in. (150 mm). Load was measured with a load cell placed at the end of the jacking assembly. The setup for the loading assembly is shown in Figure 8. Displacement transducers were used on both sides of the block to measure the

displacement at the jacking and free ends of the strand. Figure 9 shows the pull-out block and the pull-out test in progress.

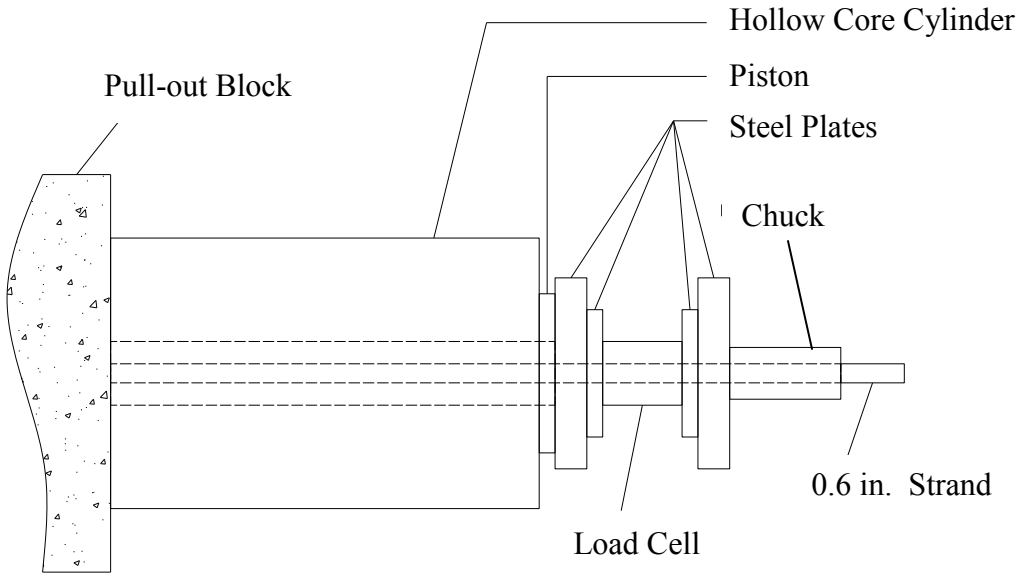

Figure 8 Pull End Setup for LBPT

Pull End Setup

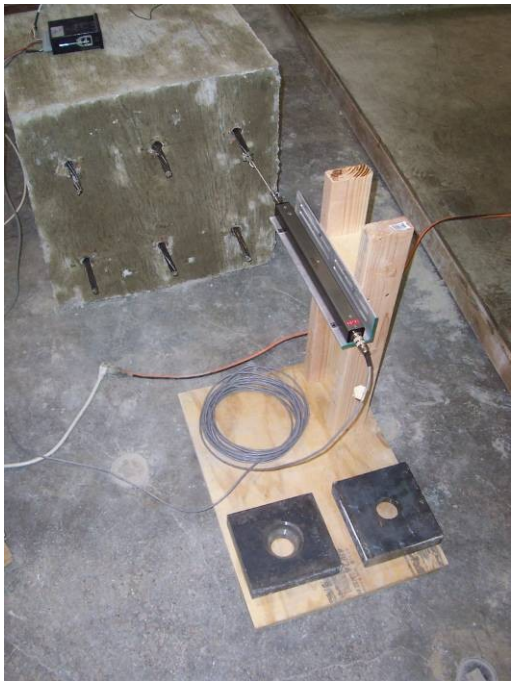

Free End Setup

Figure 9 Test Setup for Large Block Pull-out Test

3.2.3 Procedure

The pull-out tests were performed two days after casting of the concrete block. The testing procedure basically followed the recommendations by Logan. However, due to the limitations of equipment and working space, the pull-out tests in this study were performed with some differences as follows:

a. The tests performed by Logan were in the vertical direction, however, for this study, the pull-out tests were conducted in the horizontal direction. The reason for this change was the desire to obtain relative slip measurements at the jacking and free ends of the strand.
b. Logan suggested that the jacking load should be applied at an approximate rate of 20 kips per minute until maximum load is reached. The loading rate obtained with the equipment in this study varied between 15 kips to 23 kips per minute.
c. The average compressive strength for the concrete in the block was 5,912 psi, which was determined by uniaxial compressive test on 4 in. X 8 in. cylinders. This concrete strength is close to the suggested concrete strength for the large block pull out test by Logan, which is 3500 psi to 5900 psi.

3.2.4 Test Results

The results from the six pull-out tests are shown in the following:

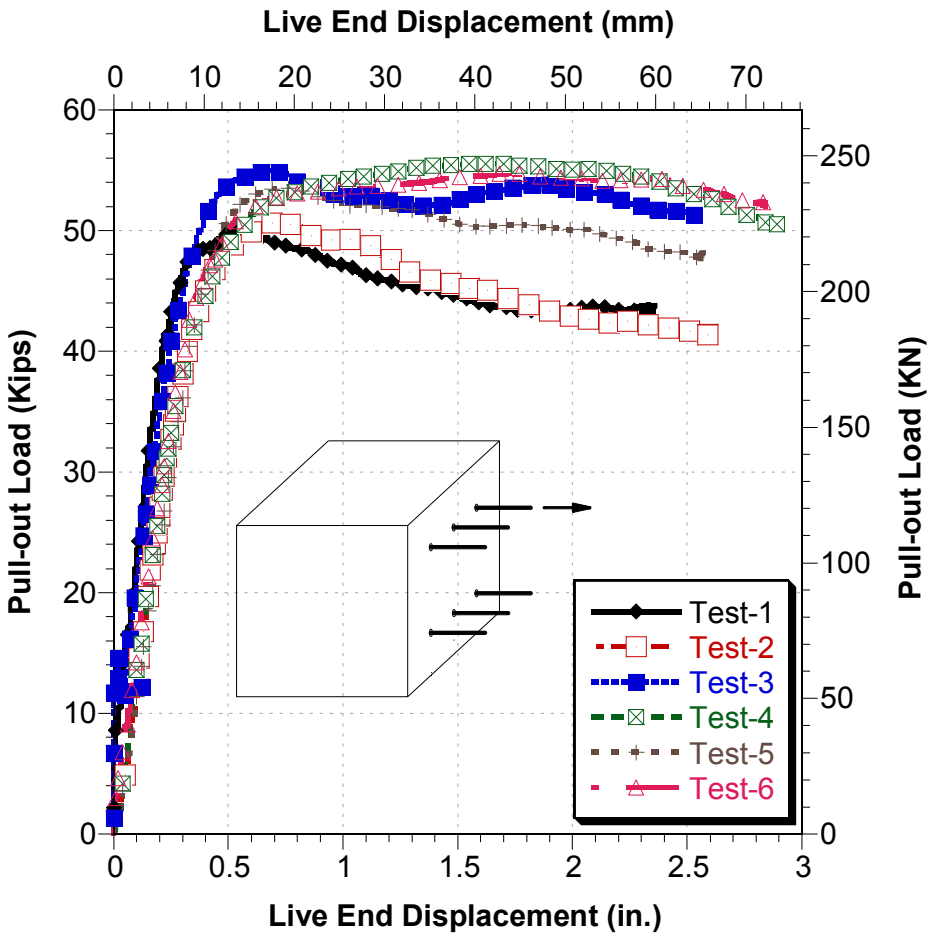

Figure 10 Plot of Pull-out Load vs. Displacement of Strand Live End

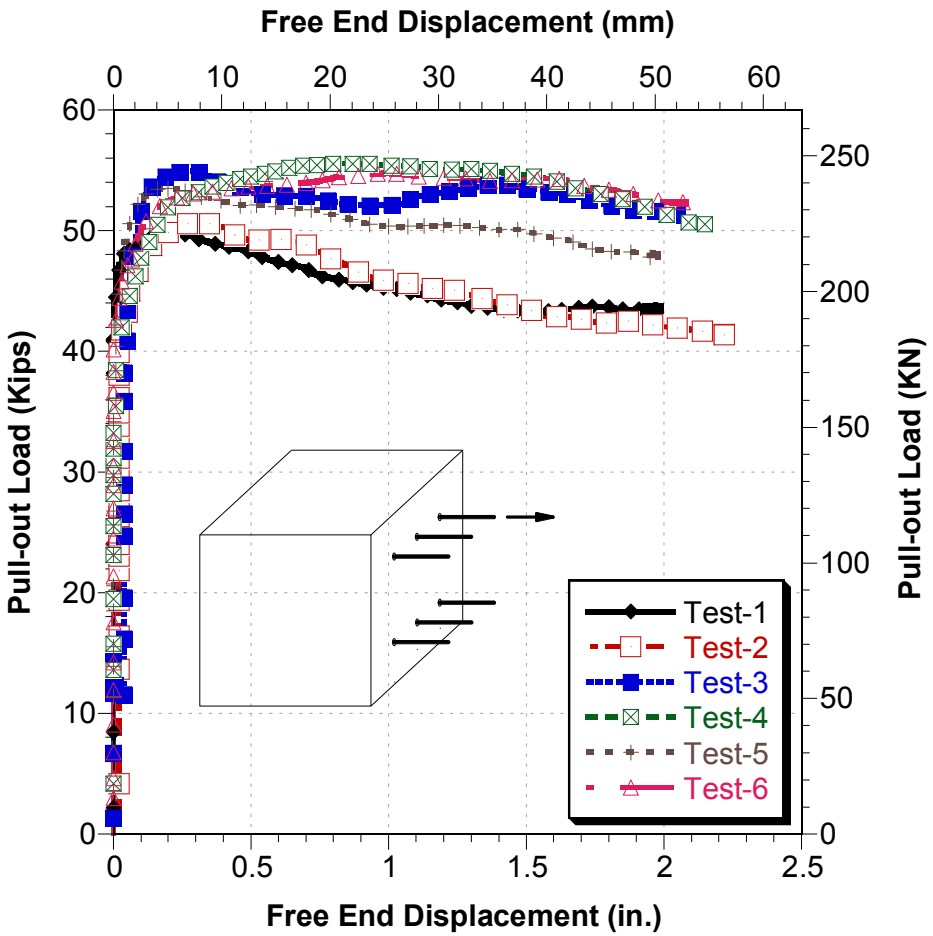

Figure 11 Plot of Pull-out Load vs. Displacement of Strand Free End

Table 1 Results of Large Block Pull-out Tests

Test No.	Load at First Slip (kips)	Peak Load (kips)	Final Free End Movement (in.)
1	7	49.93	2.0
2	N/A	50.77	2.22
3	15	54.98	2.07
4	N/A	55.58	2.15
5	N/A	53.50	1.98
6	N/A	54.74	2.08
Average	11	53.25	2.08
Standard Deviation	51.4%	4.4%	

3.2.5 Discussion

An average maximum pull-out load of 53.25 kip was obtained with a standard deviation of 7.4 percent. This satisfies the benchmark suggested by Logan for the 0.6 in. diameter strands.

The average pull-out load at first slip was 11 kips, which is lower than the suggested value by Logan. However, it was found difficult to locate the first slip in most of the load-displacement curves of large block pull-out test. A magnified plot of load-displacement curves is shown in Figure 12, in which we can see that only curves for Test 1 and 3 show the "straight up" part at the beginning while other curves start to move almost right after the test starts. As a result, it is decided just to compare the maximum pull-out forces with the benchmark suggested by Logan.

The strands were pulled out an average of 2.08 inches (from free end) and the average maximum pull-out load satisfies the benchmark suggested by Logan. The bond performance of the strand used in this experiment was thus considered to be acceptable.

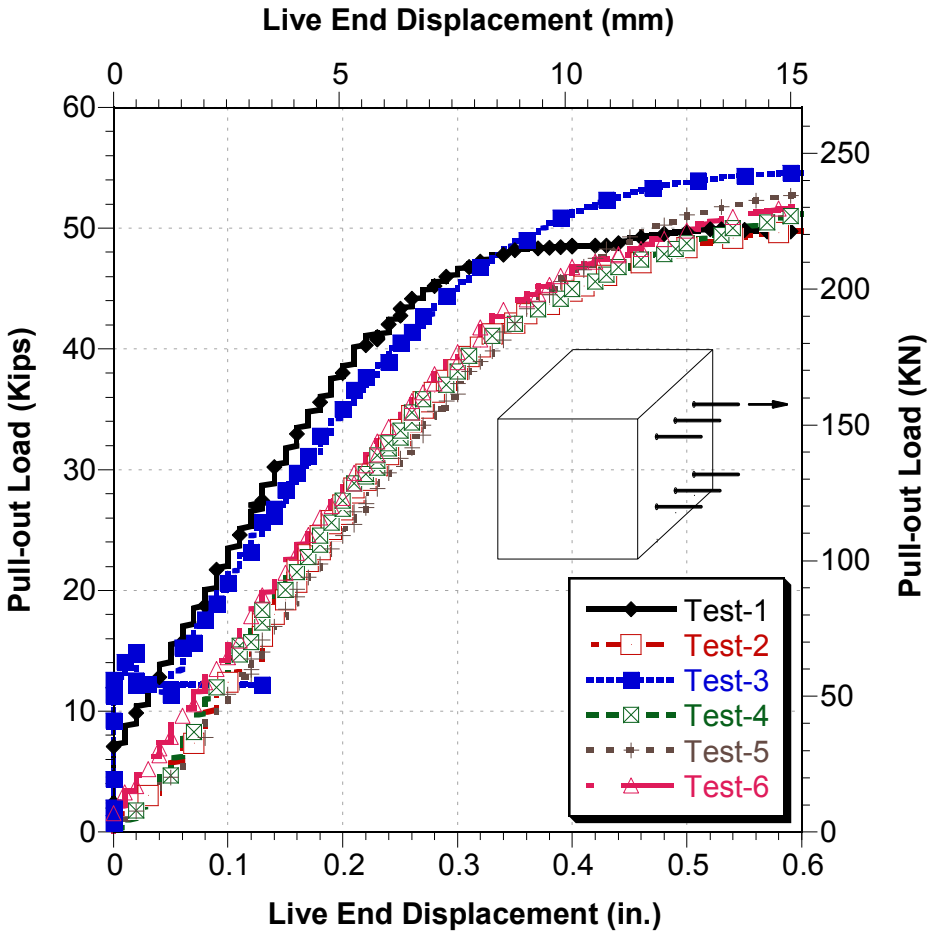

Figure 12 Magnified Load-Displacement Curve of Strand Live End

3.3 Material Properties

3.3.1 Concrete

There are a total of eight concrete casting in the experiment of this research. After each casting the cast members are covered with wet burlaps and plastic sheets to maintain a moist curing process.

The concrete strength for each casting was determined by compression tests of 4 in. X 8 in. concrete cylinders. Concrete cylinders are cast at the same time with the testing members and generally separated into two groups. One group of concrete cylinders were covered with wet burlaps and plastic sheets and kept close to the testing members in order to be cured under similar conditions while the other group of cylinders are moist cured in the curing room. The purpose of the compression tests on concrete cylinders is to determine the concrete strength at the day of testing. Some of the cylinders were tested between the casting day and testing day to keep track of the concrete strength. During the compression test, cylinders from both groups were tested. However, the testing results of the cylinder close to the testing members are considered to be of greater importance and the concrete cylinders in the curing room are just for comparison purposes. As a result, the concrete strength mentioned in this project is the strength determined based on the compression test results of the concrete cylinders close to the testing members.

The concrete strength of each casting at the day of testing is shown in Table 2, and a column chart is plotted Figure 13.

Table 2 Concrete Compressive Strength at Day of Testing

Casting No.	Age at Testing (Days)	f'_{ci} (psi)	$\sigma(f'_{ci})$ (psi)	Description	E_c (psi)
1	**2**	**5912**	**523**	**Large Block**	**4382703**
2	**6**	**5860**	**128**	**C1R1-1st**	**4363386**
3	**4**	**6050**	**157**	**C1R1-2nd**	**4433560**
4	**5**	**7153**	**233**	**R2-1st**	**4820798**
5	**7**	**7372**	**43**	**R2-2nd**	**4894040**
6	**4**	**7371**	**156**	**R4-1st**	**4893708**
7	**5**	**5707**	**23**	**R4-2nd**	**4306047**
8	**4**	**6857**	**62**	**R4-3rd**	**4719999**

In Table 2, f'_{ci} is the concrete compressive strength at the day of testing, $\sigma(f'_{ci})$ is the standard deviation of f'_{ci} and E_c is the modulus of elasticity of concrete, which is calculated using the following equation:

$$E_c(\text{psi}) = 57,000\sqrt{f'_{ci}(\text{psi})} \qquad \textbf{(Equation 3-1)}$$

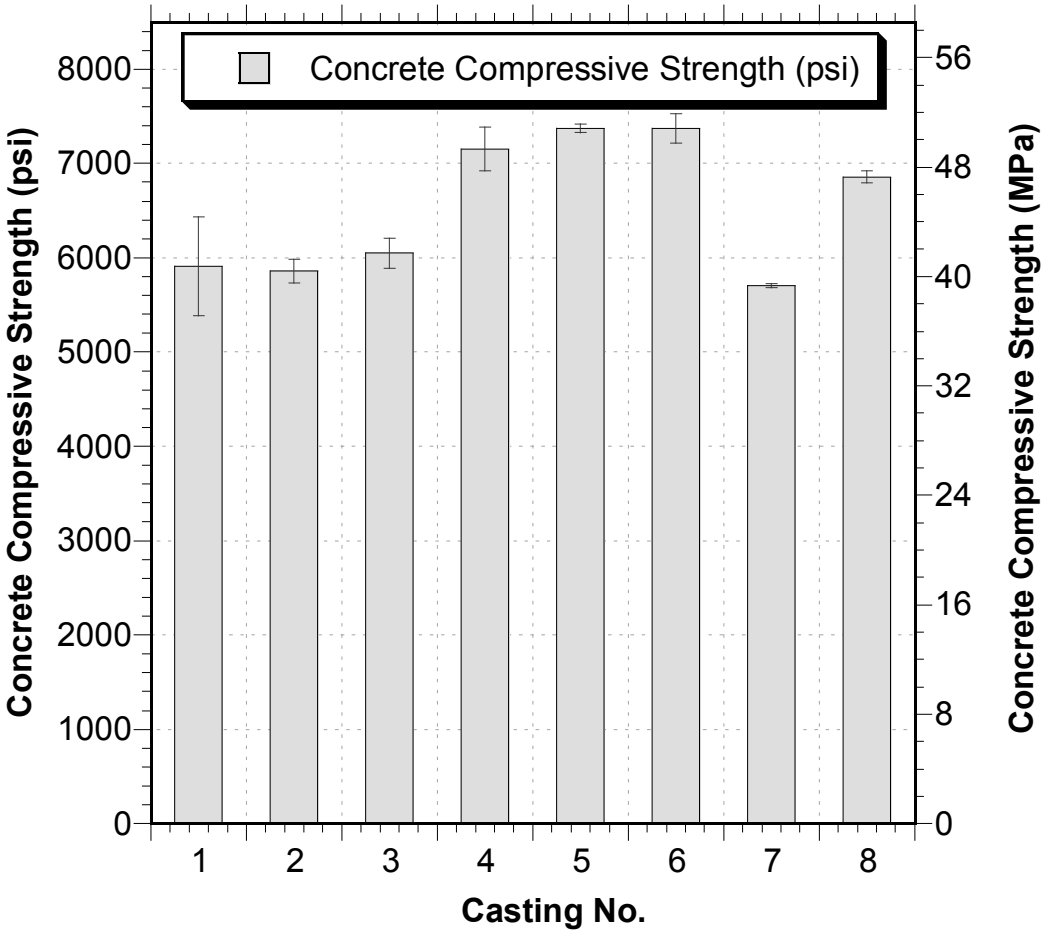

Figure 13 Column Plot of Concrete Compressive Strength

3.3.2 Prestressing Strand

0.6 in. diameter prestressing strand is used for this project and the material properties provided by the manufacture (Insteel Wire Products) are shown in Table 3.

Table 3 Strand Information

Company Name	Insteel Wire Products
Description	.600 7W 270 LR ASTM A416
Ultimate Breaking Strength	60133 lb (267 kN)
Load @ 1% Extension	54144 lb (241 kN)
Ultimate Elongation	7.4%
Rep. Area	0.218 in^2 (140.6 mm^2)
Actual Area	0.2175 in^2 (140 mm^2)
Avg Modulus of Elasticity	29.0 Mpsi (199948 MPa)

3.4 Pull-out Tests on Unstressed Strand

3.4.1 Introduction

Concrete cylinder pull-out tests were conducted to investigate the basic characteristics of bond mechanism between 0.6 in. 7-wire strand and concrete. The bond mechanism between strand and concrete in the concrete cylinder tests are different from the one in the small beam units due to the fact that the strands in the concrete cylinders were not stressed. As a result, the concrete cylinder pull-out tests will not be used to calibrate the FE models.

3.4.2 Test Details

The dimensions of the concrete cylinder cast for the pull-out tests are shown in Figure 14. The cylinder had a diameter of 6 in. and a height of 24 in. The strand was placed in the center of the concrete cylinder and debonded 2 in. on each end using pieces of PVC pipes. The purpose of the debonding detail in the test setup is to eliminate the influence of the confinement effect due to friction between the end surface of the concrete cylinder and the jack on the bonding behavior in the end region. The actual bonded length between strand and concrete in the cylinders is 20 in which is the same as the bonded length in the big block pull-out test.

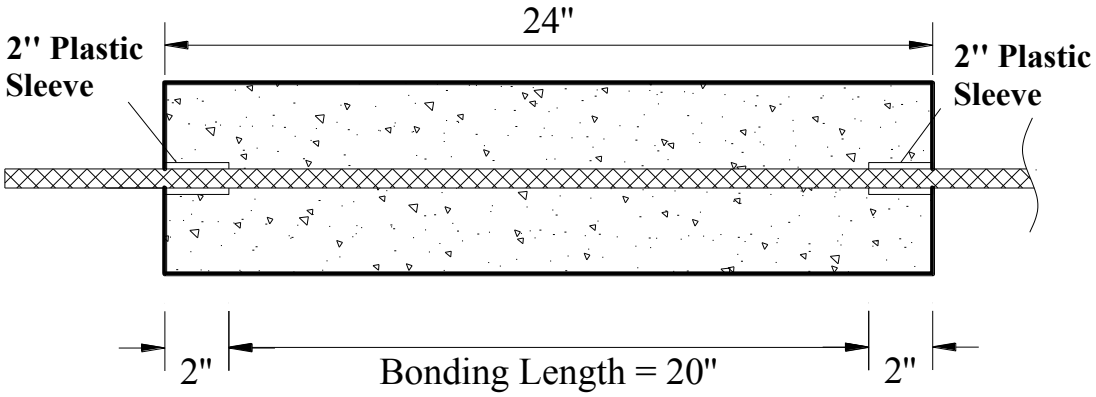

Figure 14 Details of Pull-out Cylinder

Figure 15 Confinement for Strand

The concrete cylinders were cast vertically in a way that the jacking end of the cylinder is on the bottom to make a smooth surface. The cylinders were cast at the same time with each batch of the small beam units using the same batch of concrete. There are a total of 7 batches of concrete cylinders cast. With a purpose of compare strand with and without debonding material, two types of cylinders were cast, namely, fully bonded and debonded in each batch. In the debonded concrete cylinders strand is debonded using double layers of soft material. 9 cylinders were cast for each batch, except the first casting, in which only 6 cylinders were made. In the 7^{th} casting, confinement was put around strand inside the concrete cylinder to investigate the effect

of confinement. The confinement is made by rolling a No. 3 rebar into a spiral shape with a diameter of about 2.5 in (Figure 15). The basic information of each casting is shown in Table 4.

Table 4 Information of Casting for Concrete Cylinder Pull-out Tests

Batch No.	Total No. of Cylinders	No. of Fully Bonded Cylinders	No. of Debonded Cylinders
1	6	3	3
2	9	6	3
3	9	6	3
4	9	6	3
5	9	6	3
6	9	6	3
7	9	9 (3 confined)	0

Figure 16 Form Work of Pull-out Cylinders

3.4.3 Procedure

The test procedure of concrete cylinder pull-out test is similar to the one of large block pull-out test. The concrete cylinder was placed on a formwork and tested horizontally. As seen in Figure 17, the placement of instrumentation is similar to that of the big block pull-out test. Strand was pulled out horizontally by the jack, while the displacement of the live end and free end of the strand were measured by the LVDTs, which were placed on the two ends of the cylinder. The pull-out force was measured by a 100 Kips load cell placed on the live end of the cylinder. The two LVDTs and the load cell were connected to the Data Acquisition System, which recorded all the data.

Each concrete cylinder pull-out test will be terminated in the following situation:

i) The observed value of pull-out force starts to drop or swing up and down after the maximum force was obtained and a displacement of about 6in. was obtained on the live end;

ii) The strand part outside of the concrete cylinder on the free end is almost pulled inside the cylinder;

iii) Crack or spalling is observed on the concrete cylinder and it is not suitable for more loading.

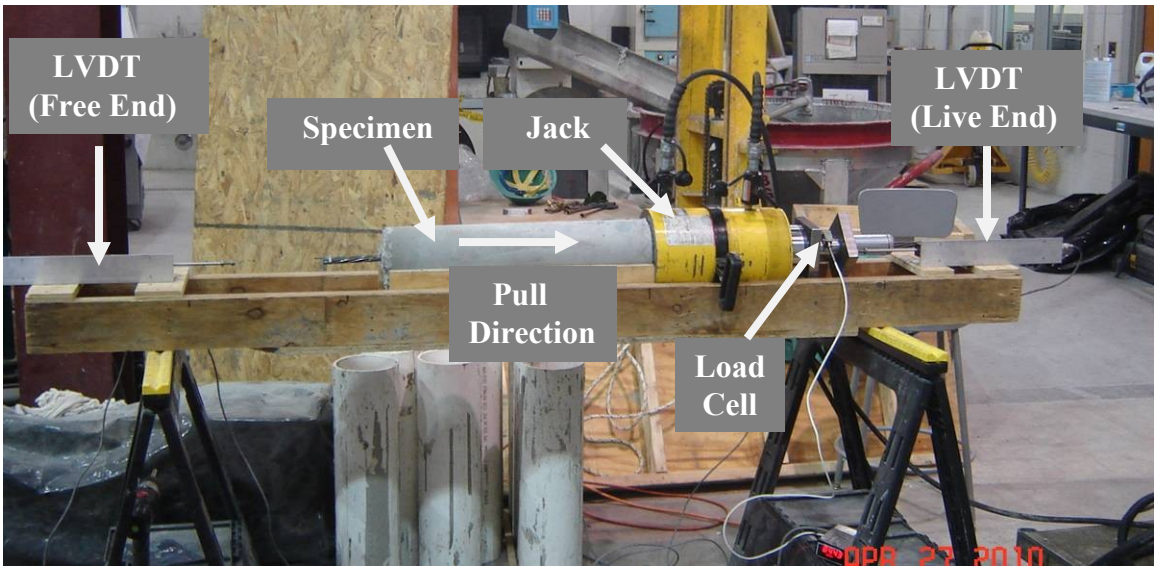

Figure 17 Test Setup for Concrete Cylinder Pull-out Test

3.4.4 Results

Table 5 shows the summary of the results from concrete cylinder pull-out tests.

Table 5 Summary of Results of Concrete Cylinder Pull-out Tests

Batch No.	f'_c (ksi)	F_{max_b} (kips)	σ_{max_b} (kips)	F_{max_d} (kips)	σ_{max_d} (kips)	$\frac{F_{max\_d}}{F_{max\_b}}$	F_{max_c} (kips)	σ_{max_c} (kips)	$\frac{F_{max\_c}}{F_{max\_b}}$
1	5860	32.53	5.18	1.27	0.43	3.9%	-	-	-
2	6050	41.55	2.28	1.33	1.22	3.2%	-	-	-
3	7153	39.12	4.05	0.45	0.29	1.2%	-	-	-
4	7100	31.99	2.04	0.51	0.31	1.6%	-	-	-
5	7371	38.87	2.78	1.14	0.69	2.9%	-	-	-
6	5990	35.48	3.78	0.46	0.26	1.3%	-	-	-
7	7365	35.83	2.49	-	-	-	42.33	2.07	118.1%
AVG	6698	36.48	3.54	0.86	0.42	2.4%	42.33	2.07	118.1%

f'_c = Concrete compressive strength at test day (ksi);

F_{max_b} = Maximum pull-out force of fully bonded concrete cylinders (kips);

σ_{max_b} = Standard deviation of maximum pull-out force of fully bonded concrete cylinders (kips);

F_{max_d} = Maximum pull-out force of debonded concrete cylinders (kips);

σ_{max_d} = Standard deviation of maximum pull-out force of debonded concrete cylinders (kips);

F_{max_c} = Maximum pull-out force of fully bonded concrete cylinders with confinement (kips);

σ_{max_c} = Standard deviation of maximum pull-out force of fully bonded concrete cylinders with confinement (kips);

A column chart is plotted for the experiment results of concrete cylinder pull-out tests. (Figure 18)

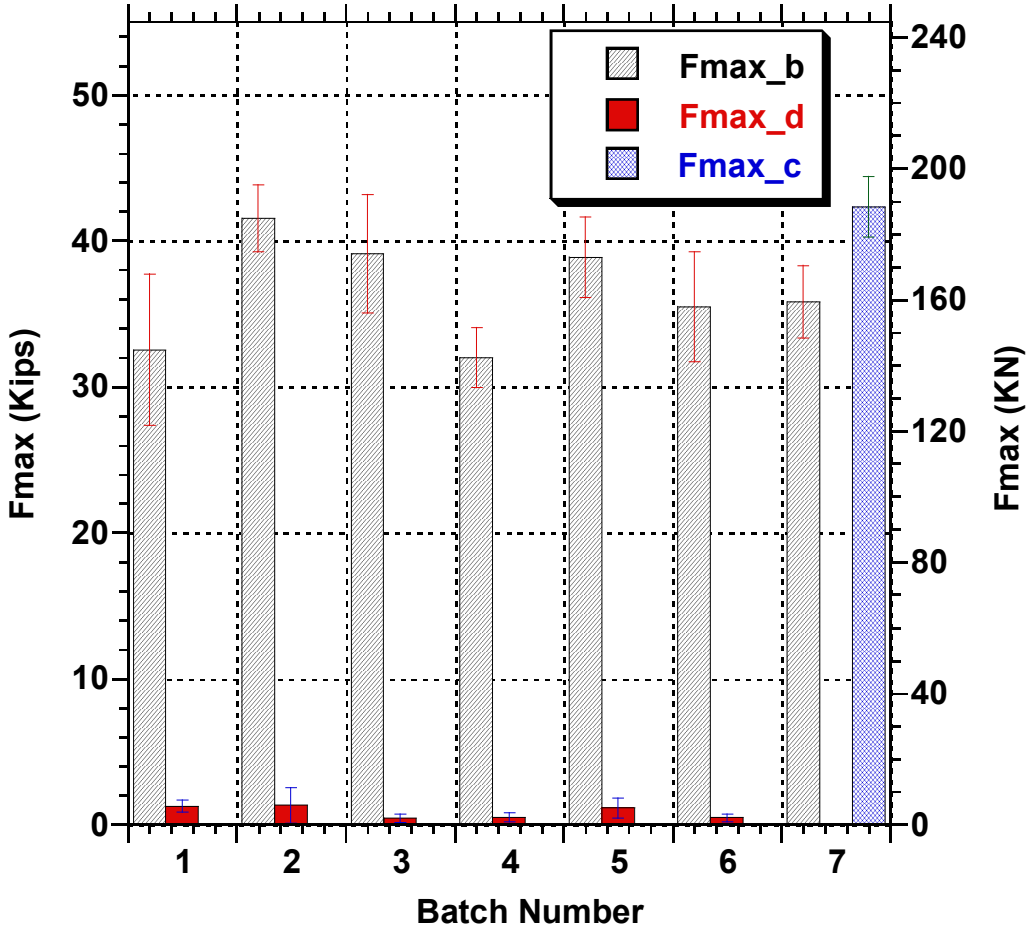

Figure 18 Column Chart of Results of Concrete Cylinder Pull-out Tests

3.4.5 Discussion

Concrete strength of each casting batch for concrete cylinders is different from each other. Some researchers suggest that the bonding strength between strand and concrete is proportional to $\sqrt{f'_c}$. If the bonding strength is assumed to be uniform along the bonded region, then:

$$F = \pi d_s L_b U \qquad \textbf{(Equation 3-2)}$$

where,

F = Pull-out force (kips);

d_s = Diameter of strand (in.);

L_b = Bonded length of strand (in.);

U = Bonding strength between strand and concrete (ksi).

To account for the effect of concrete strength, the pull-out forces are converted by assuming a 5000 psi concrete strength. The modified pull-out force is calculated using the following equation and the modified results are shown in Table 6.

$$F_{\max}' = F_{\max} \frac{\sqrt{5000}}{\sqrt{f'_c}} \qquad \textbf{(Equation 3-3)}$$

Several discussions about the experiment results are shown in the following:

i) According to the modified results of concrete cylinder pull-out tests, the average maximum pull-out force for a 5000 psi concrete is about 31.6 kips with a standard deviation of 3.4 kips. This maximum pull-out force is lower compared to the experiment results of large block pull-out tests (average is about 49.2 kips for 5000 psi concrete) and the reason may be that the large block in LBPT was reinforced and more massive, which means strand is confined by more concrete.

ii) The bonding strength between debonded unstressed strand and concrete is considerably small. Compared to the maximum pull-out force of a concrete cylinder with fully-bonded strand, the maximum pull-out force is less than 4%. A lower force is expected if rigid material is used for debonding, since rigid material has a better performance in debonding.

iii) Confinement around strand can increase the bonding performance between strand and concrete. It can be seen from the experiment result that concrete cylinders with confinement has about an 18% percent greater maximum pull-out force, compared to the cylinders without confinement in the same batch.

Table 6 Modified Results of Concrete Cylinder Pull-out Tests

Batch No.	f'_c (ksi)	F_{max_b}' (kips)	σ_{max_b}' (kips)	F_{max_d}' (kips)	σ_{max_d}' (kips)	$\frac{F_{max\_d}'}{F_{max\_b}'}$	F_{max_c}' (kips)	σ_{max_c}' (kips)	$\frac{F_{max\_c}'}{F_{max\_b}'}$
1	5860	30.05	4.78	1.17	0.40	3.9%	-	-	-
2	6050	37.78	2.07	1.21	1.11	3.2%	-	-	-
3	7153	32.70	3.39	0.38	0.24	1.2%	-	-	-
4	7100	26.85	1.71	0.43	0.26	1.6%	-	-	-
5	7371	32.01	2.29	0.94	0.56	2.9%	-	-	-
6	5990	32.41	3.46	0.42	0.24	1.3%	-	-	-
7	7365	29.52	2.06	-	-	-	34.88	1.71	118.1%
AVG	-	31.62	3.40	0.76	0.39	2.4%	34.88	1.71	118.1%

F_{max_b}' = Modified maximum pull-out force of fully bonded concrete cylinders (kips);

σ_{max_b}' = Standard deviation of modified maximum pull-out force of fully bonded concrete cylinders (kips);

F_{max_d}' = Modified maximum pull-out force of debonded concrete cylinders (kips);

σ_{max_d}' = Standard deviation of modified maximum pull-out force of debonded concrete cylinders (kips);

F_{max_c}' = Modified maximum pull-out force of fully bonded concrete cylinders with confinement (kips);

σ_{max_c}' = Standard deviation of modified maximum pull-out force of fully bonded concrete cylinders with confinement (kips);

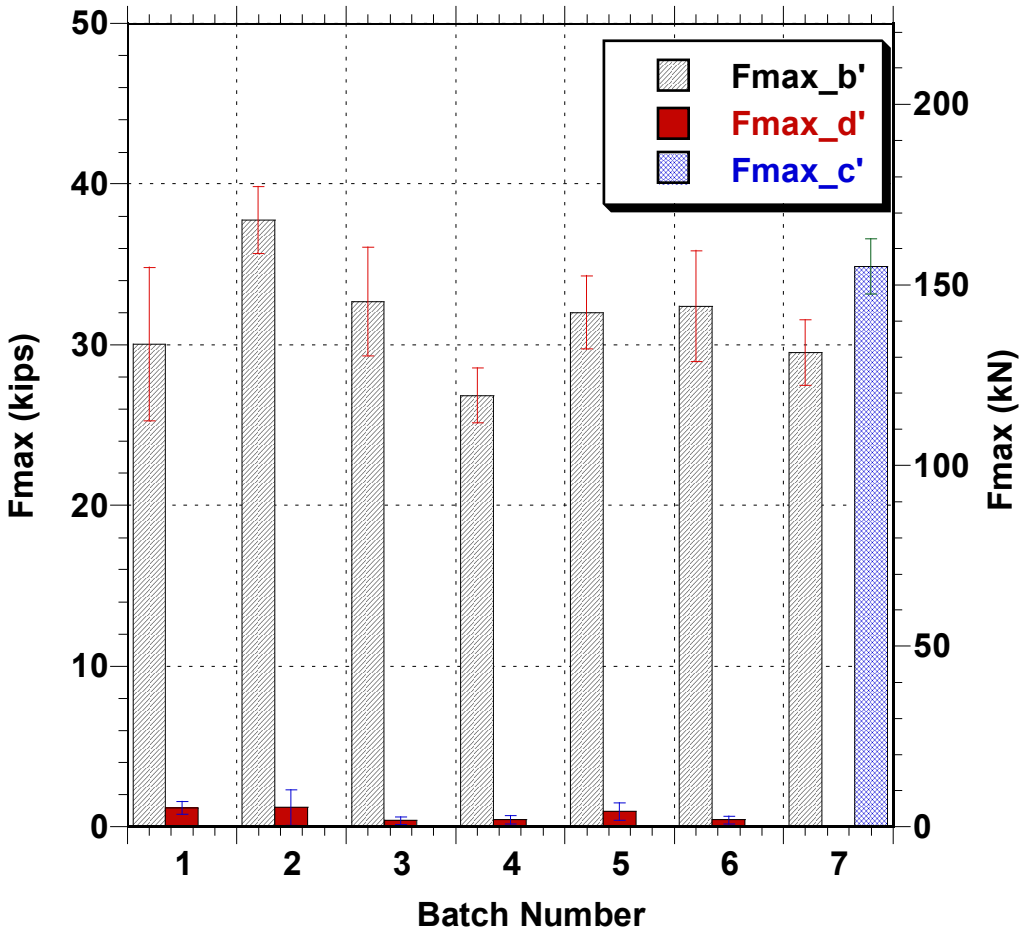

Figure 19 Column Chart of Modified Results of Concrete Cylinder Pull-out Tests

Chapter 4 Stress Transfer Performance of Bonded and Debonded Strand

4.1 Introduction

The basic bond behavior between strand and concrete was studied based on cylinder pull-out tests. However, the bond mechanism between strand and concrete is different under a stressed condition and as it transfers its force to a concrete element. The reason for the difference is that in a prestressed concrete beam, the prestressing strand will experience shortening in the longitudinal direction after releasing, while at the same time it will dilate in the radial direction due to its Poisson's ratio. The dilation of prestressing strand, which is maximized at the end of the beam due to the lack of constraint and which decreases along the length of the strand into concrete beam is called "Hoyer's Effect." This effect generates pressure between the surface of strand and the surrounding concrete and it is thought to have an effect on increasing bond strength. As a result, the bond mechanism between prestressing strand and concrete in a prestressed concrete beam is different to the bond mechanism of unstressed strand in a cylinder pull-out test, in which there is no Hoyer's effect.

Based on the discussion above, it is necessary to experimentally evaluate the fundamental mechanism of stress transfer between the pre-tensioned seven-wire prestressing steel strand and concrete in prestressed concrete beams to support the development and validation of simulation models. The experiments described herein are not meant to replicate the actual beam end conditions but rather aimed at isolating fundamental behavior. Twenty-four small beam units, with different parameters considered, were cast and tested for this purpose. The experimental method was the release of the pre-tensioned strands on to the hardened concrete beams, i.e. the prestress transfer operation. The resulting data was used for the calibration of numerical models that could simulate the bond mechanism of bonded and debonded prestressing strands in concrete.

The most importance parameter to be obtained from the experiment was the transfer length in the prestressed concrete beams after strand release. Two techniques were used to determine transfer length: (i) measurement of concrete surface strains along the length of the beam, and (ii) measurement of concrete internal strains along the beam length using an instrumented rod.

4.2 Test Units and Test Matrix

The parameters considered to evaluate basic bond behavior of stressed strand were: (1) debonded length, (2) debonded material, (3) free strand length, (4) confinement reinforcement, and (5) release methodology. These parameters were studied through a test matrix composed of 24 small-scale prestressed concrete beams.

4.2.1 Units Details

Twenty-four (24) small-scale prestressed concrete beam units were cast with conventionally consolidated concrete and prestressed with 0.6 in. diameter strand. The cross-section geometry and reinforcement layout for these beams are shown in Figure 20.

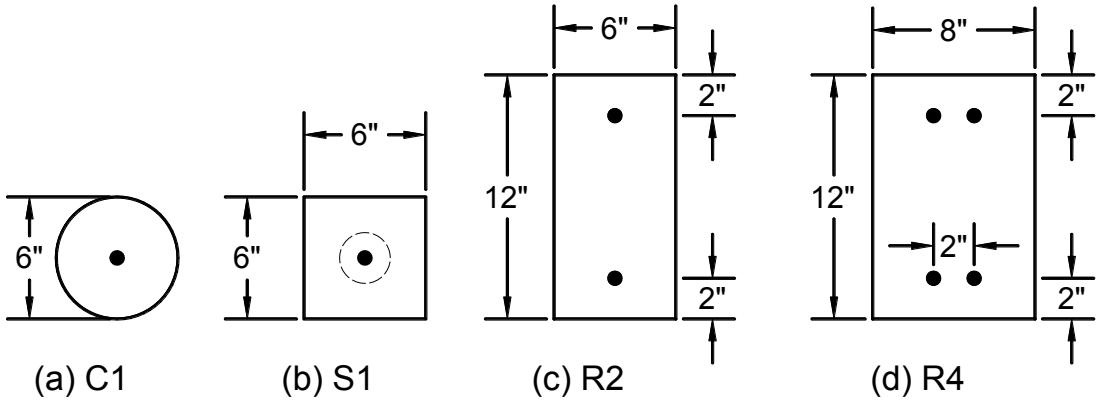

Figure 20 Cross-sections of Small-scale Pre-tensioned Beam Units

The purpose of having beam sections with a single strand was to investigate the possible cracking pattern due to strand dilation after release and the effect of confinement on the bond transfer mechanisms. The beam sections with multiple strands investigate the restraining effect of free strand length and the development of any splitting cracks between adjacent strands.

4.2.2 Parameters Considered in Test Units

To study the effect of different parameters, each test beam was assigned with a unique configuration. The test matrix and the different key parameters considered are shown in Table 7. For each of the noted cross sections (Figure 20) there were 6 beams with different configuration of parameters (debonded length, debonded material, strand releasing method, free length, and confinement level). The parameters considered in this study are discussed next.

Table 7 Test Matrix for Stress Transfer Evaluation of Pre-tensioned Strand

Beam ID	Beam L (ft)	Lb (ft)	Lu (ft)	Lu/Lb (%)	Sleeve	Conf.	Release
C1-1	20	20	0	0	NA	NA	Annealed
C1-2	20	20	0	0	NA	NA	Sudden
C1-3	20	17	1.5	7.5	Soft	NA	Annealed
C1-4	20	17	1.5	7.5	Soft	NA	Sudden
C1-5	20	17	1.5	7.5	Rigid	NA	Annealed
C1-6	20	17	1.5	7.5	Rigid	NA	Sudden
S1-1	20	20	0	0	NA	9 in.	Annealed
S1-2	20	20	0	0	NA	9 in.	Sudden
S1-3	20	14	3	15	Soft	NA	Annealed
S1-4	20	14	3	15	Soft	NA	Sudden
S1-5	20	10	5	25	Soft	9 in.	Annealed
S1-6	20	10	5	25	Soft	9 in.	Sudden
R2-1	20	20	0	0	NA	NA	Sudden
R2-2	20	17	1.5	7.5	Soft	NA	Sudden
R2-3	44	44	0	0	NA	NA	Annealed
R2-4	44	44	0	0	NA	NA	Sudden
R2-5	20	14	3	15	Soft	NA	Sudden
R2-6	20	10	5	25	Soft	NA	Sudden
R4-1	20	20	0	0	NA	NA	Sudden
R4-2	20	17	1.5	7.5	Soft	NA	Sudden
R4-3	20	14	3	15	Soft	NA	Sudden
R4-4	20	10	5	25	Soft	NA	Sudden
R4-5	20	14	3	15	Rigid	NA	Sudden
R4-6	20	10	5	25	Rigid	NA	Sudden

Note: L = Beam length, Lb = Length of bonded region, Lu = Length of unbounded region.

Debonded Length/ Free Length

In pre-tensioned concrete beams, the debonded length of different strands can vary. The free length of strand is the distance from the point of anchorage (in the stressing bulkheads) to the point where debonding ends. Thus longer debonded length implies more free length. Compared to strand in a fully bonded beam unit, strand in a debonded beam unit has more strain energy stored within the debonded region since bond transfer is delayed. According to Mirza and Tawfik [8], the free length of uncut strand may be one of the reasons of end cracking in

prestressed concrete members. The effect of different debonded lengths was investigated by comparing the results from beam units C1-1 and C1-3. The effect of free length of uncut strand was studied with multiple strand beam units R2-1 vs. R2-2 or R4-1 vs. R4-2.

Debonded Material

As discussed in section 2.4.2, two different types of materials can be used for strand debonding in prestressed concrete. Different debonding materials have different debonding efficiency due to their characteristics. Specifically, a softer debonding material is considered to have lower capacity of debonding and thus the bond between prestressing strand and concrete is not completely eliminated. As a result, some stress may be transferred within the debonded region if soft debonding material is used. The effect of different debonding material was investigated by comparing beams with same configuration of parameters other than the debonding material, such as beams C1-3 and C1-4.

The split-sheathing used in this project consisted of a flexible polymer plastic slit tubing (Concrete Accessories. Inc., Norcross, GA) and the rigid debonding material consisted of a polymer plastic closed tubing with an outside diameter of 0.725 inches and a wall thickness of 0.04 inches.

Releasing Method

Two different methods were used to release the prestressing strands in the experiment, namely, sudden release and annealed release. The sudden release of a pre-tensioned strand transfers the stress onto the concrete at a much higher rate compared to an annealed cutting procedure. The kinetic energy generated during sudden releasing is thus much higher than during gradual release. Details of these two cutting methods are discussed in Section 4.4 and the effect of release methodology was studied by comparing beam units pairs such as C1-1 vs. C1-2 and S1-3 vs. S1-4.

Confinement

It was found from the concrete cylinder pull-out tests that confinement reinforcement can improve the bond strength between strand and concrete. Confinement was placed in beam S1-1, S1-2, S1-5 and S1-6.

4.3 Test Setup

Figure 21 shows the test setup for the strand stress transfer evaluation, which essentially consisted of a casting bed for pre-tensioned concrete beams. Two anchorage blocks were anchored to the floor with post-tensioned steel rods. The beam units were cast and tested (strand release) between the two anchorage blocks. When possible, two beams were cast in a row.

Figure 21 Form Work of Small Prestressing Concrete Beam Units

A total of seven casts were conducted by grouping the beam units in the setup as shown in Figure 22. With the exception of the fourth cast, beams R2-3 and R2-4 (44-ft long), the 20-ft long beams were cast such that there were two units in a row.

Table 8 Beam Units Combination of Casting

Cast No.	No. of Strands	Combination of Beam Units
1	3	C1-1, C1-3, C1-5, S1-1, S1-3, S1-5
2	3	C1-2, C1-4, C1-6, S1-2, S1-4, S1-6
3	4	R2-1, R2-2, R2-5, R2-6
4	4	R2-3, R2-4
5	4	R4-1, R4-2
6	4	R4-3, R4-4
7	4	R4-5, R4-6

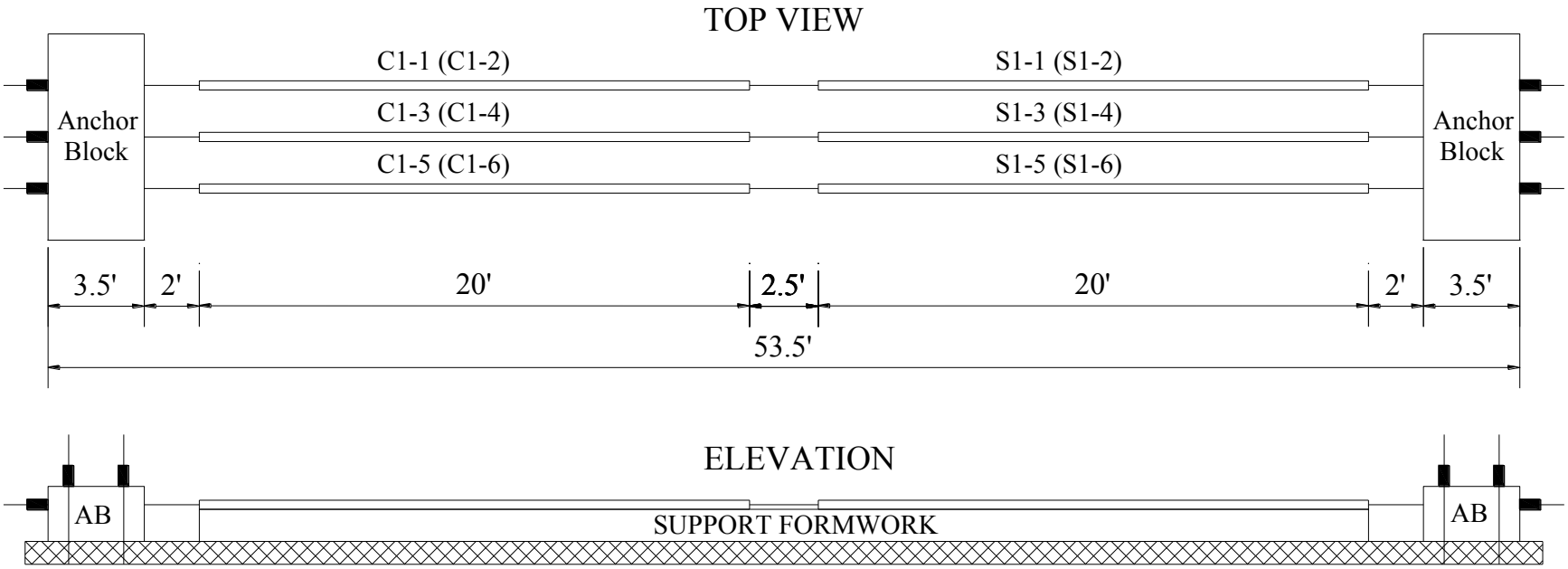

Figure 22 Schematic Layout of Casting Bed for Beam Units C1 and S1

4.4 Pre-tensioning Procedure

The strands for all beam units were tensioned to a target initial (transfer) level of 75% of their ultimate tensile strength (f_{pu}). However, to account for seating loses the strands were tensioned to approximately 80% of f_{pu}. It is estimated that after the seating loses the tensile stress was very near the desired target of $0.75 f_{pu}$.

Different instruments were used to monitor the force during strand pre-tensioning. First, a 100-kip load cell was placed in series with the stressing jack to measure the jacking force. Second, a strain gage was placed on the strand surface to measure the tensile strain. The load cell and strain gage were connected to a data acquisition system (DAQ) and the data of these two instruments during prestressing was recorded. In addition, the strand movement (deformation) during pre-tensioning was also manually monitored with a measuring tape.

4.5 Strand Release Procedure

In all cases, the prestressing strands were released from both ends of the beam units. For setups with two beams in a row, strands were cut simultaneously at three points (Figure 23) and both beams in the same row were released at the same time. For beam units R2-3 and R2-4, for which there was only one beam unit in a row, the strands were cut simultaneously at both ends of the beam. The strands in the R2 beam units were cut from top to bottom; and the strand cutting sequence for the R4 beam units is shown in Figure 24.

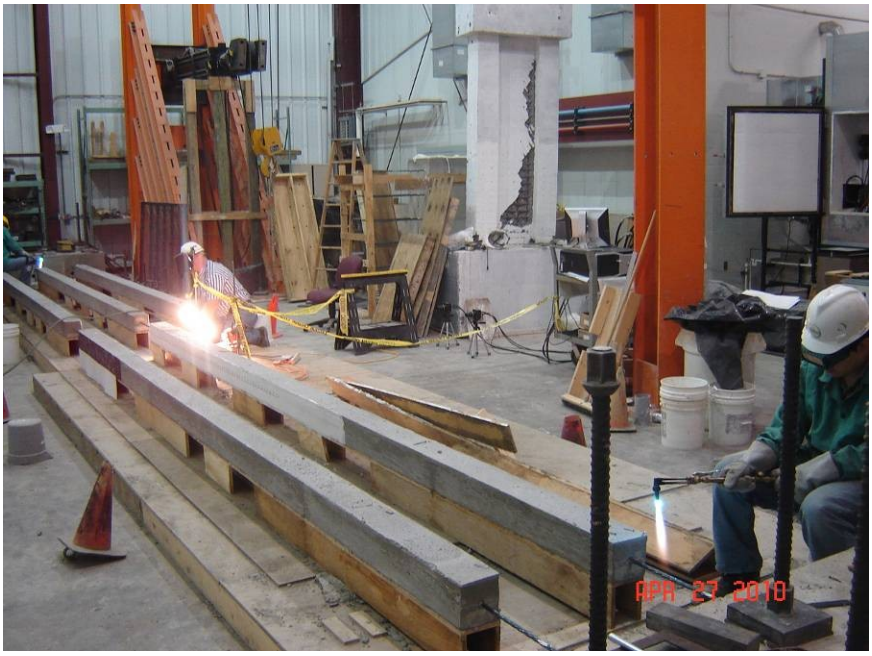

Figure 23 Releasing of Prestressing Strand

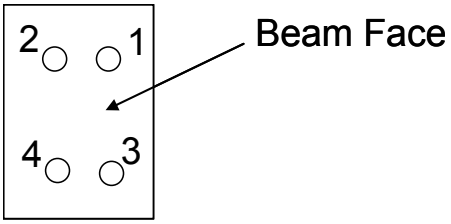

Figure 24 Strand Cutting Sequence of R4 Beam Units

As mentioned in the previous section, two release methodologies were used in this research, namely sudden and annealed (or gradual) release. Sudden strand release was achieved by heating and cutting a strand in a very short period. During the cutting process, the flame was pointed to a fixed location on the strand and the total cutting process takes about 5~10 seconds. Simultaneous cutting and both ends of beam units was attempted for beam units with sudden strand releasing but it was difficult to achieve a simultaneous cut at three locations. As a result, it was decided that the first cut take place at the beam end where measurements were being taken. The other end of the beam was cut immediately after the sound of the first cut was heard.

Gradual or annealed release of the pre-tensioned strand consists on slowly heating up the steel strand so that the tension in the strand drops due to the reduction of the steel modulus of elasticity with heat. A strain gage was placed on the strand away from the cutting points to

monitor the annealing procedure. The annealing process was done in three stages. First, the strand was heated up gradually by moving the cutting torch with a broad flame back and forth along the strand within a region of about 8 in.. Only the very outer part of the flame was used to heat up the strand during the first step. Once it was observed that about half of the total prestress has been transferred (due to a drop in the strain gage reading), the heated region was narrowed to about 4 in. and the flame was moved closer to the strand. The third and final stage takes place when most of the prestress (about 5/6) has been transferred. The time taken during the annealing release procedure was between 10 and 15 minutes.

4.6 Instantaneous Pre-tension Losses

4.6.1 Anchorage Seating Losses [5]

The initial jacking stress is not completely maintained in a prestressing tendon after the prestressing process due to the slight slip at the jacking end where the wedges adjust to seat themselves into the anchorage chuck. This anchorage slip (δ) is assumed to produce a uniform strain over the length of the strand (L), which is an anchorage loss. This loss is estimated by:

$$\Delta f_{pA} = \frac{\delta}{L} E_p \qquad \textbf{(Equation 4-1)}$$

where, E_p is the modulus of elasticity of the prestressing strand.

Electrical strain gages were installed on the prestressing strand so that the stress retained in strand after anchorage loss could be calculated based on the strain gage reading. Table 9 lists the strain and tension force (from load cell) data before and after anchorage seating. The load after seating was calculated using the following equation:

$$\Delta F_{pA} = \frac{\varepsilon_{pi} - \varepsilon_{pas}}{\varepsilon_{pi} - \varepsilon_0} F_{pi} \qquad \textbf{(Equation 4-2)}$$

where, ε_{as} is the reading from the strain gage, F_{as} is the tension force after seating, ε_{MAX} and F_{MAX} are the maximum strain and tension force, or strain and tension force before seating, and ε_i is the initial strain gage reading.

4.6.2 Elastic Shortening Losses [5]

Once the prestressing strands are released, the concrete member will be subjected to compression, which leads to shortening from instantaneous elastic effects. Due to strain compatibility between the concrete and the strand, the prestressing strand will shorten as well. This shortening of the prestressing strand will lead to a loss in the prestress force transferred. The loss due to elastic shortening of concrete (Δf_{pES}) is calculated by equating the strain in the tendon due to the change in prestress and the strain in concrete due to the concrete stress at the strand centerline:

$$\Delta f_{pES} = \frac{E_p}{E_{ci}} f_{cgp} \qquad \textbf{(Equation 4-3)}$$

where, E_{ci} is the modulus of elasticity of the concrete at transfer. The value of f_{cgp} is obtained from the elastic uncracked properties of the section as:

$$f_{cgp} = \pm\frac{P}{A} \pm \frac{Pey}{I} \pm \frac{M_D y}{I} \qquad \textbf{(Equation 4-4)}$$

where, P is the total initial prestress force at the centroid line of the strand group, e is the eccentricity of the tendon from the centroid of the section, y is the fiber at which the stress is computed (in this case, $y = e$), M_D is the moment due to self-weight and I is the moment of inertia of the section.

For all cross-sections the centroid of the strand region and the beam section was the same, that is:

$$e = 0$$

$$\text{and } y = e = 0;$$

Then,

$$f_{cgp} = \pm\frac{P}{A_c} = \frac{F_{pas}}{A_c} \qquad \textbf{(Equation 4-5)}$$

The calculated prestress losses due to elastic shortening are shown in Table 10.

Table 9 Prestressing Forces of Beam Units

Beam ID	Strand	F_{pi}	ε_0	ε_{pi}	ε_{pas}	ΔF_{pA}	$F_{pas} = F_{pi} - \Delta F_{pA}$
		kips	μs	μs	μs	kips	kips
C1-1		46.80	-847	6960	6660	2.07	44.73
C1-2		46.70	-280	7850	7558	1.68	45.02
C1-3		47.03	-926	6995	6655	2.02	45.01
C1-4		46.70	-300	7440	7130	1.87	44.83
C1-5		46.80	-1086	6983	6635	2.02	44.78
C1-6		46.80	-679	7402	7100	1.75	45.05
S1-1		46.80	-847	6960	6660	2.07	44.73
S1-2		46.70	-280	7850	7558	1.68	45.02
S1-3		47.03	-926	6995	6655	2.02	45.01
S1-4		46.70	-300	7440	7130	1.87	44.83
S1-5		46.80	-1086	6983	6635	2.02	44.78
S1-6		46.80	-679	7402	7100	1.75	45.05
R2-1	Top	46.60	-871	6732	6378	2.17	44.43
	Bottom	46.43	-766	6692	6398	1.83	44.60
R2-2	Top	46.60	-871	6732	6378	2.17	44.43
	Bottom	46.43	-766	6692	6398	1.83	44.60
R2-3	Top	47.00	-916	6436	6130	2.85	44.15
	Bottom	46.80	-830	6841	6590	2.44	44.36
R2-4	Top	46.88	-910	6622	6340	2.66	44.22
	Bottom	46.60	-1100	6531	6321	2.20	44.40
R2-5	Top	46.56	-829	6431	6119	2.00	44.56
	Bottom	46.41	-780	6665	6299	2.28	44.13
R2-6	Top	46.56	-829	6431	6119	2.00	44.56
	Bottom	46.41	-780	6665	6299	2.28	44.13
R4-1	1	46.98	-1311	6490	6212	2.58	44.40
	2	47.00	-872	6746	6499	2.43	44.57
	3	46.86	-1183	6071	5818	2.54	44.32
	4	47.03	-1188	6380	6010	2.33	44.70
R4-2	1	47.00	-872	6746	6499	2.43	44.57
	2	46.98	-1311	6490	6212	2.58	44.40
	3	47.03	-1188	6380	6010	2.33	44.70
	4	46.86	-1183	6071	5818	2.54	44.32
R4-3	1	46.90	-766	6349	6047	2.01	44.89
	2	46.95	-854	6525	6010	4.17	42.78
	3	46.90	-1060	6032	5708	3.06	43.84
	4	46.85	-866	6367	6014	3.20	43.65
R4-4	1	46.95	-854	6525	6010	4.17	42.78
	2	46.90	-766	6349	6047	2.01	44.89
	3	46.85	-866	6367	6014	3.20	43.65
	4	46.90	-1060	6032	5708	3.06	43.84

Table 9 (cont'd) Prestressing Forces of Beam Units

Beam ID	Strand	F_{pi}	ε_0	ε_{pi}	ε_{pas}	ΔF_{pA}	$F_{pas} = F_{pi} - \Delta F_{pA}$
R4-5	1	47.01	-765	7080	6711	2.22	44.79
	2	46.95	-838	6829	6449	2.34	44.61
	3	47.10	-937	7151	6682	3.63	43.47
	4	46.99	-816	6996	6543	2.73	44.26
R4-6	1	46.95	-838	6829	6449	2.34	44.61
	2	47.01	-765	7080	6711	2.22	44.79
	3	46.99	-816	6996	6543	2.73	44.26
	4	47.10	-937	7151	6682	3.63	43.47

Table 10 Prestress Loss Due to Elastic Shortening

Beam ID	A_s	A	A_c	F_{pas}	Δf_{pES}	ΔF_{pES}
	in^2	**in^2**	**in^2**	**kips**	**ksi**	**kips**
C1-1	0.2175	28.3	28.06	44.73	10.43	2.27
C1-2	0.2175	28.3	28.06	45.02	10.67	2.32
C1-3	0.2175	28.3	28.06	45.01	10.49	2.28
C1-4	0.2175	28.3	28.06	44.83	10.62	2.31
C1-5	0.2175	28.3	28.06	44.78	10.44	2.27
C1-6	0.2175	28.3	28.06	45.05	10.67	2.32
S1-1	0.2175	36.0	35.78	44.73	8.18	1.78
S1-2	0.2175	36.0	35.78	45.02	8.36	1.82
S1-3	0.2175	36.0	35.78	45.01	8.23	1.79
S1-4	0.2175	36.0	35.78	44.83	8.33	1.81
S1-5	0.2175	36.0	35.78	44.78	8.19	1.78
S1-6	0.2175	36.0	35.78	45.05	8.37	1.82
R2-1	0.435	72.0	71.57	89.03	7.37	3.21
R2-2	0.435	72.0	71.57	89.03	7.37	3.21
R2-3	0.435	72.0	71.57	88.51	7.44	3.24
R2-4	0.435	72.0	71.57	88.63	7.45	3.24
R2-5	0.435	72.0	71.57	88.69	7.34	3.19
R2-6	0.435	72.0	71.57	88.69	7.34	3.19
R4-1	0.87	96.0	95.13	178.00	11.09	9.65
R4-2	0.87	96.0	95.13	178.00	11.09	9.65
R4-3	0.87	96.0	95.13	175.16	12.40	10.79
R4-4	0.87	96.0	95.13	175.16	12.40	10.79
R4-5	0.87	96.0	95.13	177.13	11.44	9.95
R4-6	0.87	96.0	95.13	177.13	11.44	9.95

4.6.3 Summary of Prestressing Forces

The summary of prestressing force and stress is shown in Table 11, where F_{pi} = total initial jacking force; ΔF_{pA} = anchorage seating loss; ΔF_{pES} = elastic shortening loss, of concrete member; F_{pas} = prestressing force after anchorage seating loss, f_{pas} = prestress after anchorage seating loss; F_{pT} = prestress force after instantaneous losses; and f_{pT} = prestress after instantaneous losses.

Table 11 Summary of Prestressing Forces of Small Beam Units

Beam ID	F_{pi}	ΔF_{pA}	ΔF_{pES}	F_{pas}	F_{pT}	f_{pas}	f_{pT}
	kips	**kips**	**kips**	**kips**	**kips**	**ksi**	**ksi**
C1-1	46.80	2.07	2.27	44.73	42.46	205.6	195.2
C1-2	46.70	1.68	2.32	45.02	42.70	207.0	196.3
C1-3	47.03	2.02	2.28	45.01	42.73	206.9	196.4
C1-4	46.70	1.87	2.31	44.83	42.52	206.1	195.5
C1-5	46.80	2.02	2.27	44.78	42.51	205.9	195.4
C1-6	46.80	1.75	2.32	45.05	42.73	207.1	196.5
S1-1	46.80	2.07	1.78	44.73	42.95	205.6	197.5
S1-2	46.70	1.68	1.82	45.02	43.20	207.0	198.6
S1-3	47.03	2.02	1.79	45.01	43.22	206.9	198.7
S1-4	46.70	1.87	1.81	44.83	43.02	206.1	197.8
S1-5	46.80	2.02	1.78	44.78	43.00	205.9	197.7
S1-6	46.80	1.75	1.82	45.05	43.23	207.1	198.8
R2-1	93.03	4.00	3.21	89.03	85.82	204.7	197.3
R2-2	93.03	4.00	3.21	89.03	85.82	204.7	197.3
R2-3	93.80	5.29	3.24	88.51	85.27	203.5	196.0
R2-4	93.48	4.85	3.24	88.63	85.39	203.7	196.3
R2-5	92.97	4.28	3.19	88.69	85.49	203.9	196.5
R2-6	92.97	4.28	3.19	88.69	85.49	203.9	196.5
R4-1	187.87	9.87	9.65	178.00	168.35	204.6	193.5
R4-2	187.87	9.87	9.65	178.00	168.35	204.6	193.5
R4-3	187.60	12.44	10.79	175.16	164.37	201.3	188.9
R4-4	187.60	12.44	10.79	175.16	164.37	201.3	188.9
R4-5	188.05	10.92	9.95	177.13	167.18	203.6	192.2
R4-6	188.05	10.92	9.95	177.13	167.18	203.6	192.2

4.7 Bond Transfer Evaluation

4.7.1 Introduction

The experimental evaluation of bond transfer consisted in measuring the transmission of strains from the pre-tensioned strand to the concrete element. The following instrumentation was used:

- A threaded rod instrumented with strain gages placed along the centroid of the strands in order to measure the transfer of stress from the strands to the concrete. The location of the strain gage rod is shown in Figure 28.
- Target points on the surface of prestressed concrete beams.
- Accelerometers at the location of bond between the strand and the concrete to evaluate the dynamic effect due to the longitudinal stress wave after release of the strand load.
- Transverse, or radial, strain gages on the C1 test units along the transfer length region to estimate dilation strains and consequently bursting pressure.

In addition to the noted instrumentation, any cracks developed on the test units were carefully monitored to serve as qualitative information for correlation with the finite element analyses.

As mentioned before, the distance from the concrete beam end to the point where the entire stress force from the prestressing strand is transferred to concrete beam is defined as the transfer length. The stress in the strand and the compressive strain of concrete beams are both zero at the beam end and increase rapidly along the transfer length until becoming constant at the end of transfer length, where they both reach a maximum value. As a result, the transfer length can be determined by measuring the compressive strains along the concrete beam longitudinal axis and locating the point at which strains become constant. Two methods were used to measure concrete strains, namely, concrete surface strain measurements and concrete internal strain measurements. Details on these methods are discussed in the following.

4.7.2 Concrete Surface Strain Measurements

Concrete surface strain measurements were conducted using a DEMEC (Detachable MEChanical) strain measurement system. The DEMEC system consists of a caliper and small stainless discs. Each stainless disc has a small hole in the center which was designed to fit the feet of the caliper. The discs were glued to the surface at certain spacing over the region in which

the concrete compressive strain needs to be measured. Strains are obtained by measuring the change of length between measuring points before and after strand releasing.

One line of target points along the beam longitudinal centerline and was attached to the beam side surface (Figure 25). For the beams with one strand the target points were at the same height as the strand. For beams with two or four strands, the center line of the side surface was in the middle of the top and bottom strand(s).

Figure 25 Target Points on Small Beam Unit

The length of beam region with target points was different for each beam since each had a different debonding length. The target points were spaced at 2 in. (51 mm) along the beam length.

Measurements were taken before and after prestress release. For the beam units with two or four prestressing strands, an intermediate measurement was taken after the top strand(s) were released. It should be noted that the initial strain measurements were taken one day before the day of release and most of the final strain measurements were taken late afternoon on the day of release. As a result, the time lapse between the initial and final measurements was approximately 20 to 24 hours. The creep and shrinkage of concrete during this period was considerable and led to higher concrete compressive strains than expected. This will be discussed in the result section.

The concrete surface strain measurements were taken along a 2 in. (51 mm) increment for beam units with one strand (C1 and S1 beams). However, the results were found to be highly inaccurate and it was unlikely to be able to obtain transfer length based on those results. It is

thought that the reason of this problem is due to the accuracy of the caliper used in this project. As a result, an overlapped increment of 8 in. (203 mm) was used for beam units tested later (R2 and R4 beam units). (Figure 26)

The method of concrete surface strain measurement was conducted in the following way. Strain values were determined by dividing the difference of the distance between two target points before and after prestressing by the original distance between these two points. The two target points for each measurement were approximately 8 in. from each other (1 and 4, 2 and 6, 3 and 7, etc in Figure 26), while the first target point was located 1 in. from the beam end. Three readings were taken for each measurement on a given beam unit and the average values were used to determine the strain value. The compressive strain value obtained based on the measurement between each target points pair was assigned to the point in the middle. For example, the compressive strain ε1 determined between point 1 and 5 is assigned to point 3. In addition, the average of three consecutive strain values were averaged and assigned to the middle point using the following equation:

$$\varepsilon_{i,smooth} = \frac{\varepsilon_{i-1} + \varepsilon_i + \varepsilon_{i+1}}{3} \qquad \textbf{(Equation 4-6)}$$

For example, strain value ε1, ε2 and ε3, which are the strain values assigned for target points 3, 4 and 5 respectively, are averaged and the average value is assigned to target point 4. The averaging procedure was conducted with the purpose of smoothing the data curve.

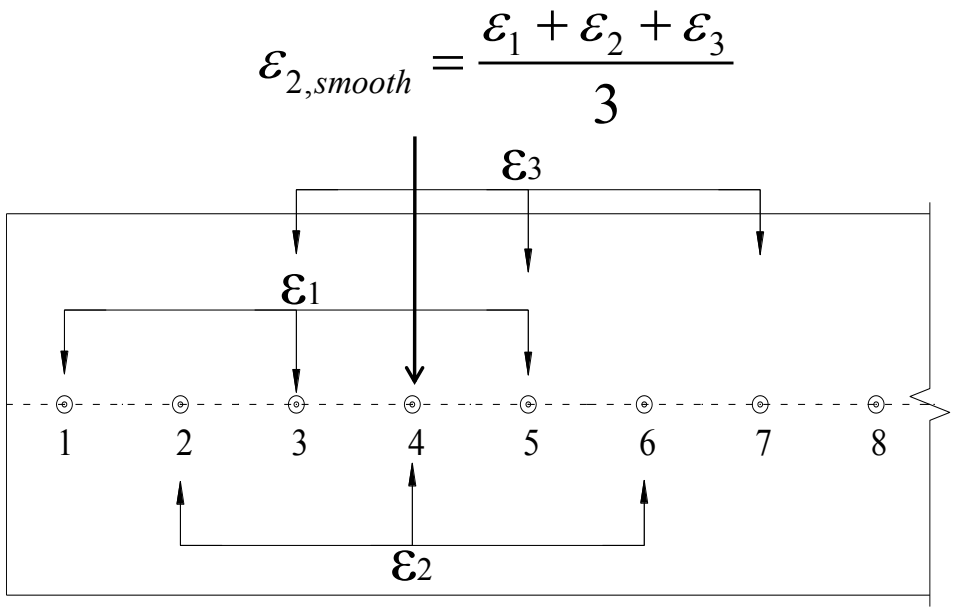

Figure 26 Averaging of Strain Values of CSSM

After the strain are assigned to each target points, the concrete compressive strain profile was plotted against the distance of the target points from the end of the beam. The transfer length was determined using the method of 95% average maximum strain (AMS), which is discussed later.

4.7.3 Concrete Internal Strain Measurements

In addition to the concrete surface strain measurements, concrete strains were also measured inside the element by means of an instrumented rod. Some researchers have installed strain gages directly on the strand surface to measure the internal strain. However, this methodology has limitations. First, the strain gages can easily get damaged since they are located at the interface between strand and concrete where the prestress is transferred. Second, attaching strain gages on the surface of strand would interfere with the bond behavior. Finally, the prestressing strand consists of 6 independent wires helically wound around a center one and each wire may have a slightly different strain when the strand is released. As a result, if the strain gages are attached to different wires, the strain difference would disturb the resulting data.

The internal measurement conducted in this project was realized by embedding a 0.25-in. diameter threaded bar instrumented with strain gages and placed inside the beam units parallel to

the prestressing strand (see Figure 27). The reason for using a threaded bar is to ensure good bond mechanism between the bar surface and surrounding concrete. The area of the bar is also considerably small compared to the area of the cross sections of beam units so that its influence on the behavior of beam units after prestress release could be ignored.

Theoretically, if perfect bond is achieved at the interface of instrumented bar and the concrete, the strain of the threaded bar would be the same as the strain of the surrounding concrete. As a result, the concrete strain profile can be obtained by measuring the strain of the threaded bar. Even though the actual bond mechanism may not be perfect, the strain along the instrumented threaded bar is thought to be very close to the state of in the concrete. Nevertheless, since the purpose of this measurement is to determine the changing trend of concrete strains, the strain level, or magnitude, was thought to be less important.

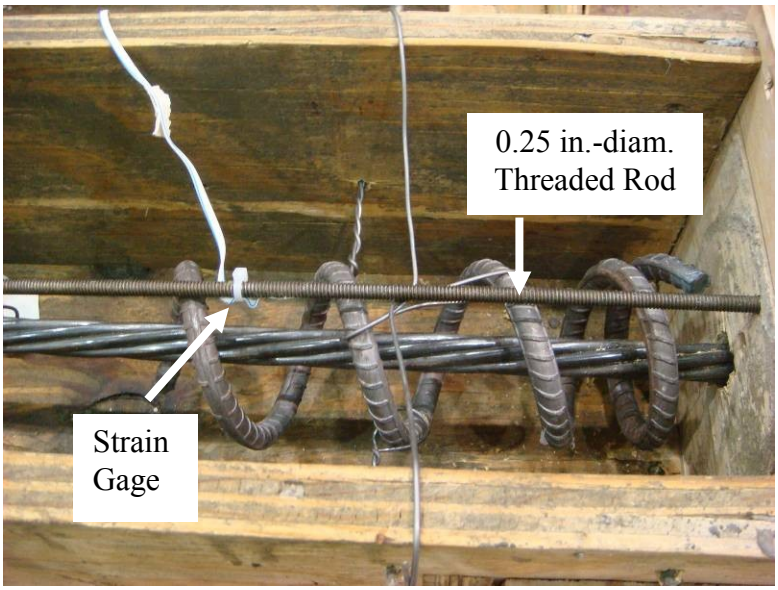

Figure 27 View of Instrumented Threaded Rod in S1 Beam

The location of the threaded rebar in the different beam units is shown in Figure 28. For beam units with one strand, the threaded bar was located along the beam length and was about one inch from the strand surface. For beam units with two or four strands, the threaded bar was located along the beam length at the centroid of the beam cross section.

The spacing of strain gages on the threaded bar varied with the distance from the beam end. Smaller spacing was used for strain gages close to the estimated end of transfer length and larger spacing was used within the region close to the beam end and beyond the region of potential transfer length end. The strain gage layout varied for each of the beam units and details of strain gage locations are shown in Appendix A.

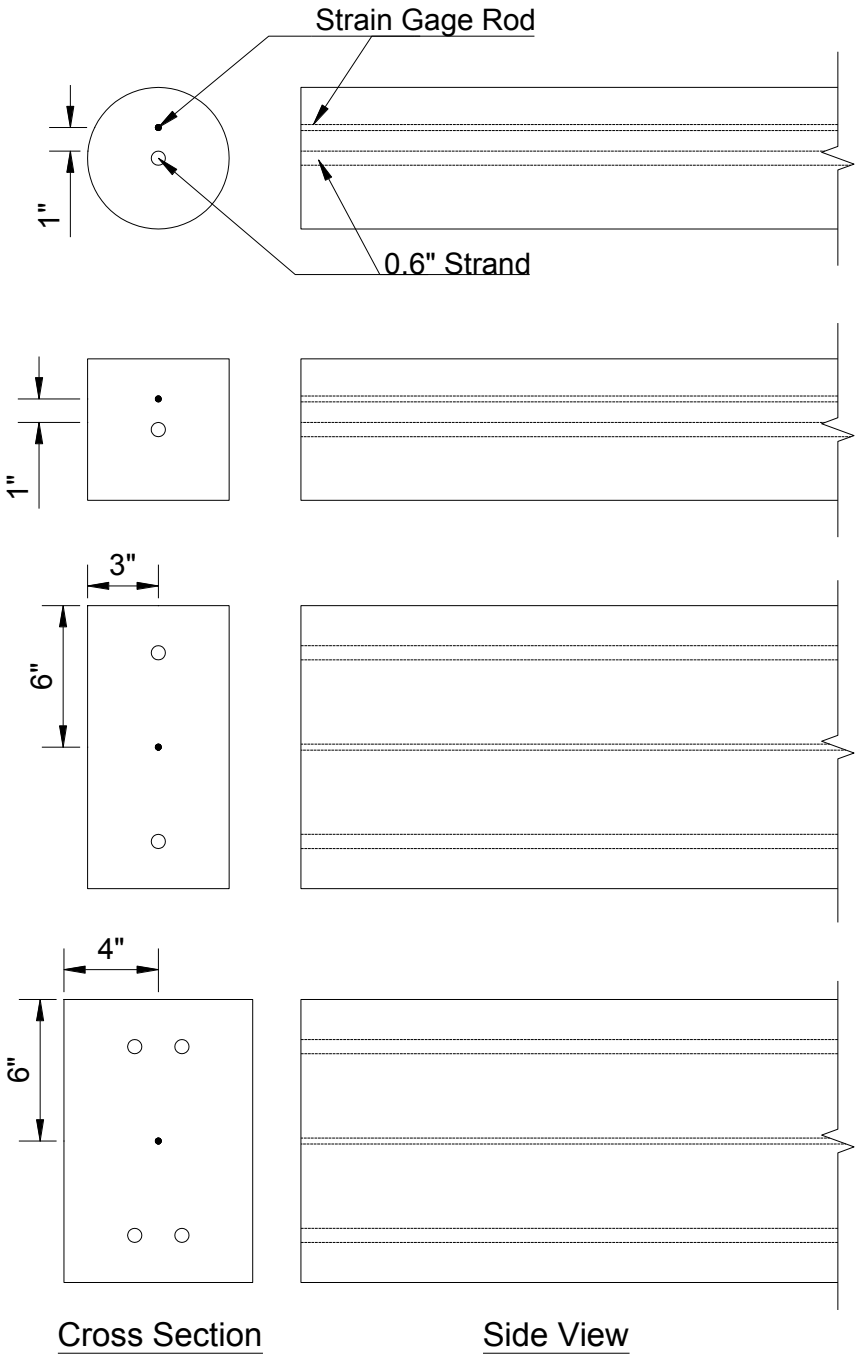

Figure 28 Location of Instrumented Rod within Beam Units

4.7.4 Average Maximum Strain (AMS) Method for Determining Transfer Length

The 95% average maximum strain (AMS) method [33] was adopted to experimentally determine transfer length. The AMS is the average of all the strains contained on or near the plateau of the concrete strain curve. Strain values in the plateau region in the concrete strain curve for each beam units were visually inspected and the average values were calculated (Figure 29). Even though this method is subjective since it requires visual definition of the plateau region, the AMS value will not change significantly if one or two data points are included or excluded from the average.

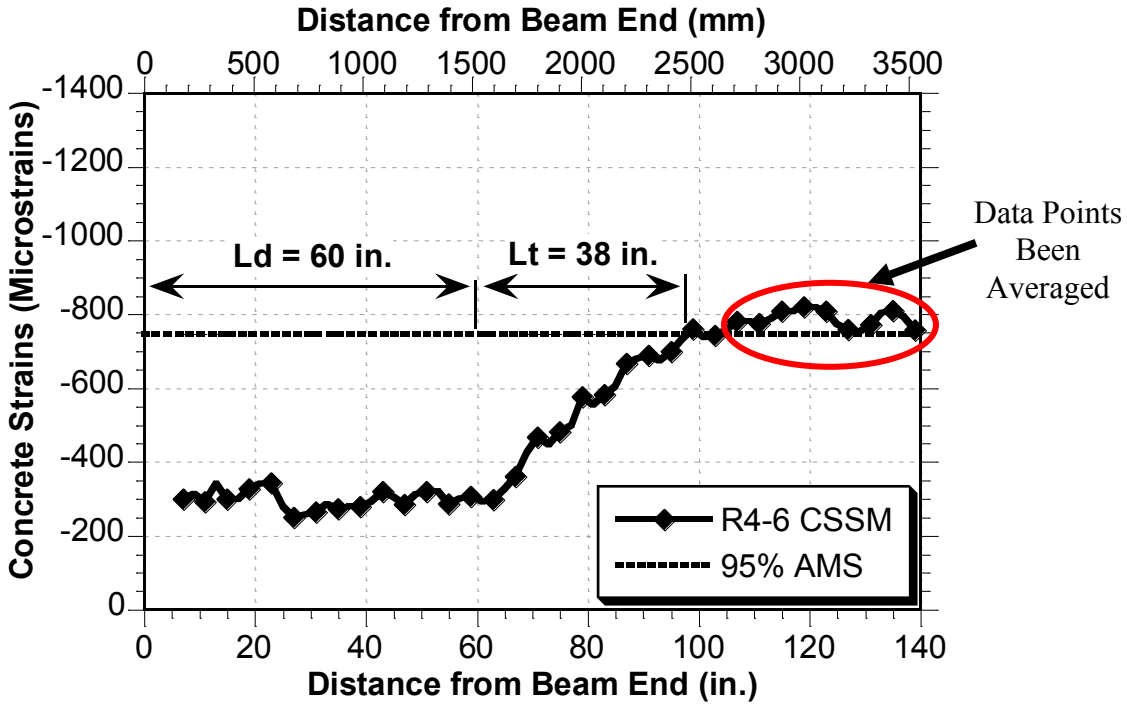

Figure 29 Concrete Strain Data of Beam Unit R4-6 (CSSM)

Concrete strain curves were plotted along the length of the beam and a horizontal line representing the 95% AMS value for the particular strain curve was also plotted. The transfer length was obtained as the value of the distance from the beam end to the point where the 95% AMS line intersected the concrete strain curve for fully bonded beam units, while for the debonded beam units the transfer length was considered to be from the end of debonding region to the intersection point.

4.7.5 Experimental Results on Stress Transfer

Results from the surface and internal strain measurements are discussed in this section. Considering the complex material characteristic of concrete and the fact that each beam unit is unique, results from each beam unit may not be able to represent a general estimate for similar prestressing members from a statistical point of view. However, the primary objective of the experiments on small-scale beams was to provide a reference for the calibration of bond mechanism simulation in numerical models rather than determining precise values for certain features such as transfer length.

The main parameter analyzed from the experiments on small-scale prestressed beams was the transfer length. As discussed before, two different methods were used to measure concrete strains in the longitudinal direction and thus two sets of data were obtained. It needs to be noted that not all of the beam units have reliable data from both methods. Surface strain measurements are not available for beam units with single strand (C1 and S1 beams) due to mistakes made in the measurement methodology for the first two set of tests. And for the S1-5, R2-1, R2-2, R2-5 and R2-6 beam units, too many strain gages were damaged during the test and thus the transfer length could not be determined based on the internal strain measurements on these beam units.

Differences were observed between the two measuring methods. The reasons may be: i) the measurements are taken on different locations in the beam unit; ii) creep and shrinkage effect have influence on concrete strain and the influence is different for each methods; and iii) each measuring method has a different error level due to the different measurement equipment that causes differences in results.

As a result, the experiment data from two measuring methods were analyzed separately. And since most of the beams have data from internal strain measurements, it was decided to use the results from strain gages as a reference for the calibration of bond simulations in the numerical studies. Thus, results from the concrete surface strain measurements are only used for overall evaluation and comparison purposes.

Among several parameters, transfer length depends heavily on concrete compressive strength and the effective strand prestressing level. In general, weaker concrete and higher prestressing force will lead to longer transfer length. Based on the equation for estimating transfer length from AASHTO [1], the prestressing force after losses is linearly related to transfer length. And some researchers have suggested that bond strength is proportional to $\sqrt{f'_c}$.

If we assume that the prestressing force is transferred linearly along the transfer length, the following equation can be formulated to relate dependency of transfer length with bond strength:

$$L_t = \frac{f_{se} A_s}{\pi d U} \qquad \textbf{(Equation 4-7)}$$

where d and A_s are the diameter and area of the prestressing strand, respectively; and U is the bond strength between strand and the surrounding concrete, which is proportional to $\sqrt{f'_c}$. Then it can be assumed that transfer length is proportional to the prestressing force and $1/\sqrt{f'_c}$. For practical purposes, the initial prestress f_{si} is used instead of f_{se}.

In order to compare transfer lengths from different small beam units, a concrete strength with $f'_c = 4600$ ksi and an initial prestressing force $f_{si} = 0.75 \times 270 = 202.5$ ksi were assumed and all transfer lengths were normalized to these reference values through the factors in Table 12. It needs to be noted that the assumed concrete strength and initial prestressing level follow from the parameters to be used for the evaluation of strand bond effects on the anchorage zones of full-size box girders presented in Chapter 6 The two factors in Table 12 were calculated using the following equations: (f'_c and f_{si} are in ksi)

$$\phi_{f'_c} = \frac{\sqrt{f'_c}}{\sqrt{4600}} \qquad \textbf{(Equation 4-8)}$$

$$\phi_{f_{si}} = \frac{202.5}{f_{si}} \qquad \textbf{(Equation 4-9)}$$

Table 12 Normalization Factors for Experimental Transfer Length Values

Beam ID	$\phi_{f'_c}$	$\phi_{f_{si}}$	Beam ID	$\phi_{f'_c}$	$\phi_{f_{si}}$
C1-1	1.15	0.98	**R2-1**	1.27	0.99
C1-2	1.13	0.98	**R2-2**	1.27	0.99
C1-3	1.15	0.98	**R2-3**	1.25	0.99
C1-4	1.13	0.98	**R2-4**	1.25	0.99
C1-5	1.15	0.98	**R2-5**	1.27	0.99
C1-6	1.13	0.98	**R2-6**	1.27	0.99
S1-1	1.15	0.98	**R4-1**	1.27	0.99
S1-2	1.13	0.98	**R4-2**	1.27	0.99
S1-3	1.15	0.98	**R4-3**	1.11	1.00
S1-4	1.13	0.98	**R4-4**	1.11	1.00
S1-5	1.15	0.98	**R4-5**	1.22	0.99
S1-6	1.13	0.98	**R4-6**	1.22	0.99

4.7.5.1 Concrete Surface Strain Measurements

As previously mentioned, surface strain measurements for the C1 and S1 beams were inaccurate due to the resolution of the caliper and the measured gage length. Hence, results for the C1 and S1 beams are not presented in this section. The transfer lengths determined based on concrete surface strain measurements for the R2 and R4 beam units are presented in Table 13.

Table 13 Transfer Lengths Results of R2 and R4 Beam Units (CSSM)

Beam Unit ID	Debonded Length (in.)	Debonding Material	Transfer Length (in.)	Factored Transfer Length (in.)
R2-1	0	NA	26.0	32.5
R2-2	18	Soft	21.0	26.2
R2-3	0	NA	30.5	37.8
R2-4	0	NA	34.0	42.0
R2-5	36	Soft	24.0	30.1
R2-6	60	Soft	27.0	33.9
R4-1	0	NA	29.5	36.9
R4-2	18	Soft	24.0	30.0
R4-3	36	Soft	19.0	21.2
R4-4	60	Soft	18.0	20.1
R4-5	36	Rigid	30.0	36.3
R4-6	60	Rigid	38.0	46.0

4.7.5.2 Concrete Internal Strain Measurements

Table 14 shows the measured transfer length of small beam units based on concrete internal strain measurement. The measurement data for beam unit S1-5, R2-1, R2-2, R2-4 and R2-5 are not available due to the fact that too many strain gages were damaged during the test.

Table 14 Transfer Lengths Results of Small Beam Units (CISM)

Model ID	Debonded Length (ft)	Debonding Material	Transfer Length (in.)	Factored Transfer Length (in.)
C1-1	0	NA	18.0	20.3
C1-2	0	NA	40.5	44.6
C1-3	1.5	Soft	20.0	22.4
C1-4	1.5	Soft	41.0	45.4
C1-5	1.5	Rigid	29.5	33.2
C1-6	1.5	Rigid	30.5	33.6
S1-1	0	NA	18.5	20.8
S1-2	0	NA	32.0	35.3
S1-3	3	Soft	16.5	18.5
S1-4	3	Soft	22.0	24.3
S1-5	5	Soft	N/A	0.0
S1-6	5	Soft	20.3	22.3
R2-1	0	NA	N/A	0.0
R2-2	1.5	Soft	N/A	0.0
R2-3	0	NA	26.0	32.2
R2-4	0	NA	32.0	39.6
R2-5	3	Soft	N/A	0.0
R2-6	5	Soft	N/A	0.0
R4-1	0	NA	26.0	32.5
R4-2	1.5	Soft	28.5	35.6
R4-3	3	Soft	26.5	29.6
R4-4	5	Soft	25.5	28.5
R4-5	3	Rigid	33.0	40.0
R4-6	5	Rigid	32.0	38.8

4.7.6 Comparison with Hand Calculations

The maximum longitudinal strain in the concrete obtained from strain measurements was compared to hand calculation with the purpose of verifying the results. Concrete strain after prestress transfer can be calculated using the equations immediately below and the results are shown in Table 15.

$$\varepsilon_c = \frac{F_{pT}}{(EA)_e} \qquad \textbf{(Equation 4-10)}$$

$$(EA)_e = E_{ci} A_c + E_p A_p \qquad \textbf{(Equation 4-11)}$$

Table 15 Hand Calculation of Maximum Concrete Strain

Beam ID	Strain	Beam ID	Strain
C1-1	3.25E-04	**R2-1**	2.37E-04
C1-2	3.32E-04	**R2-2**	2.37E-04
C1-3	3.27E-04	**R2-3**	2.38E-04
C1-4	3.30E-04	**R2-4**	2.39E-04
C1-5	3.25E-04	**R2-5**	2.36E-04
C1-6	3.32E-04	**R2-6**	2.36E-04
S1-1	2.60E-04	**R4-1**	3.43E-04
S1-2	2.66E-04	**R4-2**	3.43E-04
S1-3	2.62E-04	**R4-3**	3.78E-04
S1-4	2.65E-04	**R4-4**	3.78E-04
S1-5	2.61E-04	**R4-5**	3.53E-04
S1-6	2.66E-04	**R4-6**	3.53E-04

The maximum longitudinal concrete strain from CISM and hand calculation is compared in Figure 30. From the figure it can be seen that there is a big difference between the results from concrete internal and surface strain measurements and the hand calculation. The reason is attributed to shrinkage and creep effects, which are not considered in the simple hand calculations noted above.

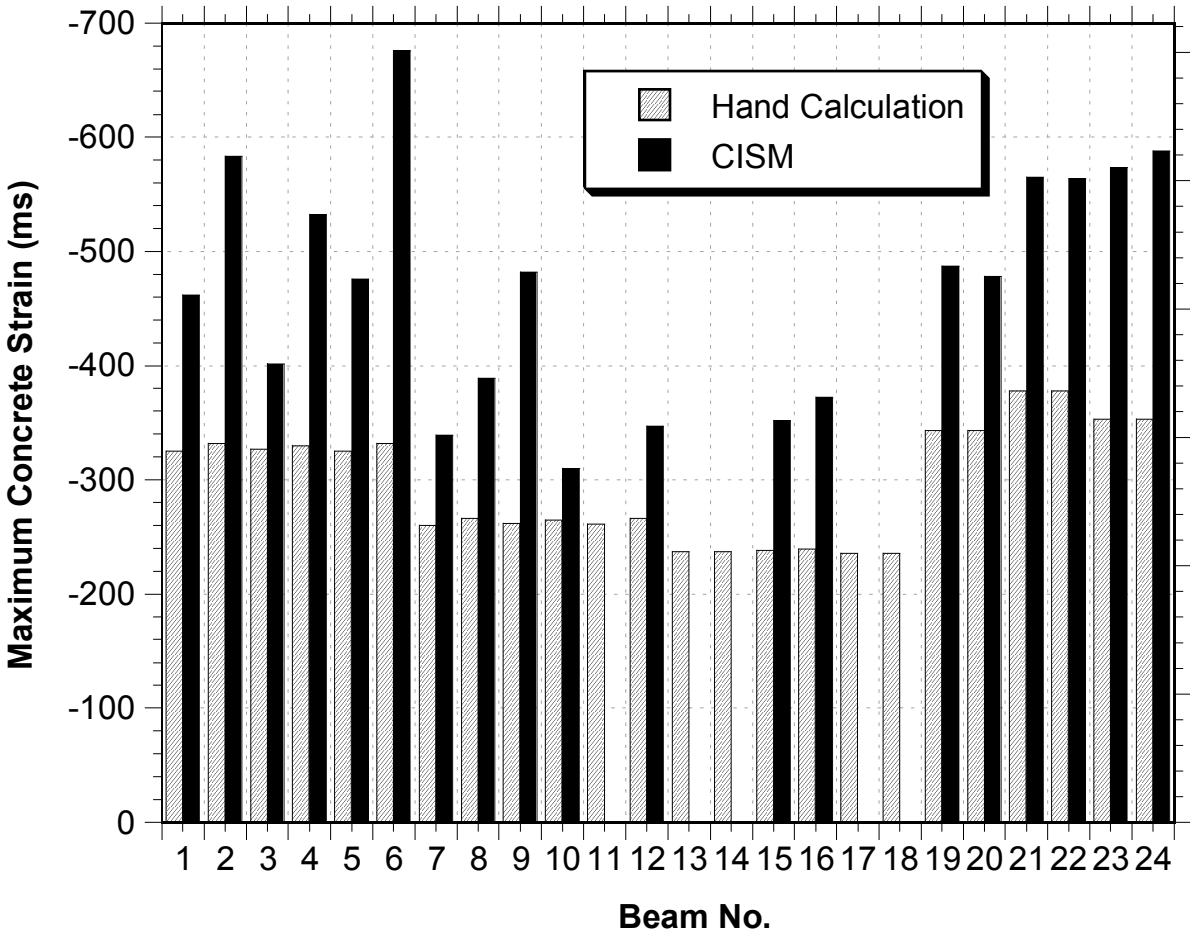

Figure 30 Comparison of Maximum Concrete Strain from CISM and Hand Calculation

As previously mentioned, the method used to obtain surface strain measurements is very time consuming and the testing process (release of strands and measurements after each strand release) took between 6 and 12 hours, during which shrinkage and creep of concrete can be significant. Considering the level of sustained load and the small cross sectional areas of the beam units in this project, the effect of creep may be considerably high. And due to the fact that the initial reading of concrete surface strain measurement was taken usually one day before the testing day, the strain change due to shrinkage between the initial reading, middle and final readings was accounted as part of the measurements, which leads to a bigger "error." As a result, an estimate of concrete strain due to creep and shrinkage was conducted.

4.7.7 Concrete Strain Due to Shrinkage [29]

Shrinkage is the volume decrease of concrete during hardening and drying under constant temperature. The amount of shrinkage increases with time. The estimation of concrete shrinkage strain in this research was conducted using the procedures established by the Euro-International Concrete Committee (CEB) [29]. The axial shrinkage strain, ε_{cs}, occurring between time t_s at the start of shrinkage and t in plain concrete can be predicted from the equation:

$$\varepsilon_{cs}(t,t_s) = \varepsilon_{cs0}\beta_s(t,t_s) \quad \textbf{(Equation 4-12)}$$

where ε_{cso} is the basic shrinkage strain for a particular concrete and relative humidity, and $\beta_s(t,t_s)$ is a coefficient given to describe the development of shrinkage between time t_s and t as a function of the effective thickness of the member. The expression to calculate ε_{cso} is:

$$\varepsilon_{cso} = \varepsilon_s(f_{cm})\beta_{RH} \quad \textbf{(Equation 4-13)}$$

where,

$$\varepsilon_s(f_{cm}) = 1.2\left[160 + \beta_{sc}(9 - f_{cm}/f_{cmo})\right]\times 10^{-6} \quad \textbf{(Equation 4-14)}$$

In which f_{cm} is the mean concrete compressive strength at 28 days, psi. And it can be taken equal to f'_{cr} as given by the equation below:

- When $f'_c \le 5000\,psi$, use the larger value of:

$$f'_{cr} = f'_c + 1.34s \quad \textbf{(Equation 4-15)}$$

$$f'_{cr} = f'_c + 2.33s - 500 \quad \textbf{(Equation 4-16)}$$

- When $f'_c > 5000\,psi$, use the larger value of:

$$f'_{cr} = f'_c + 1.34s \quad \textbf{(Equation 4-17)}$$

$$f'_{cr} = 0.90f'_c + 2.33s \quad \textbf{(Equation 4-18)}$$

where,

$f_{cmo} = 1450\,psi$ (based on the recommended value in Reference [29])

$\beta_{sc} = 50$ for Type I cement and 80 for Type III cement, and

β_{RH} = coefficient that accounts for the effect of relative humidity on shrinkage.

For RH between 40 and 99 percent,

$$\beta_{RH} = -1.55\left[1 - \left(\frac{RH}{RH_0}\right)^3\right] \qquad \textbf{(Equation 4-19)}$$

When RH is equal to or greater than 99 percent,

$$\beta_{RH} = +0.25$$

where RH is the relative humidity of the ambient atmosphere in percent

$$RH_0 = 100 \text{ percent}$$

The development of shrinkage with time is given by

$$\beta_s(t, t_s) = \left[\frac{(t - t_s)/t_1}{350(h_e/h_0)^2 + (t - t_s)/t_1}\right]^{0.5} \qquad \textbf{(Equation 4-20)}$$

where h_e is the effective thickness in inches to account for the volume/surface ratio and is given by:

$$h_e = 2A_c/u \qquad \textbf{(Equation 4-21)}$$

where,

A_c = the area of the cross section, in^2

u = the perimeter of the cross section exposed to the atmosphere, in.

$h_0 = 4$ in.

t = the age of the concrete, days

t_s = the age of the concrete in days when shrinkage or swelling started, generally taken as the age at the end of moist-curing, and

$t_1 = 1$ Day

4.7.8 Concrete Strain Due to Creep [29]

When concrete is loaded by a sustained load, in addition to the instantaneous elastic strain, creep strains will develop with time. The creep strains can be on the order of one to three times the instantaneous elastic strains. As a result, it is necessary of estimate concrete strains due to creep.

Creep is estimated in this research using the method from the CEB-FIB Model Code 1990 [29]. The total strain, $\varepsilon_c(t)$, at time t in a concrete member uniaxially loaded with a constant stress $\sigma_c(t_0)$ at time t_0 is:

$$\varepsilon_c(t) = \varepsilon_{ci}(t_0) + \varepsilon_{cc}(t) + \varepsilon_{cs}(t) + \varepsilon_{cT}(t) \quad \textbf{(Equation 4-22)}$$

where,

$\varepsilon_{ci}(t_0)$ = initial strain at loading $= \sigma_c(t_0) / E_c(t_0)$

$\varepsilon_{cc}(t)$ = creep strain at time t where t is greater than t_0

$\varepsilon_{cs}(t)$ = shrinkage strain at time t

$\varepsilon_{cT}(t)$ = thermal strain at time t

$E_c(t_0)$ = modulus of elasticity at the age of loading

The stress-dependent strain at time t is:

$$\varepsilon_{csd}(t) = \varepsilon_{ci}(t_0) + \varepsilon_{cc}(t) \quad \textbf{(Equation 4-23)}$$

For a stress σ_c applied at time t_0 and remaining constant until time t, the creep strain ε_{cc} between time t_0 and t is:

$$\varepsilon_{cc}(t,t_0) = \frac{\sigma_c(t_0)}{E_c(28)} \phi(t,t_0) \quad \textbf{(Equation 4-24)}$$

where $E_c(28)$ is the modulus of elasticity at the age of 28 days, and $\phi(t,t_0)$ is the creep coefficient, given by:

$$\phi(t,t_0) = \phi_0 \beta_c(t,t_0) \quad \textbf{(Equation 4-25)}$$

where ϕ_0 is the basic creep given by:

$$\phi_0 = \phi_{RH} \beta(f_{cm}) \beta(t_0) \quad \textbf{(Equation 4-26)}$$

where,

$$\phi_{RH} = 1 + \frac{1 - RH / RH_0}{0.46 (h_e / h_0)^{1/3}} \quad \textbf{(Equation 4-27)}$$

$$\beta(f_{cm}) = \frac{5.3}{\left(f_{cm} / f_{cm0}\right)^{0.5}} \quad \textbf{(Equation 4-28)}$$

$$\beta(t_0) = \frac{1}{0.1 + (t_0 / t_1)^{0.2}} \qquad \textbf{(Equation 4-29)}$$

And $\beta_c(t, t_0)$ is a coefficient to account for the development of creep with time, given by

$$\beta_c(t, t_0) = \left[\frac{(t - t_0)/t_1}{\beta_H + (t - t_0)/t_1} \right]^{0.3} \qquad \textbf{(Equation 4-30)}$$

where,

$$\beta_H = 150\left[1 + \left(1.2 \frac{RH}{RH_0} \right) 18 \right] \frac{h_e}{h_0} + 250 \le 1500 \qquad \textbf{(Equation 4-31)}$$

4.7.9 Results of Concrete Strain Due to Creep and Shrinkage

The results of concrete strain due to creep and shrinkage are shown in Table 16, where ε_{ci} = the instantaneous concrete strain at prestress transfer, ε_{cs} = the concrete strain due to shrinkage, ε_{cc} = the concrete strain due to creep, and ε_c = the total concrete strain.

Table 16 Estimation of Concrete Strain Due to Creep and Shrinkage

Beam ID	ε_{ci}	ε_{cs}	ε_{cc}	ε_c
	in./in.	**in./in.**	**in./in.**	**in./in.**
C1-1	-3.25E-04	-6.67E-05	-1.40E-04	-5.32E-04
C1-2	-3.32E-04	-6.82E-05	-1.38E-04	-5.38E-04
C1-3	-3.27E-04	-6.67E-05	-1.41E-04	-5.35E-04
C1-4	-3.30E-04	-6.82E-05	-1.37E-04	-5.36E-04
C1-5	-3.25E-04	-6.67E-05	-1.40E-04	-5.32E-04
C1-6	-3.32E-04	-6.82E-05	-1.38E-04	-5.38E-04
S1-1	-2.60E-04	-6.66E-05	-1.12E-04	-4.39E-04
S1-2	-2.66E-04	-6.81E-05	-1.10E-04	-4.45E-04
S1-3	-2.62E-04	-6.66E-05	-1.13E-04	-4.41E-04
S1-4	-2.65E-04	-6.81E-05	-1.10E-04	-4.43E-04
S1-5	-2.61E-04	-6.66E-05	-1.12E-04	-4.40E-04
S1-6	-2.66E-04	-6.81E-05	-1.11E-04	-4.45E-04
R2-1	-2.37E-04	-4.39E-05	-7.19E-05	-3.53E-04
R2-2	-2.37E-04	-4.39E-05	-7.19E-05	-3.53E-04
R2-3	-2.38E-04	-4.38E-05	-7.56E-05	-3.57E-04
R2-4	-2.39E-04	-4.38E-05	-7.57E-05	-3.58E-04
R2-5	-2.36E-04	-4.39E-05	-7.16E-05	-3.52E-04
R2-6	-2.36E-04	-4.39E-05	-7.16E-05	-3.52E-04
R4-1	-3.43E-04	-3.61E-05	-1.06E-04	-4.86E-04
R4-2	-3.43E-04	-3.61E-05	-1.06E-04	-4.86E-04
R4-3	-3.78E-04	-4.41E-05	-1.50E-04	-5.72E-04
R4-4	-3.78E-04	-4.41E-05	-1.50E-04	-5.72E-04
R4-5	-3.53E-04	-3.89E-05	-1.20E-04	-5.12E-04
R4-6	-3.53E-04	-3.89E-05	-1.20E-04	-5.12E-04

There are several issues that need to be noted about the calculation of concrete strain due to shrinkage and creep:

i) Concrete compressive strength at the day of test (release) was used;

ii) The relative humidity is assumed to be 40%, which is a relatively low value;

iii) It is assumed that moist curing ends the day before testing, and thus $t_s = t + 1$;

iv) Strand was generally released in the morning and the measurement were finished in late afternoon. Thus for creep strain calculation it was assumed that $t = t_0 + 0.5$.

From Figure 31 we can see that by considering creep and shrinkage effects the hand calculation of maximum concrete is much closer agreement to the results of concrete internal strain measurements. This supports the hypothesis that the difference noticed before between experimental and simple calculations (see Figure 30) was mainly due to creep and shrinkage effect. However, it should be noted that the estimate of concrete strain due to creep and shrinkage effect is just an approximate value since in reality each test is different from others in terms of material properties, environmental conditions and time to test. It is thus too difficult to get precise values for all the related parameters such as relative humidity, concrete strength, and the time period during which creep and shrinkage effects took place.

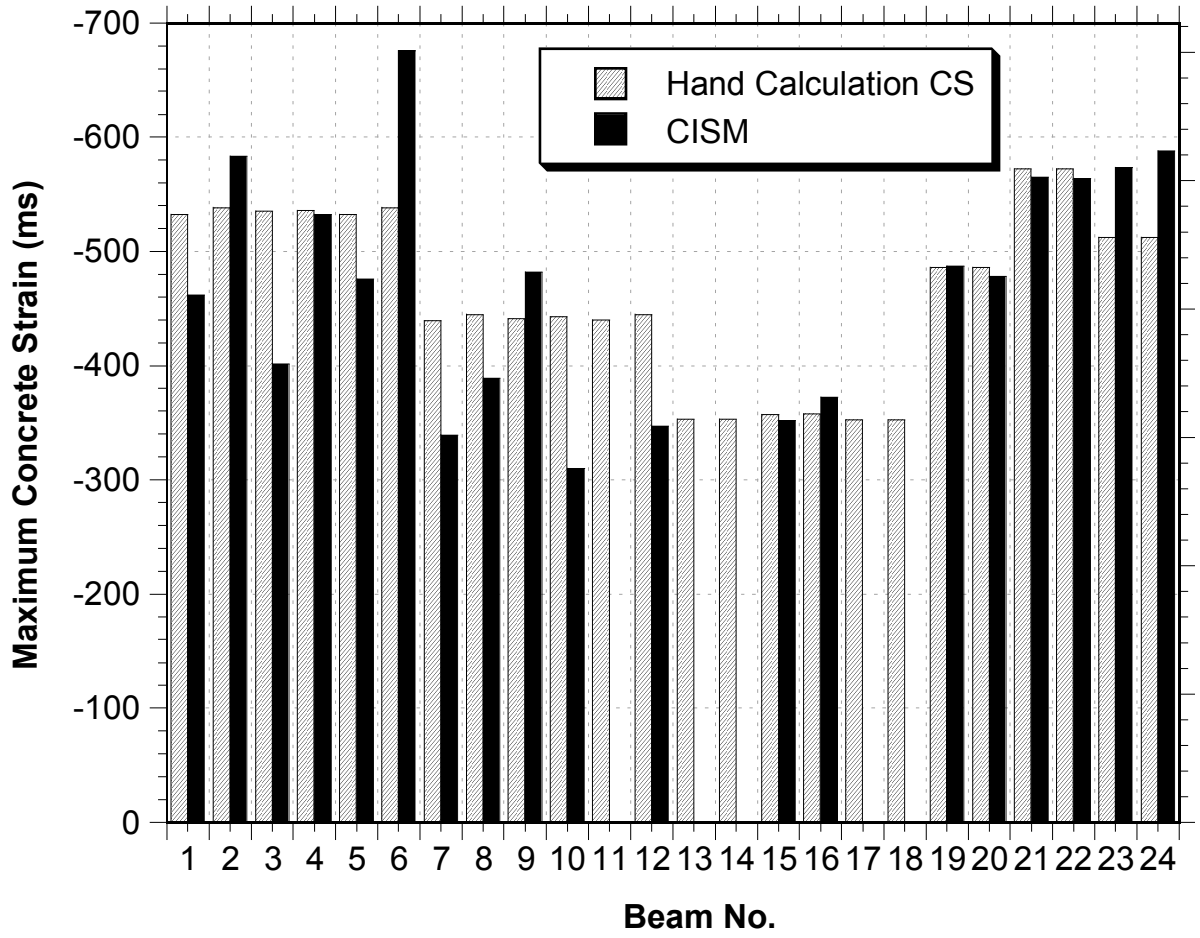

Figure 31 Comparison of Maximum Concrete Strains from CISM and Hand Calculation Considering Shrinkage and Creep

4.8 Effect of Parameters on Stress Transfer

This section presents comparisons of the results obtained from the different beam units in the test matrix with the objective to evaluate the effects of the different considered parameters, i.e., debonded length, free strand length, debonding material, confinement, and release method, on bond stress transfer, which in this case is consists on the experimentally determined value for transfer length.. Since differences were observed between the concrete internal strain measurements (CISM) and concrete surface strain measurements (CSSM) methods, only results from the same measurement method are compared.

4.8.1 Sudden vs. Annealed Release

Figure 32 shows the comparison of transfer lengths obtained from internal strain measurements for beams with different release methods. It can be seen that beams in which prestress was transferred by sudden release had a longer transfer length than those that were released gradually, or by annealing the strand. This is consistent with expectations since sudden release leads to higher kinetic energy upon release compared to the annealed process (as discussed in section 4.2.2) It should be noted that the transfer length of the sudden released beams C1-2 and C1-4 were much higher compared to the corresponding gradually released beams C1-1 and C1-3. Not enough evidence is available to rationalize such significant increase. A possible reason is that, according to the conservation of momentum, the effect of release rate is related to the mass of the concrete beam and the effect may be higher in beams with smaller cross section (i.e., less massive). It can be seen from Figure 32 that the effect of releasing rate on transfer length in the larger beams was not as significant as for the C1 beam units. It can also be seen that the transfer length for beam C1-5 is noticeably high. This is attributed to the fact that strand was inadvertently cut from overheating during the annealing process. Thus, the strand in beam C1-5 was essentially released in a sudden manner. The comparison of beams C1-5 and C1-6 does not make matters easier. The transfer length of beam unit C1-6 (sudden released with rigid debonding material) was much shorter than expected. Unfortunately, it is difficult to rationalize such result since there are many parameters that might affect the transfer length for a specific beam unit.

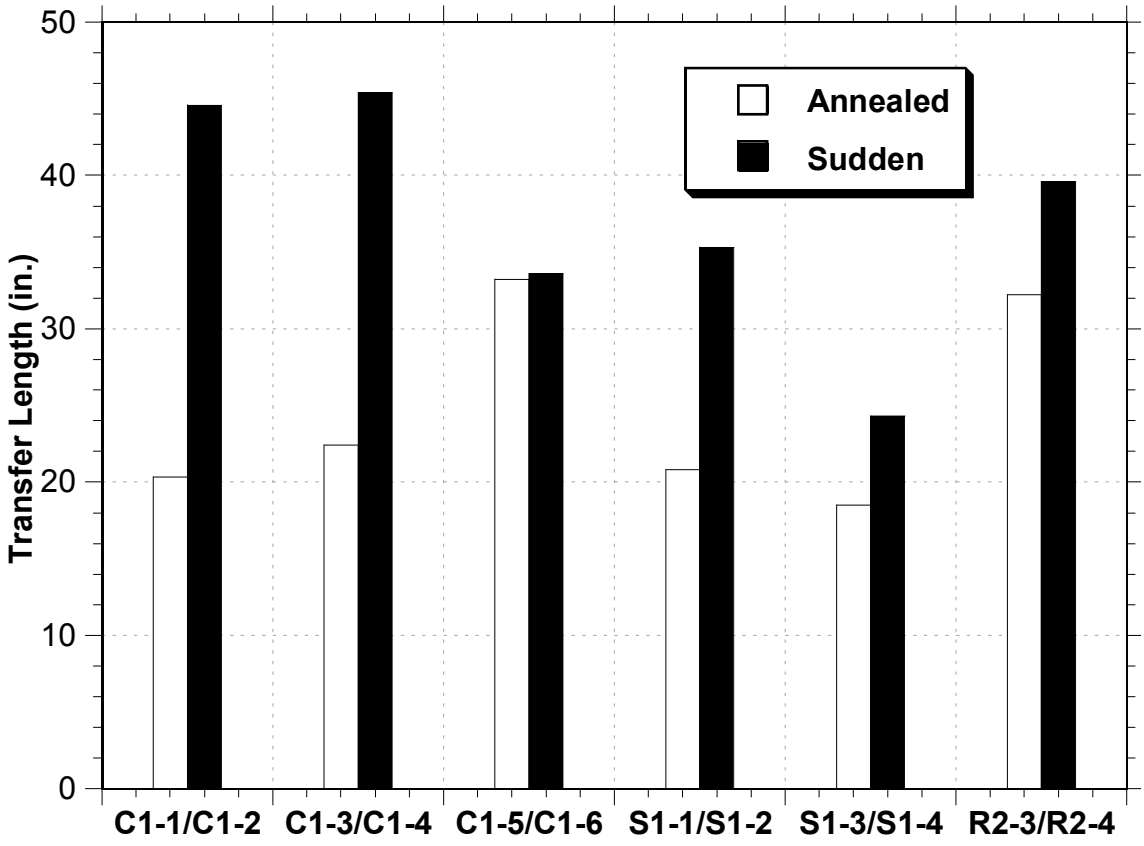

Figure 32 Effect of Different Release Methodology (CISM)

Transfer lengths for beams R2-3 and R2-4 are shown in Figure 33. R2-3 and R2-4 beams are identical except for the releasing methodology. R2-3 was released gradually while the strands for beam unit R2-4 were cut suddenly. It can be seen from the figure that the transfer length of beam unit with sudden release (R2-4) is larger than that of beam unit with gradual release (R2-3). It was calculated based on the experiment data that the transfer length of beam units with sudden release is 58% longer compared to that of beam units with gradual release.

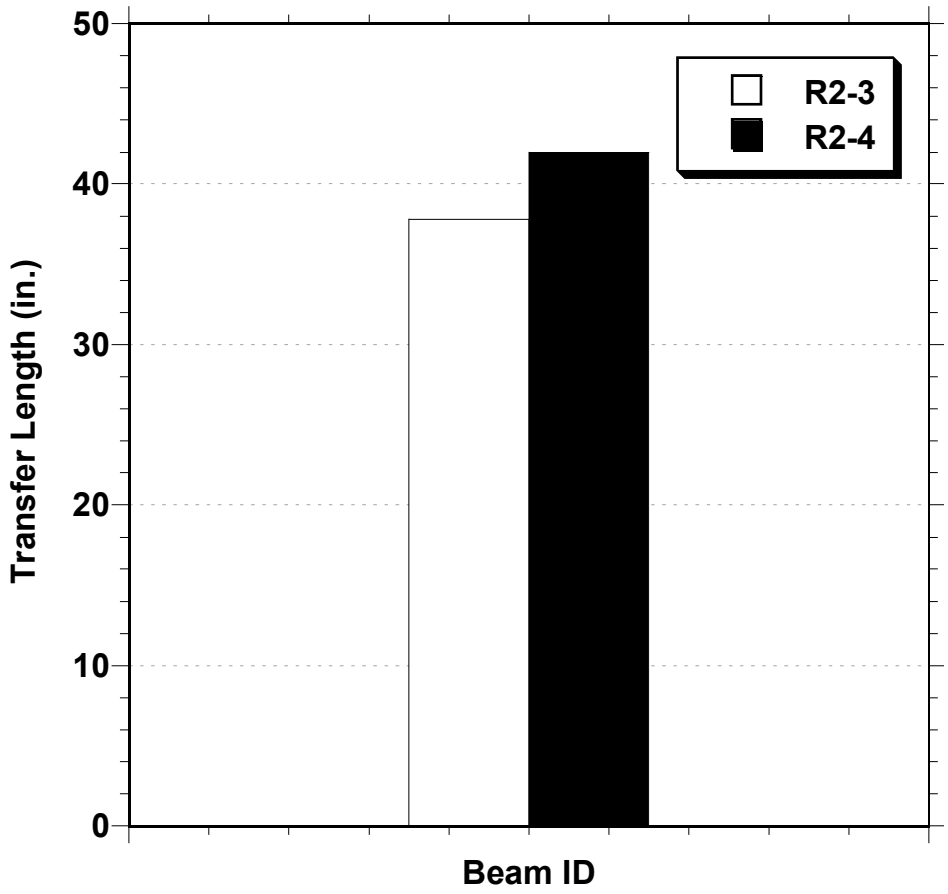

Figure 33 Comparison of Transfer Lengths of R2-3 and R2-4 (CSSM)

4.8.2 Soft vs. Rigid Debonding/Blanketing Material

Transfer length results of beam units with different debonding, or blanketing, material from internal strain measurements are shown in Figure 34. It can be seen that beam units with rigid debonding material generally had longer transfer lengths than those beams with soft debonding material, with the exception of beam unit C1-6. However, as mentioned in the previous section, the transfer length of beam unit C1-6 was much shorter than expected. Considering that the transfer length of beam unit C1-6 was the only one that shows different trend in Figure 34, this data point is considered unreliable and may thus be disregarded from the current and later comparisons. It is again noted that the transfer length for beam C1-5 can be considered uncharacteristically long for a gradually released beam. As previously discussed, the strand in this beam was accidentally released in a sudden manner during the annealing process.

Thus, the transfer length for beam C1-5 may be considered closer for the expected value for a suddenly released strand.

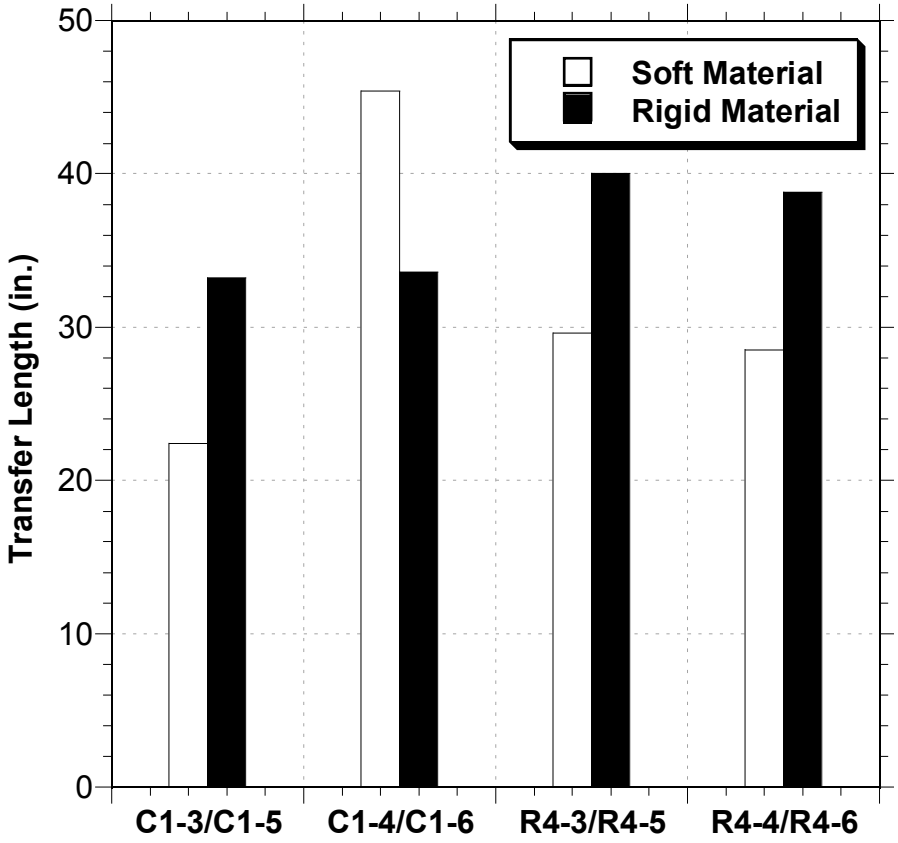

Figure 34 Effect of Debonding/Blanketing Material (CISM)

Figure 35 shows the comparison between beams with multiple strands debonded with soft material (R4-3 and R4-4) and those debonded with rigid material (R4-5 and R4-6). Beams R4-3 and R4-4 were debonded for 3 ft while beams R4-4 and R4-6 were debonded for 5 ft. From the Figure 35, it can be seen that in both cases using rigid debonding material will lead to a longer transfer length. This can be explained by recognizing that some stress has been transferred along the debonded region in the beams with soft debonding material since the bonding mechanism is not completely eliminated. On average, using rigid debonding material will lead to a 49% increasing in transfer length according to the experiment data in this research.

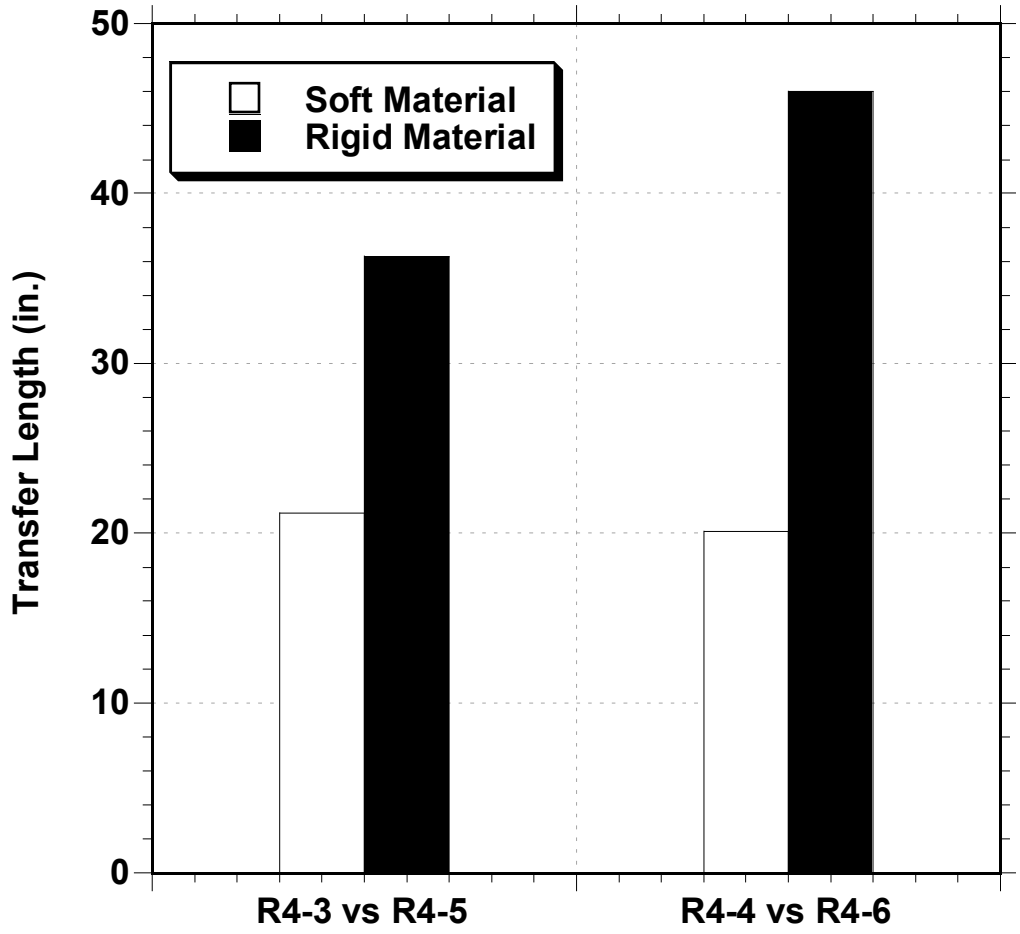

Figure 35 Effect of Debonding Material (CSSM)

4.8.3 Bonded vs. Debonded

Figure 36 shows a comparison of experiment results (CISM) for the C1 beams with different lengths of strand debonding and different debonding material. Information on the parameters for the beam units are given in Table 17. The beam units in the left group (C1-1, C1-3 and C1-5) were gradually released while the other group (C1-2, C1-4 and C1-6) was released suddenly. It can be seen that the transfer lengths for the beam units debonded with soft material are close to that in the fully bonded beams for both groups. However, the beam units with rigid debonding material (C1-5 and C1-6) show a different trend in each group. The transfer length of beam unit C1-5 was longer compared to C1-1 and C1-3 due to the relatively higher strand release rate, as mentioned in previous sections. The expected result was for beam C1-5 to have a transfer length closer to that of beams C1-1 and C1-3 if the strand had been appropriately annealed. The

transfer length of beam unit C1-6 is much shorter than expected without a good justification. The result was thus disregarded from the current comparison.

Table 17 Basic Description of C1 Beam Units

Beam ID	Ld (ft)	Debonding Material
C1-1 & C1-2	0	N/A
C1-3 & C1-4	1.5	Soft
C1-5 & C1-6	1.5	Rigid

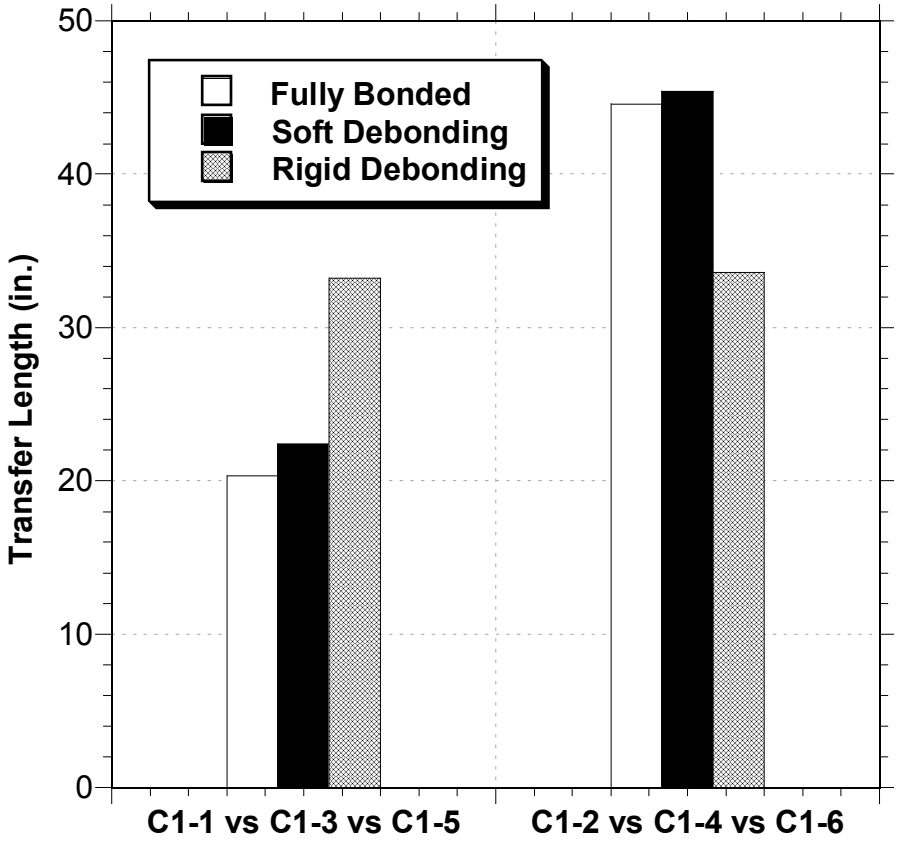

Figure 36 Effect of Debonding Length on C1 Beam Units (CISM)

Figure 37 shows a comparison of experimental results (CISM) of the S1 beams with different debonding lengths. Beams S1-1 and S1-3 were released gradually while S1-2, S1-4 and S1-6 were released suddenly. The debonded length of each beam unit is shown in Table 18 and in all cases the debonded material was soft. A similar trend can be found from the two comparison groups; that is, fully bonded beam units had the longest transfer length. By comparing S1-2, S1-4 and S1-6 it can also be seen that if soft debonding material is used, longer

debonded length may lead to shorter transfer length. This can be explained that some bonding strength still exists in the debonded region and some prestress in strand force has already been transferred to concrete through the residual bonding. As a result there is less force need to be transferred at the point where debonded region ends, which resulted in a shorter transfer length. It can be imagined that longer debonded region will increase such phenomenon.

Table 18 Basic Description of S1 Beam Units

Beam ID	Ld (ft)	Debonding Material
S1-1 & S1-2	0	N/A
S1-3 & S1-4	3	Soft
S1-5 & S1-6	5	Soft

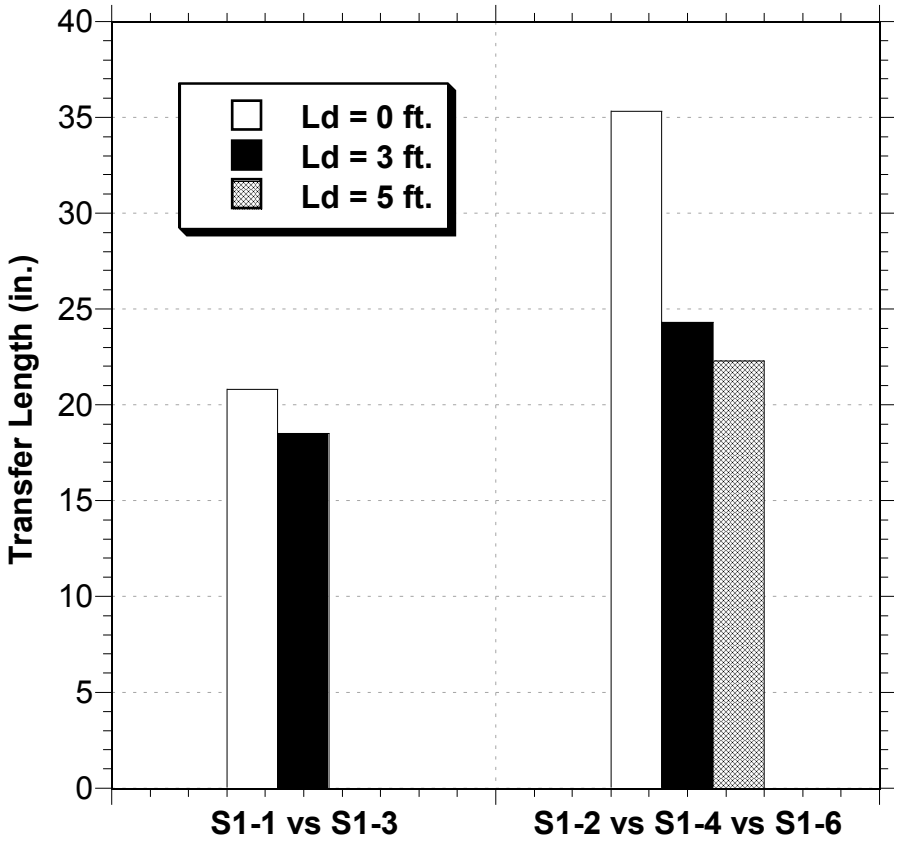

Figure 37 Effect of Debonding Length on S1 Beam Units (CISM)

Results (CISM) for the R4 beams with different debonding lengths are shown in Figure 38 and the basic information of these beam units is shown in Table 19. It can be seen from the

figure that in general, the beams with debonded strand using soft sheathing material (R4-2, R4-3, R4-4) had shorter transfer lengths (except R4-2) compared to the fully bonded beams. However, longer transfer lengths were observed when rigid debonding material was used (R4-5 and R4-6). This may be due to the combination of the two reasons: i) the debonded strand has more stored strain energy; and ii) concrete-strand bonding is mostly eliminated when rigid debonding material is used and thus little (if any) prestress is transferred within the debonded region. Even though more strain energy is also stored in strands in beam units with soft debonding material, part of prestress is transferred within the debonded region through residual bond strength and thus the transfer length after debonded region may still be reduced. It can also be observed from Figure 38 that beams with longer debonded length using soft sheathing had shorter transfer lengths. The effects of free length of uncut strands were not quite clear based on measurements taken and the observations during the test (release).

Table 19 Basic Description of R4 Beam Units

Beam ID	Ld (ft)	Debonding Material
R4-1	0	N/A
R4-2	1.5	Soft
R4-3	3	Soft
R4-4	5	Soft
R4-5	3	Rigid
R4-6	5	Rigid

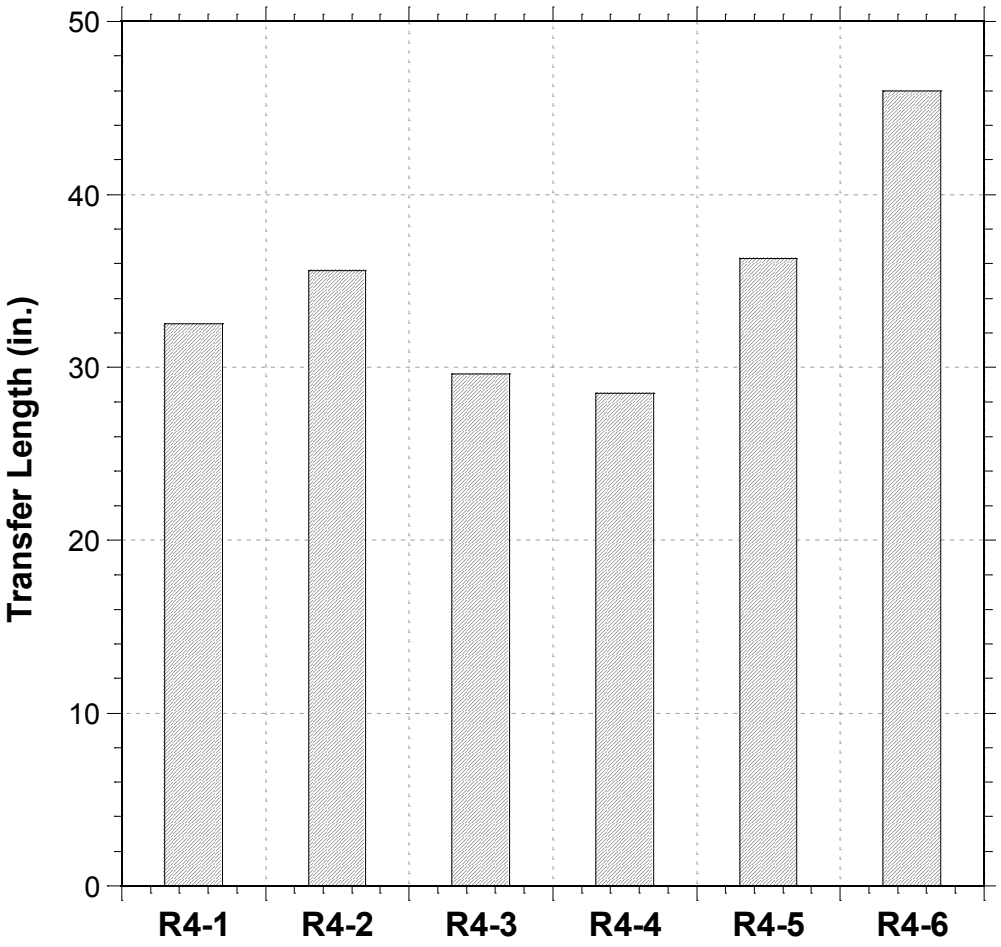

Figure 38 Effect of Debonding Length on R4 Beams (CISM)

Figure 39 shows the comparison of transfer lengths (CSSM) of beam units R2-1, R2-2, R2-5 and R2-6, which were debonded for 0, 1.5, 3 and 5 ft., respectively with soft debonding material. The calculated transfer lengths based on strain measurements show that the soft debonding material did not lead to shorter transfer lengths in all cases for the R2 beam units. It is clear that for the R2-2 beam, which had its strands debonded 18 in. from the ends had a shorter transfer length than the fully bonded beam (R2-1). When the debonded length was increased to 3 ft (R2-5) and 5 ft (R2-6) the transfer lengths were actually longer than for the fully bonded beam. A possible explanation for this may be that for the beams with longer debonded length, the strain energy that is accumulated along the debonded length increases. This energy is then transformed into kinetic energy upon release. It is hypothesized that if the strain energy (or kinetic energy) is large enough to overcome the friction resistance in the debonded region from the flexible sheathing, then the stress transfer into the concrete element from the point of full bond is

increased, thus leading to a longer transfer length. Again, the effect of free length of uncut strand could not be determined based on the obtained data and observations.

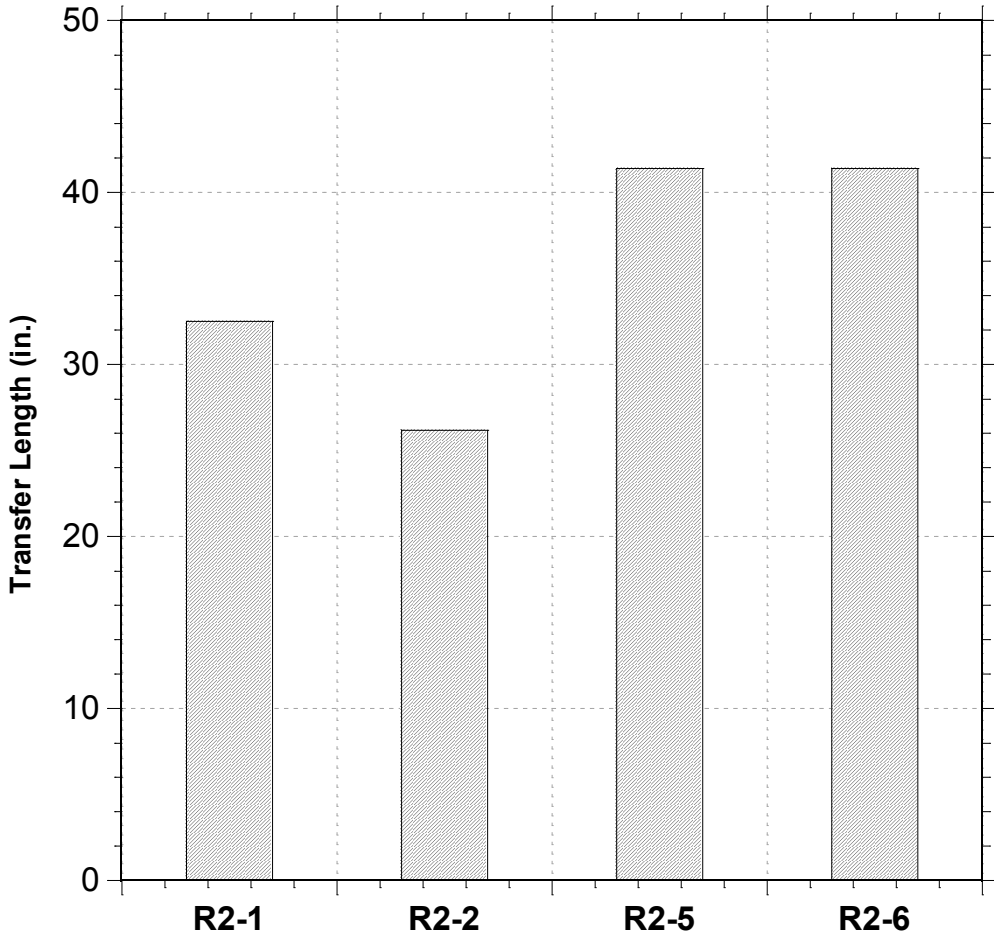

Figure 39 Effect of Debonding Length on R2 Beams (CSSM)

Figure 40 shows a comparison of the CSSM results for the R4 beam units. Similar trends can be observed in this figure compared to the CISM results in Figure 38. It is noted that debonding with soft sheathing material reduces the transfer length of the beam compared to the fully bonded case (beams R4-2, R4-3, and R4-4 vs. beam R4-1). However, it can be seen that the reduction in transfer length from beam R4-3 (3 ft unbonded length) to beam R4-4 (5 ft unbonded length) is not much. This may again be attributed to the counter effect that the larger accumulated strain energy in the debonded strand has on increasing transfer length and on degrading the marginal bond strength within the debonded length. Again, the transfer lengths for the beams with rigid debonding are larger than all cases, but with little difference between 3 ft (R4-5) and 5 ft (R4-6) unbonded length.

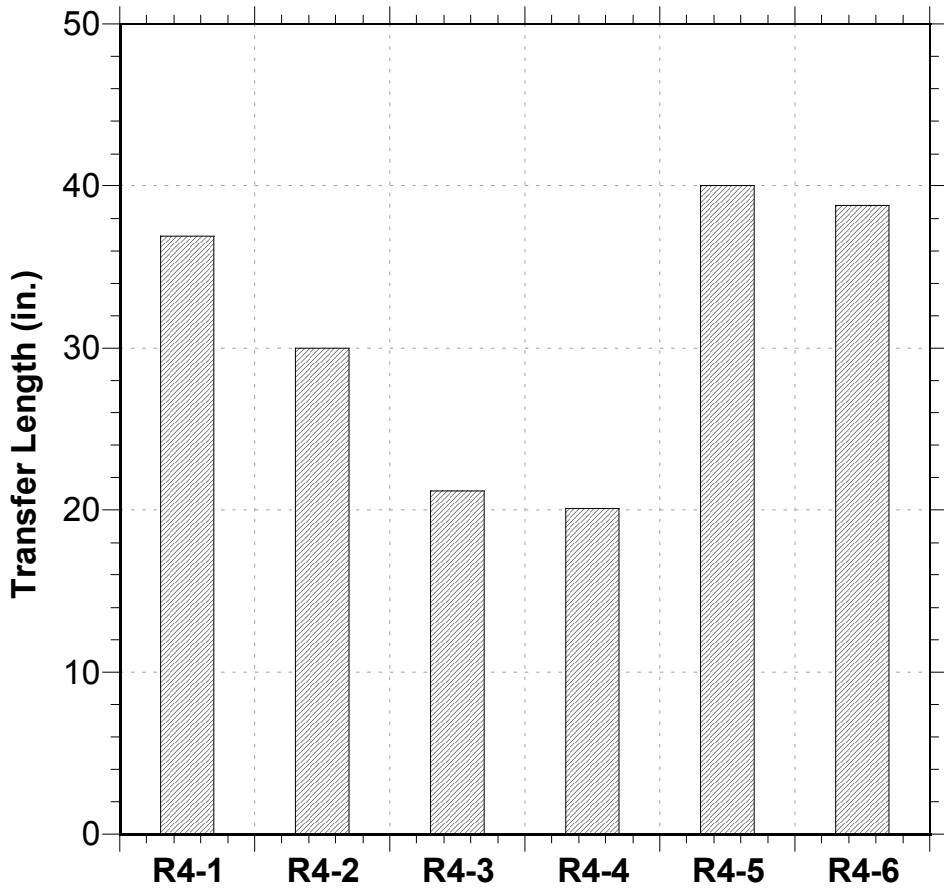

Figure 40 Effect of Debonding Length on R4 Beams (CSSM)

Based on the experiment data in this research, beam units with rigid debonding material have a 16% longer transfer length on average compared to the fully bonded beam units. On the other hand, if the beam units are debonded with soft material, the transfer length will be 10% less than that of fully bonded beam units.

4.8.4 Summary

The following findings are offered based on the experimental data and discussion provided in this chapter:

i) Compared to annealed or gradual release of the prestressing strands, sudden release, or flame cutting, will lead to longer transfer lengths (~58% based on experiment data). This is attributed to the much larger kinetic energy that is transferred from the pre-tensioned strand to the concrete element upon sudden release;

ii) In general, transfer lengths in beam units with rigid debonding material were longer than for beams with soft debonding material (~49% based on experiment data). This is attributed to the fact that the soft material cannot completely eliminate the bonding mechanism between strand and concrete, due to partial mechanical interlock between the deformed tight sheathing in the strand and the concrete, and the increased friction resistance that develops in the strand/concrete interface as a consequence of the dilation of the strand as it loses load due to the minimal bond shear strength.

iii) Debonded beam units with rigid material generally had longer transfer lengths compared to those with fully bonded strands (16% based on experiment data). This is attributed to strain energy stored in the prestressing strand which is transformed into kinetic energy after strand release, and thus larger concrete region is needed to dissipate such energy. When soft debonding material was used, transfer length is not only affected by the additional strain energy stored in the debonded region, but also the force transfer due to residual bonding in the debonded region. The stored strain energy and residual bonding forces have opposite influences on transfer lengths and thus it depends on which phenomenon is greater.

Chapter 5 Simulation of Strand Bond Behavior

5.1 Introduction

As previously presented the bond between strand and concrete can be attributed to adhesion, mechanical interlock and friction, depending upon the stage of bond development and the nature of the strand surface. While considerable research has been done on the bond performance of prestressing strands in the longitudinal direction, not much attention has been paid to the lateral behavior of prestressing strand in concrete members. The damage observed in prestressed beams with debonded strands has brought to question the bond behavior of blanketed strand. Due to the lack or reduced bond strength of a debonded strand, the full three-dimensional (3D) behavior needs to be evaluated. As a result, it is of importance and necessity to evaluate the bonding mechanism simulation with a 3D strand.

The three-dimensional behavior of strand bond in pre-tensioned concrete was simulated by developing full 3D finite element models for the small-scale beam test program presented in Chapter 4 . Both concrete and strand were modeled as deformable solids with the aim at capturing axial and radial interaction and characterizing the interface (e.g., bond) behavior. The strand geometry was modeled as a circular rod and contact interaction definitions were used to simulate bond behavior. A nonlinear material model was implemented on the concrete part of the models to assess damage resulting from the pre-tension release process. The parameters required to define the interaction properties between strand and concrete were calibrated based on the experimental data of the small-scale beam tests. The finite element analyses were established in the general-purpose finite element program ABAQUS. Evaluation of the results provided further insight into the behavior of bond behavior for debonded strands. The bond parameters were normalized for use in the simulation of full-size bridge girders in Chapter 6 .

5.2 Objective and Approach of Finite Element Simulation

The primary objective of finite element (FE) simulation is to establish a valid simulation of the bond mechanism between fully-bonded and debonded (or blanketed) prestressed strand and concrete. FE models of prestressing concrete beams have been established by previous researchers; however, few of them have considered the three-dimensional behavior of the strand.

In reality, a strand will expand in radial direction due to Poisson's ratio once it is released. This expansion is thought to be one of the possible reasons for end cracking in concrete girders.

Evaluating the 3D bond behavior of strand thus requires simulation of the strand as a three-dimensional object in order to captures its radial interaction with the surrounding concrete. The actual shape of the strand is a bundle of seven twisted wires. It is the helical shape of the twisted pitch that provides the mechanical interlock component to bond. Modeling such geometry leads to much complications in the numerical simulation of contact interaction between the strand and concrete surfaces. Further, such complexities were deemed unrealistic for the simulation of real prestressed beams that have a large number of strands. Thus, the strand geometry was simplified to a circular cross-section with equal area as the actual 7-wire strand.

Since the mechanical interlock component to bond resistance cannot be explicitly captured by modeling the strand as a smooth rod, the interaction property defined between the circular strand and the surrounded concrete included the effects of adhesion and mechanical interlock. The Poisson's, or Hoyer, effect was automatically included in the simulation by virtue of modeling the strand as a 3D deformable solid.

The bond simulation was established by calibrating the contact interaction parameters in the 3D FE models with the experimental data on small-scale beams (Chapter 4).

5.3 Material Constitutive Models

5.3.1 Concrete

In order to capture the potential damage to the concrete during release of the pre-tensioned strand, inelastic material behavior was used for the concrete material definition in the FE models. The concrete damage plasticity model [34], available in ABAQUS was adopted for this purpose. An overview on the theory behind this constitutive formulation for 3D nonlinear behavior of concrete is given in Section 5.4. The same elastic modulus calculated in Section 3.3.1 was used for concrete material model and the Poisson's ratio was assumed to be 0.2.

5.3.2 Prestressing Strand and Passive Reinforcement

The prestressing strand and the passive confinement reinforcement (S1) remains within its proportionality limit during the stressing and transfer stages. Thus, the 3D strand elements and

the embedded passive reinforcement elements were assigned a linear elastic material. The modulus of elasticity was 29,000 ksi and the Poisson's ratio was assumed to be 0.3.

5.4 Concrete Damaged Plasticity Model [28]

5.4.1 Introduction

Inelastic material behavior definition was adopted in this research for most of the numerical models to have a more precise simulation and better investigation of the stress state in prestressed concrete members. The concrete damaged plasticity model [34] which is available in ABAQUS [28] was used.

The concrete damaged plasticity model in ABAQUS uses concepts of isotropic damaged elasticity in combination with isotropic tensile and compressive plasticity to represent the inelastic behavior of concrete. It can be used for both plain concrete and reinforced concrete structures. This material model is designed for applications in which concrete is subjected to monotonic, cyclic and/or dynamic loading under low confining pressures.

The concrete damaged plasticity model assumes that the main two failure mechanisms are tensile cracking and compressive crushing of the concrete model. The evolution of the yield surface is controlled by two hardening variables, the tensile equivalent plastic strain ($\bar{\varepsilon}_t^{pl}$) and the compressive equivalent plastic strains ($\bar{\varepsilon}_c^{pl}$).

Under uniaxial tension the stress-strain response follows a linear elastic relationship until the value of the failure stress, σ_{t0}, is reached. The failure stress corresponds to the onset of micro-cracking in the concrete material. Beyond the failure stress the formation of micro-cracks is represented macroscopically with a softening stress-strain response, which induces strain localization in the concrete structure. Under uniaxial compression the response is linear until the value of initial yield, σ_{c0}. In the plastic regime the response is typically characterized by stress hardening followed by strain softening beyond the ultimate stress.

When the concrete specimen is unloaded from any point on the strain softening branch of the stress-strain curves, the unloading response is weakened: the elastic stiffness of the material appears to be damaged (or degraded). The degradation of the elastic stiffness is characterized by two damage variables, d_t and d_c.

It is assumed that the uniaxial stress-strain curves can be converted into stress versus plastic-strain curves. However, stress versus inelastic strain $\bar{\varepsilon}_c^{in}$ curve for compressive behavior and stress versus cracking strain $\bar{\varepsilon}_t^{ck}$ curves for tensile behavior are requested in ABAQUS. The relationships between $\bar{\varepsilon}_c^{pl}$ and $\bar{\varepsilon}_c^{in}$, $\bar{\varepsilon}_t^{pl}$ and $\bar{\varepsilon}_t^{ck}$ are:

$$\bar{\varepsilon}_t^{pl} = \bar{\varepsilon}_t^{ck} - \frac{d_t}{(1-d_t)}\frac{\sigma_t}{E_0} \qquad \textbf{(Equation 5-1)}$$

$$\bar{\varepsilon}_c^{pl} = \bar{\varepsilon}_c^{in} - \frac{d_c}{(1-d_c)}\frac{\sigma_c}{E_0} \qquad \textbf{(Equation 5-2)}$$

It is needed to be noted that, since the primary investigation is about the prestressed concrete members at transfer, concrete only subject to monotonic loading in this research. As a result, it is not necessary to define damage for the concrete material, which is required for cases like cyclic loading. Thus:

$$d_t = d_c = 0 \qquad \textbf{(Equation 5-3)}$$

And then

$$\bar{\varepsilon}_t^{pl} = \bar{\varepsilon}_t^{ck} \qquad \textbf{(Equation 5-4)}$$

$$\bar{\varepsilon}_c^{pl} = \bar{\varepsilon}_c^{in} \qquad \textbf{(Equation 5-5)}$$

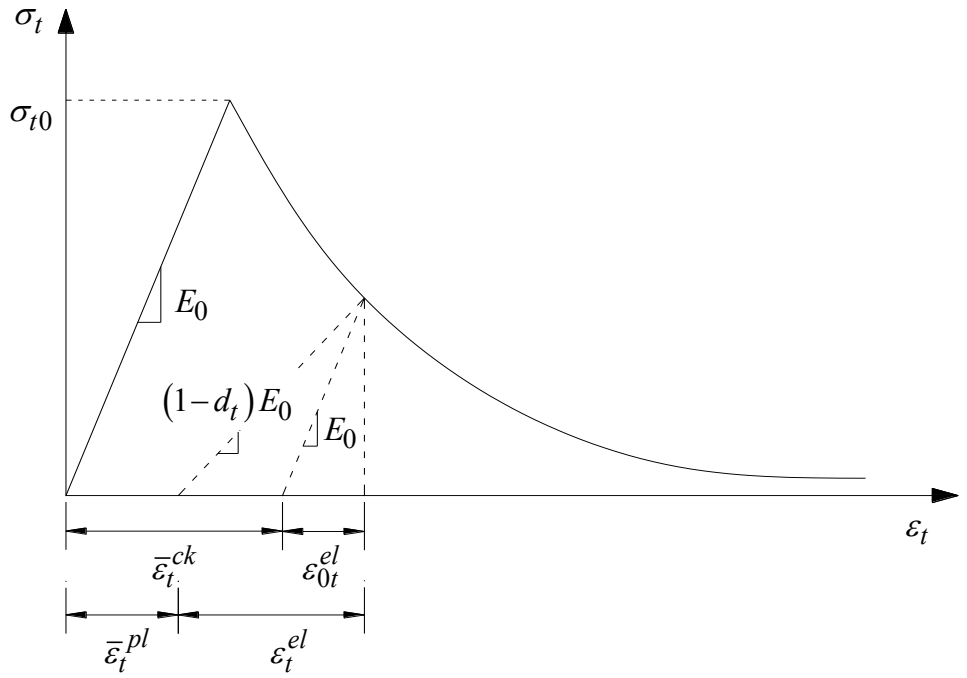

(a) Tensile Behavior of Concrete Damaged Plasticity Model

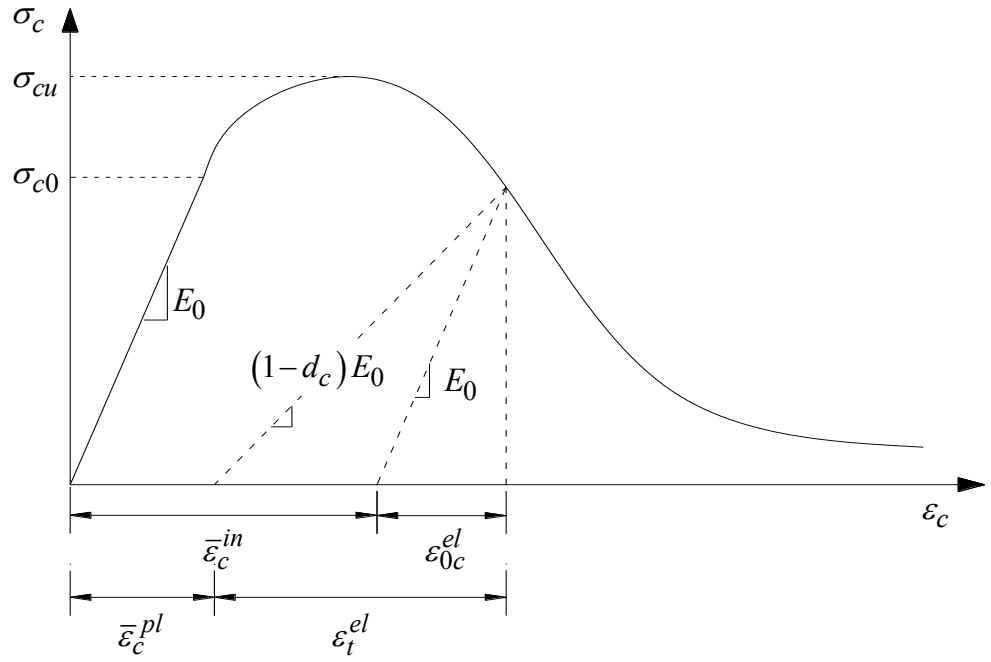

(b) Compressive Behavior of Concrete Damaged Plasticity Model

Figure 41 Tensile and Compressive Behavior of Concrete Damaged Plasticity Model [28]

5.4.2 Definition of Tensile Behavior

In this study, the tension stiffening behavior, which is required in the concrete damaged plasticity model, is specified by means of a post failure stress-strain relation, since data for the behavior of concrete with different strength under compressive and tensile load is available.

In reinforced concrete the definition of post-failure behavior generally requires providing the post-failure stress as a function of cracking strain, $\bar{\varepsilon}_t^{ck}$. The cracking strain is defined as the total strain minus the elastic strain, that is, $\bar{\varepsilon}_t^{ck} = \varepsilon_t - \varepsilon_{0t}^{el}$, where $\varepsilon_{0t}^{el} = \sigma_t / E_0$, as illustrated in Figure 41. To avoid potential numerical problems, ABAQUS enforces a lower limit on the post-failure stress equal to one percent of the initial failure stress: $\sigma_{t \geq} \sigma_{t0} / 100$.

The model by Collins [26] is used to define the tensile behavior of concrete. Five points are used to define each stress versus cracking strain curve, which are shown in Table 20. In Table 20 the first point is defined in ABAQUS by default. The second point is the point at failure tensile stress, which is the onset of strain softening. Behavior in the region between points 1 and 2 is linear-elastic. Points 3, 4 and 5 are determined by calculating the tensile stress when ε_t equals to 0.001, 0.004 and 0.01, respectively. The data used to define the stress-cracking strain curve for each beam is shown in Appendix D.

Table 20 Definition of Tensile Behavior of Concrete Material

Point No.	σ_t **(psi)**	ε_t **(in. /in.)**	$\bar{\varepsilon}_t^{ck}$ **(in. /in.)**
1	0	0	0
2	$f_t = 7.5\sqrt{f'_c}$	0.000132	0
3	$\frac{f_t}{(1+\sqrt{500\varepsilon_t})}$	0.001	0.000846
4	$\frac{f_t}{(1+\sqrt{500\varepsilon_t})}$	0.004	0.003891
5	$\frac{f_t}{(1+\sqrt{500\varepsilon_t})}$	0.010	0.009919

5.4.3 Definition of Compressive Behavior

Compressive stress data is provided as a tabular function of inelastic (or crushing) strain, $\bar{\varepsilon}_c^{in}$. Positive (absolute) values are given for the compressive stress and strain. The stress-strain curve can be defined beyond the ultimate stress, into the strain-softening regime.

Hardening data are given in terms of an inelastic strain, $\bar{\varepsilon}_c^{in}$, instead of plastic strain, $\bar{\varepsilon}_c^{pl}$. The compressive inelastic strain is defined as the total strain minus the elastic strain, $\bar{\varepsilon}_c^{in} = \varepsilon_c - \varepsilon_{0c}^{el}$, where $\varepsilon_{0c}^{el} = \sigma_c / E_0$, as illustrated in Figure 41.

The compressive behavior of concrete material in this research was defined using the model by Collins et al. [26]. The compressive stress versus inelastic strain curves for compressive behavior of concrete for each batch is shown in Appendix D.

5.4.4 Other Parameters

Other parameters needed in the definition of concrete damage plasticity model are [28]:

i) **Dilation Angle:** Concrete dilation angle in the p-q plane.

ii) **Eccentricity:** Flow potential eccentricity which defines the rate at which the hyperbolic flow potential approaches its asymptote.

iii) **fb0/fc0:** The ratio of initial equibiaxial compressive yield stress to initial uniaxial compressive yield stress.

iv) **K:** The ratio of the second stress invariant on the tensile meridian to that on the compressive meridian at initial yield for any given value of the pressure invariant such that the maximum principal stress is negative.

v) **Viscosity Parameter:** A parameter used for the visco-plastic regularization of the concrete constitutive equations in Abaqus/Standard analysis.

Generally the default values of these parameters in ABAQUS were adopted. The concrete dilation angle was determined according to the references [28][35] and a value of 0.005 was used for the viscosity parameter in the concrete material model in this research. The values of all the parameters are shown in Table 21.

Table 21 Parameters of Concrete Damage Plasticity Model

Dilation Angle	Eccentricity	$\sigma_{b0} / \sigma_{c0}$	K	Viscosity Parameter
37	0.1	1.16	0.67	0.005

5.5 Element Types

To better capture the bond interaction between a prestressing strand and the surrounding concrete, especially in the radial direction, solid continuum-type elements were used for both concrete and strand. Eight-node linear solid elements with reduced integration (C3D8R) were used.

The equivalent diameter of the solid strand in FE models were calculated based on the actual cross-section area of 0.6 in. diameter strand (0.2175 in.^{2}). The pre-tensioned state in the strands was modeled by introducing an "initial stress" condition, which means the strand in finite element model is already "tensioned." As a result, the diameter of the modeled strands was further reduced to account for the pre-tensioning force. The prestressing force was based on experiment data and the final diameter for strands used in the models was calculated to be 0.5245 in. for all the strands.

5.6 Simulation of Prestress Transfer

In pre-tensioned concrete elements the strands are prestressed before the concrete beam is cast. As a result, unlike most analysis procedures, in which stresses and strains appear after the analysis begins, there should be stresses already in the model, i.e., in the prestressing strand, before the analysis starts. Some researchers have suggested the use of temperature (specifically a temperature decrease) to simulate the effect of prestress release when the strands are modeled with one dimensional truss elements. A temperature decrease leads to the shortening in these one dimensional strands in the longitudinal direction, while at the same time there is no lateral effect. The concrete, in which the strands are placed, would thus become compressed and then the prestressing transfer is successfully simulated.

When considering the strand as a 3D deformable solid the strand should not only shorten upon the release from its pre-tensioned state but it should also expand radially. This may be simulated through an applied temperature field to a 3D solid with orthotropic thermal properties. However, the definition of additional material parameters makes the use of temperature to simulate prestress transfer cumbersome.

The definition of an "Initial Stress" was used instead to simulate the process of force transfer from a tensioned strand onto the concrete beam. Using this feature from the program ABAQUS initial stresses can be defined to certain parts of a model before the analysis starts. The

initial stress state, based on the strand jacking force minus seating losses, can then be applied to the strand in the longitudinal direction using this approach. When the analysis starts, the part with initial stress will starts to deform so the pre-defined stress can be transferred, if there are no boundary conditions to "hold" this behavior. For the beam models with a single strand (C1 and R1 beams), there is no need to hold the stress transfer. On the other hand, for those models with multiple strands (R2 and R4 beams), in which the strands may be supposed to be released in specified sequence, boundary conditions are used to restrain the strands from releasing until it is prescribed in the analysis, thus simulating a strand release sequence.

In the simulation process, prestress losses due to elastic shortening are taken into account automatically by the model. However, the concrete strains due to creep and shrinkage were directly applied to concrete part of the model, which essentially allowed the model to incorporate the associated prestress losses. The magnitude of "initial stress" applied to the strands was thus the stress level in the strand after losses from anchorage seating (f_{pas}). The determination of prestress after anchorage seating loss was discussed in Section 4.6.1.

5.7 Definition of Bond Behavior

5.7.1 Introduction

One of the primary goals of this research is to capture the bond behavior between concrete and strand, which is the mechanism that permits the force transfer from the strand to the concrete upon release of the pre-tensioned strand. In the finite element models, this was realized by defining an interaction constraint between the neighboring concrete and strand elements. Researchers have followed different approaches to simulate strand bond behavior, including perfect bond, non-linear spring elements, and surface friction interaction. The latter allows a more realistic representation of the bond phenomena and was the one used in this work.

After the pre-tensioned strand is released, the strand will shorten and as it deforms to recover its original (shorter) length the strand can be said to 'move' into the concrete element. At the end region on a prestressed beam, where the shear stress between strand and concrete is relatively high, the bond between concrete and strand may exceed the capacity and slip will occur. This bond-slip phenomenon cannot be simulated if perfect bond is defined between concrete and strand. A perfect (limitless) bond definition would lead to unrealistic high stresses in the end region of the concrete, beam which will disturb the investigation on beam end

cracking in this research. Other researchers have used non-linear spring elements to simulate "breakable" bond between concrete and strand. However, the strand model in these kind of efforts is typically simplified using truss or beam elements, in which case there is limited number of nodes in the strand model and defining one-to-one node pairs is possible. However, in this study, as the result of using solid elements for both concrete and strands, the large amount of nodes generated along the two three-dimensional surfaces makes it unpractical to define spring elements with node-to-node bond characteristics.

Based on the discussion above, the interaction between concrete and strand in this research was simulated by defining a surface-to-surface contact constraint in ABAQUS [28]. In the contact interaction the outer surface of the strand that has direct contact with the concrete is defined to be a "master" surface while the concrete surface surrounding the strand is defined as a "slave" (or constrained) surface. "Hard" contact was defined between the two surfaces in their normal direction, which means that the strand and concrete surfaces cannot penetrate into each other. In other words, normal pressure can be generated between the strand and concrete surfaces. The interaction in the lateral direction, which controls the bond-slip behavior, was defined using a non-linear friction model. Details on this friction model follow.

5.7.2 Basic Coulomb friction model

The basic concept of the Coulomb friction model is to relate the maximum allowable frictional (shear) stress across an interface to the contact pressure between the contacting bodies. In the basic form of the Coulomb friction model, two contacting surfaces can carry shear stresses up to a certain magnitude across their interface before they start sliding relative to one another; this state is known as sticking. The Coulomb friction model defines this critical shear stress, τ_{crit}, at which sliding of the surfaces starts as a fraction of the contact pressure p, between the surfaces ($\tau_{crit} = \mu p$). The stick/slip calculations determine when a point transitions from sticking to slipping or from slipping to sticking. The fraction, μ, is known as the coefficient of friction.

It this research work it was assumed that μ was the same in all directions (isotropic friction). For a three-dimensional simulation there are two orthogonal components of shear stress (τ_1 and τ_2) along the interface between the two bodies. In ABAQUS, these two shear stress components are combined into an "equivalent shear stress", $\overline{\tau}$, for the stick/slip calculations,

where $\bar{\tau} = \sqrt{\tau_1^2 + \tau_2^2}$. The stick/slip calculations define a surface in the contact pressure-shear stress space along which a point transitions from sticking to slipping. A two-dimensional representation is shown in Figure 42. As a result, the two primary parameters required to define friction between the strand and concrete surfaces are the friction coefficient and the pressure between the two contacting surfaces.

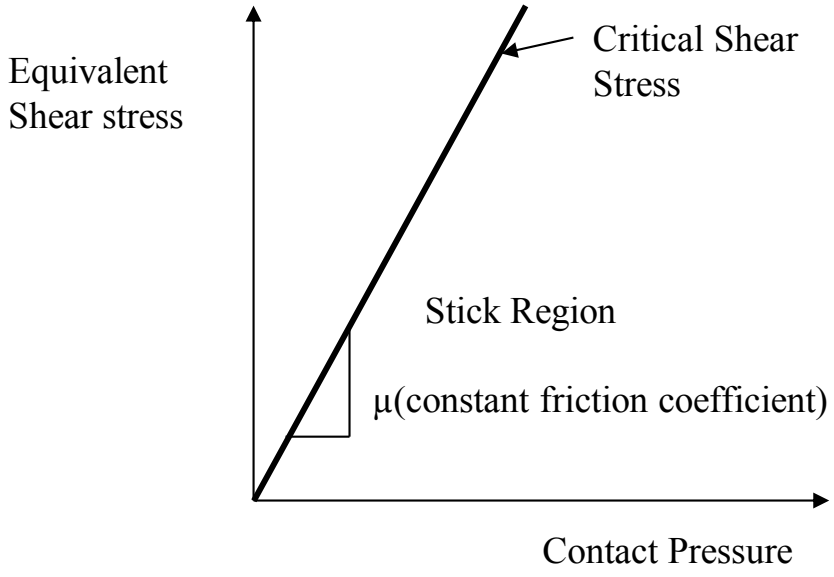

Figure 42 Basic Coulomb Friction Model

As mentioned in previous section, when prestressing strand is released, it will shorten in the longitudinal direction; while at the same time dilate in the lateral direction due to Poisson's ratio. As one can imagine, the strand dilation is constrained by the hardened concrete. Thus, the strand will "push" the surrounding concrete. In this study, the pressure generated between the strand surface and the surrounding concrete was used as the pressure that is necessary for the friction model. The model is therefore allowed to develop the interaction surface pressure "on its own" as the pre-tensioned strand release is simulated through the 'initial stress' option. As a result, the friction coefficient controls the friction force per unit area for a given surface interaction pressure. In other words, the friction coefficient μ controls the bond-slip response and bond-strength between the strand and concrete. The value for the friction coefficient was

determined by calibrating the 3D FE models with experimental data from the small-scale prestressing concrete beam units presented in Chapter 4 .

It is needed to be noted that the numerical analysis in this research is static, thus the effect of releasing rate cannot be taken into account. As a result, it was decided to obtain two average friction coefficients based on the calibration of models of beam units for sudden and annealed release, respectively. And the friction coefficient for sudden release will be used in the box girder model which will be discussed in Chapter 6 .

5.7.3 Simulation of Debonded/Blanketed Strand

The bond strength between strand and concrete is expected to be zero when rigid material is used since the rigid material for strand blanketing is oversized and thus eliminates all contact between strand and concrete. On the other hand as shown by the results of cylinder pull-out tests (Section 3.4), the pull-out force for strand debonded with soft material is not zero, which means that the soft debonding material is not able to eliminate the bonding strength completely. However, the maximum pull-out force was considerably small compared to that of fully bonded strands. In addition, the experimental results on inner concrete strains for the small-scale beams indicated that the longitudinal strain level in the debonding region of beam units with soft debonding material was very small compared to the maximum concrete strain. Thus the bond strength between strand surface and surrounding concrete in the debonding region for all the beam units with soft debonded material was defined to be zero. “Hard” contact was used in the normal direction for the cases in which soft debonding material was used so that normal pressure could be generated at the interface of the strand and concrete surfaces.

The responses to lateral pressure are expected to be different when different debonding materials are used. Rigid debonding material is expected to have less deformation under lateral pressure compared to soft material. As a result, one can expect that in the debonding region of prestressed concrete members, the soft debonding material will be tightly compressed to the strand due to the self-weight of concrete, while in the case of rigid debonding material some room is expected between strand surface and the inner surface of debonding material. As a result, the strand is thought to be able to expand more freely in the debonding region with rigid debonding material and then result in a lower radial pressure on the concrete.

In the FE models the difference in strand debonding approach was considered by simulating that an over-sized hole was cut around the strand in the debonded region for strands blanketed with rigid debonding material such that the strand will not touch the concrete even after its expansion after release. The diameter of the hole around strand debonded with rigid debonding material was defined to be 0.6 inches. (the diameter of the simplified strand in the numerical simulation was 0.5245 inches.) For strands blanketed with soft debonding material, the size of the hole around the strand was the same as the size of the strand to represent a tight contact, i.e., both the strand rod and the concrete hole had a diameter of 0.5245 inches.

5.8 Model Geometry and Mesh

An equivalent diameter was used as the diameter of the strands in the numerical models, as discussed in Section 5.5. The initial stress in strands was calculated based on the actual prestressing force.

Numerical models were established in ABAQUS for all 24 small beam units in the experimental program (Chapter 4). The beam cross-sections are shown in Figure 43 and the test matrix defining the test parameters for the 24 different cases is given in Table 7. Images of the different beam models are shown in Figure 44.

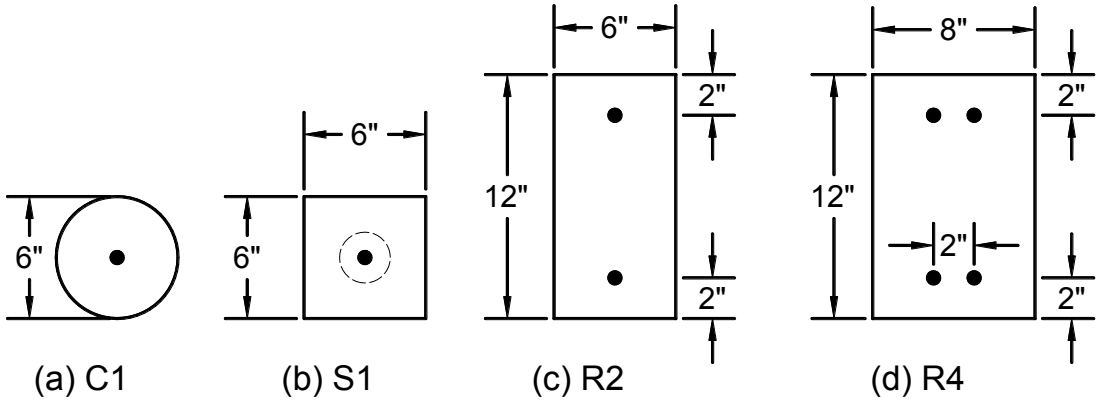

Figure 43 Cross-sections of Small-scale Pre-tensioned Beam Units

In all cases, only half the beam length was modeled because the beams are symmetric about the mid-section. Boundary conditions in the longitudinal direction were applied to the nodes on the mid-section of FE models. The centroid of the mid-section was fixed to eliminate the rigid body translation of the beam models.

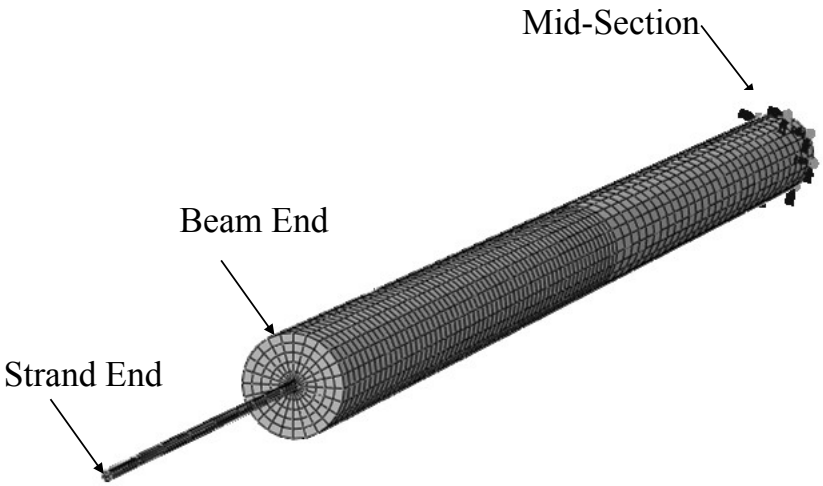

(a) Model of C-1 Beam Unit

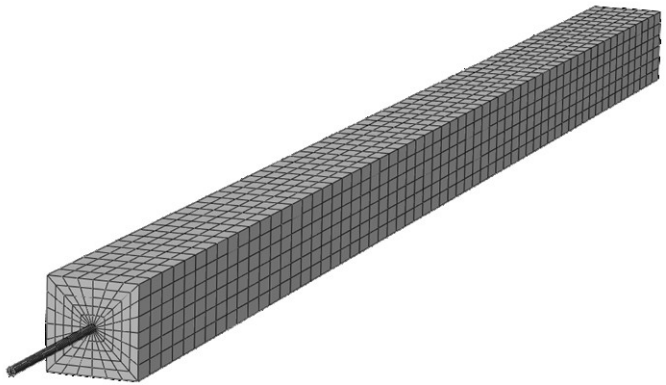

(b) Model of C-1 Beam Unit

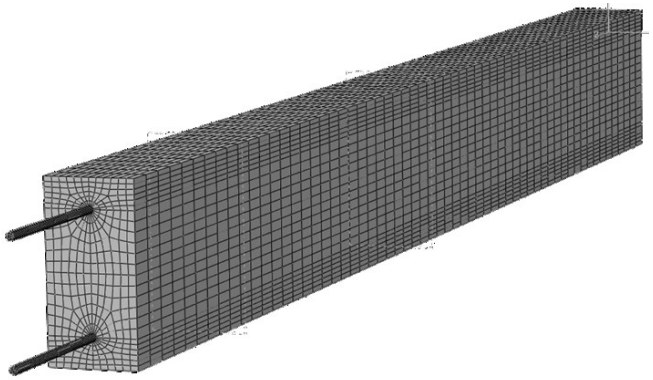

(c) Model of R-2 Beam Unit

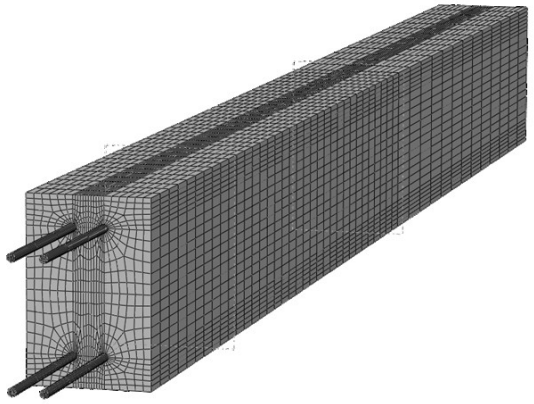

(d) Model of R-4 Beam Unit

Figure 44 Numerical Models for Small Beam Units

Confinement in the S1-1 and S1-5 beams was modeled with truss element "embedded" into the concrete part using the ABAQUS "embedded region" feature. The confinement spiral reinforcement was modeled using discrete rings with a diameter of 2.5 in. and the section definition of a #3 rebar. Five rings with a spacing of 2.3 in. were used to model the 9 in. long spiral confinement in the experiment.

Three-dimensional solid elements were used in this research for both concrete and strand and a friction model was used to define the interaction properties between the two parts. Due to the round shape of the strand cross-section and the need to have a smooth contact surface pairs, it was necessary to have a relatively fine mesh at the interaction between the concrete and strand model parts. The perimeter along the strand cross-section (Figure 45) was defined such that it would have 24 element sides along that edge. The same amount of element sides was used for the mesh level of the inner surface of the concrete surrounding the strand.

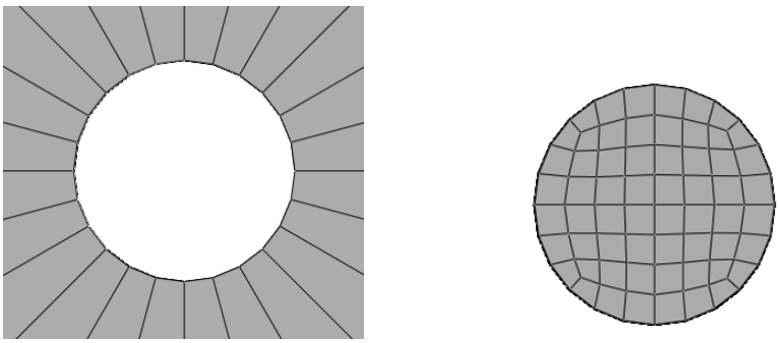

Figure 45 Details of Mesh in FE Models

5.9 Simulation of Creep Strain

As discussed in Chapter 5, concrete strain in the small beam units due to creep and shrinkage were considerably high and it was necessary to take them into account to compare 'hand calculations' with experimental data. It is equally necessary to account for creep and shrinkage strain in the simulation studies in order to calibrate the finite element models.

The additional concrete strain due to creep and shrinkage was added to the numerical model by introducing a temperature field on the concrete part. The magnitude of the temperature field was determined by the simple thermal expansion equation:

$$\varepsilon = \alpha \cdot \Delta T \qquad \textbf{(Equation 5-6)}$$

where ε is the strain due to temperature, α is the coefficient of expansion and T is the change in temperature. To adjust only one parameter, the thermal coefficient of expansion was set to one. As a result, the additional strain from creep and shrinkage that needed to be added to the model is equal to the temperature field:

$$\varepsilon = \Delta T \qquad \textbf{(Equation 5-7)}$$

The estimation of concrete strain due to creep and shrinkage conducted in Section 4.7 was approximate due to the lack of precise values for related parameters. The additional creep and shrinkage strains have the effect of shifting the effective strain in the beam but do not change the transfer length, i.e., the bond transfer behavior is not affected. Thus, since the goal is to calibrate the coefficient of friction that simulates stress bond transfer and not to numerically capture volume changes, it was decided that it was unnecessary to add the estimated concrete creep and shrinkage strains. Rather, the additional concrete volume strains for each beam unit were determined by calculating the concrete strain difference between the experimental result and the simple hand calculations without considering creep and shrinkage in the region where prestress is fully transferred, i.e., in the strain plateau region.

It was mentioned in Chapter 2 that the prestress is not fully transferred to the entire cross section within the transfer length region. Further, little stress is transferred within the debonded region of a strand since the bonding mechanism was eliminated. As a result, the longitudinal compressive stress in the small beam units after strand releasing is close to zero in the debonded region and increases along the transfer length until reaching a maximum. This maximum longitudinal stress stays constant in the region beyond the transfer length.

It is known that creep in concrete is related to the compression stress level, and thus creep will not happen if in the concrete region has no stress. As a result, in the small beam units it is expected that the distribution of longitudinal concrete strain due to creep is similar to the distribution of longitudinal compressive stress. Therefore, the temperature field applied to introduce additional strain cannot be uniform but must vary in different regions.

As shown in the estimates in Chapter 5, concrete creep strains are much higher than shrinkage strains. Due to the difficulty of determining the exact values for creep and shrinkage strains separately for each beam unit, it was assumed that all the additional concrete strain applied to the finite element models is stress related. The temperature field was then applied to the finite element beam models in the following way:

i) The magnitude of the total additional strain required to introduce volume changes was determined by comparing the strain level in the region beyond transfer length from the concrete internal strain measurements and the results from the finite element model;

ii) No temperature field was applied within debonded strand regions. In other words, the additional strain in debonded regions was zero;

iii) A temperature field with a magnitude equal to the total additional volume strain was applied to concrete region beyond the transfer length;

iv) The bond transfer region, which is that from the end of debonded region to the end of transfer length, was partitioned into nine equal length segments and the magnitude of the temperature field applied to each segment was determined by linear interpolation using the following equation:

$$T_i = \varepsilon_{ai} = i \times \frac{\varepsilon_a}{10} \qquad \textbf{(Equation 5-8)}$$

where, ε_a is the total additional strain, ε_{ai} is the additional strain for segment "i", T_i is the magnitude of the temperature field applied to segment "i" to represent the additional strain. The first segment for a fully bonded beams or the first segment after the debonded region for a debonded beam is considered to be the first segment (i=1) and the segment at the end of bond transfer region is considered to be the last segment (i=9).

It should be noted that, the additional concrete strain applied to the model corresponds to the prestress losses due to concrete shrinkage and creep, and are thus automatically taken into account by the model in reducing the effective prestressing stress. Hence, as discussed in section 5.6, the magnitude of initial stress for the numerical models should be the prestress after anchorage set losses (f_{pas}).

The value of additional strain for each beam unit is shown in Table 22; where, ε_{ci} = maximum concrete instantaneous strain due to prestress transfer; ε_{CISM} = average maximum concrete strain measured by CISM; and $\varepsilon_a = \varepsilon_{CISM} - \varepsilon_{ci}$ = additional concrete strain applied to the model.

Experimental data from the CISM is not available for beam units S1-5, R2-1, R2-2, R2-5 and R2-6. Thus, the additional concrete strain applied on the models of these beams was determined by the sum of the concrete strain due to shrinkage and creep as discussed in Section 4.7.9.

Table 22 Additional Strain on Small Beam Units' Models

Beam ID	ε_{ci}	ε_{CISM}	ε_a
	in./in.	**in./in.**	**in./in.**
C1-1	-3.25E-04	-4.62E-04	-1.37E-04
C1-2	-3.32E-04	-5.83E-04	-2.51E-04
C1-3	-3.27E-04	-4.02E-04	-7.49E-05
C1-4	-3.30E-04	-5.32E-04	-2.02E-04
C1-5	-3.25E-04	-4.75E-04	-1.50E-04
C1-6	-3.32E-04	-6.76E-04	-3.44E-04
S1-1	-2.60E-04	-3.39E-04	-7.87E-05
S1-2	-2.66E-04	-3.89E-04	-1.23E-04
S1-3	-2.62E-04	-4.82E-04	-2.20E-04
S1-4	-2.65E-04	-3.10E-04	-4.52E-05
S1-5	-2.61E-04	N/A	-1.79E-04*
S1-6	-2.66E-04	-3.47E-04	-8.06E-05
R2-1	-2.37E-04	N/A	-1.16E-04*
R2-2	-2.37E-04	N/A	-1.16E-04*
R2-3	-2.38E-04	-3.52E-04	-1.13E-04
R2-4	-2.39E-04	-3.72E-04	-1.33E-04
R2-5	-2.36E-04	N/A	-1.16E-04*
R2-6	-2.36E-04	N/A	-1.16E-04*
R4-1	-3.43E-04	-4.87E-04	-1.44E-04
R4-2	-3.43E-04	-4.78E-04	-1.35E-04
R4-3	-3.78E-04	-5.65E-04	-1.87E-04
R4-4	-3.78E-04	-5.64E-04	-1.86E-04
R4-5	-3.53E-04	-5.74E-04	-2.21E-04
R4-6	-3.53E-04	-5.88E-04	-2.36E-04

* $\varepsilon_a = \varepsilon_{cs} + \varepsilon_{cc}$

5.10 Calibration of Finite Element Models

5.10.1 General

As discussed in Section 4.7, the bond mechanism between strand and concrete was simulated using a friction model in which the normal pressure between strand surface and surrounding concrete is generated by the expansion of the strand after release due to its Poisson's

ratio. As a result, the main parameter that needs to be calibrated is the friction coefficient used along the strand bonded region.

The magnitude of friction coefficient essentially controls the bond strength between strand and concrete, and which in turns dictates the transfer length of prestress in the concrete member. Calibration of friction coefficient was conducted by comparing the transfer length obtained from the finite element model with the one obtained experimentally (see Section 4.7.4). The transfer lengths of the numerical beam units' models were determined using the same method (95% AMS) as that for the experiment data. Since some difference was observed from the results of the two bond transfer evaluation methods used in this project (concrete surface strand measurement and concrete internal strain measurement), it was decided to calibrate the numerical models only with the experiment results of one method. Since results of concrete surface strain measurement are not available for the C1 and S1 beams, the results from concrete internal strain measurement (CISM) were used to calibrate the finite element beam models. Figure 46 shows the comparison of concrete strain curves from experiment and numerical model for beam unit R4-4 after calibration.

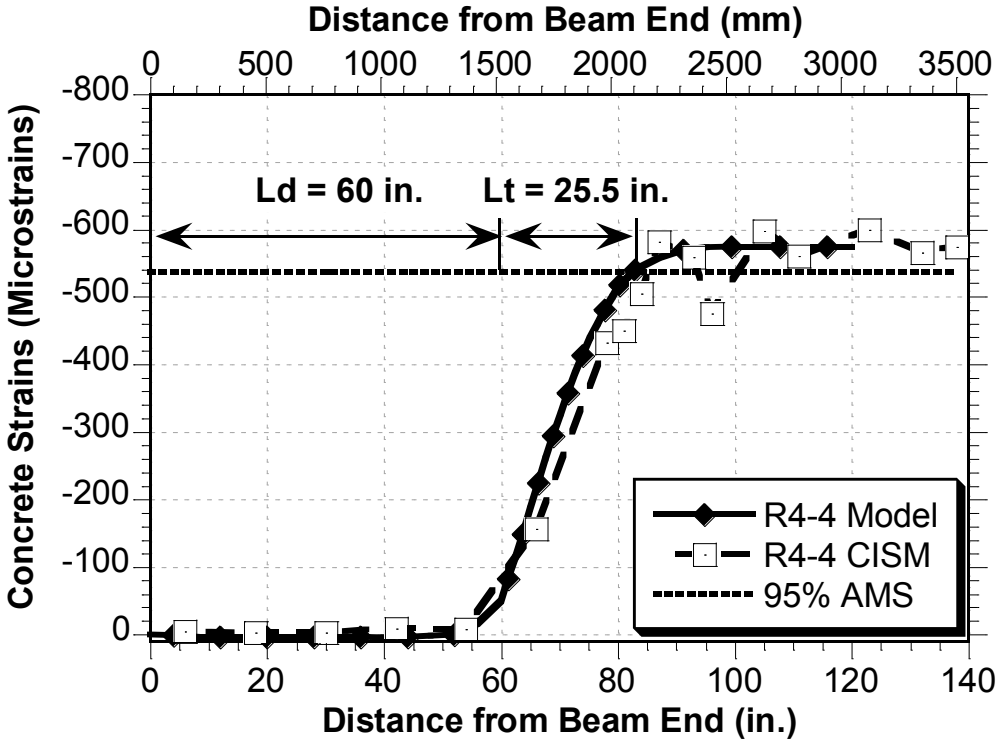

Figure 46 Calibration of FE Model of R4-4 Beam Units

5.10.2 Effect of Strain Gage Rebar

As discussed in Section 4.7.3, the concrete internal strain measurements were achieved by embedding a threaded rebar instrumented with electrical resistance strain gages. The additional rebar may act as reinforcement and lead to additional stiffness to the beam unit. A comparison was thus conducted using numerical models to estimate such effect.

The model of beam unit C1-1 was used to carry out this comparison. Another model was established by placing a 0.25 in.-diameter bar in the C1-1 model. The threaded bar was simulated with truss elements and embedded into the concrete region at the same location as in the experiment (about 1 in. above the strand surface). The bar was assigned elastic material properties for steel as for the confinement reinforcement used in other models.

The two models were thus identical except for the embedded bar. The initial stress was assumed to be 202.5 ksi and no additional strain was applied to the model. Since transfer length is the primary parameter used for the calibration purpose in this research, the results of concrete longitudinal strain at the location of strain gage rebar from these two models was compared. The results are shown in Figure 47. It can be seen from the figure that the longitudinal strain of concrete profile for both models is almost identical. Thus, it was concluded that the effect of the strain gage rebar on the overall behavior of beam unit was negligible and the rebar was not modeled in the set of simulations on the small-scale beams.

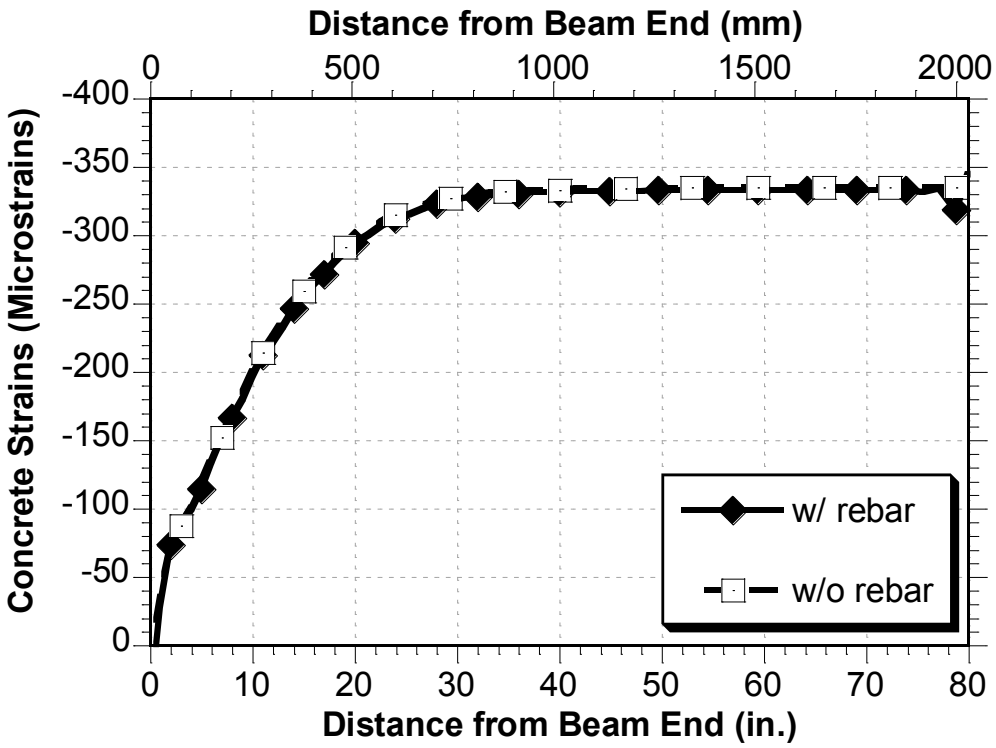

Figure 47 Comparison of C1-1 Beam Unit Models w/ and w/o Rebar

5.10.3 Calibrated Friction Coefficients

The friction coefficient, μ, was calibrated for each beam unit based on the experiment result of each beam unit. The calibrated friction coefficients for each beam are shown in Table 23. The table also provides the transfer length obtained from experimental data ($L_{t,\,CISM}$) and that obtained from the finite element model (L_{FEM}). The calibrated coefficient of friction corresponds to the value that was found to provide the closest match between the experimental and numerical values of transfer length. The calibration process was done by trial and error.

Table 23 Calibrated Friction Coefficients of Beam Models

Model ID	$L_{t,CISM}$	L_{FEM}	μ	Model ID	$L_{t,CISM}$	L_{FEM}	μ
	in.	**in.**			**in.**	**in.**	
C1-1	18.0	17.0	0.60	**R2-1***	N/A	33.0	0.38
C1-2	40.5	39.0	0.23	**R2-2***	N/A	33.0	0.38
C1-3	20.0	22.0	0.50	**R2-3**	26.0	27.0	0.60
C1-4	41.0	40.5	0.23	**R2-4**	32.0	32.0	0.35
C1-5	29.5	29.0	0.35	**R2-5***	N/A	33.0	0.38
C1-6	30.5	29.0	0.50	**R2-6***	N/A	33.0	0.38
S1-1	18.5	18.5	0.55	**R4-1**	22.5	26.0	0.50

S1-2	32.0	33.0	0.30	**R4-2**	28.5	27.5	0.51
S1-3	16.5	17.5	0.50	**R4-3**	26.5	25.0	0.70
S1-4	22.0	23.5	0.45	**R4-4**	25.5	25.0	0.70
S1-5*	N/A	24.0	0.44	**R4-5**	33.0	31.5	0.45
S1-6	20.3	21.0	0.50	**R4-6**	32.0	32.0	0.40

* Experiment data not available, overall friction coefficient is used.

5.10.4 Normalization of Calibrated Coefficient of Friction for Bond Simulation

In order to obtain an overall friction coefficient that can be adopted for 3D FEA on the effect of debonded strands on the anchorage zones of full-size bridge girders, statistical analyses were conducted on the calibrated friction coefficients of the small-scale beam units. Of particular interest is the case study of a 48 in. wide skewed box girder that experience end cracking during production that is hypothesized to be caused by the detailing of debonded strands. Friction coefficients of small beam units were thus first normalized to the concrete compressive strength at transfer of the box girder of interest (4,600 psi) and it was assumed that the friction coefficient is proportional to the square root of f'_c. The initial stress in the prestressing strand was also considered to have influence on the calibration of the friction coefficients since a larger prestressing force will lead to a longer transfer length. However, the standard deviation of the initial prestress is considerably small compared to the mean value of prestressing stress (less that 2%). Further, it is difficult to assume a precise value for the prestressing force during the real manufacturing process. With these facts considered, it was decided to ignore the influence of prestressing stress on the calibration of friction coefficients.

It should be noted that the finite element models developed in this research project are not capable of capturing time-dependent effects. In addition, the influence of release methodology (sudden or annealed) cannot be captured either. However, as shown in the experiment results (see Section 4.8.1), the release method influences bond transfer behavior and it is thus necessary to distinguish beam units with different release method. Consequently, the beam test units were grouped according to the releasing method (sudden or annealed) and an independent friction coefficient was obtained for each group.

Table 24 shows the calibrated friction coefficients from the FE models for beams prestressed by the annealed release method; while Table 25 shows the calibrated friction coefficients for the beams prestressed by the sudden release method. Since the concrete internal measurements for beam S1-5, R2-1, R2-2, R2-5 and R2-6 are not available, the respective

average value of the friction coefficient with annealed or sudden releasing method was used in these beam models. In these beam models μ is the calibrated friction coefficient, $\phi_{f'_c}$ is a factor that accounts for the difference of concrete compressive strength, and μ' is the factored friction coefficient. $\phi_{f'_c}$ and μ' are calculated using the following equations:

$$\mu' = \phi_{f'_c} \mu \qquad \textbf{(Equation 5-9)}$$

$$\phi_{f'_c} = \sqrt{4600} / \sqrt{f'_c} \qquad \textbf{(Equation 5-10)}$$

Table 24 Factored Friction Coefficients for Annealed Released Beams

Model ID	f'_c	μ	$\phi_{f'c}$	μ'
C1-1	6050	0.6	0.87	0.52
C1-3	6050	0.5	0.87	0.44
C1-5	6050	0.35	0.87	0.31
S1-1	6050	0.55	0.87	0.48
S1-3	6050	0.5	0.87	0.44
S1-5	6050	N/A	0.87	N/A
R2-3	7153	0.6	0.80	0.48

Table 25 Factored Friction Coefficients for Sudden Released Beams

Model ID	f'_c	μ	$\phi_{f'c}$	μ'
C1-2	5860	0.23	0.89	0.20
C1-4	5860	0.23	0.89	0.20
C1-6	5860	0.5	0.89	0.44
S1-2	5860	0.3	0.89	0.27
S1-4	5860	0.45	0.89	0.40
S1-6	5860	0.5	0.89	0.44
R2-1	7372	N/A	0.79	N/A
R2-2	7372	N/A	0.79	N/A
R2-4	7153	0.35	0.80	0.28
R2-5	7372	N/A	0.79	N/A
R2-6	7372	N/A	0.79	N/A
R4-1	7371	0.5	0.79	0.39
R4-2	7371	0.51	0.79	0.40
R4-3	5707	0.7	0.90	0.63
R4-4	5707	0.7	0.90	0.63
R4-5	6857	0.45	0.82	0.37
R4-6	6857	0.4	0.82	0.33

Table 26 shows the average value and standard deviation of the calibrated friction coefficients from the numerical models with different release methods. It can be seen that the friction coefficient for sudden release is smaller than that for annealed release. This is consistent with the phenomenon observed from the experimental results which showed that sudden release lead to a longer transfer length.

Table 26 Average Friction Coefficients for Sudden and Annealed Release

	Mean	Standard Deviation
μ **Annealed**	0.44	0.075
μ **Sudden**	0.38	0.135

5.11 Analysis and Summary

The primary objective of the finite element models of small prestressed concrete beams was to establish a valid simulation of the strand bonding mechanism and strand stress transfer. The previous section has shown how this was successfully done by means of a calibrated coefficient of friction to simulate the contact interaction between strand and concrete in a finite

element model. This section highlights results and provides comparisons from the beam models with the aim of obtaining a better understanding of the bond stress transfer behavior inside the beam, especially in the debonded region.

5.11.1 Hoyer's effect

As mentioned in Chapter 2 , Hoyer's effect is one of the primary mechanisms that contribute to the stress transfer between strand and concrete. Since prestressing strands were simulated using solid element in the finite element models, expansion of the strand due to Poisson's ratio after strand release (Hoyer's effect) is captured automatically. Since the expansion of strand is very small and not observable without greatly exaggerating the resulting deformed shape, a stress contour of the model of small beam unit C1-1 is shown for discussion.

Figure 48 shows the contour of the vertical transverse stress (S22) in the end region of beam C1-1. It can be seen that the stresses in the concrete region close to strand are negative, which means that it is in compression. This compressive stress is maximized at the end of the beam and decreases along the beam length. This behavior follows from the fact that the strand part outside the beam is free to expand while the expansion is mostly restrained by the surrounding concrete in the region beyond the transfer region. Thus, strand expansion within the transfer region is maximum at the beam end and decreases along transfer length.

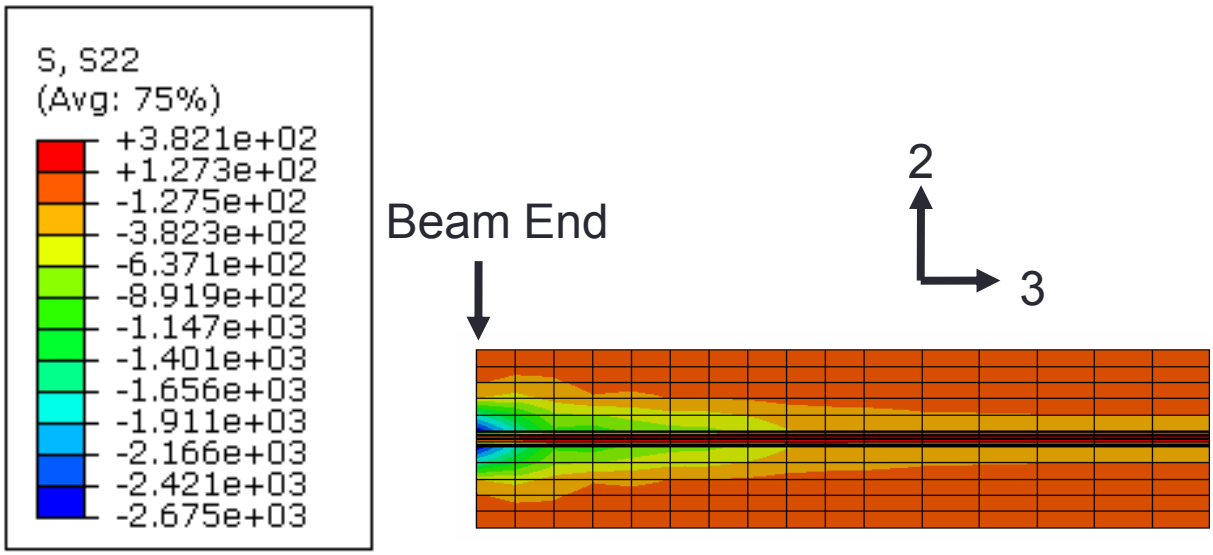

Figure 48 Contour of S22 along Vertical Mid-plane for C1-1 Beam

5.11.2 C1 Beams

In this section, the finite element models of the C1 beams are compared and discussed. There are six beam units with C1 cross-section (6 in. diameter circular beam with a single concentric strand). The beam units compared are C1-2, C1-4 and C1-6, which were all suddenly released. C1-2 beam had a fully bonded strand, while the strand in beams C1-4 and C1-6 were debonded for 1.5 ft with soft and rigid debonding material, respectively.

Figure 49 and Figure 50 shows contours and plot along the indicated path of the equivalent plastic strain (PEEQ) for beams C1-2, C1-4 and C1-6. It can be seen that plastic strains are computed for the region close to the strand. For beam C1-2 (fully bonded), plastic strains concentrates in the region close to beam end and decrease along the beam length. For beam C1-6, in which the strand is ideally debonded (rigid debonding), some plastic strain can be visualized from the point where bonding starts. No plastic strains are predicted within the debonded region for beam unit C1-6. However, it can be observed that the C1-4 model predicts plastic strains all along the debonded region and the trend of plastic strains beyond debonded length is similar to the end region of fully bonded beam unit.

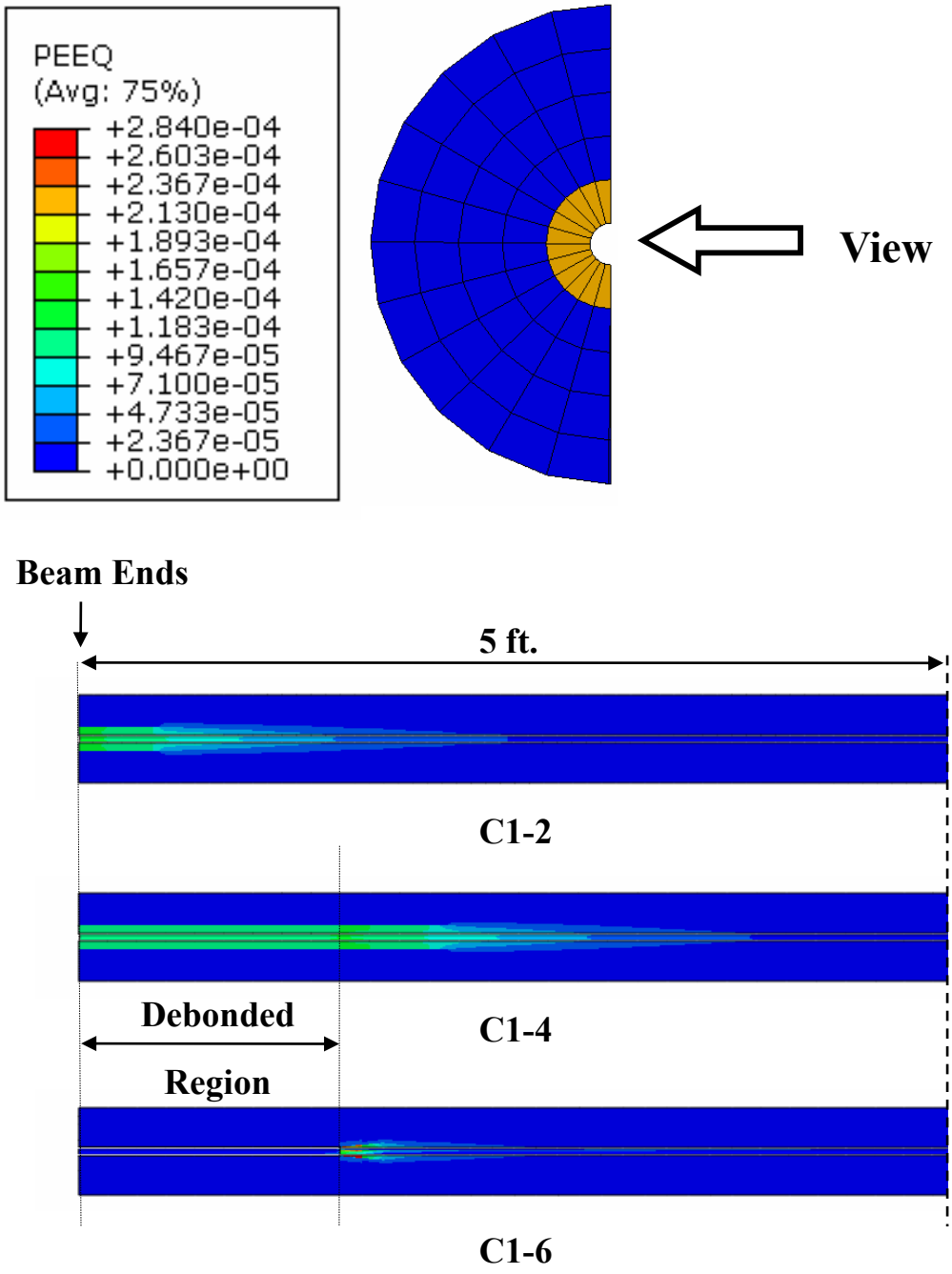

Figure 49 Equivalent Plastic Strains (PEEQ) in Vertical Mid-plane of C1 Beams

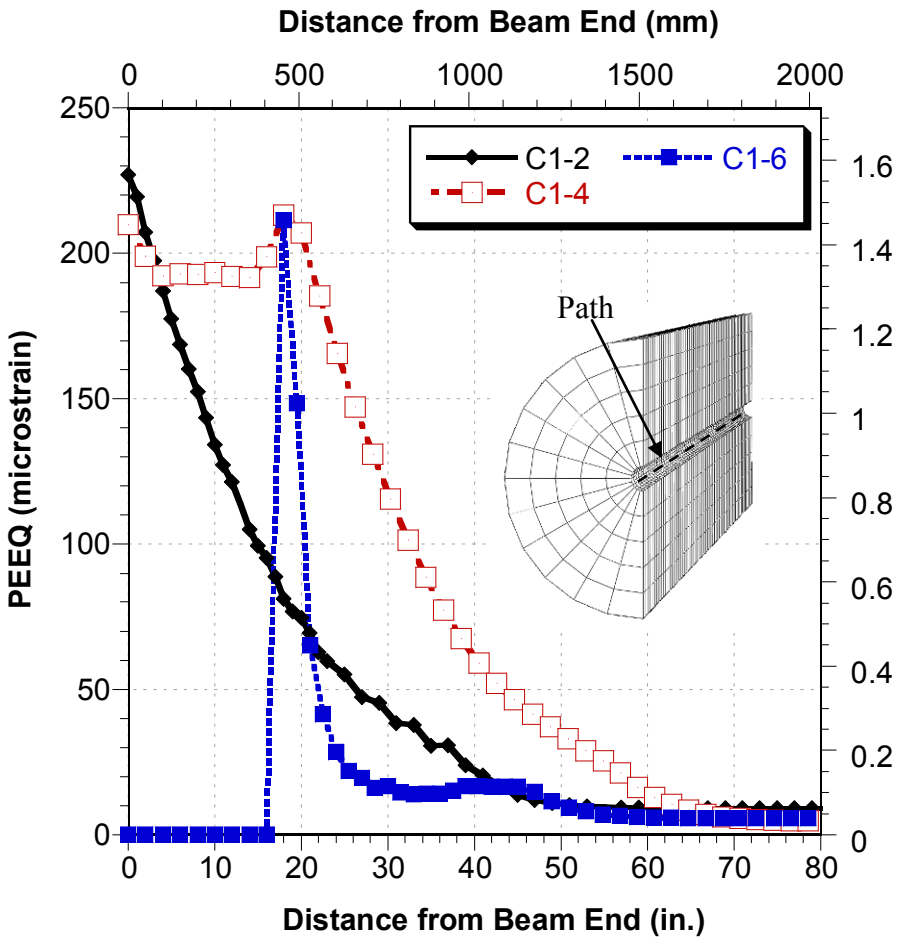

Figure 50 Comparison of PEEQ along Strand Path in C1 Beams

Figure 51 and Figure 52 shows the contours and plot along the indicated path of maximum principal stress of three C1 beams. The maximum principal stress is the maximum tensile stress since in ABAQUS [28] tension is defined to be positive. As seen from Figure 51, the distribution of maximum principal stresses is similar to that of the equivalent plastic strains (see Figure 49). The reason is that concrete will fail in tension (cracking) and a consequence plastic strain will develop at the locations where tensile stress exceeds the tensile strength of the concrete.

Similar to the distribution of plastic strain, the maximum principal stresses have higher values close to beam end for the fully bonded beam (C1-2) and decrease along the beam length. In the idealized debonding scenario (C1-6 beam), the maximum principal stress in the debonded area is essentially eliminated, while the stress level beyond the debonded region is also reduced.

By comparing beams C1-2 and C1-4, it can be seen that debonding with soft material and close-fitting space delays the decrease of maximum principal stresses, while high value stress are maintained within the debonded region.

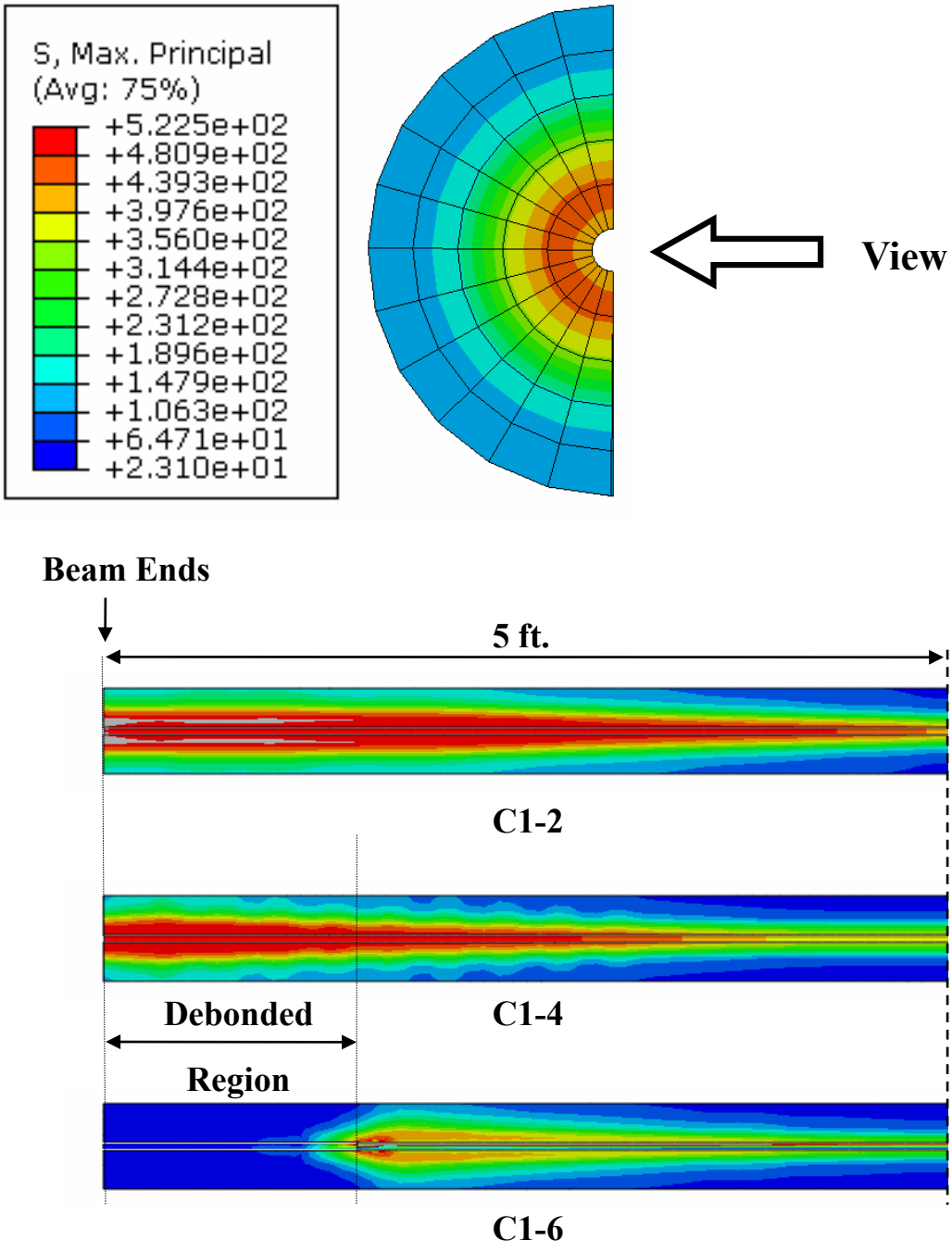

Figure 51 Maximum Principal Stresses in Vertical Mid-plane of C1 Beams

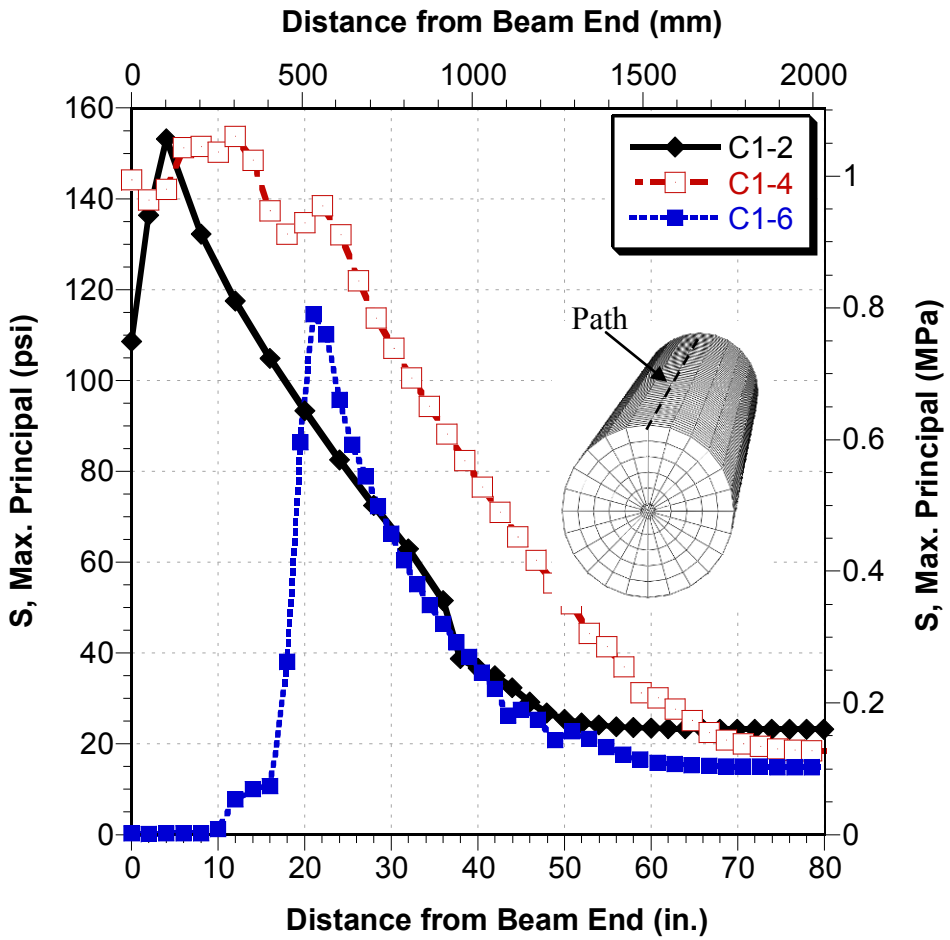

Figure 52 Comparison of Maximum Principal Stress along Top Surface of C1 Beams

5.11.3 S1 Beams

The models for beam units with S1 cross-section revealed a behavior similar to that presented above for the C1 beams (**Figure 53**). Plastic strains and a region with high tensile stresses can be observed close to the strand. The only difference is that the regions at the corners in S1 cross-section have lower stress state since they are further away from the strand compared to the center region of the vertical and horizontal surfaces of the beam.

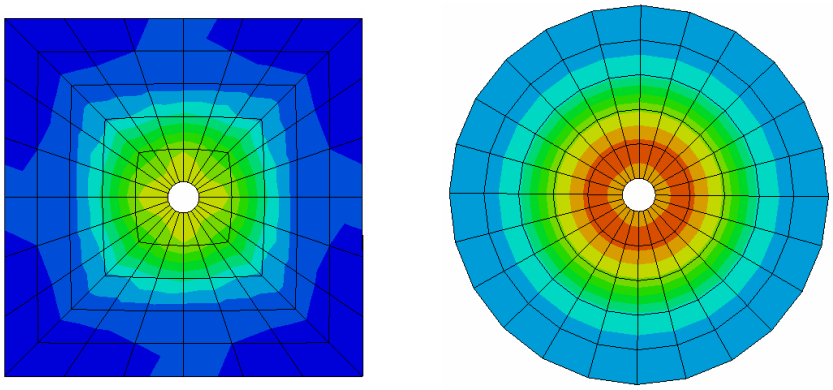

S1-1 C1-1

Figure 53 Contour of Maximum Principal Stress at End Section of C1 and S1 Beams

5.11.4 R2 Beams

As mentioned in previous sections, the distribution of plastic strains in the numerical models is similar to that of the maximum principal stresses and cracks can be assumed to happen at the location where the tensile stress exceeds the concrete tensile strength. As the plastic strains seem to develop only in a small region close to the strand and thus more difficult to compare, the distribution of maximum principal stresses was considered for evaluation of the R2 beams.

Figure 54 and Figure 55 show the contour and plot of maximum principal stresses for beams R2-1, R2-2, R2-5 and R2-6, which were debonded using soft material for 0 ft. (fully bonded), 1.5, 3, and 5 ft, respectively. From Figure 54 we can see that the high tensile stress region around the strands tend to develop towards the top and bottom surface of the beam units, which can also be seen in Figure 56 (contour of maximum principal strains). This is different from the distribution of high tensile stress region of the beam units with one strand, in which the high stress region was uniformly distributed around the strand. This change in response is attributed to the reduced concrete cover above and below the top and bottom strands in the R2 beam. The cover concrete for the strand in the R2 beams was 2 in., while the cover for the C1 and R1 beams was 3 inches.

Figure 55 shows plots of the maximum principal stress along a path centered on the top surface of the beam. It can be seen that for the beams with debonded strand the tensile stresses along the debonded length are higher than the maximum stress value of the fully bonded beam. Further, the results show that strand debonding delays the tensile stress reduction on the top surface of the beam.

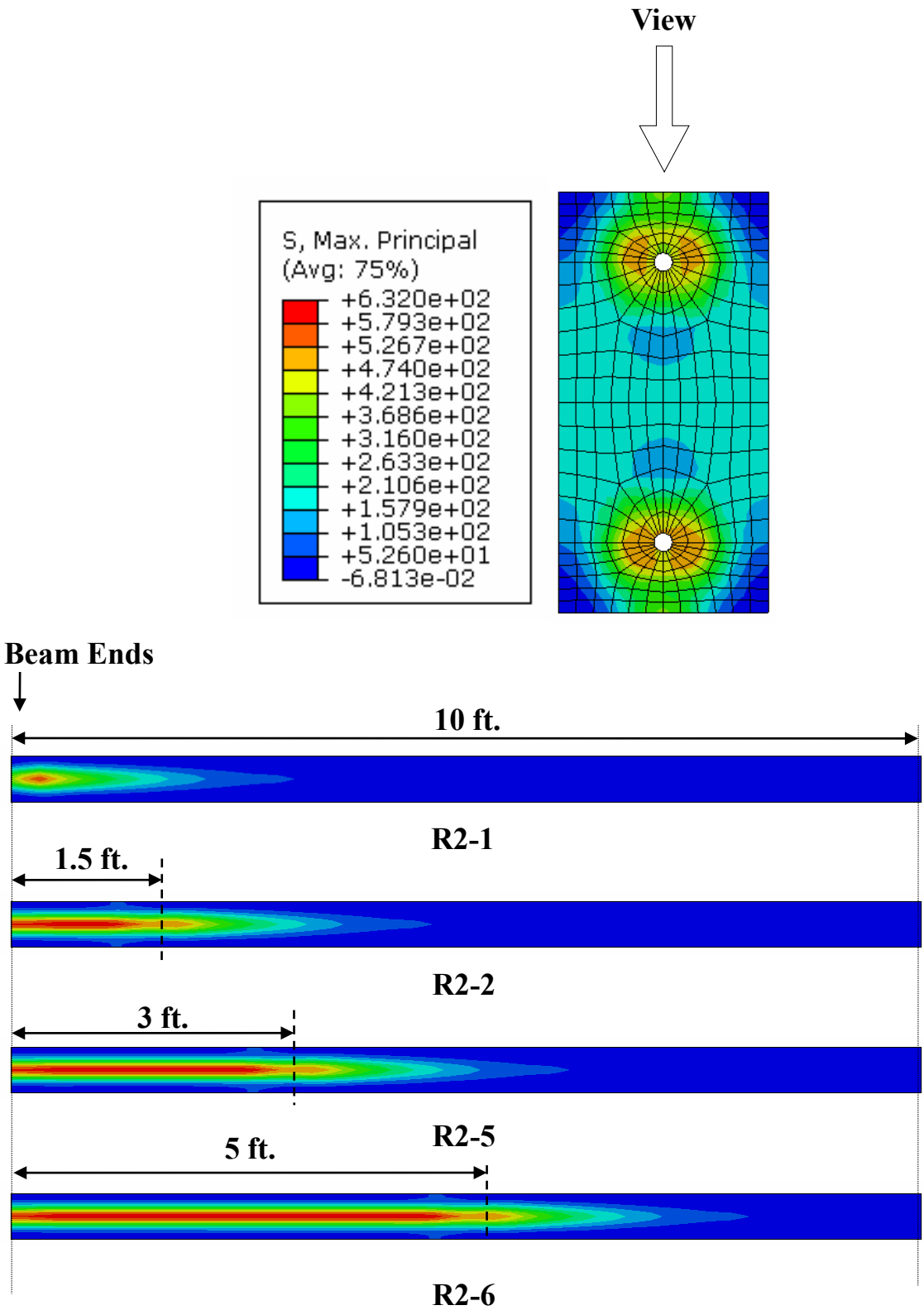

Figure 54 Maximum Principal Stresses on Top Surface of R2 Beams

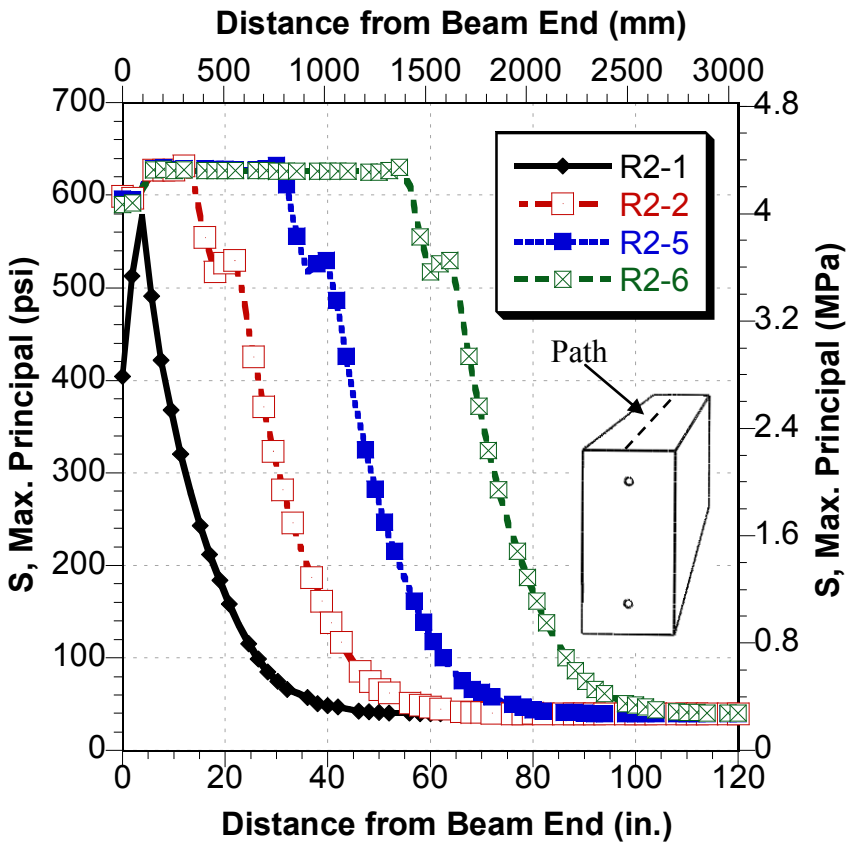

Figure 55 Maximum Principal Stresses along Top Surface Path of R2 Beams

Figure 56 shows contours of maximum principal strains at the end section of beams R2-1 and R2-2. It can be seen that in the debonded case (R2-2) the strain level around strand is higher and it is more likely to produce a vertical crack at the top and bottom surfaces of the beam. Figure 57 shows maximum principal stress contours of the R2 beams on a vertical mid-plane of the beam. Similar trends to those discussed before can be observed from the figure, which clearly shows the higher stress levels in the concrete along the strand debonded.

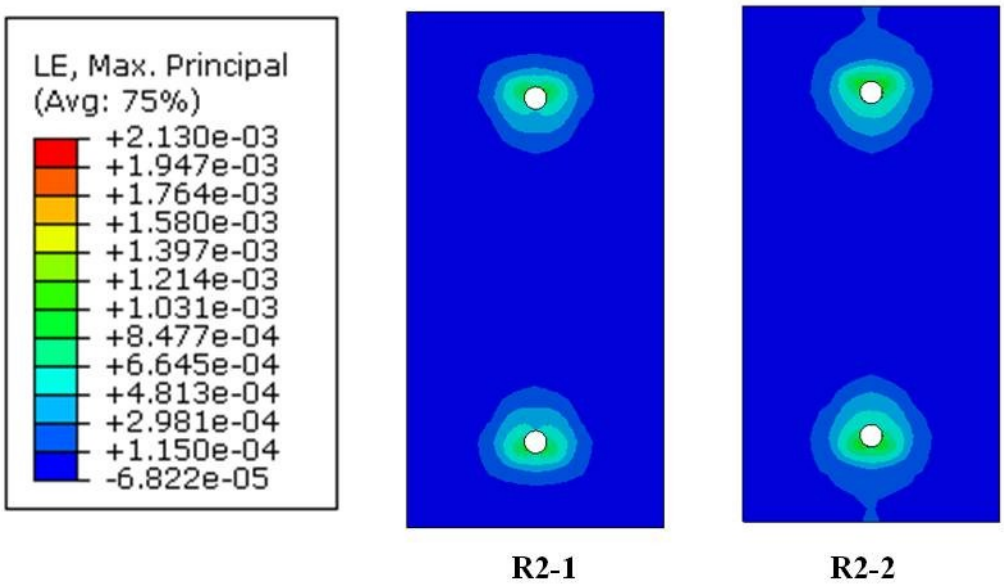

Figure 56 Max Principal Strain Contours of R2-1 and R2-2 Beams at End Section

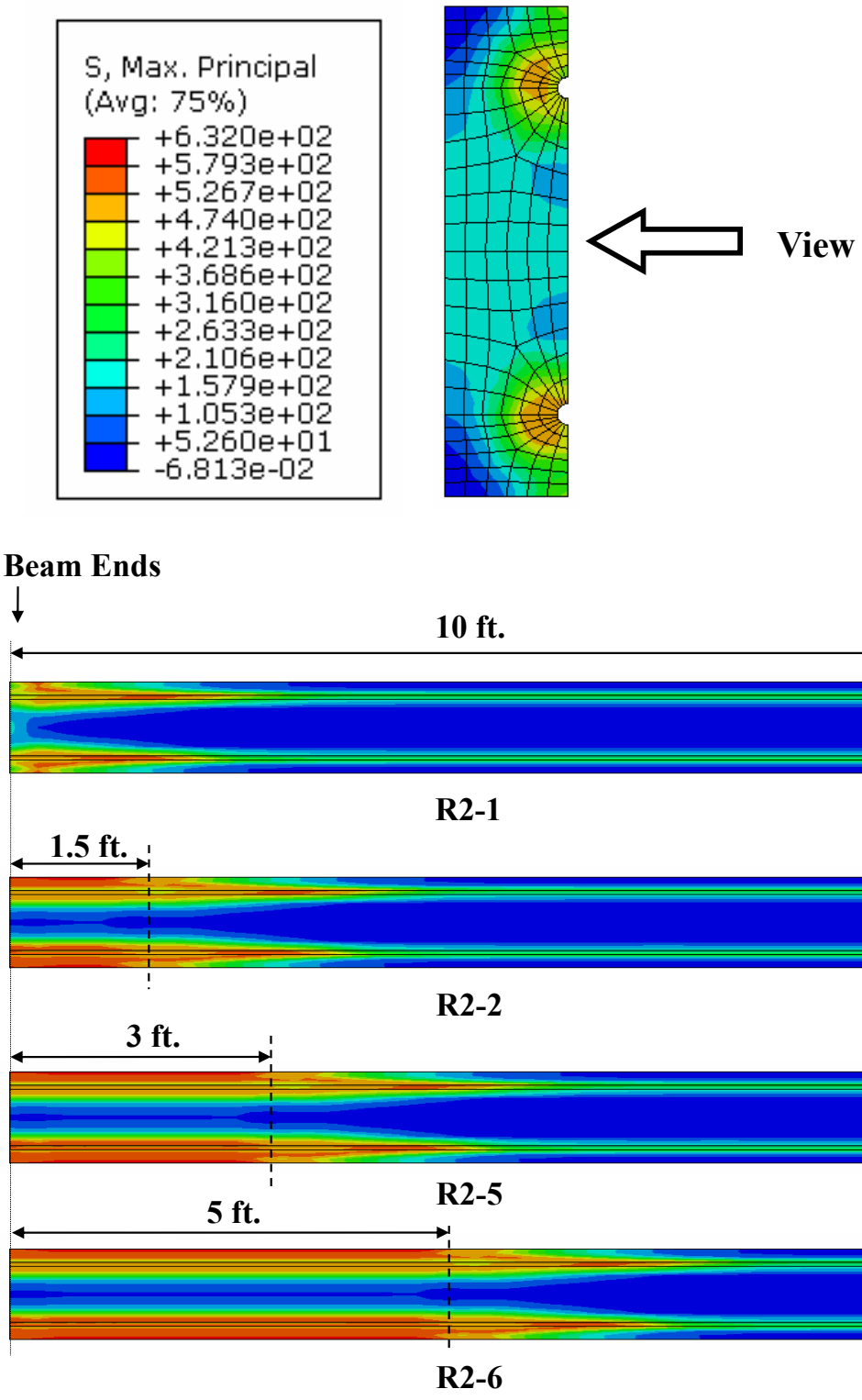

Figure 57 Maximum Principal Stresses on Vertical Mid-plane of R2 Beams

5.11.5 R4 Beams

Results from the finite element simulation on the R4 beams are compared and discussed in this section. Results are presented for beams R4-1, R4-3, R4-4 and R4-5. Details for these beams are given in Table 7. Since the R4 beams featured multiple strands, particular attention was paid to the effect of adjacent strands when evaluating the simulation results.

Figure 58(a) shows contours of the equivalent plastic strains on the beam-end cross section of the R4 beams. It can be observed that plastic strains develop around all strands in the beam units except for beam R4-5, which is the beam with rigid and oversized debonding material. The plastic strain regions around the top and bottom strands in the first beams are close to each other although they do not merge. However, one can expect that if the concrete tensile strength is lower, the two plastic regions may join together, which would imply that cracks would develop between the two strands. Evidence to this effect can be seen in **Figure 58**(b), which shows contours of maximum principal strains. The contours reveal that the strain in the region between top strands and between bottom strands in the first three beam units is actually very high. A small high strain region on the top and bottom of the beam surface is apparent for beams R4-3 and R4-4, which indicates that cracking may propagate to these surfaces.

Figure 59 shows contours of the maximum principal strains in a horizontal section across the top strands for the R4 beams. It can be seen from the figure that the high strain region between the top two strands in the R4-1 and R4-5 beams only exits within the bond force transfer region. However, for beams R4-3 and R4-4, the high strain region includes not only the region of full bond transfer but also the entire region along the strand debonded length.

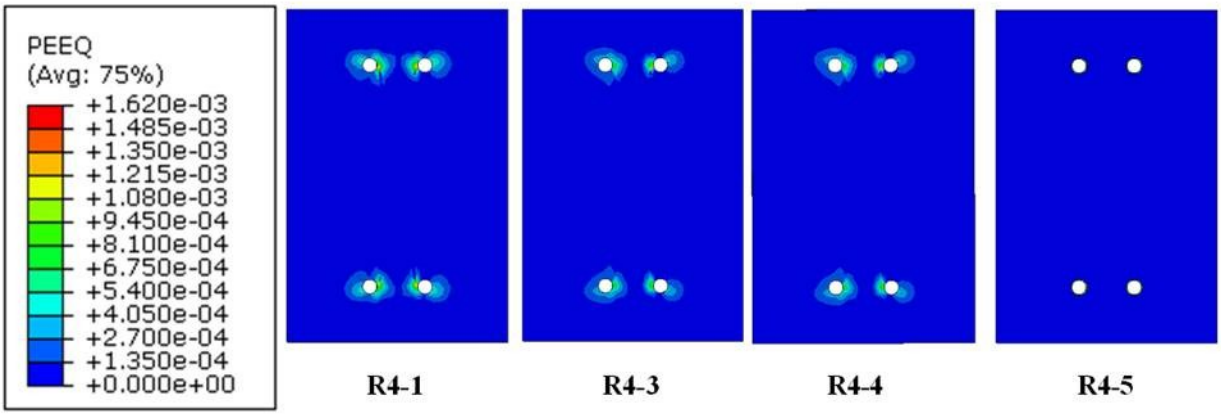

(a) Equivalent Plastic Strains (PEEQ)

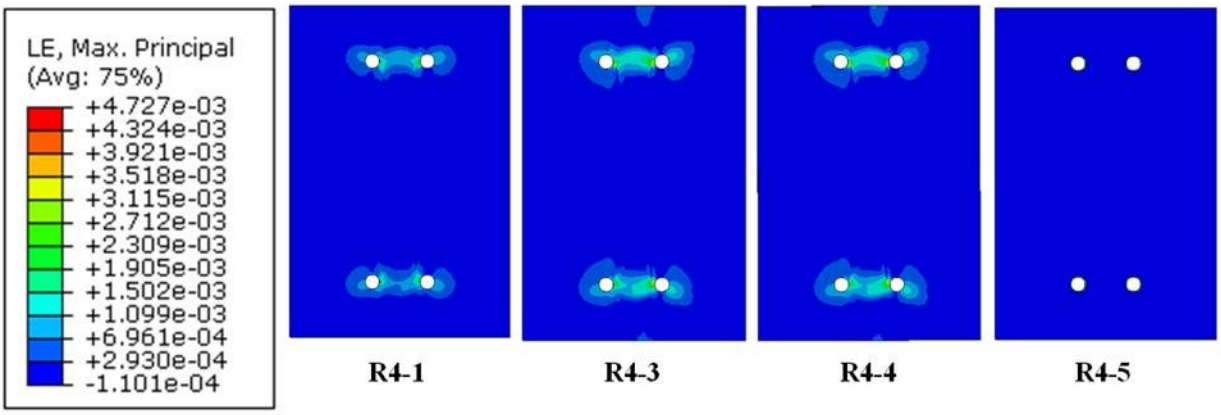

(b) Maximum Principal Strain

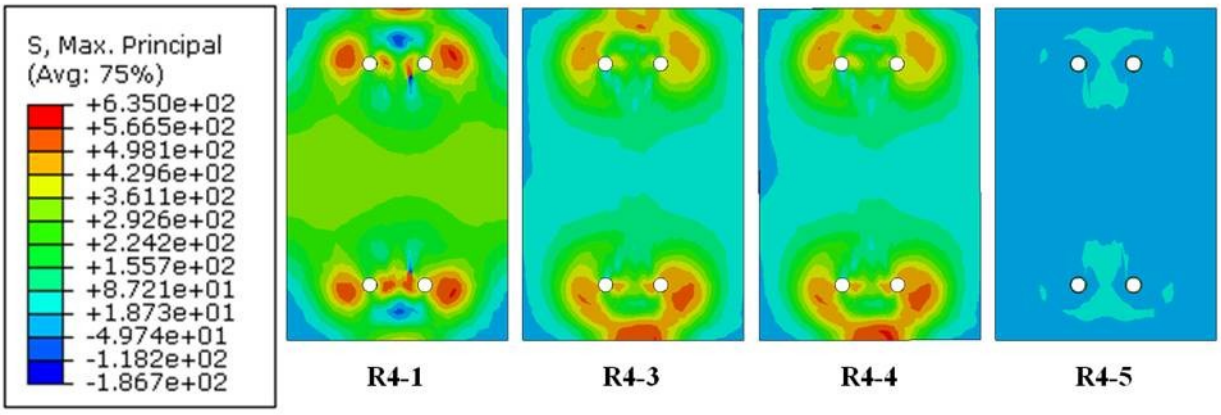

(c) Maximum Principal Stress

Figure 58 Strain and Stress Contours at the End Cross Sections of Beam R4-1

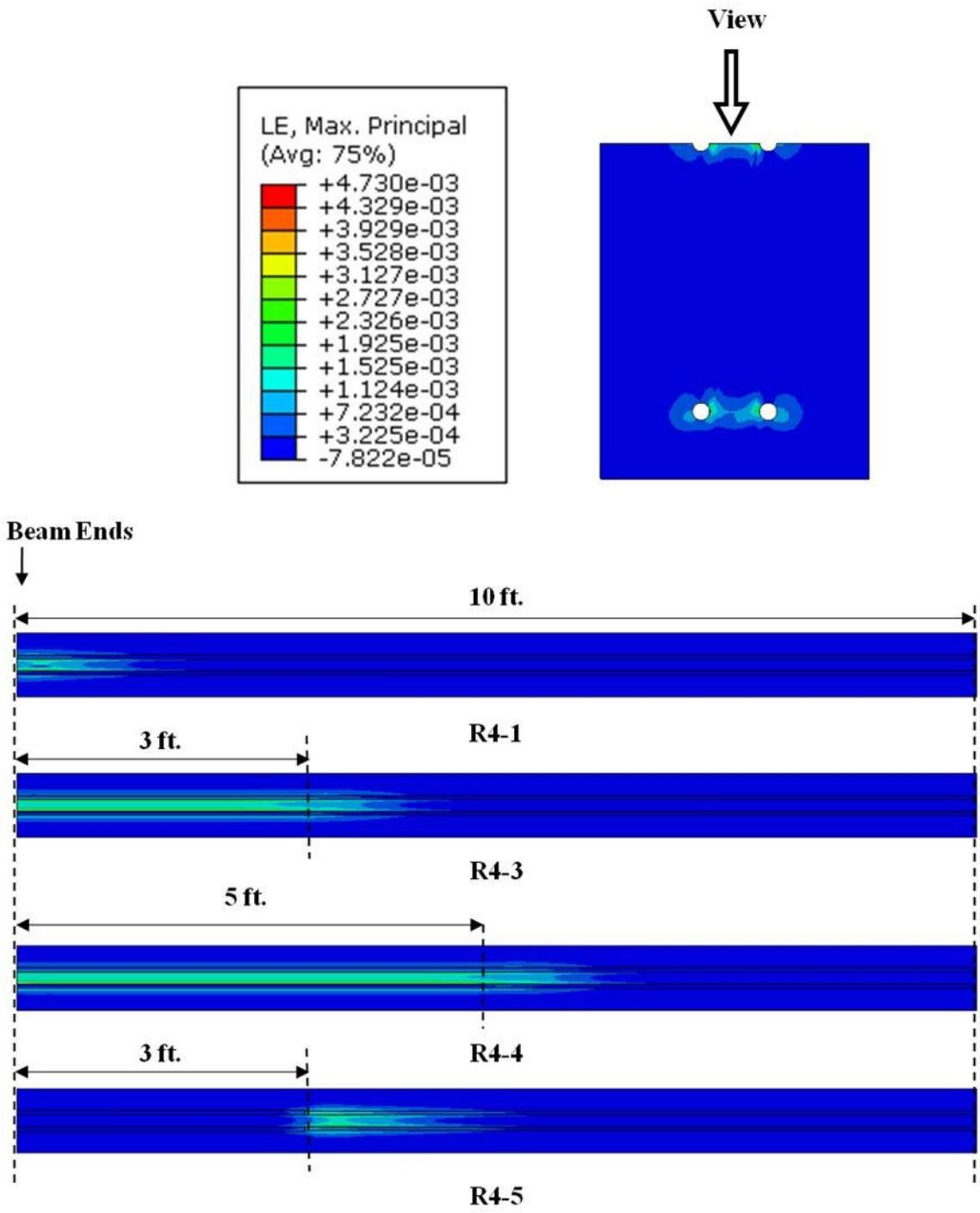

Figure 59 Max. Principal Strain of R4 Beams on Horizontal Section along Top Strands

From **Figure 58**(c) it can be seen that the high tensile stress region in the first three beams was generally located close to the strands. However, considerably high stresses are predicted at the top and bottom surfaces for beams R4-3 and R4-4. For these models, the stress

level between the top and bottom strand pairs are lower since the concrete in these regions has lost stiffness due to damage. From these figures it can be seen that the propagation of high tensile stress region can be separated into two forms: i) the high tensile stresses between adjacent strands will propagate horizontally and merge; and ii) the high tensile stresses propagate towards the nearest free edge at an angle of approximate 45 degrees and create high stress regions on top of the beam surface.

Figure 60 shows contour plots of the maximum principal stresses for beams R4-1, R4-3, R4-4 and R4-5 along the top surface of the beams. The high-stress regions are those caused by the vertical propagation of high tensile stresses from the top strands, as discussed above. It can be seen that for the fully bonded beam units, this region only forms near the beam end. For the R4-5 beam the high stress region shifts from the beam end to the onset of full strand bond transfer due to the ideal debonding that can be provided by rigid and oversized strand blanketing. The stress levels within the debonded region are caused by the stress transfer mechanism inside the beam but their magnitude is much smaller. Conversely, for beams R4-3 and R4-4 the region with high tensile stress in not only present at the onset of full strand bond transfer but high tensile stresses develop along the full length of debonding. This behavior follows from the radial expansion of the debonded strand and the pressure that it exerts onto the concrete by virtue of having a “tight fit” between the strand and concrete.

Figure 61 shows the maximum principal stresses for the R4 beam along the center line of top surface. This figure shows in a different way the same behavior that has been previously discussed in the prior contour plots. The traces show that the tensile stress distribution for beams R4-1 and R4-5 reach a peak value a few inches after the start of full bond, decreasing rapidly after that. Further, it can be seen that the tensile stress level in the debonded region for beam R4-5 is quite low. For beams R4-3 and R4-4, the maximum tensile stresses also occur a few inches after the full bond condition starts and it decays rapidly as well. However, there the principal tensile stress values for these beams along the debonded length of the strand are significant. Further, unlike the R2 beams models, the stress level in the debonded region is much lower than the maximum stress level. This means that the concrete in debonded region in the R4-3 and R4-4 beam models has already suffered damaged, which leads to a drop in the stress level. This is reasonable since the concrete strength for beam units R4-3 and R4-4 was relatively low.

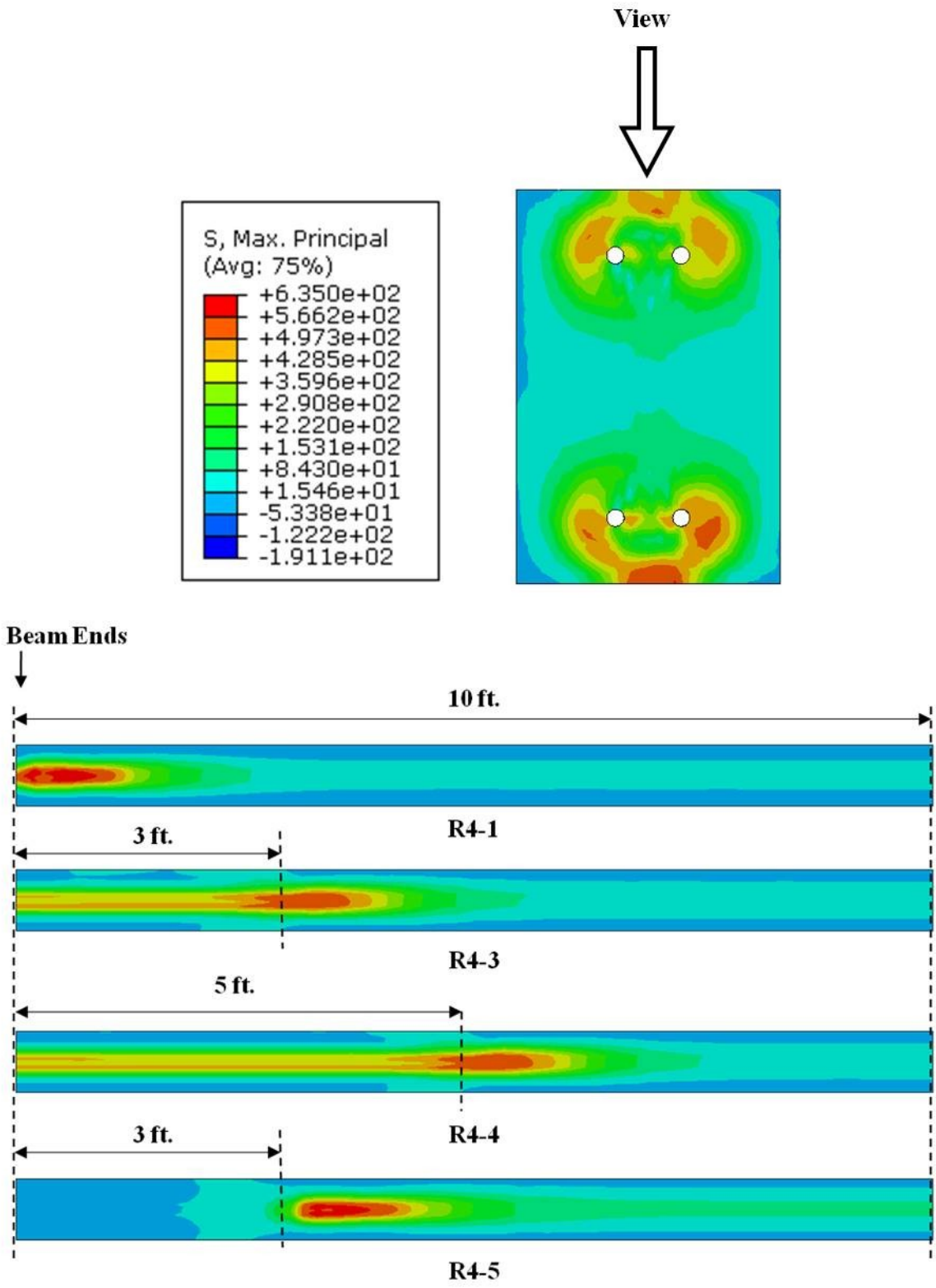

Figure 60 Maximum Principal Stresses on the Top Surface of R4 Beams

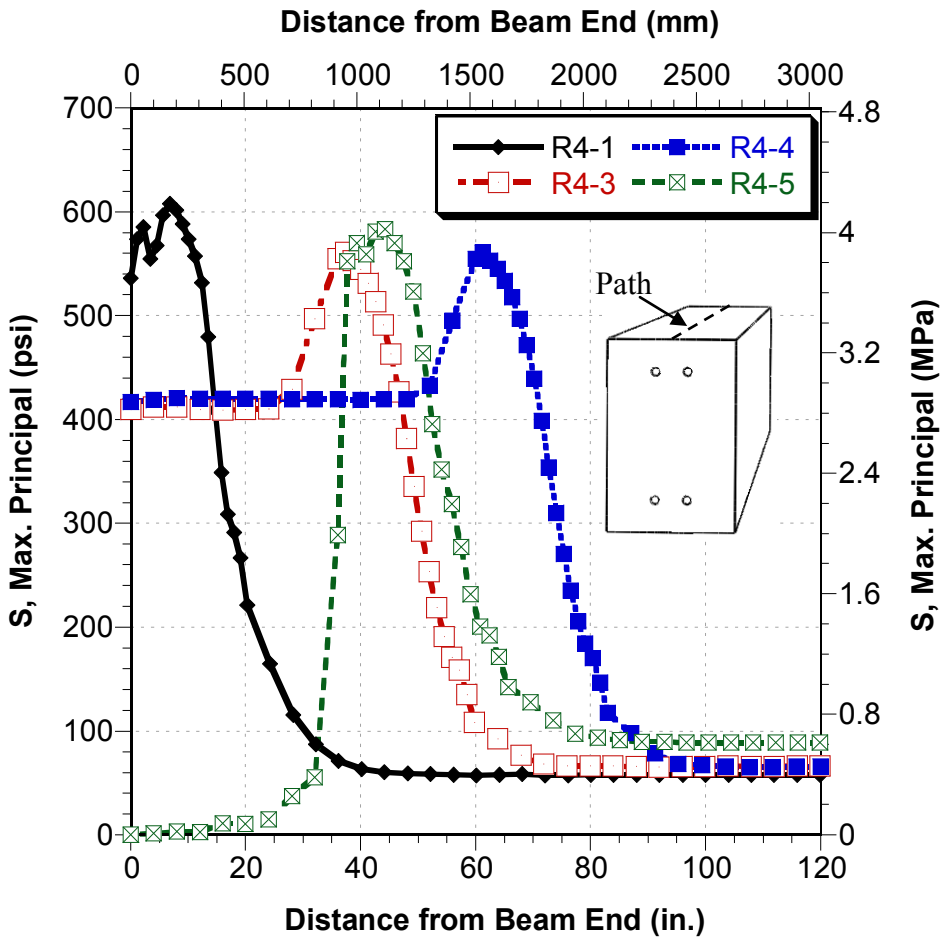

Figure 61 Maximum Principal Stresses along Top Surface Path of R4 Beams

5.11.6 Discussion and Summary

Based on the results and discussion from the previous sections, it can be seen that concrete around the strand will be highly stressed within the debonded region if the strand and concrete have a tight contact. The reason follows from the fact that the absence of bond strength will maximize expansion of the strand after release. This phenomenon is explained in the following paragraphs with reference to the equivalent system shown in Figure 62.

Consider a section of strand in which the expansion of the strand after pre-tension release is represented by an equivalent axial compressive force F. Force F can be considered to be the force drop in the strand segment along the transfer region after release. The bonding strength between strand and concrete is modeled with two springs in the horizontal direction with

stiffness K_z and the radial interaction (or normal interaction between strand and concrete surfaces) is modeled with two springs in the vertical direction with stiffness K_r.

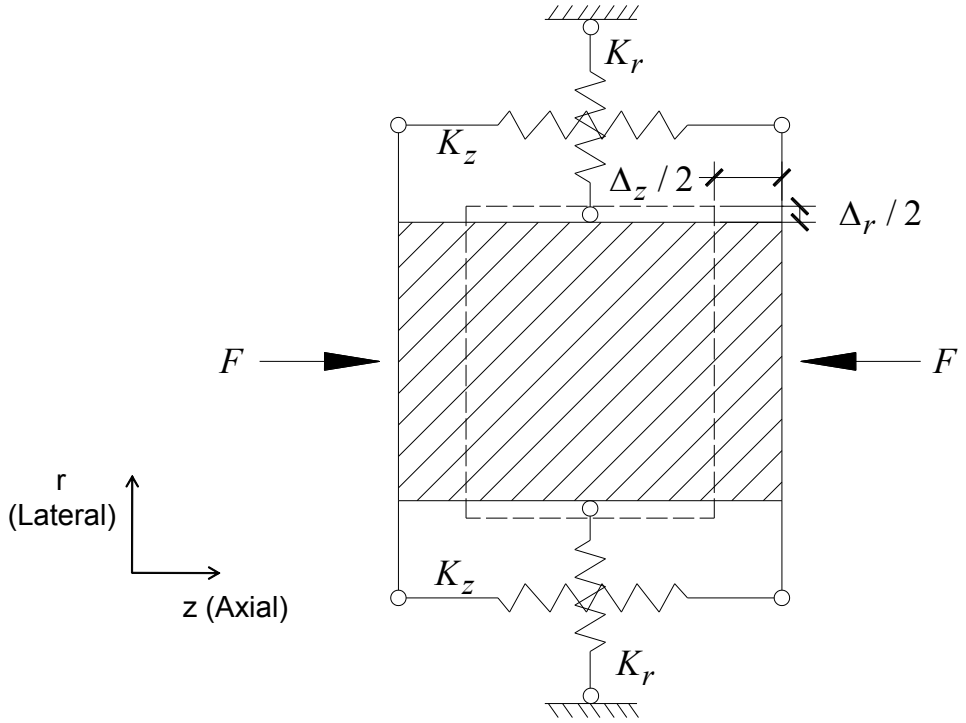

Figure 62 Free Body Diagram of Strand Section

By considering equilibrium for the system and loading in Figure 62, if the stiffness K_z is significantly high (bond strength is high) the axial force F will be balanced by the force in the two horizontal springs with very small longitudinal deformation (Δ_z). Thus the lateral deformation (Δ_r), which depends on Δ_z due to the strand's Poisson's ratio, is very small. As a consequence, the force in the vertical springs $F_r = \Delta_r K_r$ will be very small.

On the other hand, if the longitudinal springs have a very low stiffness (poor bond strength) the force F won't be balanced until a relatively large longitudinal deformation takes place. Consequently, the lateral strand deformation will be greater and so will be the force in the vertical springs. It follows that if the stiffness K_z is zero (no bond strength at all) the force F will be completely balanced by the longitudinal strand deformation and its lateral expansion will

be maximized. This is the reason why the finite element simulations have shown that concrete within debonded region will be highly stressed if there is no room for the strand to expand freely.

Based on the provided results, comparisons and discussion from the finite element simulations, several findings can be highlighted:

i) If the strand is ideally debonded and there is enough room around the strand for it to dilate freely, the stress level in the debonded region can be significantly reduced. However, if the concrete and strand have a tight contact, the internal pressure on the concrete surrounding the strand may be significantly high due to the strand's radial expansion. Thus concrete in the debonded region will be highly stressed and the high stress level will be maintained within the debonded region and will only decrease after the full bond region starts.

ii) Longer strand debonded lengths may lead to a large region with high tensile stresses if the strand and concrete are in tight contact. Based on the presented finite element analyses, tensile stresses will be significant throughout the debonded length and will not decrease until a few inches after the start of the full bond region.

iii) The regions of plastic strain around adjacent strands, which indicate concrete cracking, tend to propagate and merge with each other. Based on the observed distribution of maximum principal stresses, cracks may also tend to propagate towards the closest free surface.

Chapter 6 Simulation of Anchorage Zones in Full-Size Beams

6.1 Introduction

This chapter focuses on evaluating the effects of debonded strands on the anchorage zones of full-size bridge girders by means of three-dimensional (3D) finite element (FE) simulations. The experimentally calibrated bond stress transfer parameters and simulation strategies presented in Chapter 5 are used in the evaluation of precast/prestressed AASHTO box beams. The analyses center particularly on the evaluation of a skewed box beam. The dimensions of the box beam section are 4 ft. x 3.25 ft. with a total length of 117 ft. and the skew angle at both ends was 40^{o}. The beam was designed and built for a highway bridge owned by the Michigan Department of Transportation (MDOT). The box beam was selected for this study since it experienced damage at its end during production, which is hypothesized to be due to its detailing with strand debonding using flexible sheathing and in quantities that exceeded the current AASHTO specifications for debonded strand.

A specific aim of the study was to identify the causes behind the damage observed in the bridge box beam and the roles that strand debonding may have had. Of particular interest was assessing the role of the beam skew in the observed damage. Thus, three 3D FE models were established in ABAQUS for the noted box beam. The first model simulated all features of the real box beam in terms of geometry, material properties, and pre-tensioned and passive reinforcement layout. In this model, a 'tight' contact was defined between strand and concrete surfaces in the debonded region to represent debonding with flexible sheathing The second model differed from the first only in the fact that it eliminated the skew angle, i.e., the box beam was straight. In order to investigate the effects caused solely by the dilation of the deboned strand with flexible sheathing, a third analysis model simulating strand debonding with rigid sheathing was established. The only difference of the third model, compared to the first one, is that over-sized holes were created around the strands along the debonded region. This provides room for the strand to dilate after release thus eliminating the internal pressure onto the surrounding concrete that would otherwise be generated along the debonded region.

Since it is of interest to simulate the potential damage to the box beam, the definition of realistic material behavior in the models is very important. Unfortunately, the large size of the box beam FE models made it computationally prohibitive to adopt a nonlinear concrete model

definition. As a result, the concrete material had to be modeled with elastic properties. To better interpret the results from the box beam numerical models, a comparison between elastic and plastic material definitions was conducted based on the FE model of beam R4-3. The comparison showed that the results with the elastic concrete model could be used to identify damage by providing a cut-off to the tensile stresses equal to the tensile strength of the concrete. The predicted damage zone by this approach is shown to correspond well with the damage zone predicted by using the concrete damage plasticity model in ABAQUS (see Section 6.4).

Upon reassuring that the elastic FE analysis on the box beams can be reliably used to assess damage, a comparison is made between the results for the three box beams. The resulting damage patterns in the skew box beam model with flexible sheathing were found to be consistent with those observed in reality and the effect of skew angle and strand debonding method is assessed and discussed.

6.2 Effect of Elastic and Plastic Concrete Material Definition in FE Simulations

The friction coefficient, which is the primary coefficient in the simulation of strand-concrete bond behavior in this study, was calibrated based on experimental results using numerical models with an inelastic concrete material definition. However, the large size of the box beam FE models made it computationally prohibitive to adopt a nonlinear concrete model definition in the numerical models of box girders, and thus an elastic concrete behavior was assumed. To verify the feasibility of using the calibrated friction coefficient in box girder models and evaluate the use of an elastic model to predict damage (i.e., cracking), a comparison between models with elastic and plastic concrete material definition was performed for beam R4-3 (see Figure 43). The comparison focused on the resulting maximum principal strains, transverse strains (LE11), maximum principal stresses, and longitudinal strains (LE33).

6.2.1 Maximum Principal Strains

Figure 63 shows contours of the maximum principal strains for the elastic and plastic models of beam R4-3. As previously discussed, maximum principal strains indicate the possible cracking region. It can be seen that the contours are similar such that the region around and between adjacent to the strands have higher tensile strains. However, a long region of high tensile strain along the top beam surface is predicted by the plastic model but not in the elastic

model. The reason is attributed to the fact that the plastic model allows the redistribution of stresses after damage occurs, thus leading to the migration of large strains to the beam top.

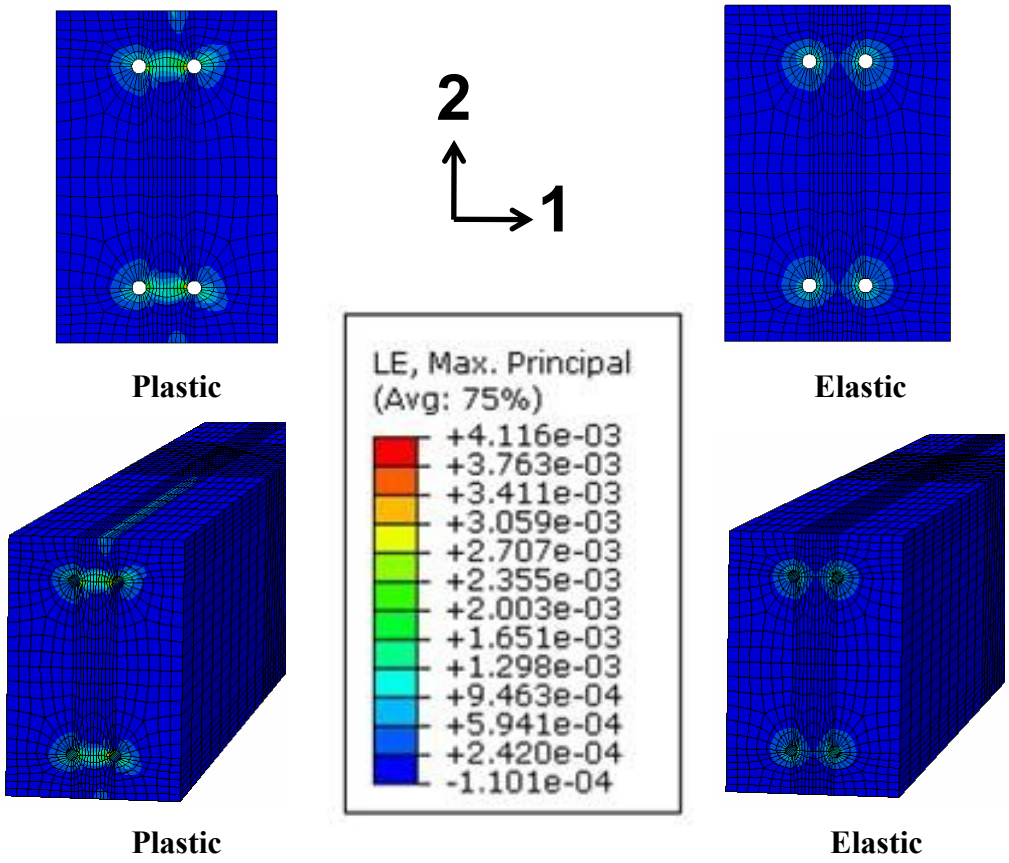

Figure 63 Maximum Principal Strains for Plastic and Elastic Models of Beam R4-3

A plot of maximum principal strains for beam R4-3 with plastic and elastic material definitions is shown in Figure 64. The figure was plotted along a path that passed through the center of the top strands along the beam end section. It can be seen that both models predict the maximum plastic strains to be higher in the region adjacent to the strands and maximum at the interface between strand and concrete. The maximum value in the plastic model is about 3,200 micro-strain and about 1,200 micro-strain in the elastic model. It can also be seen that the lowest value of maximum principal strain in plastic model (about 1,200 $\mu\varepsilon$) is about five times of that in the elastic model (about 250 $\mu\varepsilon$).

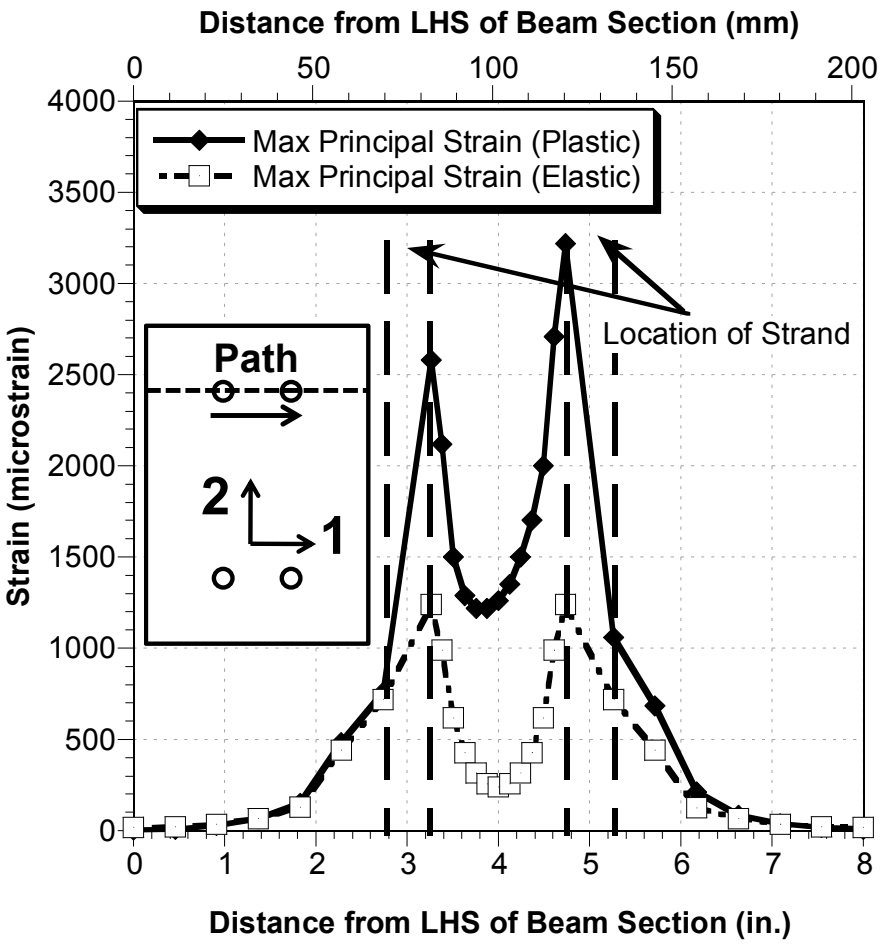

Figure 64 Max. Principal Strains in Plastic and Elastic R4-3 Models along Top Strands

Figure 65 shows a plot of maximum principal strains along the top edge of the beam (R4-3) end section. It can be seen that the strain level from the plastic model in the middle region of the path is much higher than that that of the elastic model. As previously noted, in the plastic model concrete around strand becomes damaged and additional stress get redistributed, making other concrete areas carry more stress. On the other hand, the concrete near the strand in the elastic model is able to carry stresses beyond the cracking level and thus the stresses concentrate and grow in the region close to the strand, while concrete away from strand is kept from contributing to the stress resisting mechanism.

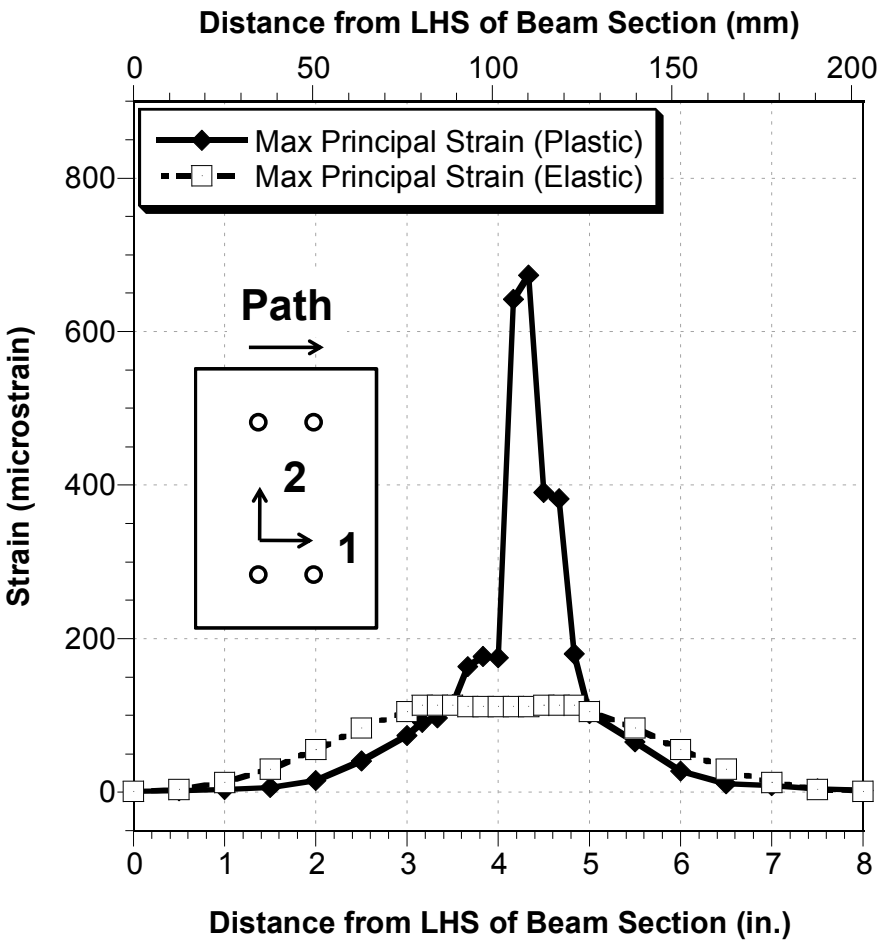

Figure 65 Max. Principal Strains in Plastic and Elastic R4-3 Models along Top Edge

6.2.2 Transverse Strains

A plot of transverse strains (LE11) along a path crossing the two top strands is shown in Figure 66. It can be seen that the horizontal strains along the path are compressive (negative) while having a similar trend as the maximum principal strains (see Figure 65). The maximum horizontal strain in the plastic model is close to that of elastic model. And the lowest value in the region between two strands in the plastic model is close to that in the elastic model (200 $\mu\varepsilon \sim 300\ \mu\varepsilon$). It follows that the inelastic concrete material model compressive stresses are similar to the elastic concrete material model.

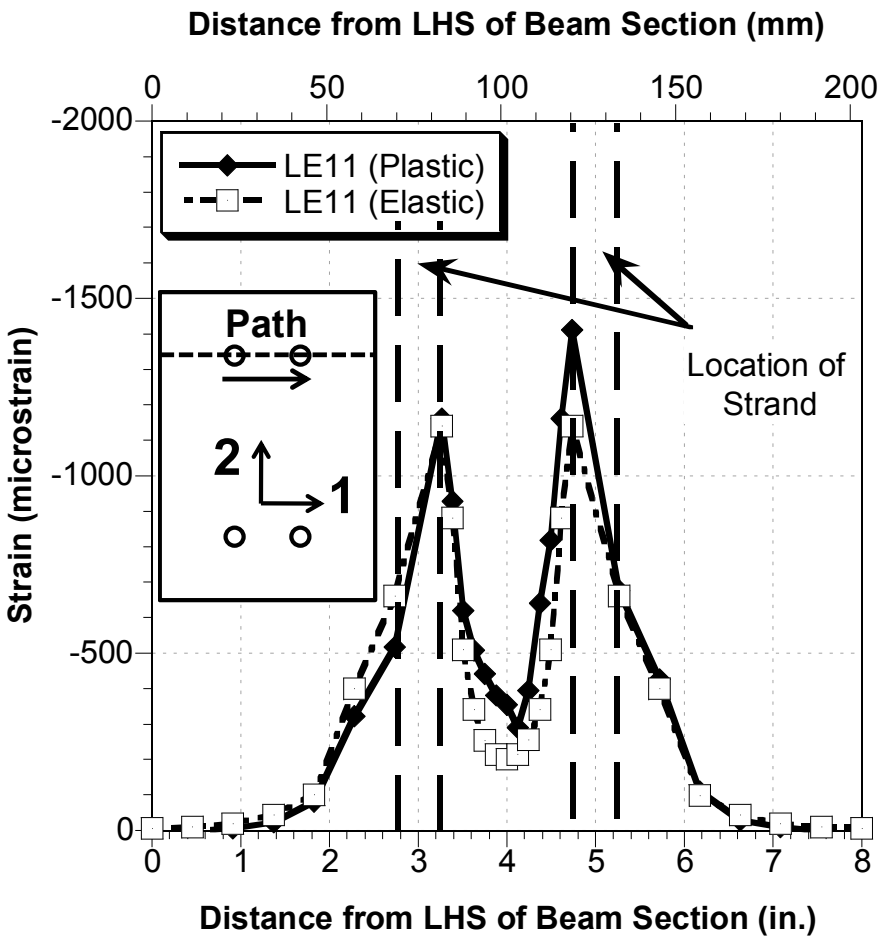

Figure 66 Horizontal Strains in Plastic and Elastic R4-3 Models across Top Strands

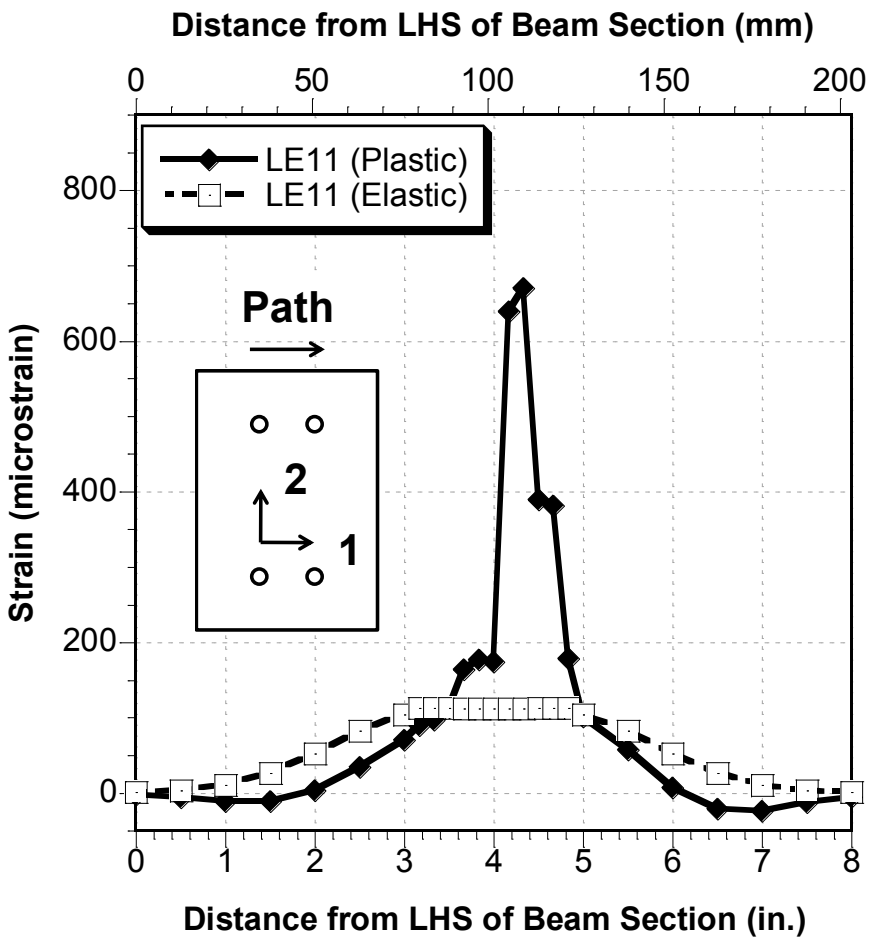

Figure 67 Horizontal Strains in Plastic and Elastic R4-3 Models along Top Edge

A plot of horizontal strains along the top edge of the beam end section is similar to the plot of maximum principal strains (see Figure 65) since the tensile strains on the top surface are mostly along the horizontal direction. However, the figure shows that the region close to the corner of the section in the plastic model is slightly in compression in the horizontal direction, which is again a result of the stress redistribution form the concrete damaged around the strand.

6.2.3 Maximum Principal Stresses

Figure 68 shows contours for the maximum principal stresses in the elastic and plastic models for beam R4-3. To compare the results, an upper limit for the concrete tensile strength of $f_t = 7.5\sqrt{f'_c}$ was set for the stress contour plots from the elastic model. As previously mentioned, maximum principal stresses are basically maximum tensile stresses. It can be seen

from the figure that the distribution of maximum principal stresses is similar in both cases such that high tensile stresses develop in the region between the adjacent strands and in the center region of the beam top and bottom surfaces within the debonded region. However, the contours from the elastic model show that the tensile stresses in the region close to the strand have already exceeded f_t while the stress is lower in the same region in the plastic model. This is attributed to the fact that the concrete around the strands in the plastic model cracks, and its response enters into the tension stiffening stage and the stress level drops. Nonetheless, both models show that the stress is highly concentrated in the region close to the strands.

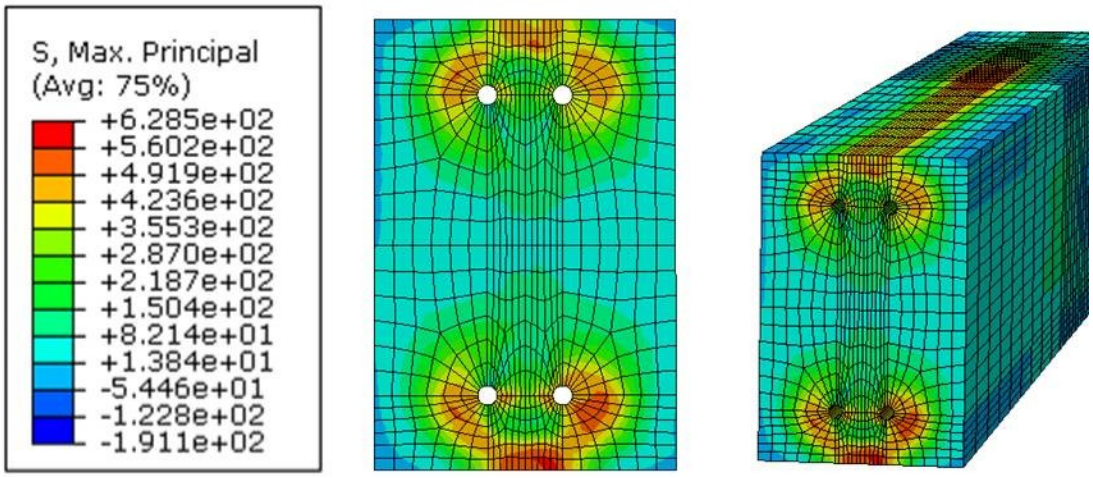

Plastic Model

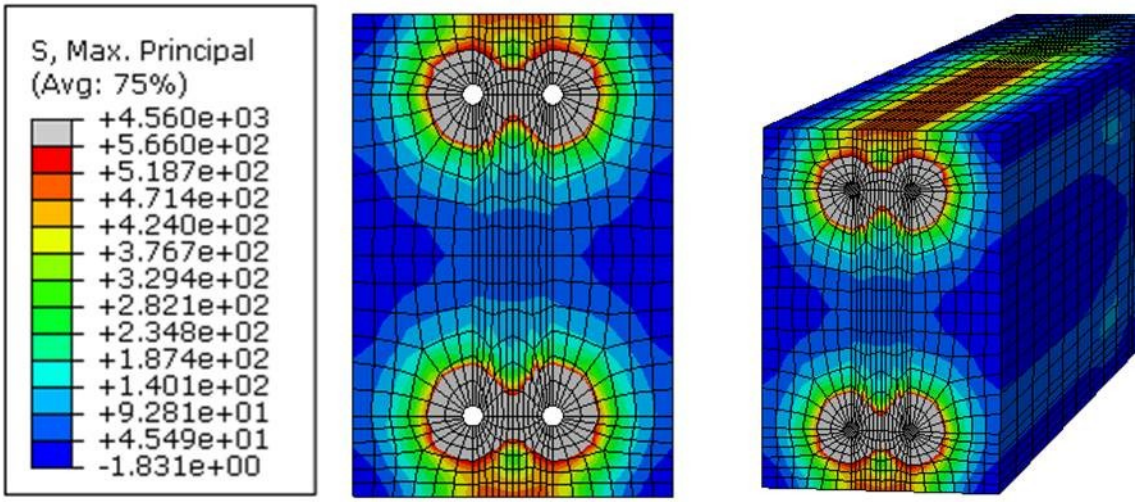

Elastic Model

Figure 68 Contours of Maximum Principal Stress

The maximum principal stresses along a transverse path across the top strands are plotted in Figure 69. It can be seen that the stress level close to strands is much higher than that close to beam surface. In the elastic model, the stresses near the strands exceeds the upper limit of f_t, while the stresses are lower than this limit in the plastic model results. As discussed before, this follows from the fact that the plastic model can capture the concrete damage (cracking), thus leading to a stress drop. It can be noted, however, that the region above upper limit in the elastic model is close to the region that has been damaged in the plastic model. Thus it can be

considered feasible to check the "damaged" or "cracked" region in an elastic model by defining a tensile stress limit.

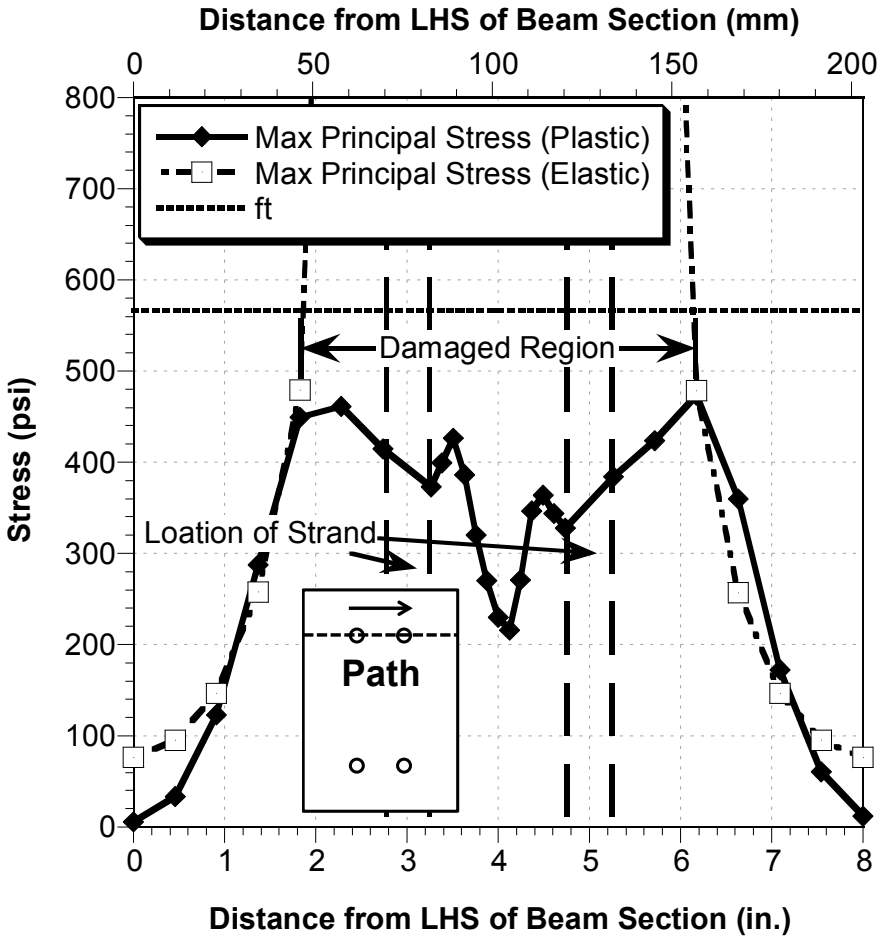

Figure 69 Max. Principal Stresses in Plastic and Elastic R4-3 Models across Top Strands

Figure 70 shows the distribution of maximum principal stresses along the top edge at the beam end cross section. As discussed before, concrete in the middle region of the top surface of beam in plastic model is stressed more load than that in elastic model. However, unlike the plot for maximum principal strains (Figure 65) the stress level in the middle region of the plastic model is lower than that of elastic model. This means that the concrete in this region has cracked and its now in the tension stiffening/softening stage, in which strain increases with a rapid decrease in stress. It can be seen that the maximum principal stresses on the surface from the elastic model do not exceed the tensile limit f_t. Thus, the elastic model did not predict the damaged region on the surface. However, the region with greatest maximum principal stress is

still similar to the damaged region in the plastic model and it is still considered feasible to investigate the "damaged region" in elastic models by checking the region with high maximum principal stresses.

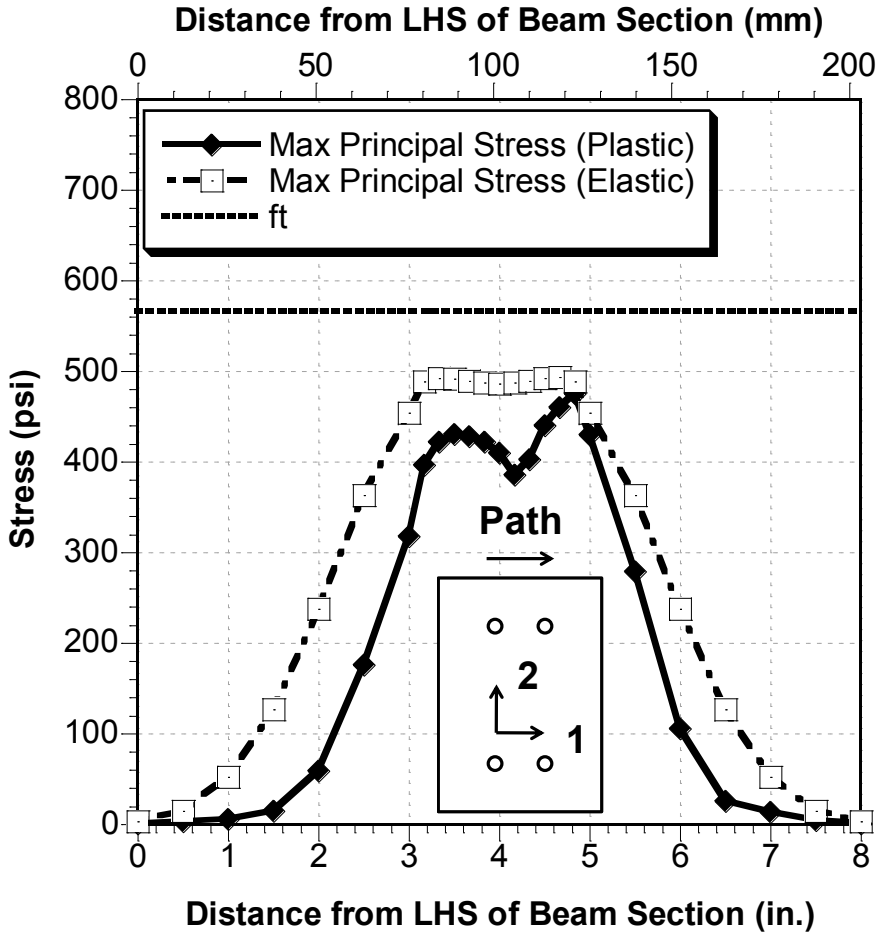

Figure 70 Max. Principal Stresses in Plastic and Elastic R4-3 Models along To Edge

6.2.4 Concrete Longitudinal Strains and Transfer Length

A comparison of concrete longitudinal strains for beam R4-3 was conducted using the coefficient of friction calibrated with the nonlinear concrete model as presented in Section 5.10.4. Results for the strains along the beam centroid are shown in Figure 71. It can be seen that the longitudinal strain profiles deviate slightly along the debonded and transfer regions, while the strain level is the same beyond transfer region. Transfer lengths for the two models were determined using the 95% AMS method and the predicted longitudinal strain profile from each model. In this way, the transfer lengths for the elastic and plastic model were determined to be 58 and 61 inches, respectively. Since the exact prediction of transfer length is not the primary

concern in the study, but rather the assessment of stress demands at the anchorage zone, the noted difference in results is not significant and that it thus it is feasible to use the coefficient of friction calibrated using a nonlinear concrete model in an elastic concrete model..

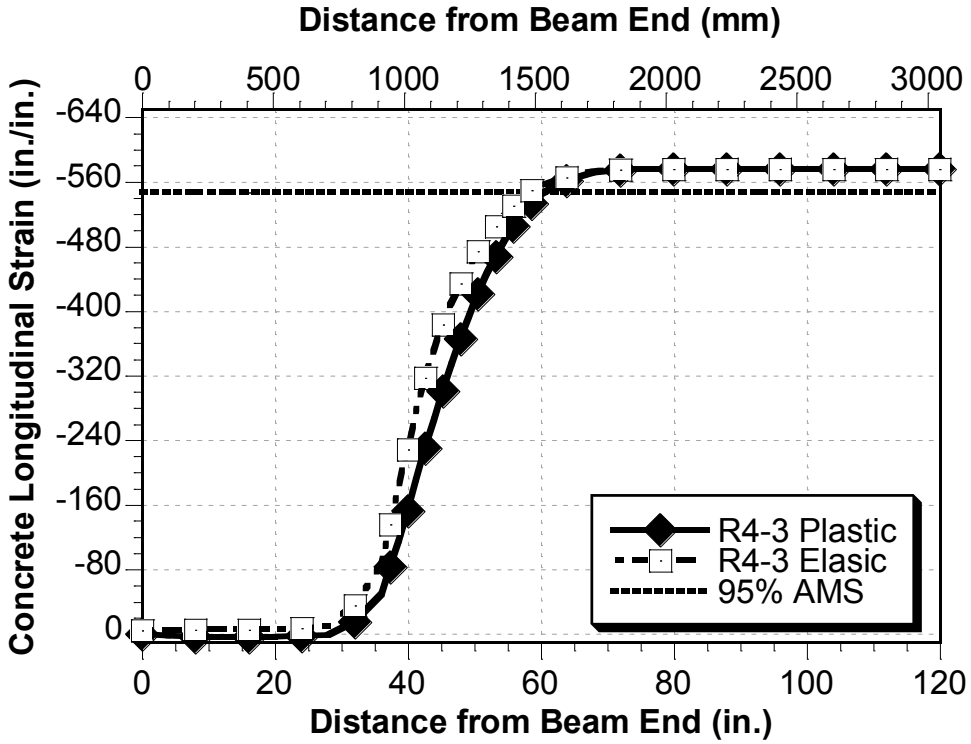

Figure 71 Longitudinal Strains in Plastic and Elastic R4-3 Models along Beam Centroid

6.2.5 Summary

Based on the results and comparisons from the finite element simulations on beam R4-3 presented in the sub-sections above, the following findings and conclusions were reached:

i) The influence of concrete material model definition (plastic vs. elastic) on transfer length is small. Since transfer length is not the primary investigation in the evaluation of full-size beams, it is considered feasible to use the calibrated friction coefficient (determined using a nonlinear concrete model) in the analysis of full size box beams with an elastic concrete model.

ii) When using an elastic concrete model, the concrete region with maximum principal stresses close or greater than f_t approximately corresponds to the

damaged region that would be predicted if a plastic material model was used. As a result, it is considered feasible to investigate damage in the anchorage zones of full-size beam models using an elastic concrete definition by checking the region with high maximum principal stresses.

iii) The maximum principal strains within the damaged region are predicted to be much higher if a plastic material definition is used in the numerical model. This implies that results from an elastic model are conservative with respect to the predicted tensile strains.

6.3 Modeling of 48-in. Wide AASHTO Box Beams

6.3.1 General

This section presents details on the finite element models used to evaluate the effect of strand debonding on the anchorage zones of full-size beams. The study is based on the simulation and study of one case study: a 48-in. wide skewed box beam built for a highway bridge in the state of Michigan. The beam suffered from concrete spalling during the manufacturing process, specifically, during the strand release process. The beam's large skew, its significant width and the large amount of debonded strand were suspect in the role that they may have had in causing the damage. Three 3D FE models were established in ABAQUS for the noted box beam, as discussed earlier in section 6.1.

6.3.2 Geometry, Reinforcement Details and Material Properties

The box beam section was 4 ft. x 3.25 ft., it had a total length of 117 ft. and a skew angle at both ends of 40^{o}. The beam was designed and built for a highway bridge owned by the Michigan Department of Transportation (MDOT). The cross-section geometry and reinforcement layout are shown in Figure 72.

Of particular importance is to notice the arrangement of debonded strand in the bottom flange of the section. It can be seen that 14 of 36 strands in the bottom flange were unbonded. Thus, the total number of unbonded strands was 38%. The percentage of debonded strand per row was: 24% in row 1 and 67% in row 2. Thus, the design exceeded the AASHTO limits for

debonded strand; that not more than 40% of the strands at any one horizontal row can be debonded, and that not more than 25% of the total strands can be debonded.

The distribution of shear reinforcement along the beam length is shown in Figure 73. Nominal elastic properties were assumed for the steel reinforcement, namely an elastic modulus of 29,000 ksi and a Poisson's ratio of 0.3. The concrete in the beam was specified in the beam manufacturing drawings to have a minimum compressive strength of 4,600 psi at prestress release. This value was used for the models, together with an assumed Poisson's ratio of 0.2.

The effect of the end blocks and intermediate diaphragms were not considered to significantly affect the stress transfer at the beam end and were thus not modeled. Neither were small geometric details such top flange depressions used for connections and the chamfer at the bottom flange corners. Reinforcement for composite connection to the slab was also ignored.

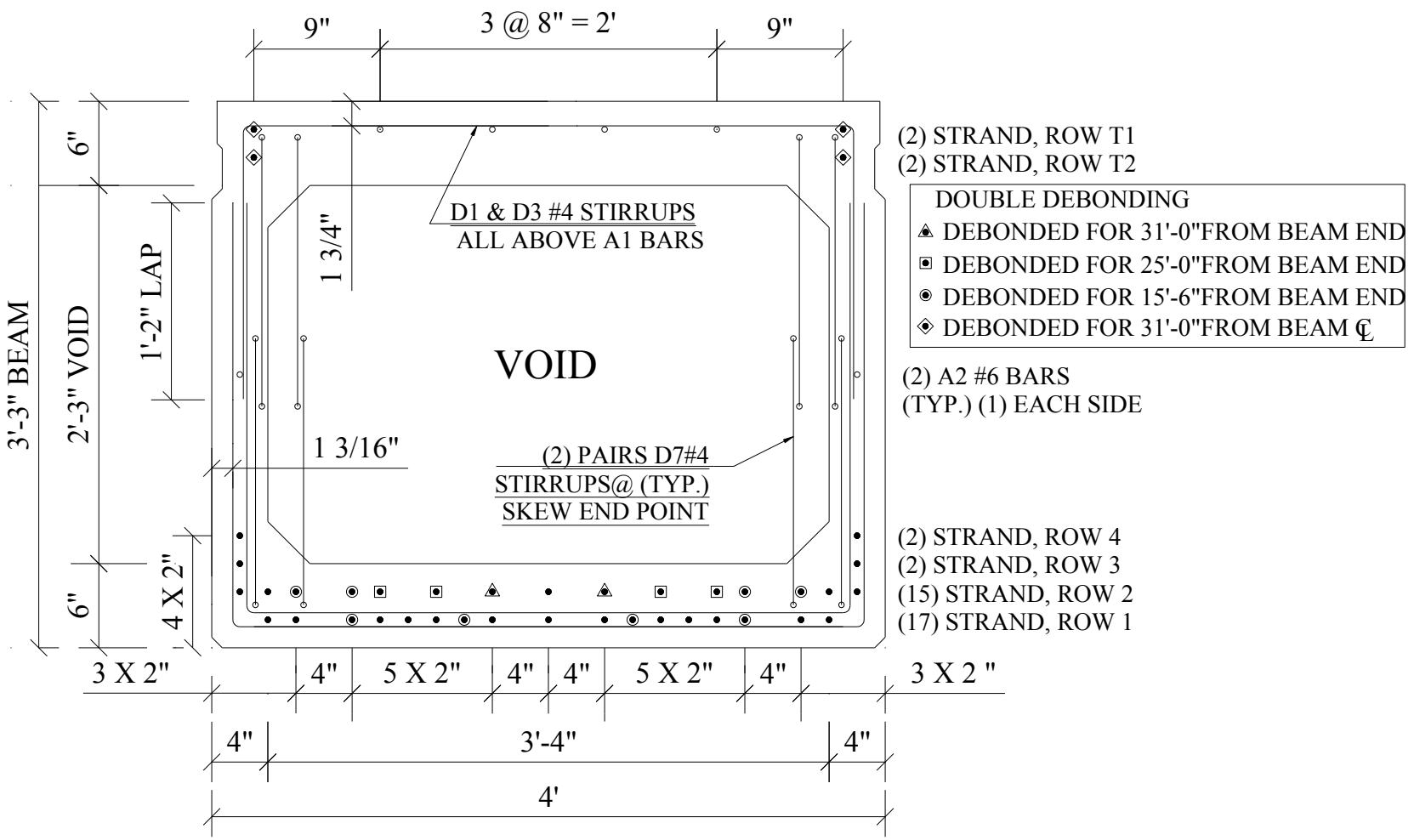

TYPICAL INTERIOR BEAM CROSS SECTION

Figure 72 Cross Section of 48-in. Wide AASHTO Box Beam

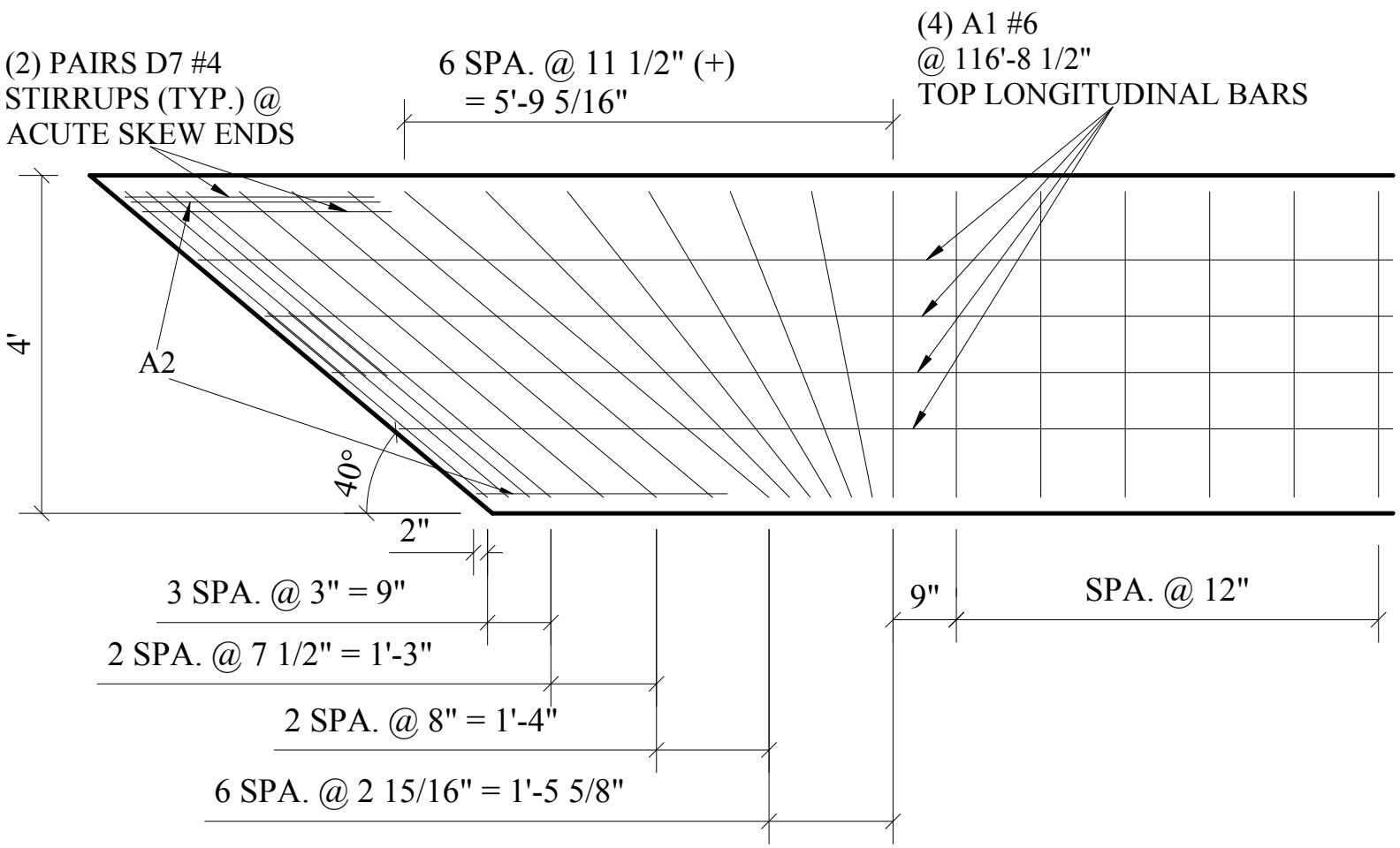

PLAN VIEW OF BEAM

Figure 73 Shear Reinforcement of 48-in. Wide AASHTO Box Beam

6.3.3 Model Geometry and Mesh

The cross-section used for the FE models was simplified to improve computational efficiency. The cross section in the FE models was assumed to be a hollow rectangular cross-section with outside dimensions of 4 ft. x 3 ft.-3 in. and inside dimension is 3 ft.-4 in. x 2 ft.-3 in.. The beam is longitudinal symmetric about the mid-section; thus, only half the length was simulated.

To reduce computational demand, solid elements were only used for part of the girder of interest, which is a rectangle at the corner of the cross-section with dimensions of 22 in. x 6 in.. The remaining part of the concrete in the section was simulated using shell elements with a thickness of 4 in. and 6 in. for the vertical and horizontal sides of the box section, respectively (Figure 74). The length of the solid region was 35 ft.-10 in., which covered the longest debonded strand length. This defines what is called the '3D concrete region,' consisting of a bottom rectangular prism of dimensions: 22 in. x 6 in. x 35 ft.-10 in.. The entire beam section was simulated with shell elements beyond the length of solid elements region. Only the strands within the 3D concrete region were simulated with solid elements, while truss elements were used for the rest of the strands.

Friction bond behavior was simulated for the 3D strands in the 3D concrete region. Strands simulated with truss elements were not defined within their respective debonded length. Thus, strand in the beam region with shell elements were only modeled during their fully bonded length. Further, these strands (truss elements) were assumed to be perfectly bonded to the concrete through the element embedding option in ABAQUS [28].

Simulation of strand debonding with flexible sheathing for the solid strands was realized using the same approach as in the small-scale beam models, which is to use a zero friction coefficient while assuming that the debonded strands have a perfect fit inside the concrete. On the other hand, oversized holes were created in the concrete part around debonded strands in the debonded region for the model in which strands were simulated to be debonded with rigid sheathing. For the strands using truss elements, debonding was simulated by simply having the debonded strand modeled only from the start of its full bond condition. In other words, no prestress transfer within the debonded region was modeled between concrete (modeled with shell elements) and the strands modeled with truss-elements.

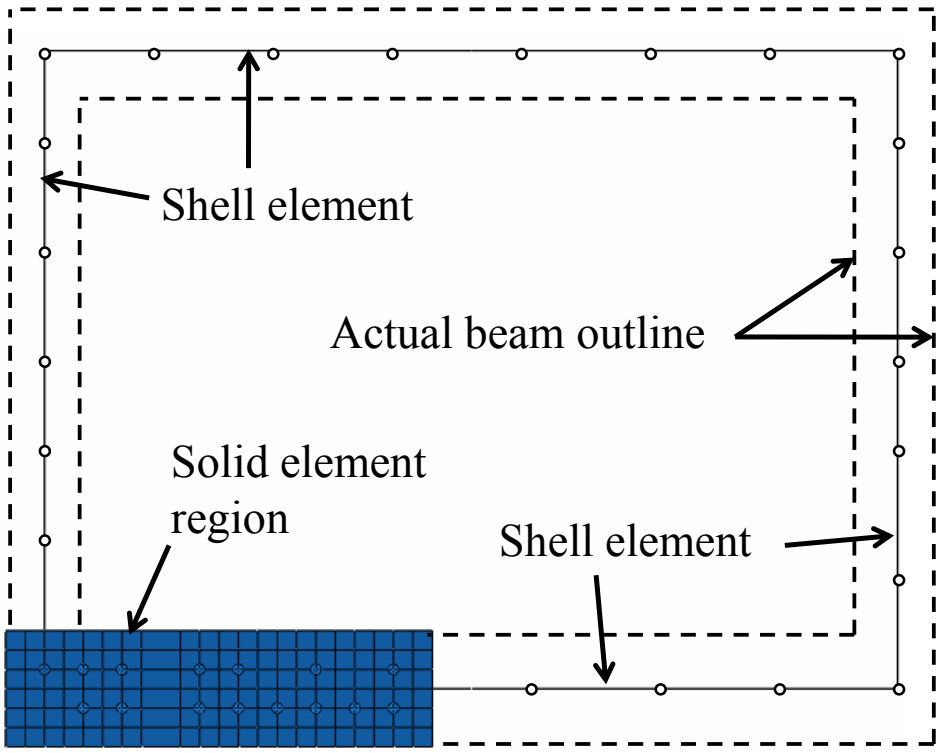

Figure 74 Simplified Cross Section of Box Girder in ABAQUS

6.3.4 Passive Reinforcement Definition

The steel reinforcement in the box beam was defined according to the manufacturing drawings. Reinforcement in the solid region was simulated using truss elements (see Figure 75). Perfect bond was assumed between reinforcement and concrete using the ABAQUS element embedding option. Passive reinforcement in regions other than the 3D concrete region was simulated using a 'rebar layer' in the shell elements, which is a modeling option in ABAQUS that allows definition of internal discrete reinforcement that is then smeared within the element for analysis purposes.

Figure 75 Top View of Discretized Shear Reinforcement in Box Girder FE Model

6.3.5 Interaction and Constraint Definitions

The interaction at the interface between concrete and strands in the 3D solid region of the box beam models was similar with that in the small-scale beam units, which is a non-linear friction model. Two overall friction coefficients were proposed in 5.10.4 based on the calibrated friction coefficients for each small-scale beam for sudden and annealed release. The plant that manufactured the box beam for this study uses flame cutting in their practice for strand de-tensioning. As discussed in Chapter 4 this leads to a sudden release of the prestressing force. Thus, the friction coefficient calibrated based on beam units with a sudden release method was adopted for the box beam models.

Table 27 Interaction and Constrains in Box Girder Models

Part A	Part B	Interaction/Constraint
Concrete (Solid)	Strand (Solid)	Surface to Surface Contact with a non-linear Friction Model
Concrete (Solid)	Concrete (Shell)	Shell to Solid Coupling
Concrete (Solid)	Strand (Truss)	Embedded Region
Concrete (Shell)	Strand (Truss)	Tie
Strand (Solid)	Strand (Truss)	Coupling
Concrete (Solid)	Reinforcement (Truss)	Embedded Region

In addition to the surface-to-surface interaction between solid strand and solid concrete, additional constraints were required in the box beam model since different elements were used for different parts of the model. The interaction/constraint definitions used between the different parts in the box beam models is shown in Table 27 in which “Part A” and “Part B” are two parts that need to be connected using certain interaction or constraint.

6.3.6 Boundary Conditions

As previously discussed, only half the beam length was modeled by considering longitudinal symmetric. As a result, boundary conditions to represent longitudinal symmetry were applied at the beam mid-section, see Figure 76. In addition, a translational constraint in the transverse direction of the beam (X’ direction in Figure 76) was prescribed to point A to restrain

rigid body motion in this direction. Vertical constrain was applied to the bottom edge of the box beam model.

The strands using solid elements were not constrained by any boundary conditions. As a result, the release and prestress transfer actions of all strands started simultaneously at the start of the analysis. Thus, sequential strand release operation was not simulated.

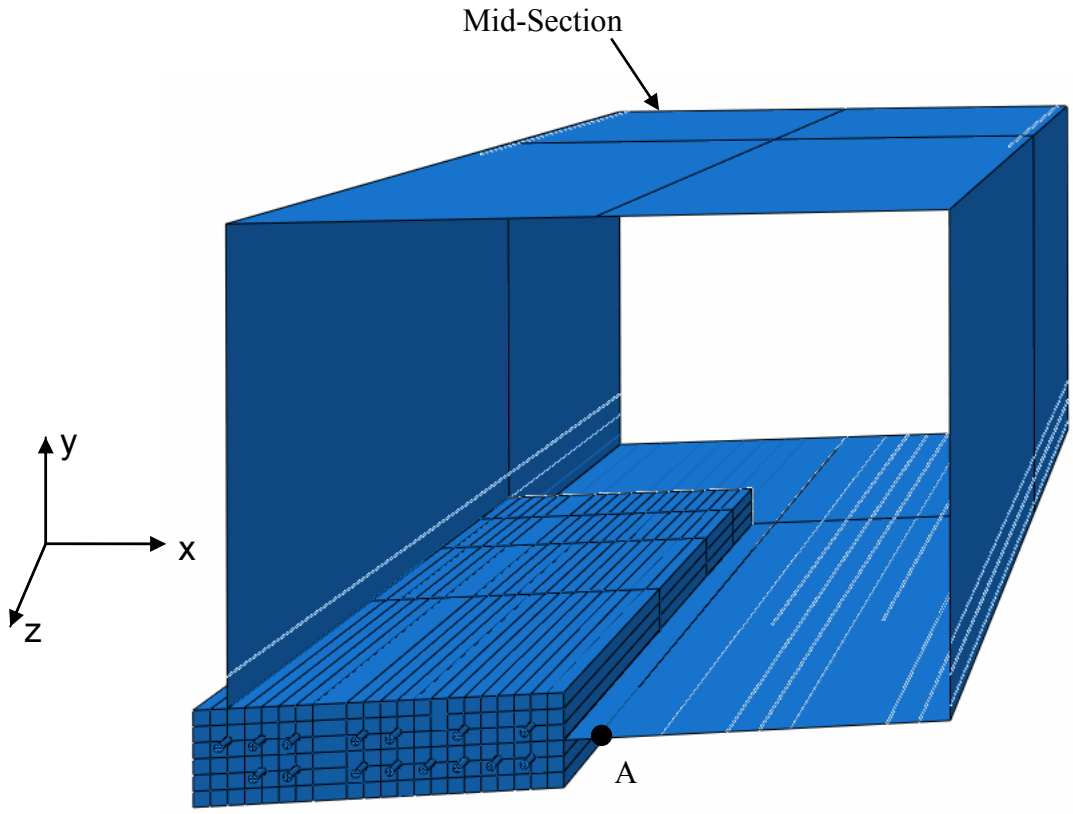

Figure 76 Boundary Condition of Box Girder Model

6.3.7 Prestressing Force

As with the small-scale beam models, an element 'initial stress' condition was used to simulate the prestressing force in the strands for the box beam models. A stress level of 75% f_{pu} was assumed as the initial stress in the strands immediately prior to transfer, which for the 0.6-in. diameter strand is equal to 202.5 ksi.

6.4 Analysis of Results

Since the concrete material in the box beam models was assumed to be elastic, the models are not able to indicate the region of possible cracking directly (region with plastic strain), as it was done for the small-scale beam models. However, the contours of maximum principal stress near the beam end region were checked. And, as discussed for the results from the small-scale beams, the maximum stress is basically the greatest tensile stress and cracks are expected to initiate at the location where the tensile stresses exceed the concrete's tensile strength.

As presented in Section 6.2, when using an elastic concrete material model, the possible cracking region can be assessed by defining an upper limit in the contour plots of maximum principal stresses. The upper limit was defined to be f_t, which was determined by:

$$f_t = 7.5\sqrt{4600\,psi} = 508\,psi \qquad \textbf{(Equation 6-1)}$$

Contours plots of the maximum principal stresses in the 3D solid concrete regions of the three box beam models are shown in Figure 77 and Figure 78. In these contours, the region with maximum principal stresses beyond the upper limit (508 psi) is indicated by a grey color and damage, i.e., cracking, may be assumed to take place in these regions.

From Figure 77 we can see that in all three cases, the concrete region above the top strand layer (Region A) is highly stressed in tension close to the girder end and that the skew beam model with flexible sheathing has a larger area under high tensile stresses compared to the other two models. These results may be affected from the fact that the end-block diaphragm was not modeled and thus there is no confinement above the top strand layer in the bottom flange and more strands in the top layer are debonded. It could be argued that the end-block diaphragm will provide confinement and reduce the tensile stresses in Region A. A high tensile stress region attributed to the boundary conditions can also be observed close to the bottom corner (Region B) in all models. This effect is real and is created by the cambering of the beam upon prestress release. However, in production practice a compliant layer or a sole plate is typically provided at such corners and edges to minimize such damage. Thus, for the purposes of studying the anchorage stress state and possible damage in this case study, the stress state in Region B is considered to be overestimated.

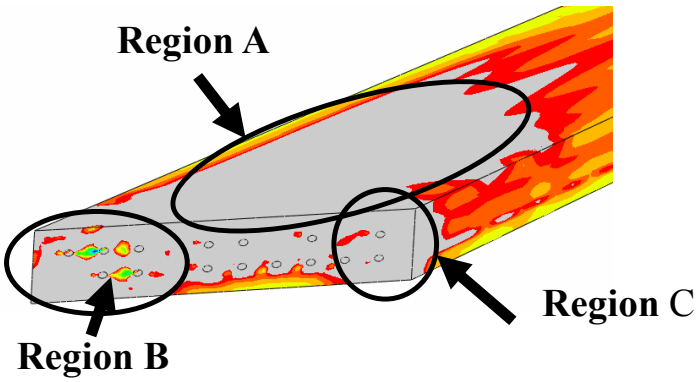

(a) Skew Box Beam with Flexible Sheathing

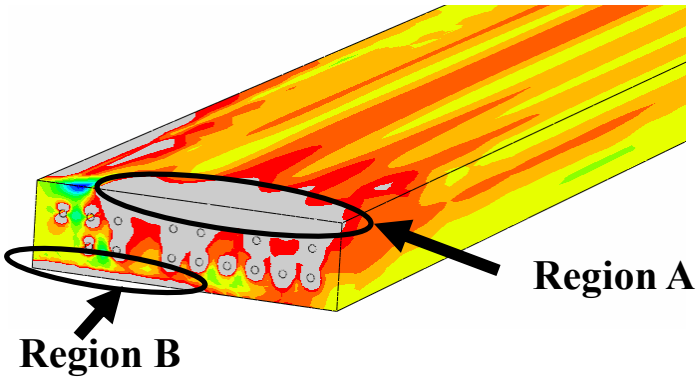

(b) Straight Box Beam with Flexible Sheathing

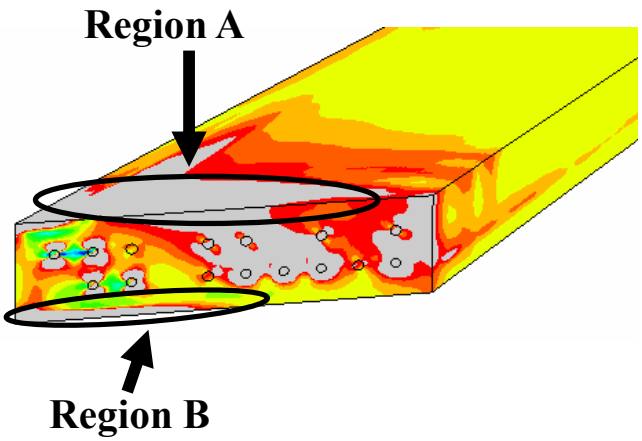

(c) Skew Box Beam with Rigid Sheathing

Figure 77 Maximum Principal Stresses for Bottom Corner of Box Girder Models (View 1)

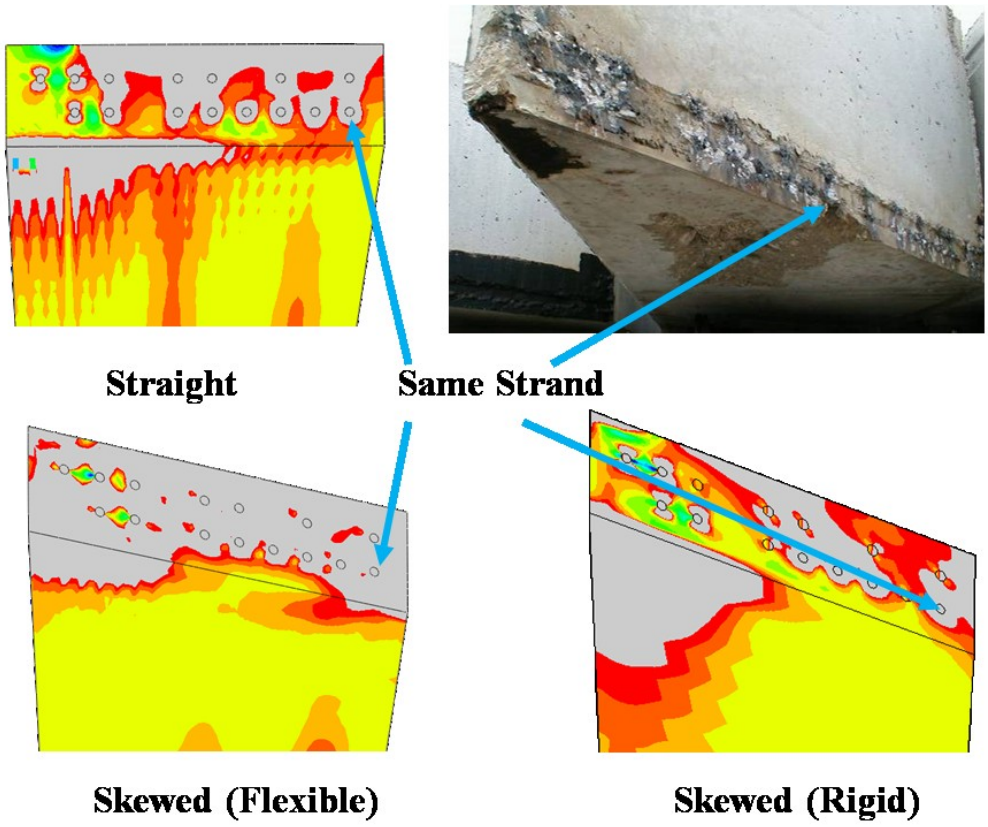

Figure 78 Maximum Principal Stresses for Bottom Corner of Box Girder Models (View 2)

In the right corner of the 3D solid concrete part (Region C), which is the center region of the bottom flange of the box beam, the skewed box girder model with flexible sheathing displays much higher tensile stresses compared to the other two beam models. Stress contours on the bottom surface of both models and a picture of the actual cracked skewed box girder are shown in Figure 78. It can be seen that concrete spalling in the real (skewed) girder happened close to Region C as predicted by the FE model. However, the spalling region is much larger in the actual box girder. The extent of the damage region predicted by the FE model was probably limited by use of the elastic material model, which, as shown in Section 6.2, will underestimate inelastic strains and damage growth due to the inability to redistribute stresses. Secondly, it should be noted that results for the straight beam model do not indicate the presence of concrete cracking near the same region. Thus, the skew geometry had a strong effect in the spalling problem experienced in the actual box girder considered in this study. However, once the dilation effect of strand in the debonded region is eliminated (i.e., in the skew box model with rigid sheathing), the overall tensile stress level at the beam end is significantly reduced. The damage close to

Region C in the model with flexible sheathing is not observed in the case with rigid sheathing simulation.

Based on the comparison between the box beam models it can be argued that the high tensile stresses are created by the internal concrete pressure due to the expansion of the strands blanketed (debonded) with soft material. And such phenomenon can be aggravated and lead to damage if the box beam has a skew geometry. Thus, the source of damage in the real girder seems to have been caused by the combined negative effects produced by debonded strands with soft material and a large skew beam angle.

6.5 Summary

Based on the discussion in results and discussion provided in the previous sections, the following findings and conclusions were obtained:

i) By modeling strand using solid elements, the skewed box girder model with flexible sheathing was able to predict damaged regions similar to those observed in the actual production of the box beam in the case study;

ii) Based on the comparison of the two skewed box beam models with different sheathing simulation, it was found that the damage at the end of box beam is caused by the high tensile stress created by the internal pressure due to the dilation of strand debonded with flexible material.

iii) In straight box beams, the damage due to dilation of debonded strand is localized and limited. However, such damage can be aggravated and lead to damage at the concrete surface by large skew geometry.

iv) Rigid sheathing, which allows the strand to dilate freely, has been proved to be a efficient approach to reduce the damage at the end of pre-tensioned box beams. And it is especially beneficial when box beams have large skew geometries, in which case the damage caused by the dilation of debonded strand is aggravated.

Chapter 7 Findings and Conclusions

7.1 Relevant Findings

Based on the results and discussions presented in this report, the following relevant findings are presented:

1. Confinement as provided by tightly spaced transverse reinforcement or spirals seems to improve the bond strength between strand and concrete (~18% based on experiment data).
2. Compared to annealed release, sudden release will lead to longer transfer length (~58% based on experiment data).
3. In general, transfer lengths in beam units with rigid debonding material were longer than in beam units with soft debonding material (~49% based on experiment data).
4. In beam units with multiple strands, debonded beam units with rigid material had longer transfer lengths compared to those with fully bonded strands. (16% based on experiment data).
5. Based on the cylinder pull-out tests, the bond strength of cylinder debonded with split-sheathing is considerably small (<4%) compared to the fully bonded case.
6. If strand is ideally debonded and there is enough room around the strand for its dilation, the stress level in the debonded region can be reduced.
7. If concrete and strand has a tight contact, the internal pressure on surrounding concrete due to the expansion may be significantly high through the whole debonded region.
8. Cracking around adjacent strands can propagate towards each other and may interact adversely.

7.2 Conclusions

The following conclusions are provided based on the experimental and numerical studies presented in this report:

1. Strand 'blanketing' with flexible sheathing is an effective way to debond it from concrete and its *pure bond strength* in an *unstressed* condition is essentially zero compared to a strand directly bonded to concrete.
2. Pre-tensioned debonded strand with flexible sheathing, as used for prestressed concrete, can transfer stresses due to mechanical interlock, and Poisson's (i.e., Hoyer's) effect.

a. The level of stress transfer is much smaller than that of a fully bonded strand.
b. Transfer lengths of debonded strand are less than those of fully bonded strands (measured from the onset of full bond condition).

3. Debonded strands with flexible sheathing can lead to cracking in concrete along the entire debonded length due to the radial expansion that it experiences as a consequence of the reduced bond strength.
    a. Damage can be more severe for adjacent debonded strands as the tensile stress states overlap.
    b. Damage is local and is only minimally affected by confinement or reinforcement.
4. Oversized rigid sheathing can avoid damage from the dilation of debonded strand.
    a. This debonding option will lead to larger transfer lengths, particularly for sudden release.
    b. This option could be beneficial in reducing vertical cracking due to increased strand free length.
5. Nonlinear finite element models were able to capture the phenomena of stress transfer from strand to concrete and provided reasonable evidence for the source of damage from debonded strand.
    a. The models also provided significant evidence to the importance of Hoyer's effect, a sometimes controversial bond mechanism.
    b. Yet, the fundamental mechanics of Hoyer's effect behind the transmission of bond by means of normal and shear stresses can also be debated.
6. Finite element models were able to capture the damage regions observed in full size beams in real conditions.
    a. Dilation from strand debonding with flexible sheathing was concluded to be the main source of damage.
    b. A large skew angle on a beam can aggravate the damage due to dilation from strand debonding with flexible sheathing.
    c. Use of rigid sheathing can significantly reduce the damage at the end of prestressed concrete beams, which is especially beneficial for wide skewed beams, such as the box beam studied in this research.

APPENDICES

APPENDIX A

LOCATION OF STRAIN GAGES IN SMALL PRESTRESSED CONCRETE BEAM UNITS FOR CONCRETE INTERNAL STRAIN MEASUREMENT (CISM)

Table 28 Strain Gage Location of C1 Beam Units

Strain Gage ID	Distance from Beam End (in.)					
	C1-1	C1-2	C1-3	C1-4	C1-5	C1-6
1	6	6	6	6	24	24
2	12	12	12	12	30	30
3	18	18	18	18	36	36
4	21	21	24	24	39	39
5	24	24	30	30	42	42
6	27	27	36	36	45	45
7	30	30	39	39	48	48
8	33	33	42	42	51	51
9	36	36	45	45	54	54
10	45	45	48	48	63	63
11	51	51	51	51	69	69
12	63	63	54	54	81	81
13			63	63		
14			69	69		
15			81			

Table 29 Strain Gage Location of R1 Beam Units

Strain Gage ID	Distance from Beam End (in.)					
	R1-1	R1-2	R1-3	R1-4	R1-5	R1-6
1	6	6	6	6	6	6
2	12	12	18	18	18	18
3	18	18	30	30	30	30
4	21	21	42	42	42	42
5	24	24	48	48	54	54
6	27	27	54	54	66	66
7	30	30	57	57	78	78
8	33	33	60	60	81	81
9	36	36	63	63	84	84
10	45	45	66	66	87	87
11	51	51	69	69	90	90
12	63	63	72	72	93	93
13			81	81	96	96
14			87	87	105	105
15			99	99	111	111

Table 30 Strain Gage Location of R2 Beam Units

Strain Gage ID	Distance from Beam End (in.)					
	R2-1	**R2-2**	**R2-3**	**R2-4**	**R2-5**	**R2-6**
1	6	9	6	6	6	6
2	12	24	12	12	18	18
3	18	30	18	18	30	30
4	21	36	21	21	42	42
5	24	39	24	24	48	54
6	27	42	27	27	54	66
7	30	45	30	30	57	78
8	33	48	33	33	60	81
9	36	51	36	36	63	84
10	45	54	45	45	66	87
11	51	63	51	51	69	90
12	63	69	63	63	72	93
13	75	81	75	75	81	96
14	87	93	87	87	87	105
15	99	105	99	99	99	111
16		117			111	123
17					123	132
18					132	138
19					138	

Table 31 Strain Gage Location of R4 Beam Units

Strain Gage ID	Distance from Beam End (in.)					
	R4-1	**R4-2**	**R4-3**	**R4-4**	**R4-5**	**R4-6**
1	6	6	6	6	6	6
2	12	12	18	18	18	18
3	18	18	30	30	30	30
4	21	24	42	42	42	42
5	24	30	48	54	48	54
6	27	36	54	66	54	66
7	30	39	57	78	57	78
8	33	42	60	81	60	81
9	36	45	63	84	63	84
10	45	48	66	87	66	87
11	51	51	69	90	69	90
12	63	54	72	93	72	93
13	75	63	81	96	81	96
14	87	69	87	105	87	105
15	99	81	99	111	99	111
16		93	111	123	111	123
17		105	123	132	123	132
18		117	132	138	132	138
19			138		138	

APPENDIX B

COMPARISON BETWEEN RESULTS FROM NUMERICAL MODEL AND CONCRETE INTERNAL STRAIN MEASUREMENT (CISM)

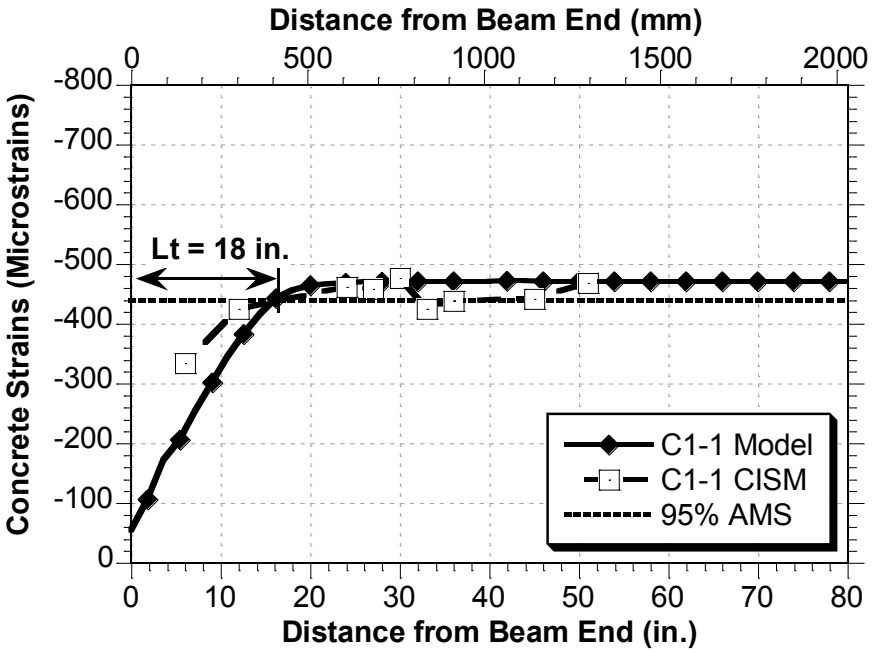

Figure 79 Comparison of Numerical Model and CISM Results of Beam Unit C1-1

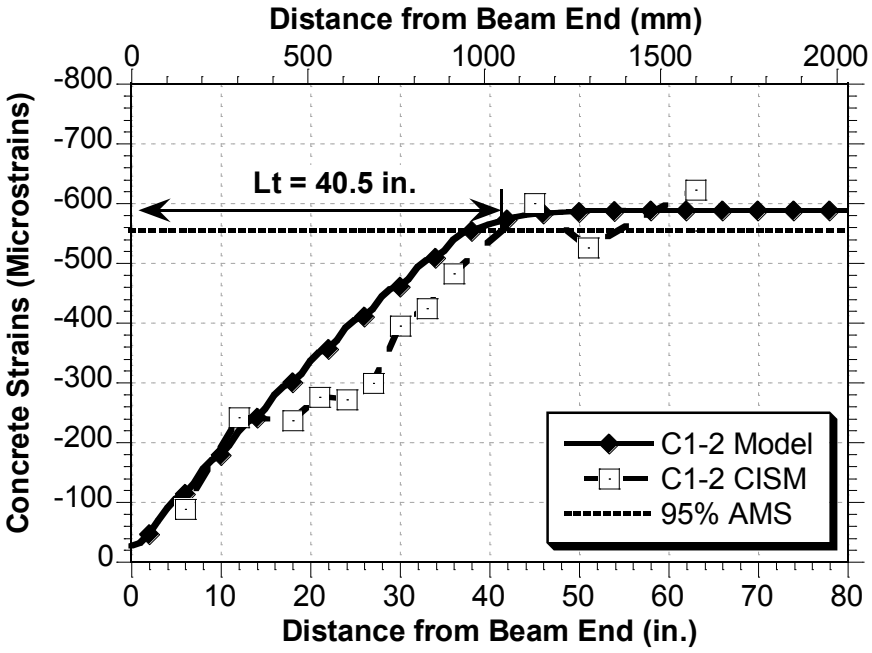

Figure 80 Comparison of Numerical Model and CISM Results of Beam Unit C1-2

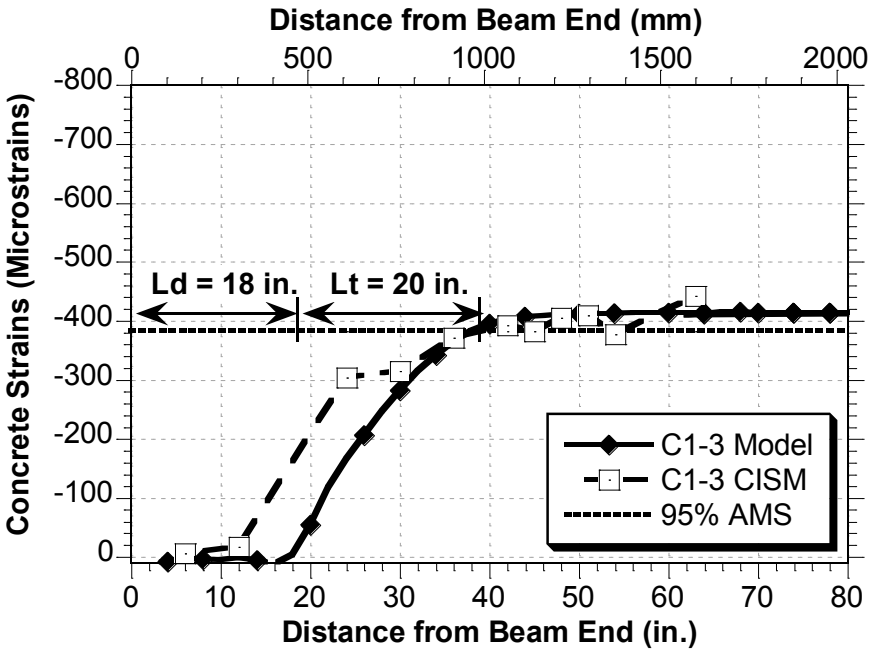

Figure 81 Comparison of Numerical Model and CISM Results of Beam Unit C1-3

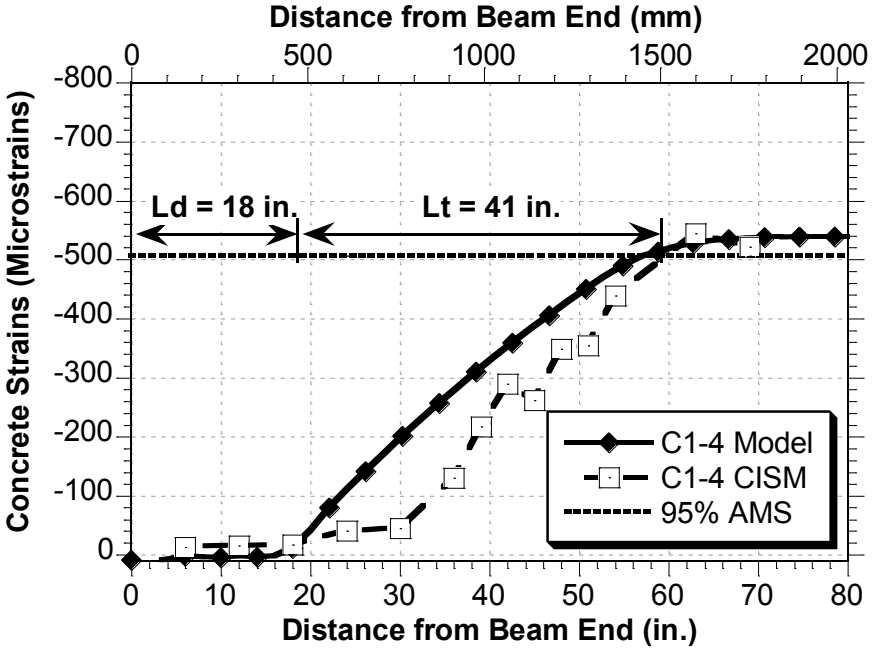

Figure 82 Comparison of Numerical Model and CISM Results of Beam Unit C1-4

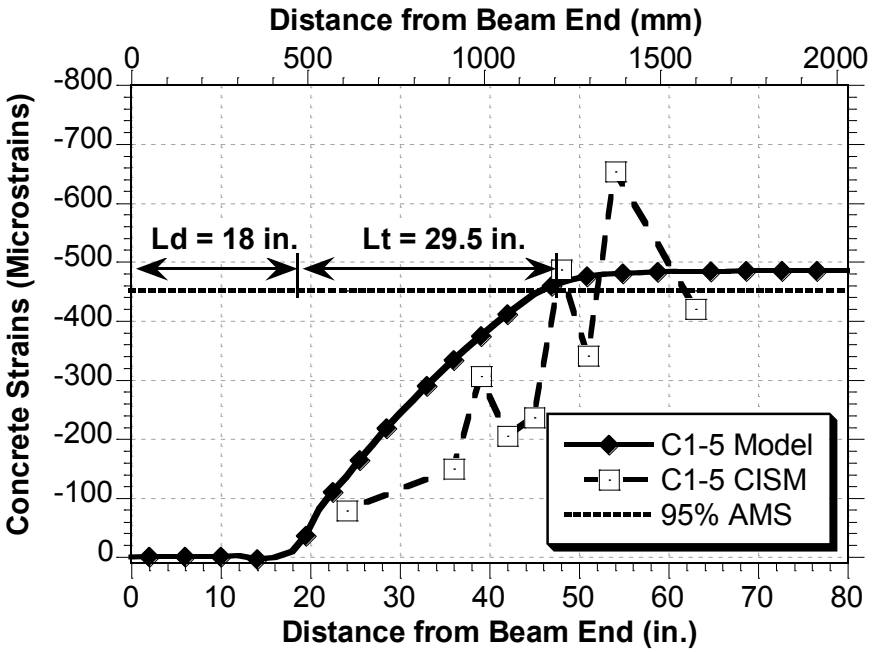

Figure 83 Comparison of Numerical Model and CISM Results of Beam Unit C1-5

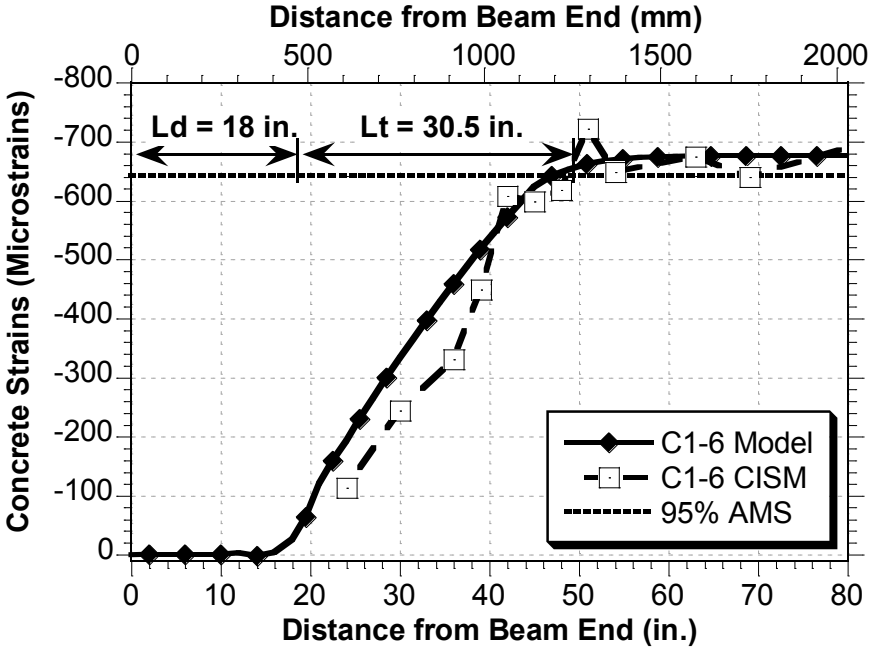

Figure 84 Comparison of Numerical Model and CISM Results of Beam Unit C1-6

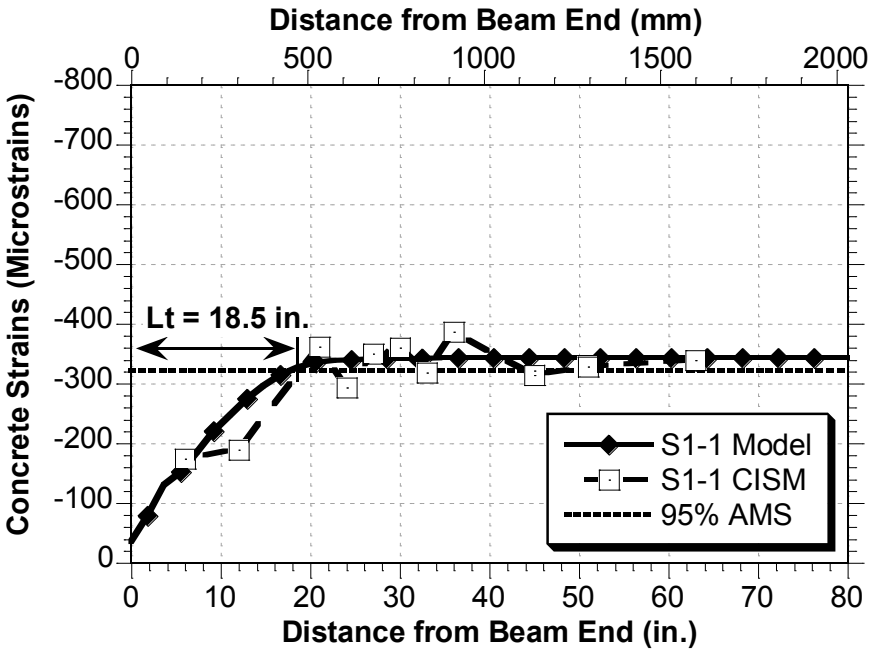

Figure 85 Comparison of Numerical Model and CISM Results of Beam Unit S1-1

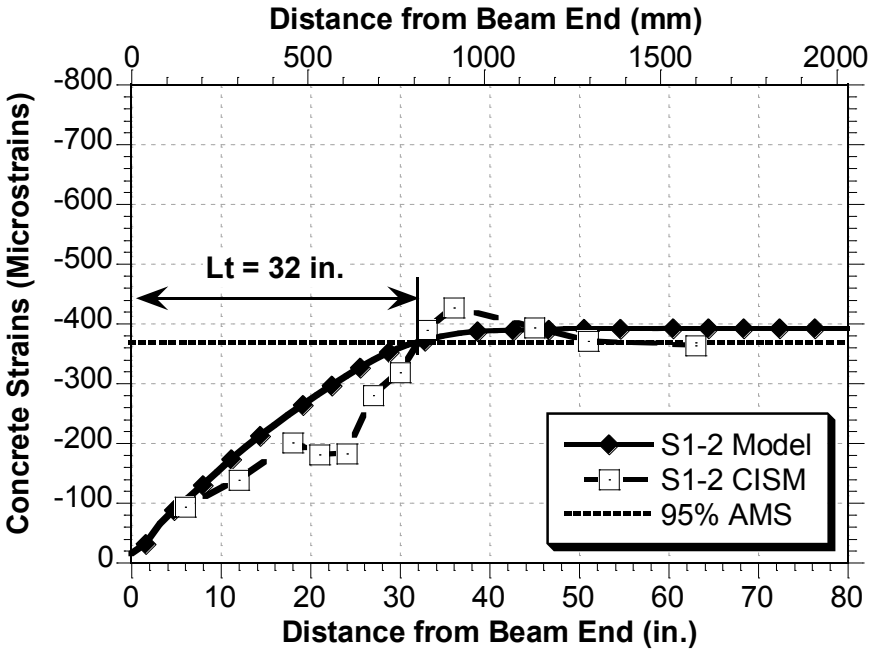

Figure 86 Comparison of Numerical Model and CISM Results of Beam Unit S1-2

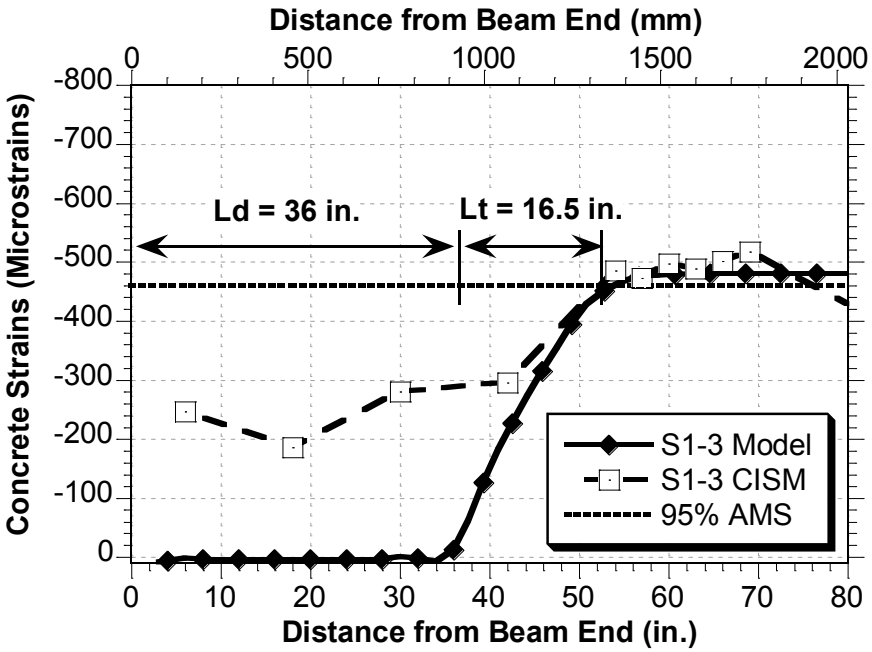

Figure 87 Comparison of Numerical Model and CISM Results of Beam Unit S1-3

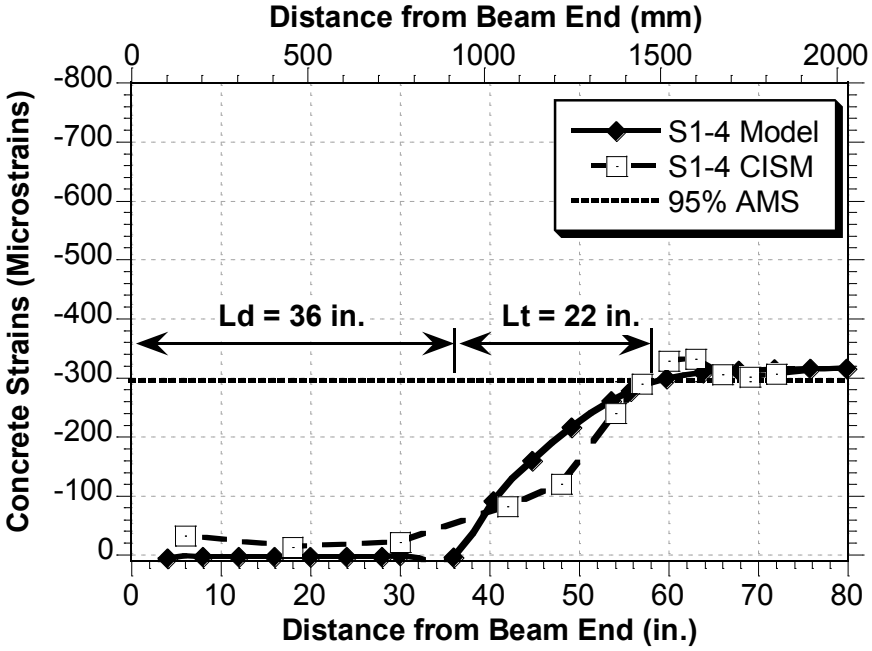

Figure 88 Comparison of Numerical Model and CISM Results of Beam Unit S1-4

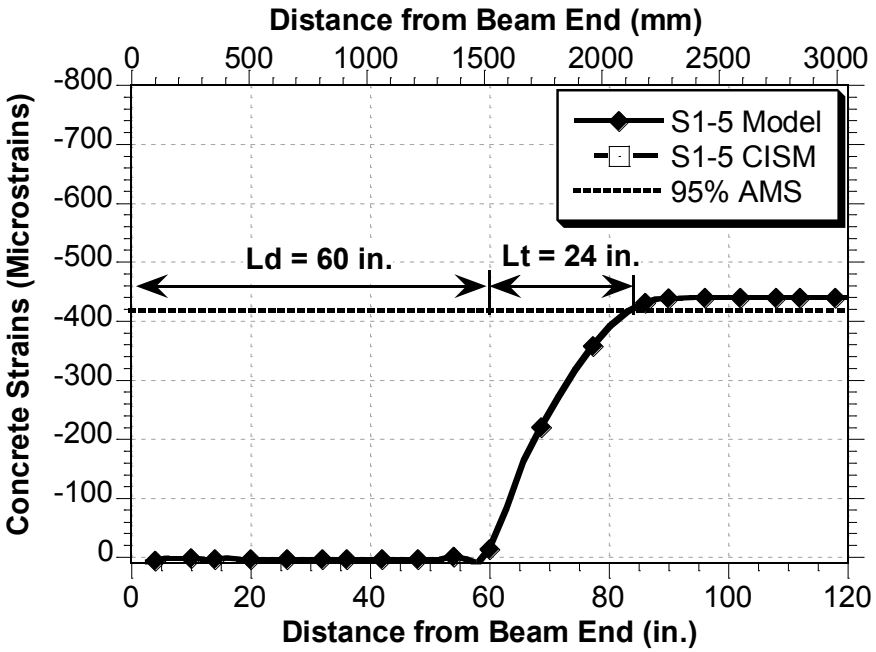

Figure 89 Comparison of Numerical Model and CISM Results of Beam Unit S1-5

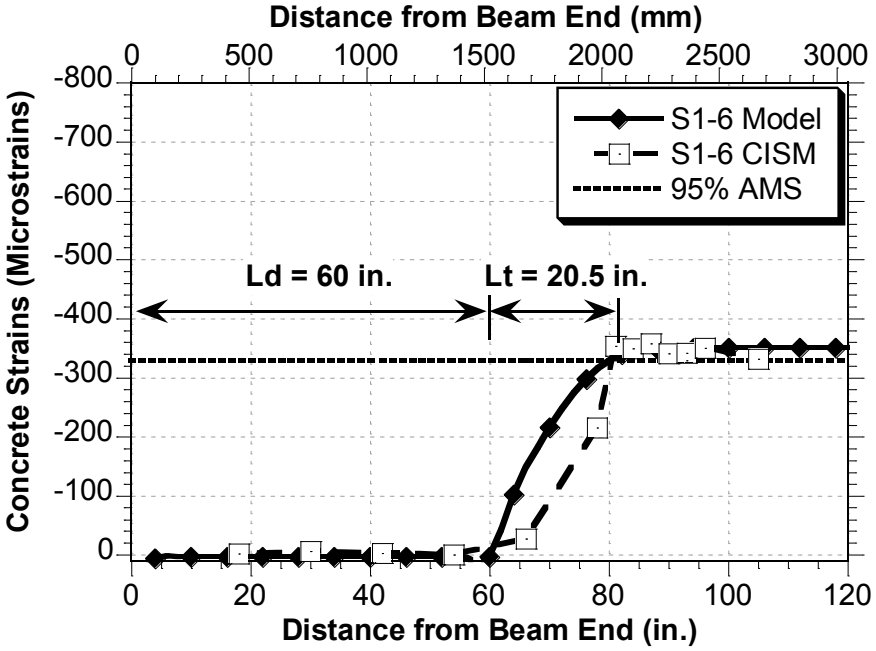

Figure 90 Comparison of Numerical Model and CISM Results of Beam Unit S1-6

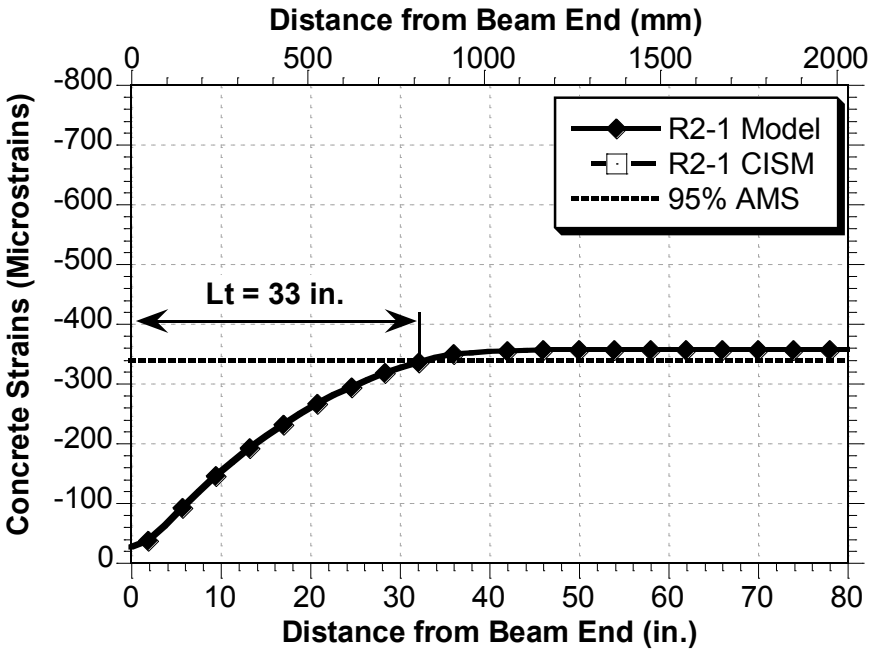

Figure 91 Comparison of Numerical Model and CISM Results of Beam Unit R2-1

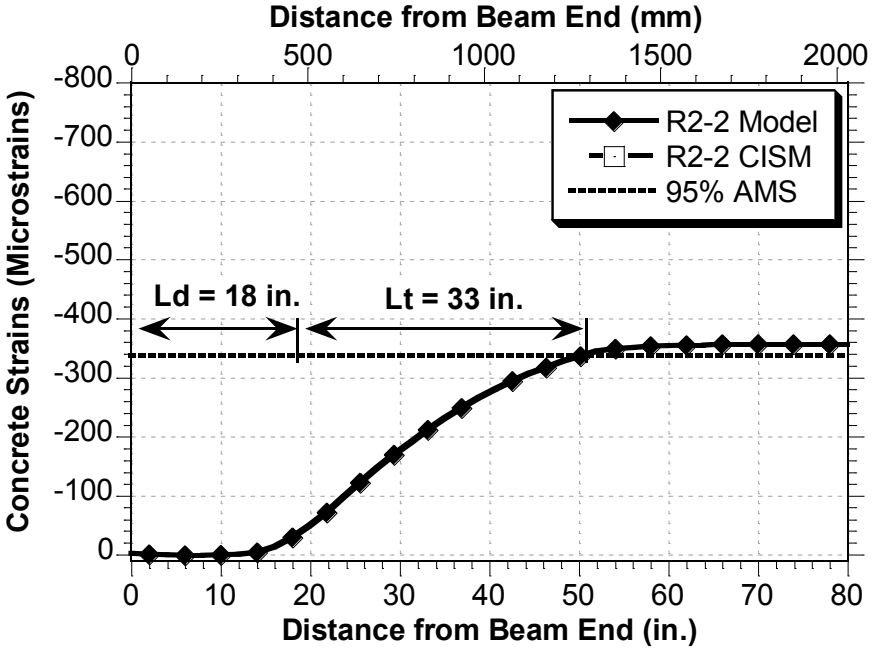

Figure 92 Comparison of Numerical Model and CISM Results of Beam Unit R2-2

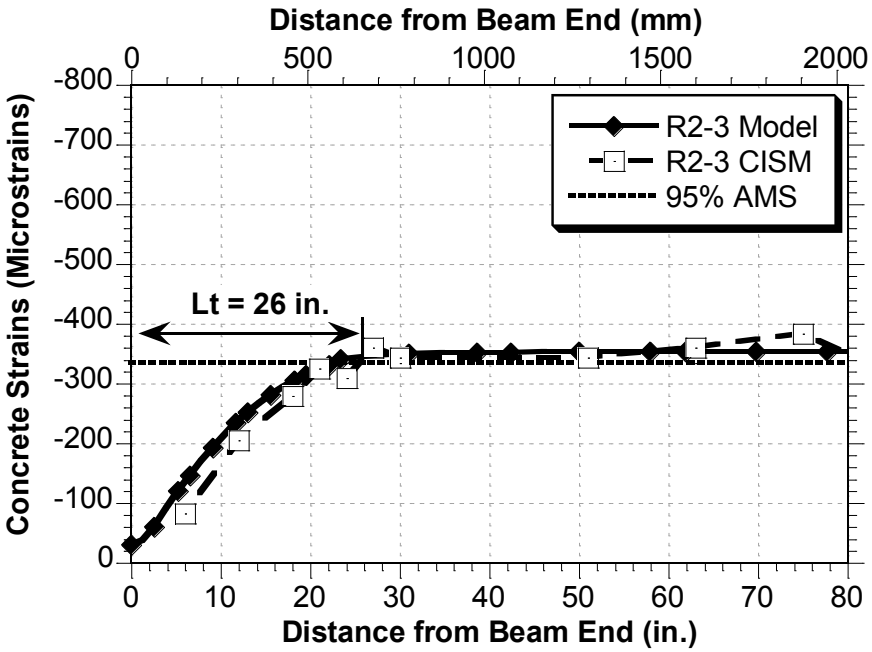

Figure 93 Comparison of Numerical Model and CISM Results of Beam Unit R2-3

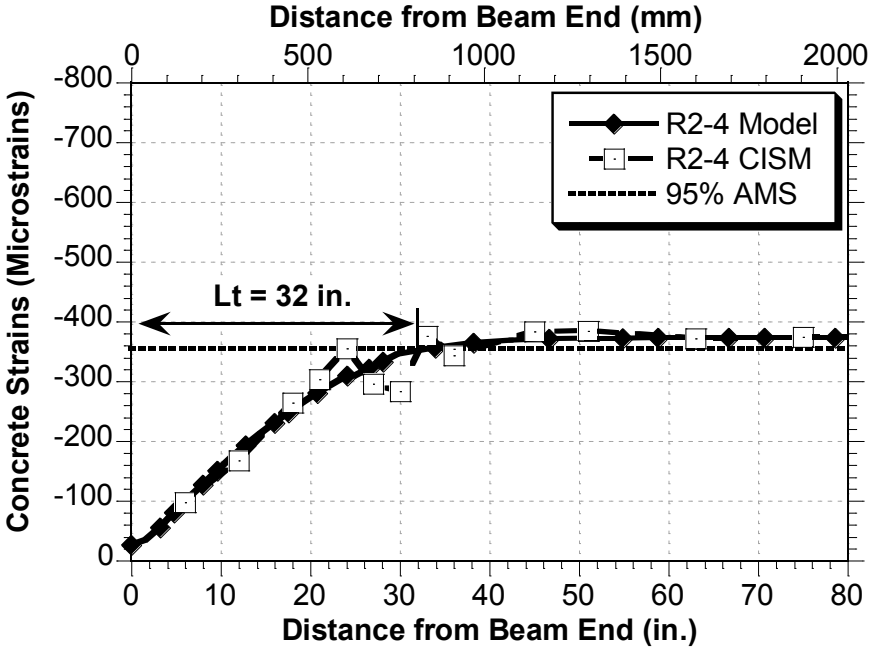

Figure 94 Comparison of Numerical Model and CISM Results of Beam Unit R2-4

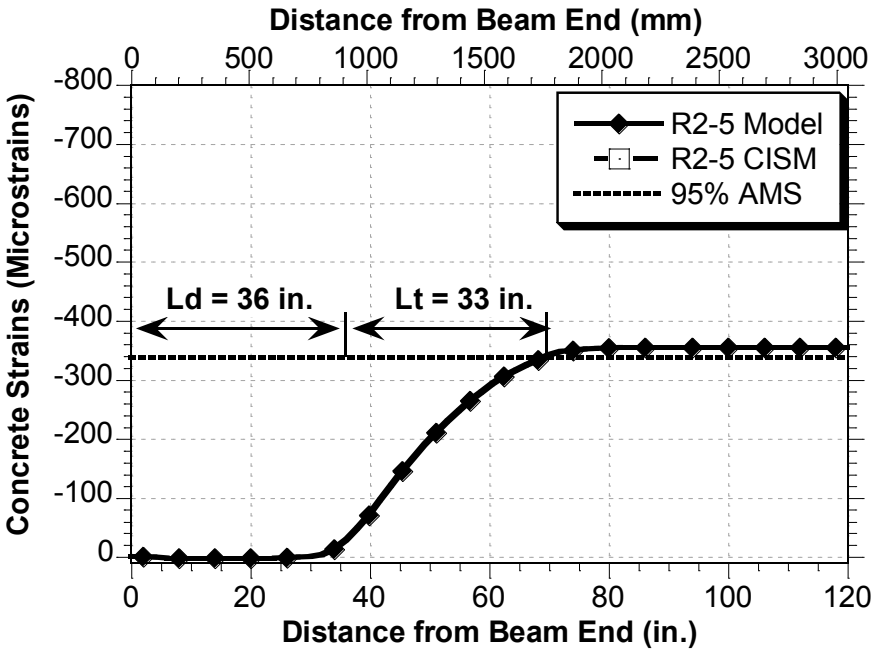

Figure 95 Comparison of Numerical Model and CISM Results of Beam Unit R2-5

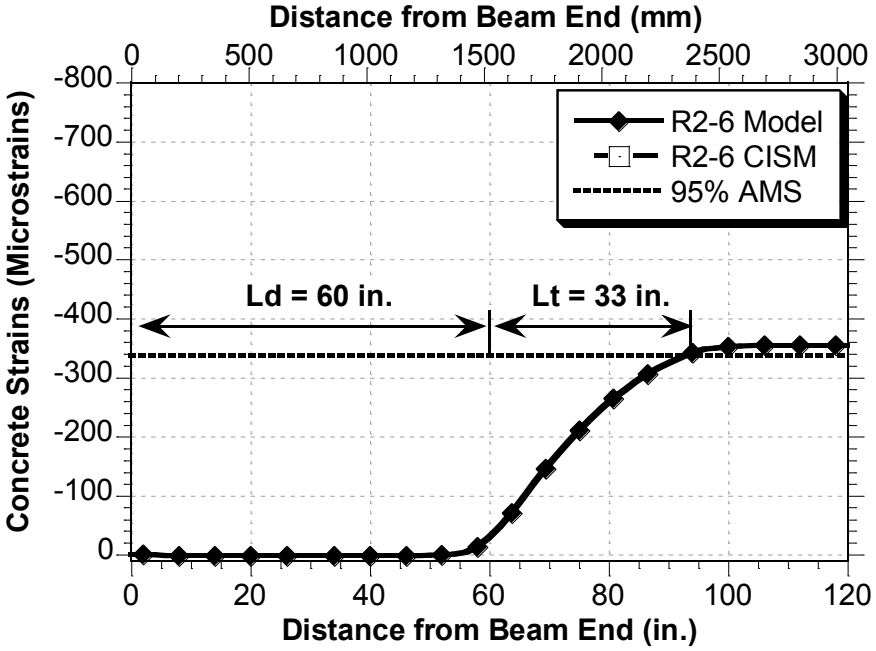

Figure 96 Comparison of Numerical Model and CISM Results of Beam Unit R2-6

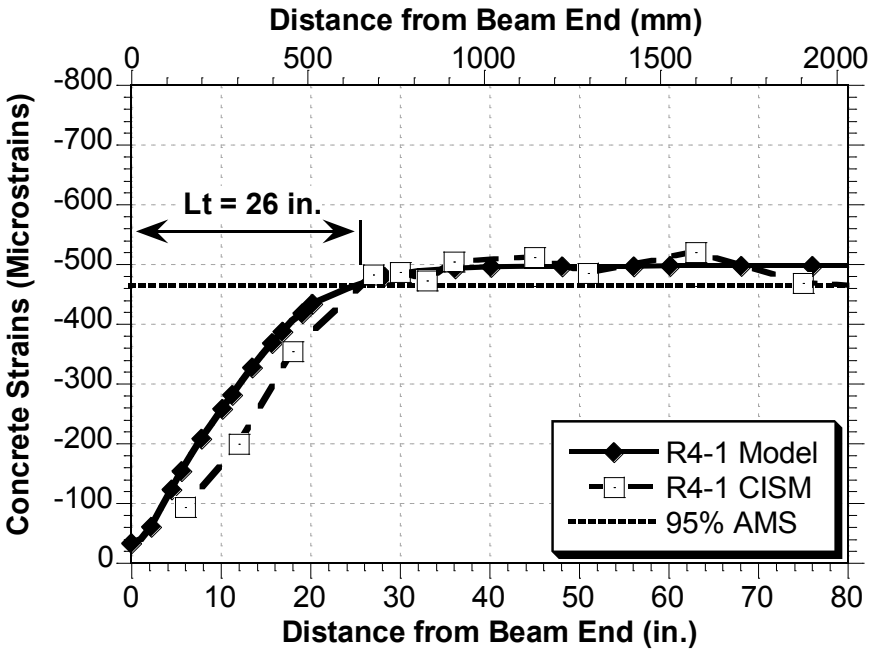

Figure 97 Comparison of Numerical Model and CISM Results of Beam Unit R4-1

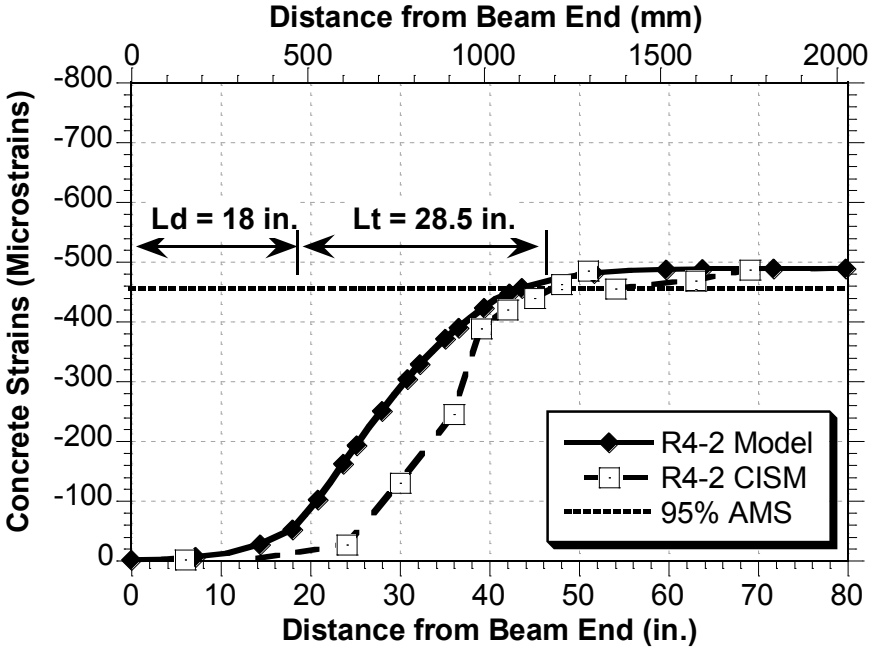

Figure 98 Comparison of Numerical Model and CISM Results of Beam Unit R4-2

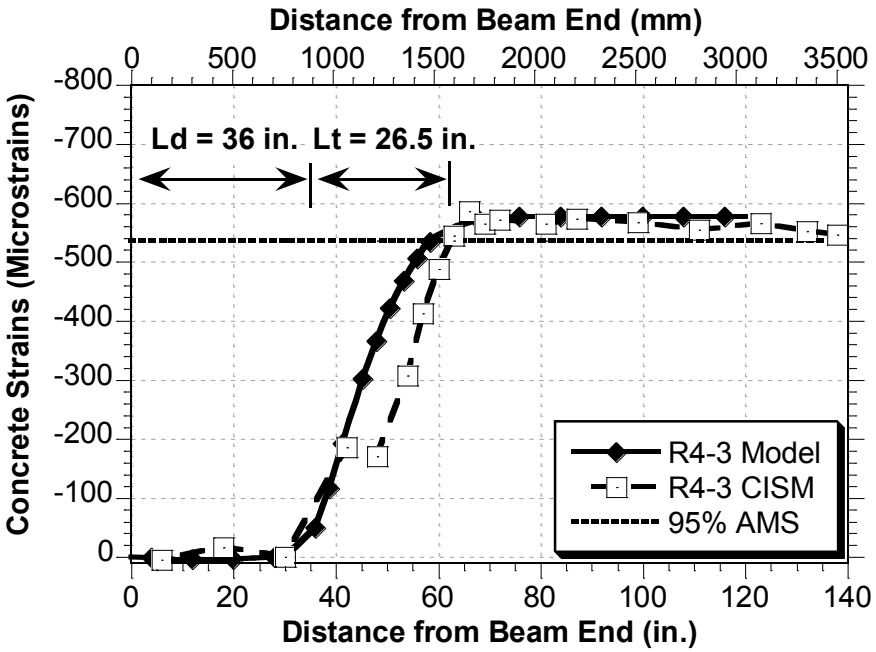

Figure 99 Comparison of Numerical Model and CISM Results of Beam Unit R4-3

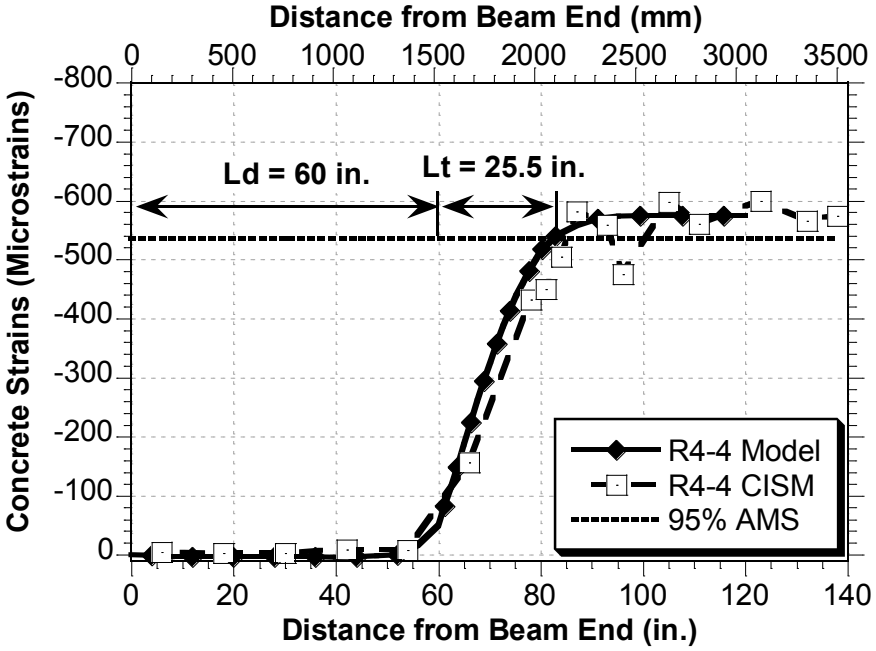

Figure 100 Comparison of Numerical Model and CISM Results of Beam Unit R4-4

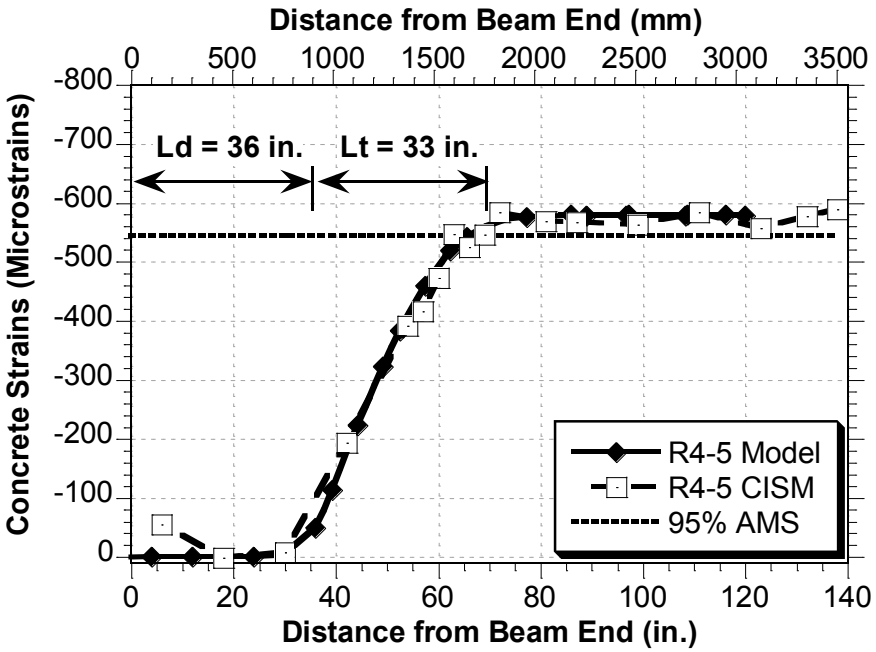

Figure 101 Comparison of Numerical Model and CISM Results of Beam Unit R4-5

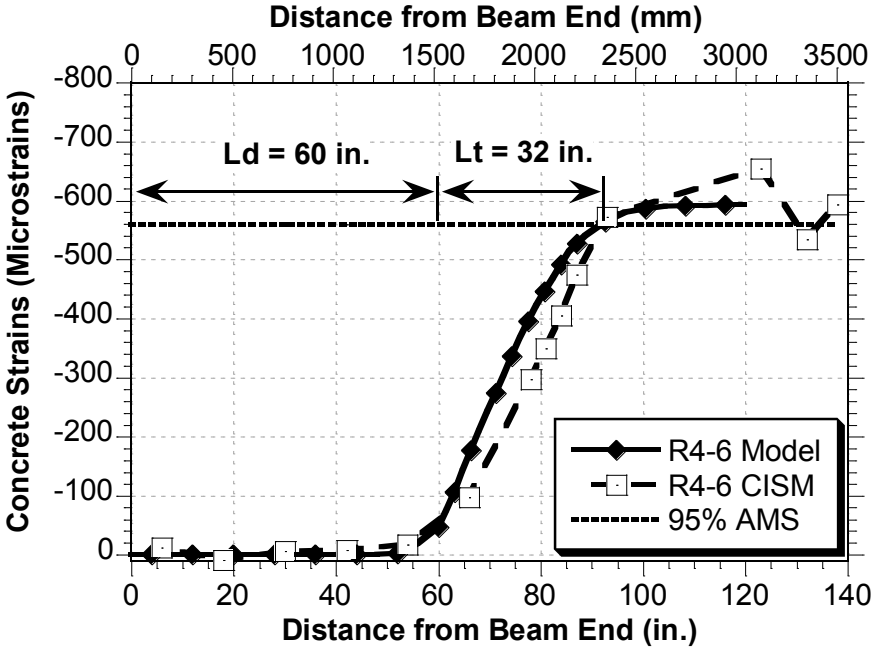

Figure 102 Comparison of Numerical Model and CISM Results of Beam Unit R4-6

APPENDIX C

RESULT OF CONCRETE SURFACE STRAIN MEASUREMENT (CSSM)

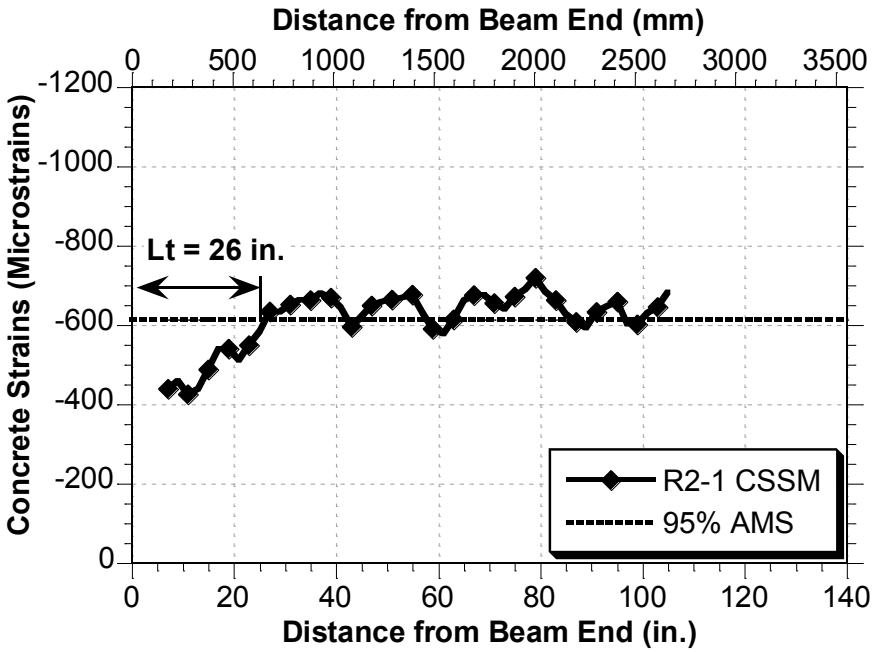

Figure 103 Results of CSSM of Beam Unit R2-1

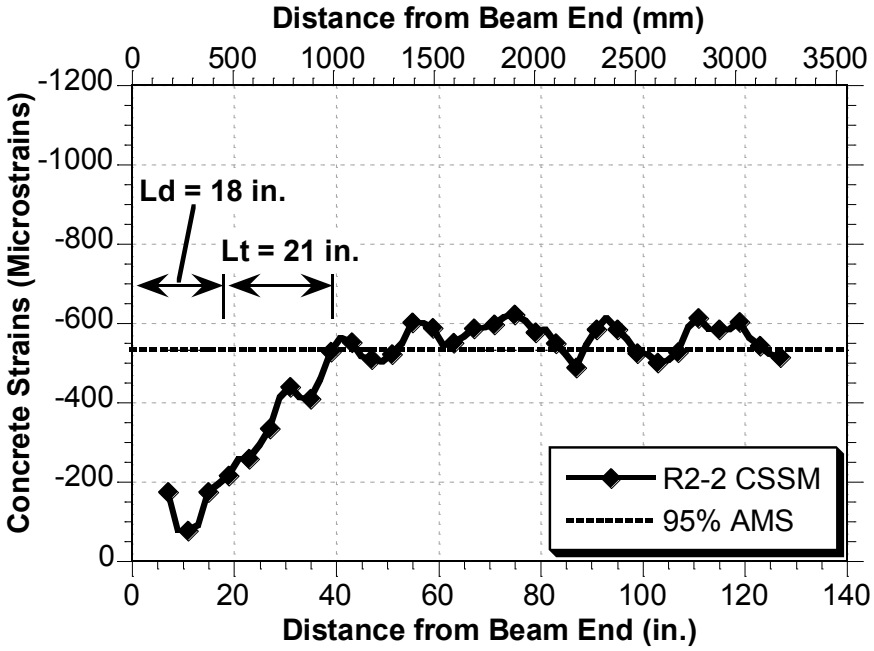

Figure 104 Results of CSSM of Beam Unit R2-2

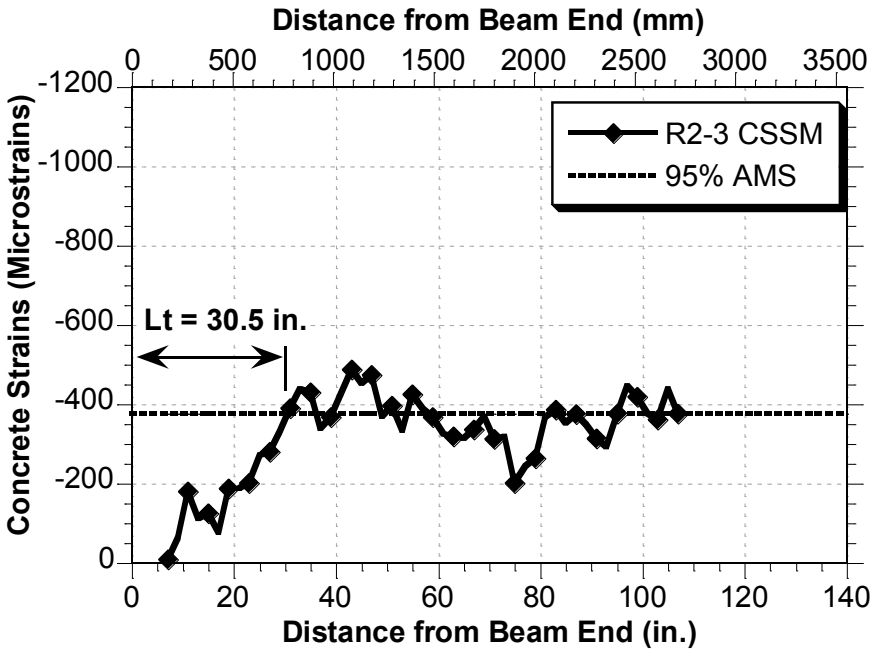

Figure 105 Results of CSSM of Beam Unit R2-3

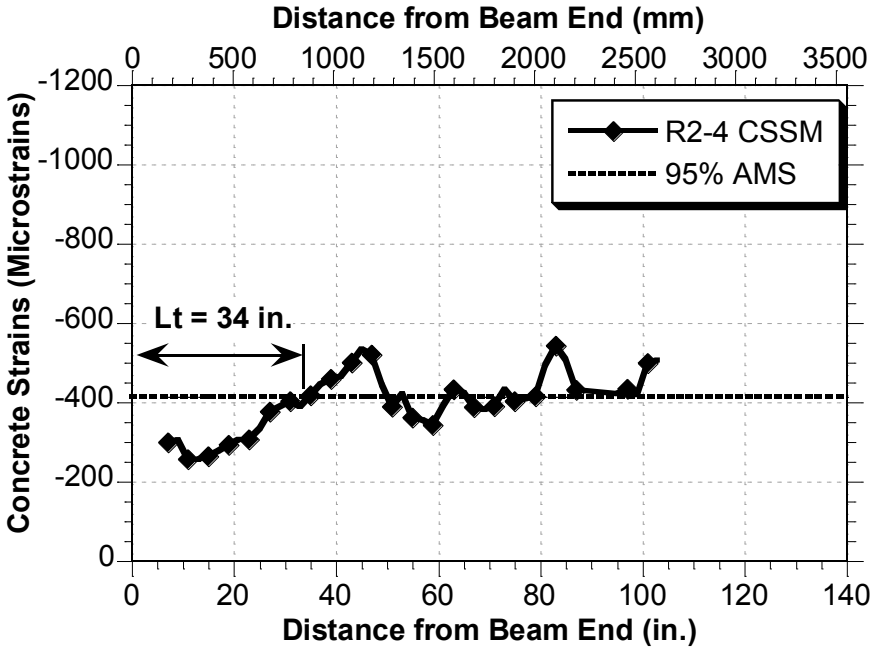

Figure 106 Results of CSSM of Beam Unit R2-4

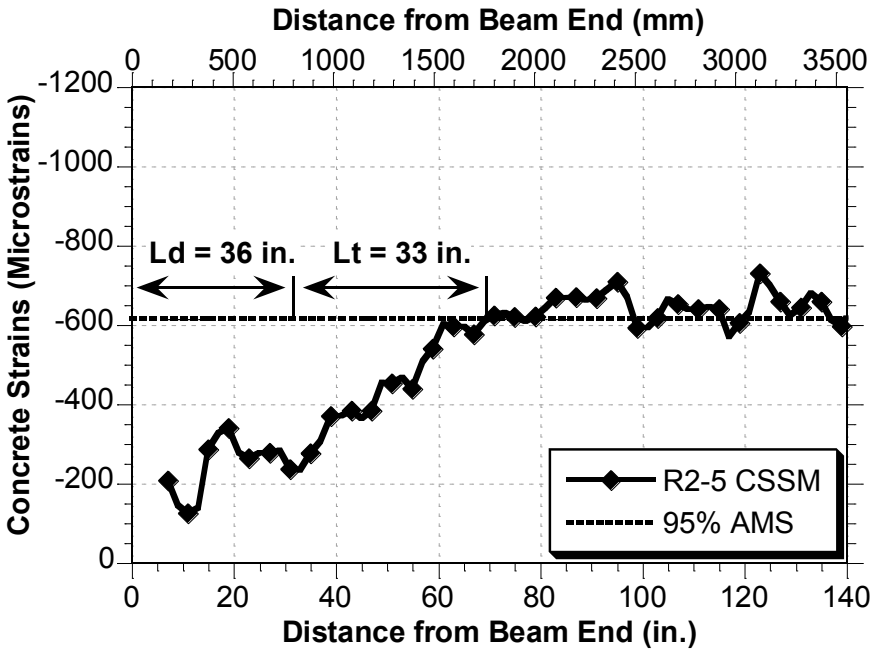

Figure 107 Results of CSSM of Beam Unit R2-5

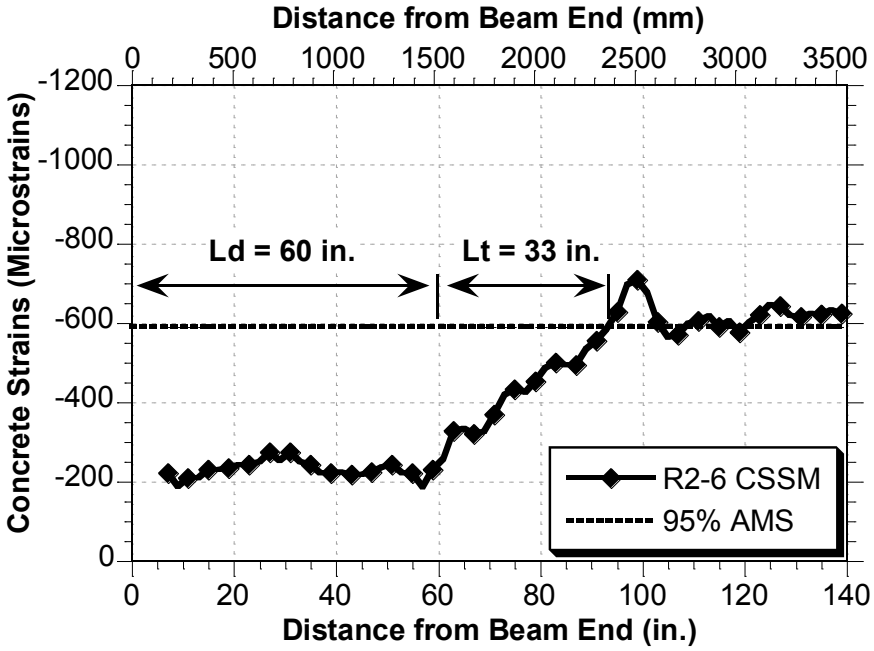

Figure 108 Results of CSSM of Beam Unit R2-6

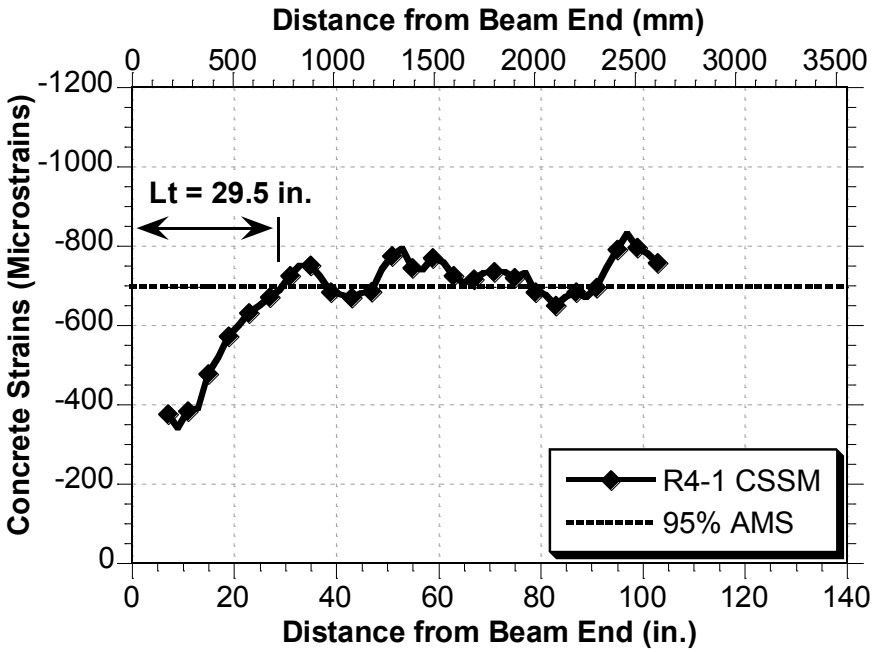

Figure 109 Results of CSSM of Beam Unit R4-1

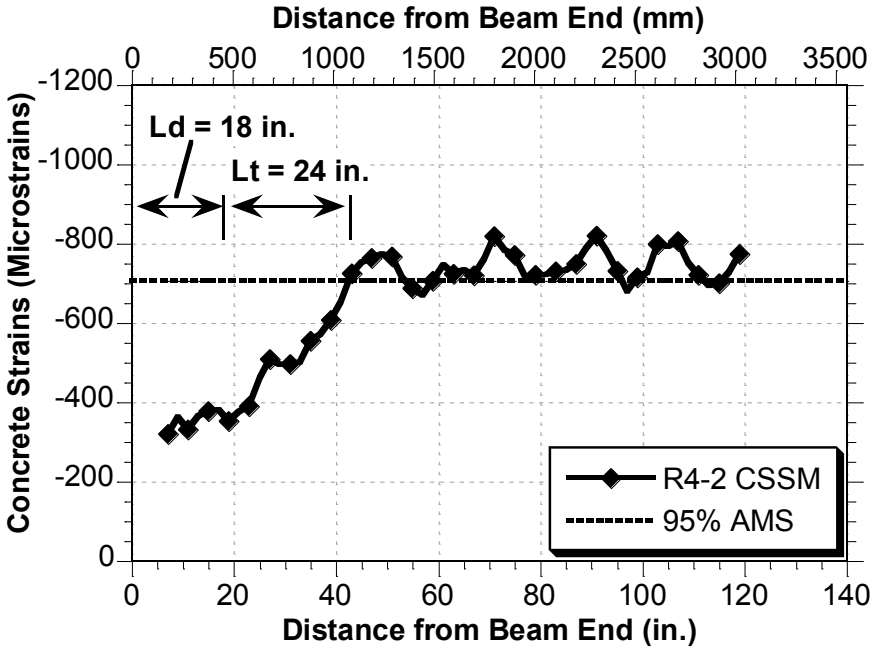

Figure 110 Results of CSSM of Beam Unit R4-2

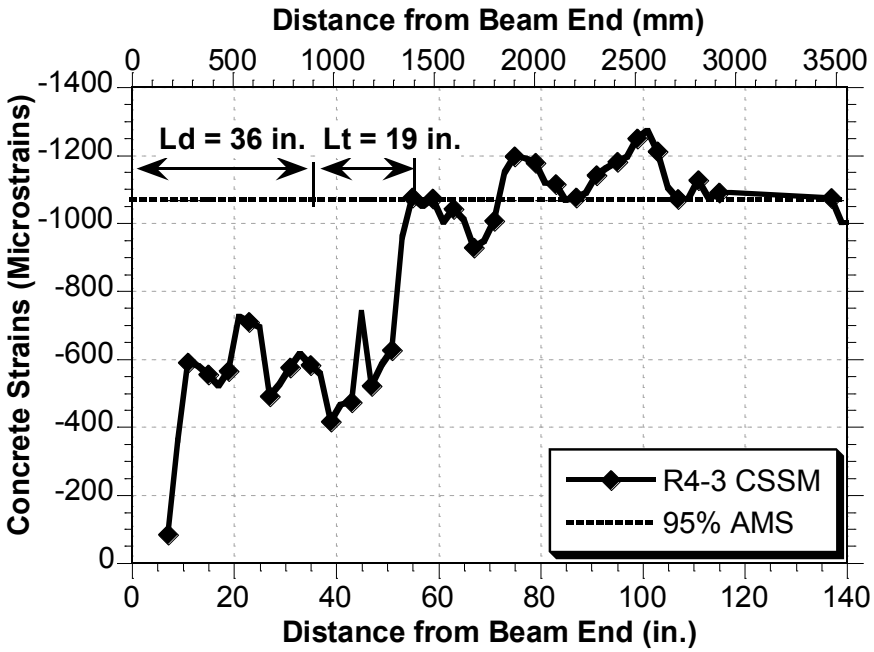

Figure 111 Results of CSSM of Beam Unit R4-3

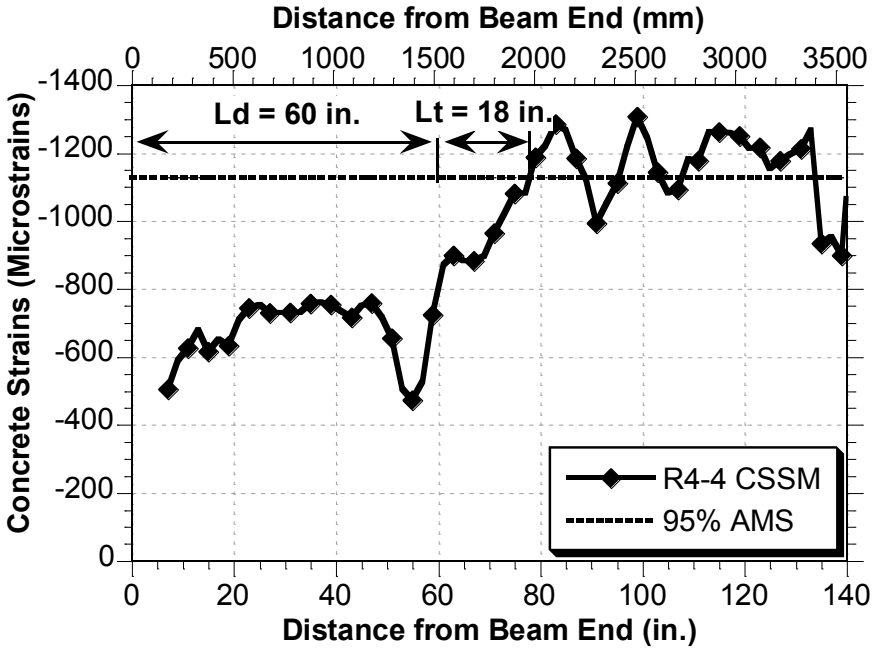

Figure 112 Results of CSSM of Beam Unit R4-4

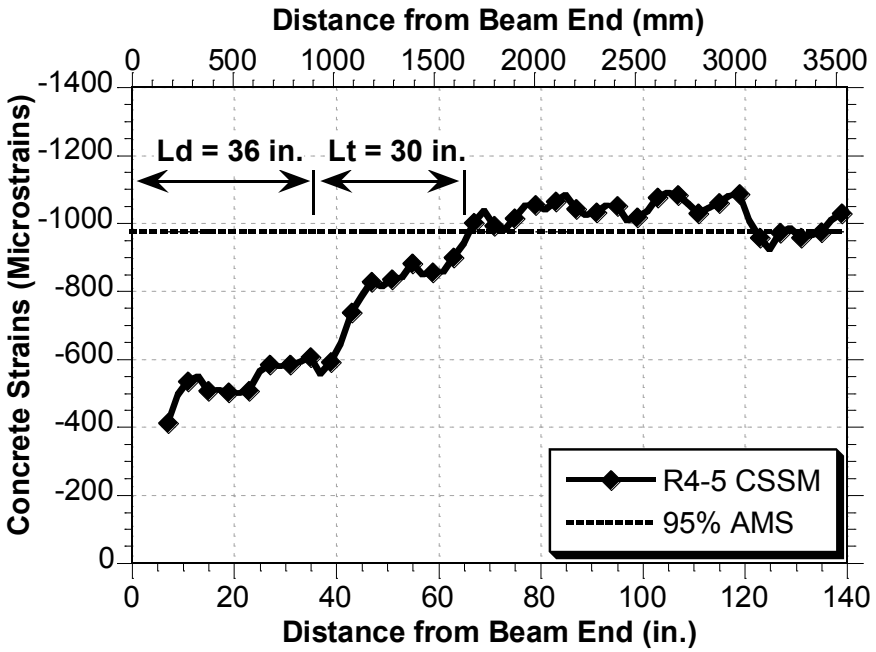

Figure 113 Results of CSSM of Beam Unit R4-5

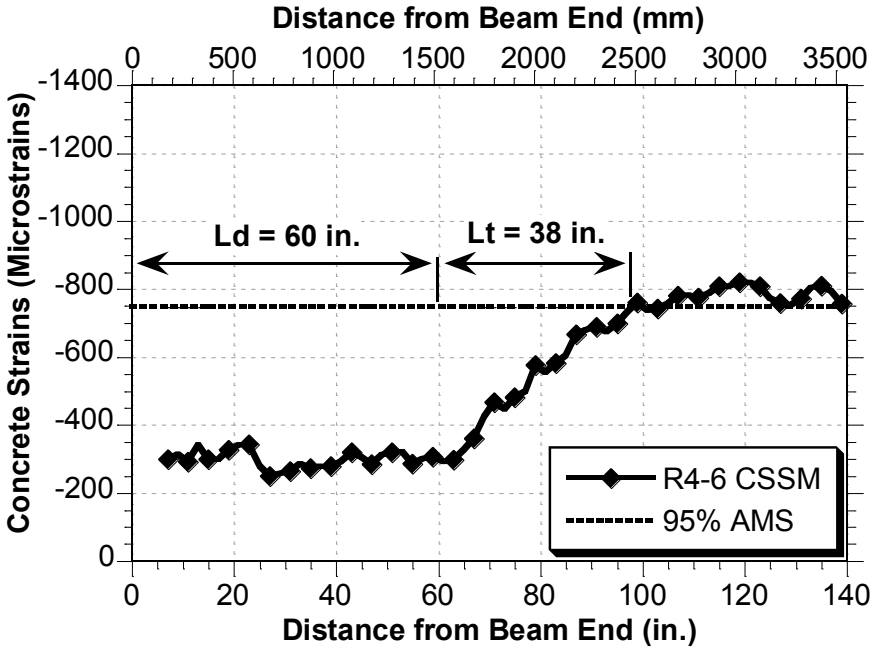

Figure 114 Results of CSSM of Beam Unit R4-6

APPENDIX D

MATERIAL DEFINITION OF CONCRETE DAMAGED PLASTICITY MODEL

Table 32 Compressive Behavior of Concrete Material Model

C1R1_1st		C1R1_2nd		R2_1st		R2_2nd	
σ_c (psi)	$\bar{\varepsilon}_c^{in}$ (in./in.)	σ_c (psi)	$\bar{\varepsilon}_c^{in}$ (in./in.)	σ_c (psi)	$\bar{\varepsilon}_c^{in}$ (in./in.)	σ_c (psi)	$\bar{\varepsilon}_c^{in}$ (in./in.)
2168	0.00E+00	2205	0.00E+00	3581	0.00E+00	3640	0.00E+00
3201	1.64E-05	3261	1.46E-05	4692	2.68E-05	4777	2.39E-05
4134	5.25E-05	4222	4.76E-05	5672	7.34E-05	5790	6.68E-05
4906	1.26E-04	5026	1.16E-04	6447	1.63E-04	6602	1.51E-04
5463	2.48E-04	5615	2.34E-04	6950	3.08E-04	7140	2.91E-04
5777	4.26E-04	5954	4.07E-04	7149	5.17E-04	7365	4.95E-04
5828	6.64E-04	6027	6.41E-04	6641	8.72E-04	6863	8.48E-04
5421	1.01E-03	5592	9.89E-04	5700	1.32E-03	5858	1.30E-03
4835	1.39E-03	4957	1.38E-03	4639	1.79E-03	4717	1.79E-03
4186	1.79E-03	4254	1.79E-03	3650	2.24E-03	3659	2.25E-03
3558	2.18E-03	3577	2.19E-03	2823	2.66E-03	2786	2.68E-03
2994	2.56E-03	2976	2.58E-03	2171	3.05E-03	2109	3.07E-03
2511	2.92E-03	2466	2.94E-03	1674	3.40E-03	1600	3.42E-03
2106	3.27E-03	2045	3.29E-03	1298	3.73E-03	1223	3.75E-03
1772	3.59E-03	1701	3.62E-03	1015	4.04E-03	943	4.06E-03
1497	3.91E-03	1422	3.93E-03	802	4.33E-03	735	4.35E-03
1272	4.21E-03	1196	4.23E-03	639	4.62E-03	579	4.63E-03
1087	4.50E-03	1012	4.52E-03	514	4.89E-03	460	4.91E-03
934	4.79E-03	862	4.81E-03	418	5.16E-03	370	5.17E-03
807	5.07E-03	738	5.08E-03	342	5.43E-03	300	5.44E-03
701	5.34E-03	636	5.36E-03	283	5.69E-03	245	5.70E-03
613	5.61E-03	551	5.63E-03	235	5.95E-03	202	5.96E-03
538	5.88E-03	480	5.89E-03	197	6.21E-03	168	6.22E-03
474	6.14E-03	421	6.16E-03	166	6.47E-03	140	6.47E-03
420	6.40E-03	370	6.42E-03				

Table 25 (cont'd) Compressive Behavior of Concrete Material Model

R4_1st		R4_2nd		R4_3nd	
σ_c (psi)	$\bar{\varepsilon}_c^{in}$ (in./in.)	σ_c (psi)	$\bar{\varepsilon}_c^{in}$ (in./in.)	σ_c (psi)	$\bar{\varepsilon}_c^{in}$ (in./in.)
3640	0.00E+00	2138	0.00E+00	3499	0.00E+00
4777	2.39E-05	3151	1.81E-05	4572	3.13E-05
5790	6.69E-05	4062	5.67E-05	5507	8.32E-05
6602	1.51E-04	4807	1.34E-04	6232	1.80E-04
7140	2.91E-04	5338	2.60E-04	6689	3.33E-04
7364	4.95E-04	5633	4.42E-04	6856	5.48E-04
6862	8.48E-04	5670	6.83E-04	6349	9.05E-04
5857	1.30E-03	5285	1.02E-03	5493	1.34E-03
4716	1.79E-03	4737	1.40E-03	4536	1.79E-03
3659	2.25E-03	4130	1.79E-03	3636	2.23E-03
2786	2.68E-03	3540	2.18E-03	2870	2.64E-03
2109	3.07E-03	3007	2.55E-03	2255	3.02E-03
1601	3.42E-03	2545	2.91E-03	1774	3.37E-03
1223	3.75E-03	2154	3.25E-03	1403	3.70E-03
943	4.06E-03	1828	3.58E-03	1118	4.01E-03
735	4.35E-03	1558	3.89E-03	898	4.31E-03
579	4.63E-03	1334	4.19E-03	728	4.60E-03
461	4.91E-03	1149	4.48E-03	595	4.87E-03
370	5.17E-03	994	4.77E-03	491	5.15E-03
300	5.44E-03	865	5.05E-03	408	5.41E-03
245	5.70E-03	757	5.32E-03	341	5.68E-03
202	5.96E-03	665	5.60E-03	288	5.94E-03
168	6.22E-03	587	5.86E-03	244	6.20E-03
140	6.47E-03	521	6.13E-03	208	6.46E-03

Table 33 Tensile Behavior of Concrete Material

C1R1_1st		C1R1_2nd		R2_1st		R2_2nd	
σ_t (psi)	$\bar{\varepsilon}_t^{in}$ (in./in.)	σ_t (psi)	$\bar{\varepsilon}_t^{in}$ (in./in.)	σ_t (psi)	$\bar{\varepsilon}_t^{in}$ (in./in.)	σ_t (psi)	$\bar{\varepsilon}_t^{in}$ (in./in.)
0	0.00E+00	0	0.00E+00	0	0.00E+00	0	0.00E+00
574	0.00E+00	583	0.00E+00	634	0.00E+00	644	0.00E+00
336	8.46E-04	342	8.46E-04	372	8.46E-04	377	8.46E-04
238	3.89E-03	242	3.89E-03	263	3.89E-03	267	3.89E-03
177	9.92E-03	180	9.92E-03	196	9.92E-03	199	9.92E-03

R4_1st		R4_2nd		R4_3nd	
σ_t (psi)	$\bar{\varepsilon}_t^{in}$ (in./in.)	σ_t (psi)	$\bar{\varepsilon}_t^{in}$ (in./in.)	σ_t (psi)	$\bar{\varepsilon}_t^{in}$ (in./in.)
0	0.00E+00	0	0.00E+00	0	0.00E+00
644	0.00E+00	567	0.00E+00	621	0.00E+00
377	8.46E-04	332	8.46E-04	364	8.46E-04
267	3.89E-03	235	3.89E-03	257	3.89E-03
199	9.92E-03	175	9.92E-03	192	9.92E-03

REFERENCES

REFERENCES

[1]. American Association of State and Highway Transportation Officials, AASHTO-LRFD Bridge Design Specifications, 4th Edition, Washington, DC, 2007.

[2]. American Concrete Institute (ACI), Building Code Requirements for Structural Concrete and Commentary, ACI 318-08, Farmington Hills, Michigan, 2008.

[3]. Abdalla, O.A., Ramirez, J.A., and Lee, R.H., "Tests on Full-Size Pre-tensioned AASHTO Beams with Debonded Strand," Structures Congress XII, 1994, p 1409-1414.

[4]. Hanson, N.W., and Kaar, P.H., "Flexural Bond Tests of Pre-tensioned Prestressed Beams", *ACI Journal, Proceedings* v 55, n 7, p 783-803, January 1959

[5]. Barker, R.M. and Puckett, J.A., "Design of Highway Bridges Based on AASHTO LRFD Bridge Design Specifications", John Wiley & Sons, Inc. New York, NY, 1997.

[6]. Belhadj, A. and Bahai, H., "Friction-Slip: An Efficient Energy Dissipating Mechanism for Suddenly Released Prestressing Bars," *Engineering Structures*, Vol. 23, 2001, p 934-944.

[7]. Kannel, J., French, C. and Stolarski, H., "Release Methodology of Strands to Reduce End Cracking in Pre-tensioned Concrete Girders," *PCI Journal*, V. 42, No. 1, January-February 1997, p 42-54

[8]. Mirza, J.F. and Tawfik, M.E., "End Cracking in Prestressed Members During Detensioning," *PCI Journal*, V. 23, No. 2, March-April 1978, p 66-78.

[9]. Shahawy, M. and Hassan, T., "Effect of Strand Debonding on Prestressed Concrete Girder Performance," Abstract from the *2004 PCI National Bridge Conference*.

[10]. Williams, M.S. and Waldron, P., "Longitudinal Stress Wave Propagation in an Unbonded Prestressing Tendon after Release of Load," *Computers and Structures*, Vol. 34, No. 1, 1990, p 151-160.

[11]. Logan, D. R., "Acceptance Criteria for Bond Quality of Strand for Pre-tensioned Prestressed Concrete Applications", *PCI Journal*, v 42, n 2, p 52-90.

[12]. Williams, M. S. and Waldron, P., "Longitudinal Stress Wave Propagation in an unbounded prestressing tendon after release of load", *Computers and Structures,* v 34, n 1, p 151-160, 1990.

[13]. Hegger, J. , Bűlte, S. and Kommer, B., "Structural Behavior of Prestressed Beam Made with Self-consolidating concrete", *PCI Journal*, v 52, n 4, p 34-42, July/August 2007.

[14]. Bolmsvid, R. and Lundgren, K., "Modeling of Bond Between Three-wire strand and concrete", *Magazine o Concrete Research*, v 58, n 3, p 123-133, 2006.

[15]. Lutz, L. A., "Bond with Reinforcing Steel", *Concrete and Concrete-Making Materials*, p 202, 1994.

[16]. De Nardin, S., Almeida Filho, F.M., Oliveira Filho, J., Haach, V.G., El Debs, A.L.H.C., "Non-linear analysis of the bond strength behavior on the steel-concrete interface by numerical models and pull-out tests", *Proceedings of the Structures Congress and Exposition*, p 1077-1088, 2005, *Metropolis and Beyond - Proceedings of the 2005 Structures Congress and the 2005 Forensic Engineering Symposium*.

[17]. "Specification for the test to determine the bond properties of prestressing tendons", *Materials and Structures*, v 6, n 35, 1973

[18]. Krishnamurthy, D., "Theory for the transmission length of prestressing tendons", *Indian Concrete Journal*, v 47, n 2, p 73-80, Feb 1973.

[19]. Shahawy, M.A., Issa, M. and deV Batchelor, B., "Strand transfer lengths in full scale AASHTO prestressed concrete girders", *PCI Journal*, p 84-96, May-June 1992.

[20]. Hwan Oh, B., Sung Kim, E., Cheol Choi, Y., "Theoretical analysis of transfer lengths in pre-tensioned prestressed concrete members", *Journal of Engineering Mechanics*, v 132, n 10, p 1057-1066, October 2006

[21]. Abrishami, H.H., and Mitchell, D., "Bond characteristics of pre-tensioned strand", *ACI Materials Journal*, v 90, n 3, p 228-235, May-Jun 1983.

[22]. Cousins, T.E., Johnston, D.W., an Zia, P., "Transfer and development length of epoxy coated and uncoated prestressing strand", *PCI Journal*, v 35, n 4, p 92-103, July-August 1990.

[23]. Russell, B.W., Burns, N.H., "Measurement of transfer lengths on pre-tensioned concrete elements", *Journal of structural engineering New York, N.Y.*, v 123, n 5, p 541-549, May 1997.

[24]. Kaar, P.H. and Magura, D.D., "Effect of strand blanketing on performance of pre-tensioned girders", *PCI Journal*, v 10, n 6, p 20-34, Dec 1965.

[25]. Ghosh, S.K. and Fintel, M., "Development length of prestressing strands, including debonded strands, and allowable concrete stresses in pre-tensioned members", *PCI Journal*, v 31, n 5, p 38-57, September-October 1986

[26]. Collins, M.P., Mitchell, D. and MacGregor, J.G., "Structural design considerations for high-strength concrete", *Concrete International*, v 15, n 5, p 27-34, May 1993

[27]. Martí-Vargas, J.R., Arbeláez, C.A., Serna-Ros, P., Fernández-Prada, M.A., Miguel-Sosa, P.F., "Transfer and development lengths of concentrically prestressed concrete", *PCI Journal*, v 51, n 5, p 74-85, September-October 2006

[28]. ABAQUS Documentation, version 6.9

[29]. Macgregor, J.G. an Wight, J.K., "Reinforced Concrete-Mechanics and Design", 4th edition, 2004

[30]. Janney, J.R. "Nature of bond in pre-tensioned prestressed concrete," *ACI Journal, Proceedings* v 25, n 9, May 1954, p 717-736

[31]. Leonhardt, F., "Prestressed Concrete – Design and Construction", Wilhem Ernst & Sohn, Berlin, 1964

[32]. Russell, B.W., and Burns, N.H., "Design Guidelines for Transfer, Development and Debonding of large Diameter Seven wire strands in pre-tensioned concrete girders." *Research Report 1210-5F. Center of Transportation Research, Bureau of Engineering Research*, University of Texas at Austin, January 1993.

[33]. Thatcher, D.B., Heffington, J.A, Kolozs, R.T., Sylva III, G.S., Breen, J.E., and Burns,N.H., "Structural Lightweight concrete prestressed girgers and panels." *Research report 1852-1 Center for transportation research. Bureau of Engineering Research*, University of Texas at Austin, January 2002.

[34]. Lee, J., Fenves, G. L., "A plastic-damage concrete model for cyclic loading of concrete structures", *J. Engng Mech. ASCE*, accepted, Aug 1998

[35]. Jankowiak, T. and Lodygowski,T., "Identification of parameters of concrete damage plasticity constitutive model". *Foundations of Civil and Environmental Engineering*, 2005, 6: 53-69.